Imperial College of Science, Technology and Medicine
Department of Earth Science and Engineering

Investigation of Foam Flow in Porous Media via Physics-based Modelling and Numerical Simulations

Haosen Zhang

Supervisors: Dr Pablo R. Brito-Parada, Prof Stephen J. Neethling, and Prof Yanghua Wang

Submitted in part fulfilment of the requirements for the degree of Doctor of Philosophy in Earth Science and Engineering and the diploma of Imperial College London, November 2023

Declaration of Originality

I hereby declare that, except where express reference is made to the work of others, the contents of this dissertation are original and have not been submitted in whole or in part for any other degree or qualification at this or any other university. This dissertation is my own work and contains nothing that is the result of collaboration with others, except as indicated in the text and acknowledgements.

Haosen Zhang

November 2023

Copyright Declaration

The copyright of this thesis rests with the author. Unless otherwise indicated, its contents are licensed under a Creative Commons Attribution-Non Commercial 4.0 International Licence (CC BY-NC).

Under this licence, you may copy and redistribute the material in any medium or format. You may also create and distribute modified versions of the work. This is on the condition that: you credit the author and do not use it, or any derivative works, for a commercial purpose.

When reusing or sharing this work, ensure you make the licence terms clear to others by naming the licence and linking to the licence text. Where a work has been adapted, you should indicate that the work has been changed and describe those changes. Please seek permission from the copyright holder for uses of this work that are not included in this licence or permitted under UK Copyright Law.

Haosen Zhang

November 2023

Acknowledgements

I would like to express my heartfelt gratitude to my supervisors, Dr. Pablo R. Brito-Parada, Prof. Stephen J. Neethling, and Prof. Yanghua Wang. Throughout my academic journey, they have fulfilled their roles as mentors with unwavering dedication, closely monitoring my scholarly progress and offering generous guidance and assistance.

Many thanks to all my PhD colleagues, as well as the staff in the Department of Earth Science and Engineering, for their help, for sharing experiences, and guidance during the process.

I also would like to express my gratitude to my parents, grandparents, siblings, and all my family who have consistently been there for me. I would like to thank Yueyue, who has consistently provided encouragement throughout the process, for her patience and support.

Finally, and not less important, I would like to express my gratitude to Prof. Yanghua Wang, Director of Resource Geophysics Academy, and the sponsors of the academy, for funding my PhD studies.

Abstract

Predicting foam dynamics in porous media poses significant challenges, primarily due to the multitude of gas-liquid interfaces within foam and their intricate interactions with confined structures. This study advances our understanding of foam physics by introducing novel foam modelling approaches and examining foam flow in representative scenarios. Three foam modelling methods are integrated and thoroughly investigated: the quasi-static soap film model, the viscous froth model, and the boundary integral method. The first method is conventionally employed to directly predict foam configurations in stationary equilibrium or in quasi-static motion, and in this thesis, it is extended to the pore-network scale. The research reveals that pressure differences between pore throats play a similar role in minimising overall surface energy as film tension does at the pore scale. The second approach pertains to the viscous froth model, originally designed for monolayer foams constrained in Hele-Shaw cells, and conventionally considered in two dimensions (2D). In this thesis, the 2D viscous froth model undergoes an extension into three dimensions (3D). This extension highlights the impact of the third dimension on foam behaviour, effectively connecting the quasi-static soap film model with the dynamic viscous froth model. Its application to a viscous froth lens in 3D reveals that the driving velocity-to-gap size ratio is a dominant factor in determining the motion of a viscous froth lens. Finally, a new method for modelling dry foam dynamics is developed based on the boundary integral method which considers the viscosity of gas, not just that of liquid, making it applicable to a broader range of foam flow rates. This method is utilised to investigate the typical problem of film motion in a diverging-converging channel, offering a new perspective on the emergence of yield stress. It is also implemented in 2D, connecting to the modelling of foam in Hele-Shaw cells.

Table of Contents

Declaration of Originality i

Copyright Declaration iii

Acknowledgements v

Abstract vii

1 Introduction 1

1.1 Foam as displacing agent 1

1.2 Porous media 4

1.3 Overview and scope 4

2 Literature review and thesis objectives 7

2.1 Foam 7

2.2 Foam generation in porous media 10

2.2.1 Leave-behind 11

2.2.2 Snap-off 11

2.2.3 Lamella division 13

2.2.4 Pinch-off 14

2.3 Foam stability and coalescence in porous media 15

2.3.1 Capillary suction coalescence 16

2.3.2 Bubble coarsening and coalescence 19

2.4 Foam flow in porous media 20

2.4.1 T1 topological transformation 21

2.4.2 Flow intermittency and bubble trapping 22

2.4.3 Increased sweep efficiency . . . 24
2.4.4 Non-Newtonian behaviour of foam . . . 26
2.5 Pore-scale modelling of foam flow . . . 29
2.5.1 Quasi-static foam modelling . . . 30
2.5.2 Force-equilibrium modelling for dynamic foam motion . . . 32
2.5.3 Computational fluid dynamics for foam . . . 34
2.6 Challenges and thesis objectives . . . 35

3 Quasi-static film motion in porous medium models with blocked throats 38
3.1 Introduction . . . 38
3.2 Porous medium models . . . 39
3.3 Pore-scale method . . . 41
3.3.1 Film tension force . . . 44
3.3.2 Volume restoring motion . . . 46
3.4 Pore network-scale method . . . 47
3.4.1 Mass conservation in pores . . . 49
3.4.2 Gradient of system energy . . . 49
3.4.3 Algorithms for surface energy minimisation . . . 54
3.5 Verification of the two-level method . . . 55
3.6 Numerical results . . . 61
3.6.1 Film motion in sharp pores . . . 61
3.6.2 Film motion in rounded pores . . . 65
3.6.3 Yield stress of film motion . . . 68
3.7 Conclusions . . . 69

4 Foam flow through confined straight channels 71
4.1 Introduction . . . 71
4.2 Viscous froth lens in straight channels . . . 74
4.3 Viscous froth model . . . 76
4.3.1 2D viscous froth model . . . 76

4.3.2 Young-Laplace equation to 2D viscous froth model 77
4.3.3 Viscous froth model in 3D 80
4.3.4 Dimensionless viscous froth model 81
4.4 Numerical methods 83
4.4.1 Numerical method for 3D viscous froth model 83
4.4.2 Steady-state configuration of 2D viscous froth lens 86
4.4.3 Scheme of numerical simulations 88
4.5 Numerical results 90
4.5.1 Steady state of 2D viscous froth lens 90
4.5.2 Evolution of 3D viscous froth lens 92
4.5.3 Drag coefficient as fitting parameter 96
4.5.4 Dependence of drag coefficient on position along film 98
4.6 Discussion 101
4.7 Conclusions 102

5 Boundary-integral modelling for dry foam in three dimensions 104
5.1 Introduction 104
5.2 Mathematical formulation 105
5.2.1 Stokes flow equations 105
5.2.2 Boundary integral equations 108
5.2.3 The extreme case of dry foam 111
5.2.4 Boundary condition on the wall 113
5.2.5 Singularity and near-singularity subtraction 113
5.2.6 Singular forces on bulk Plateau borders 115
5.3 Numerical methods 117
5.3.1 Surface representation and mesh refinement 117
5.3.2 Calculation of the film mean curvature and normal vector 119
5.3.3 Calculation of the double-layer and single-layer potentials 122
5.3.4 Discrete linear system of equations 124
5.3.5 Motion of bulk Plateau borders 126

5.3.6 Evolution of the foam configuration . . . 130
5.4 Numerical results . . . 130
5.4.1 Foam evolving in a simple shear flow . . . 130
5.4.2 Film motion in a diverging-converging channel . . . 136
5.5 Conclusions . . . 145

6 Other applications of the boundary-integral approach for dry foam 148
6.1 Introduction . . . 148
6.2 Energy consumption during film motion in channels . . . 149
6.2.1 Overall energy consumption . . . 149
6.2.2 Energy consumption of individual components of film motion . . . 150
6.2.3 Energy consumption due to imposed flow-relaxation interaction . . . 151
6.2.4 Energy transport trajectories . . . 152
6.2.5 Yield stress of film motion . . . 153
6.3 Boundary integral method in 2D . . . 157
6.3.1 Nyström method . . . 159
6.3.2 discretisation of the 2D boundary integral equation . . . 161
6.3.3 Single bubble in Hele-Shaw cells . . . 164
6.4 Conclusions . . . 167

7 Conclusions and future work 169

Bibliography 174

List of Tables

3.1 Pore dimensions used in the simulations 41

4.1 Values of H and η and mesh resolutions employed in 3D simulations 90

5.1 Two applications of the boundary integral method for dry foam 130

List of Figures

2.1 Illustration of foam structure 8

2.2 Micromodel and foam in confined Hele-Shaw cell 9

2.3 Foam generation mechanisms 12

2.4 Pinch-off mechanism 15

2.5 Foam collapse due to liquid drainage and gas diffusion 16

2.6 Isotherms of disjoining pressure and energy 17

2.7 Two-dimensional T1 topological transformation 22

2.8 Three-dimensional T1 topological transformation 23

2.9 Illustration of foam increasing sweep efficiency in porous media 26

2.10 Two regimes of steady-state foam flow in homogeneous porous media 28

3.1 Pore geometry 40

3.2 Porous medium models for studying quasi-static film motion 42

3.3 Schematic diagram for pore-scale method 43

3.4 Schematic diagram for pore network-scale method 48

3.5 Porous medium model referenced in the derivation of the steepest descent direction of total surface energy 53

3.6 Verification of pore-scale method 57

3.7 Motion of two films in a three-pore porous medium model predicted by the pore-scale method 58

3.8 Comparison of results of pressure difference across a three-pore model by the pore- and pore network-scale methods 59

3.9 Comparison of gas amount through two interior throats of a three-pore porous medium model by the pore- and pore network-scale methods 60

3.10 Pressure difference across porous medium models with different numbers of sharp downstream pores 62
3.11 Illustration of the arising of additional jump due to trapped lamellae 64
3.12 Variation of volume swept by a film in a pore as Plateau borders continuously move on pore walls 66
3.13 Pressure difference across porous medium models with different numbers of rounded downstream pores 67
3.14 Volume-averaged pressure difference across porous medium models 69

4.1 Viscous froth lens observed in two and three dimensions 75
4.2 Discrete representations of films in two and three dimensions 84
4.3 Effective film tension due to drag forces 88
4.4 Iterative convergence of viscous froth lens configuration at steady state predicted by the gradient descent method 91
4.5 Convergence history of three-fold point location at steady state predicted by the gradient descent method 92
4.6 Configurations of three-dimensional viscous froth lens in dynamic motion 93
4.7 Dynamic evolution of the z-coordinate of the four-fold node of the viscous froth lens in three dimensions 94
4.8 Z-coordinate of four-fold node or three-fold point at steady state as a function of the driving velocity-to-gap size ratio 95
4.9 Enhanced depiction of three-dimensional viscous froth lens configuration at steady state by two-dimensional viscous froth model with adapted drag coefficient 97
4.10 Relation between apparent drag force and normal velocity of surface Plateau border at $U = 0.3$ and $H = 0.2$ 99
4.11 Relation between apparent drag force and normal velocity of surface Plateau border at $U = 0.4$ and $H = 0.2$ 100

5.1 Schematic diagram of a foam consisting of three bubbles attached on the surface of a solid plate 106

5.2 Two types of grid for discretising foam films and computing single-layer potentials, respectively . . . 119

5.3 Accuracy of mean curvature and unit normal vector at the border of a film computed by the contour integral method . . . 121

5.4 Comparison between the velocity magnitudes at given field points computed using the nonsingular contour integral method and the one-point trapezoidal rule, respectively . . . 123

5.5 Basic elements on film borders . . . 127

5.6 Equilibrium configuration of a five-bubble foam . . . 131

5.7 The evolution of the five-bubble foam in a simple shear flow at Ca unity and tending to infinity, respectively . . . 132

5.8 Volume change of bubble V in the five-bubble foam without the effect of the motion of bulk Plateau borders on the motion of the remaining part of the foam . . . 134

5.9 Volume change of bubble V in the five-bubble foam with the effect of the motion of bulk Plateau borders on the motion of the remaining part of the foam . . . 134

5.10 Comparison between velocity field results within $y = 0$ plane under two different treatments of the bulk Plateau border . . . 135

5.11 Geometry of converging-diverging channel needed in the boundary integral method 137

5.12 Triangulated surface of converging-diverging channel . . . 138

5.13 Comparison between results of imposed flow by boundary integral method and finite volume method, respectively . . . 139

5.14 Film advection by imposed flow . . . 140

5.15 Mean curvature perturbation of film configuration at swept volume 0.4 . . . 142

5.16 Fourier expansion of film mean curvature perturbation . . . 142

5.17 First, third, and fifth components of curvature perturbation and the induced normal velocity of film . . . 144

5.18 Relation between film normal velocity and mean curvature deviation . . . 145

6.1 Energy transport via surface energy during film motion in diverging-converging channel153

6.2 Pressure drop and surface area change during quasi-static film motion in diverging-converging pores with different diverging angles 155
6.3 Integral of pressure drop as a function of the jump in film area 156
6.4 Film area change due to imposed flow and relaxation process during quasi-static film motion 158
6.5 Equidistant grid and Gauss-Legendre grids used in simulations by two-dimensional boundary integral method 162
6.6 Equidistant grid and Gauss-Legendre grid for simulating a bubble relaxation 165
6.7 Boundary-integral results of normal velocity of bubble boundary at different drag coefficients 166
6.8 Normal velocity of bubble boundary by viscous froth model 166

Chapter 1

Introduction

Foam is a complex fluid that consists of two phases of fluid, namely gas bubbles dispersed within a continuous liquid phase, and can be found in nature, such as sea foams and foam nests of animals [1]. Due to its special physical properties, such as low density, high specific area, and high viscosity, foam is widely used in various industries including cosmetics, fire-fighting, mineral processing, soil remediation, and oil recovery [2]. In specific applications like soil remediation and oil recovery processes, foam serves as a displacing agent that flows through porous media, redirecting in-situ fluids away from the media.

1.1 Foam as displacing agent

Utilization of foam in oil production processes is a typical scenario where foam is used as a displacing agent. There are typically three stages in the life of oil production: primary, secondary, and tertiary recovery [3]. Primary recovery stage refers to the initial oil recovery period when oil transport by the high natural pressure of the reservoir. This natural pressure, however, declines as the oil is forced out of the reservoir, which tends to cease eventually. Then, gas or water is injected into the reservoir to maintain the reservoir pressure, and oil production enters the secondary recovery stage. After the primary and secondary stages, roughly two-thirds of the original oil in reservoirs is trapped due to the capillary forces, forming connected

phases in the unswept zones or discontinuous phases in the swept zones [4].

The tertiary recovery, also known as enhanced oil recovery (EOR), is implemented to extract the remaining oil in the reservoir. This stage can lead to a final production of 40% to 60% of the total oil in place [3]. EOR techniques can be classified into two categories: thermal and non-thermal methods [5]. Thermal EOR methods supply heat to the reservoir and are better suited for heavy oil production [5]. On the other hand, non-thermal methods are typically used for light oil production, including gas flooding, solvent flooding, and chemical flooding.

Injecting gases into reservoirs, such as carbon dioxide (CO_2), nitrogen (N_2), steam, natural gas, and flue gas, is conducted in gas flooding. This process can be categorised into two types based on the miscibility of the injected gas with oil: miscible gas flooding and immiscible gas flooding. For instance, CO_2 becomes miscible with a wide range of crude oil at moderate reservoir temperature and pressure above the minimum miscibility pressure [5]. CO_2 has gained significant attention as a flooding gas due to its status as the largest global source of greenhouse gas emissions, which can be sequestrated accompanied by enhancing oil production [6]. Similar to CO_2, N_2 flooding can also become miscible flooding under certain pressure and temperature, though N_2 usually has a higher minimum miscibility pressure than CO_2. In the process of miscible flooding, a mixing zone develops at the interface between the displacing and displaced fluids. This leads to the significant reduction of interfacial tension, consequently eliminating the capillary forces that retain oil in the reservoir [7].

Gas flooding offers high microscopic efficiency in displacing oil, which results in low oil saturation after gas invades the flow path. However, it suffers from low macroscopic recovery efficiency mainly due to the adverse mobility ratio between gas and the displaced fluid namely oil. The mobility λ of a fluid is defined as, $\lambda = k_e/\mu$, where k_e and μ are the effective permeability and the viscosity of a fluid in porous media [5]. The mobility ratio M is then defined as the ratio between the mobility of the displacing fluid and that of the displaced fluid, i.e. $M = \lambda_{\text{displacing}}/\lambda_{\text{displaced}}$, which is regarded as favourable when less than unity. Gas flooding in practice typically exhibits a mobility ratio ranging from 10 to 100, indicating an unfavourable mobility ratio [8].

Under unfavourable mobility conditions and low gas density, the gas flooding process is accompanied by three phenomena that contribute to poor vertical and areal sweep efficiencies. The first phenomenon is viscous fingering, which arises from the lower viscosity of gas compared to oil [4]. The second phenomenon is gravity override, driven by the lower density of gas in comparison to oil, resulting in preferential gas flow within the uppermost layer of the reservoir [9]. The third phenomenon is flow channelling, associated with reservoir heterogeneity, where gas tends to preferentially flow through high-permeability regions due to reduced flow resistance [10]. These phenomena collectively lead to premature gas breakthrough, leaving a significant portion of the oil unrecovered.

Since the 1960s, foam has emerged as a vital mobility control agent, effectively reducing gas mobility and addressing issues like fingering, channelling, and gravity override, primarily due to its elevated viscosity. The substantial reduction in gas mobility results in the establishment of a stable displacement front, thereby enhancing sweep efficiency. In practical applications, three primary foam injection strategies have been employed: pre-formed foam injection, co-injection of surfactant solution and gas, and surfactant-alternating-gas (SAG) injection [8]. Unlike pre-generated foam, co-injection and SAG methods generate foams in-situ. SAG injection has demonstrated the capability to produce stable in-situ foams [11], leading to significantly increased trapped gas saturation within porous media [12]. Moreover, compared to the co-injection method, SAG exhibits higher gas mobility, which aids in maintaining favourable injectivity [13].

The practical use of foam as a displacing agent involves two key objects: one aqueous foams and the other the solid matrix, present as a porous medium within the reservoir. The porous medium acts as the framework through which the foam must navigate and displace the target fluid, typically oil. The geometry of this matrix plays a critical role in determining how effectively the foam can propagate through the reservoir. Understanding the complex interplay between the foam, the porous structure, and the target fluid is essential for optimizing the performance of foam-based displacement processes.

1.2 Porous media

A porous medium refers to a substance, like rocks found in subterranean reservoirs, that is composed of both a solid matrix and void spaces [14]. The proportion of the interconnected void space within the porous medium is referred to as its effective porosity. These interconnected void spaces within the porous medium serve as pathways for fluid movement into or out of the medium. In a realistic porous medium such as carbonate, sandstone, or shale, pore sizes can range widely, from 0.01μm to 100 μm, spanning six orders of magnitude in length scale [14]. This multiscale variability necessitates the characterisation of fluid flow at multiple scales, ranging from the pore to the field scale. Establishing a connection between fluid behaviour at different scales in porous media poses a challenge that may necessitate further simplifications in this so-called upscaling process.

A simplified representation of a porous medium is a pore network where the void space is partitioned into pore bodies that are connected by narrow pore throats [15]. The number of throats connected to a pore is known as its coordination number, which is equivalent to the number of the neighbouring pores of the pore. The pore network may only capture a subset of the characteristics of the actual porous medium, such as pore size and connectivity. Additionally, a pore network, such as an idealised lattice, may not be based on a realistic porous medium. Nonetheless, studies examining fluid flow through simplified porous media structures still provide valuable insights into comprehending the dynamics of flow of fluid, like foam, within porous materials [16]. These simplified porous medium models serve as important tools in grasping fundamental principles governing fluid behaviour within porous media, offering a foundation upon which more complex and realistic scenarios can be built.

1.3 Overview and scope

Effectively employing foam in industries like enhanced oil recovery and soil remediation necessitates a comprehensive grasp of foam physics within porous media, contingent upon accurately predicting the evolution of foam configuration. The primary focus of this thesis is on predicting

foam configuration through physics-based foam modelling and its applications in comprehending foam flow in porous media. In Chapter 2, the thesis initiates by conducting a thorough literature review to lay a robust background for understanding the key novel contributions of this work, which are subsequently unfolded in the following chapters. The review underscores the complex nature of foam, characterised by its intricate structure and multiscale dynamics.

The principal contribution of this work unfolds progressively in Chapter 3, 4, 5, and 6. These chapters follow a logical sequence, transitioning from quasi-static to dynamic foam flow scenarios. In all these scenarios, the assumption of dry foam is made in the foam modelling processes. In Chapter 3, quasi-static foam flow in porous medium models is further explored, particularly when dealing with the presence of trapped pore throats. The effect of these trapped pore throats on a fundamental physical property of foam flow in porous media, the yield stress, is examined. To achieve this, this work introduces a novel method operating at the pore-network scale, aimed at predicting the behaviour of quasi-static foam. The work presented in this chapter has been published in Colloids and Surfaces A: Physicochemical and Engineering Aspects, titled *Yield stress of foam flow in porous media: The effect of bubble trapping* (DOI: https://doi.org/10.1016/j.colsurfa.2022.130246).

In Chapter 4, a typical scenario of dynamic foam flow in confined straight channels, i.e. a viscous froth lens in a straight channel, is explored in 3D. The primary motivation behind this investigation is to assess how the third dimension, along the narrow channel gap, influences foam behaviour. Conventionally, this problem has been approached using numerical simulations in 2D, employing a dynamic foam model known as the 2D viscous froth model. In contrast, this work introduces a 3D mathematical model, building upon the quasi-static method discussed in Chapter 3, to account for the impact of the third dimension. In addition, also based on the quasi-static approach, this work establishes a new method to predict the steady-state configuration of the froth lens in 2D. This work has been published in Physics of Fluids, titled *A comparative study of a viscous froth lens in two and three dimensions* (DOI: https://doi.org/10.1063/5.0174974).

In Chapter 5, the boundary-integral representation of Stokes flow is explored in the context of

dry foam. A boundary integral equation is derived for low-Reynolds flow of dry foam. Various approaches for solving this equation, including singularity subtraction and numerical computation methods, are detailed in the chapter. The method is applied to two scenarios of foams in bulk and in the presence of solid walls, respectively. This work has been published in Journal of Computational Physics, titled *Investigation into three-dimensional dry foam modelling using the boundary integral method* (DOI: https://doi.org/10.1016/j.jcp.2023.112724).

Further applications of the resultant boundary integral equation for dry foam are explored in Chapter 6, extended to investigating aspects like the resistance encountered in foam flow and the potential for modelling 2D foam flow, akin to what is observed in the 2D viscous froth model discussed in Chapter 4. All of these investigations are conducted within the framework of the boundary integral method, offering valuable insights into the behaviour of dry foam. The work presented in Chapter 6 would be further extended in the future for publication purposes. Finally, overall conclusions for the thesis and possibilities for future work are presented in Chapter 7.

Chapter 2

Literature review and thesis objectives

2.1 Foam

Aqueous foam can be described as a dispersion of gas bubbles within a liquid phase network. When the liquid volumetric fraction is low, typically less than 1%, the foam is termed "dry", and the bubbles exhibit a polyhedral shape, as illustrated in the upper layer of Figure 2.1 (a). Conversely, as the liquid volumetric fraction increases, the bubbles tend to become spherical, as depicted in the lower layer. Consequently, with increasing liquid volumetric fraction, the foam undergoes a transition from densely-packed, polyhedral bubbles to a more diluted suspension of spherical bubbles. This alteration in foam morphology exerts significant impacts on its physical properties. For instance, as the liquid volumetric fraction continues to rise, the wet foam transforms into a "bubbly liquid" and the shear modulus of this bubbly liquid approaches zero.

In the case of dry foam, where the liquid volumetric fraction remains at a low level, less than 1%, its structural components exhibit distinctive length scale characteristics, as elucidated in [19]. These components encompass foam films, Plateau borders, and nodes, as depicted in Figure 2.1(b). Thin foam films, often referred to as lamellae, are stabilised by surfactant molecules residing at their gas-liquid interfaces. The surfactants orient themselves with their hydrophilic heads within the liquid phase and their hydrophobic chains within the gas phase. The length

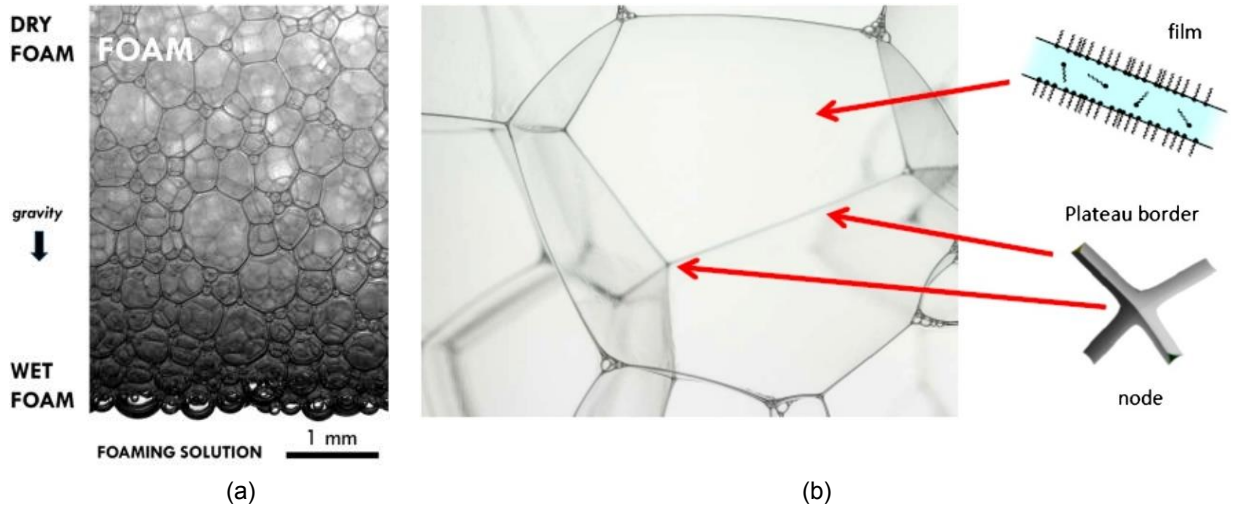


Figure 2.1: Foam structure and its constituent structural elements. (a) Foam structure under the influence of gravity, from Drenckhan and Hutzler [17]. In this scenario, gravity plays a crucial role in shaping the morphology of the foam. As observed in the top layer of the foam, the influence of gravity causes the foam to become drier and the bubbles to adopt polyhedral shapes, while the bottom layer tends to be wet and exhibit more spherical bubbles. (b) Structural elements of foam, including foam films, Plateau borders which form at the intersection of three films, and nodes that occur at the convergence of four Plateau borders, from Langevin [18]. Surfactant molecules are dispersed across the surfaces of the films to maintain the stability of the thin films.

scale across the film is significantly smaller than the dimensions in the other two orthogonal directions tangent to the film. Plateau borders serve as connectors between three adjacent lamellae, along the edges of polyhedral bubbles, and are characterised by a predominant dimension along their length. In contrast, nodes exhibit relatively uniform length scales in all directions and serve to connect Plateau borders to each other.

The static structure of dry foam adheres to Plateau's law [20], which dictates that three foam films converge at 120° angles at a Plateau border, while four Plateau borders intersect at 109.5° at a node. As the foam transitions to a wetter state, these structural elements become less discernible due to a reduction in the contrast of their length scales [19].

The overall structure of a foam can be effectively characterised by three key parameters: foam quality, foam texture, and bubble size distribution. Foam quality denotes the volumetric fraction occupied by gas within a foam. This definition is used to depict an existing foam, in contrast to another one useful in foam flooding experiments, which is defined by gas and liquid

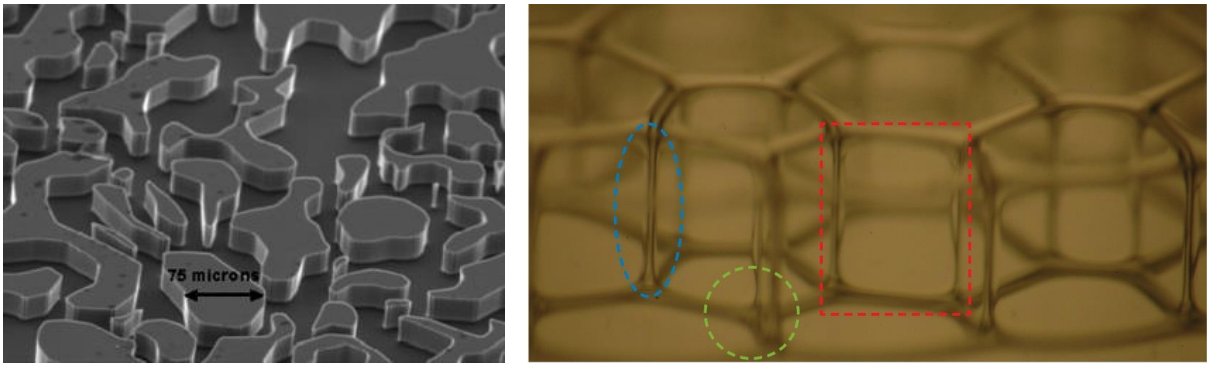


Figure 2.2: Micromodels serve as mimics of porous media, constraining foam into a monolayer state similar to foam within a Hele-Shaw cell. (a) A micromodel mimicking a porous medium, from Kovscek et al. [21]. A micromodel, like a Hele-Shaw cell, features two covering walls. However, it may incorporate numerous additional side walls that form the irregular channels. (b) A monolayer foam confined within a Hele-Shaw cell, from Arif et al. [22].

volumetric flow rates in Section 2.4.2. A foam becomes dry at a low volumetric liquid fraction, or equivalently, high foam quality. Particularly, a foam is referred to as a dry foam when the foam quality exceeds 99% [19]. Foam texture, on the other hand, refers to the density of lamellae found within a unit volume of foam. This texture significantly influences the foam's strength, with fine-textured foam featuring a high lamella density and being deemed "strong" [8]. Conversely, foam with a coarser lamella distribution is generally regarded as "weak" [8]. Based on the bubble size distribution, a foam can be classified into one of two categories: monodisperse, where bubble sizes are uniform and consistent, and polydisperse, where bubble sizes exhibit a non-uniform distribution throughout the foam's structure.

When foam is contained within a porous medium, its configuration can differ significantly from that of foam in bulk. In contrast to bulk foam, a substantial portion of foam films, Plateau borders, and nodes adhere to the solid surface, and the foam's behaviour is strongly influenced by the presence of the solid matrix. The effects of the solid matrix are primarily two-fold: it influences the shape of the bubbles as the solid surfaces act as partial boundaries, and it affects the movement of Plateau borders on the solid surfaces. For the latter, the Plateau borders are typically perpendicular to the solid surfaces when they are in a state of stationary equilibrium, but they can deviate from being normal to the solid surfaces when in motion [23]. To comprehensively grasp the impact of the solid matrix on foam motion, research has concentrated on

visualising foam flow within porous media. However, owing to the intricacies of the 3D interconnected pore space in a realistic porous medium, many experimental studies opt to employ microfluidic porous medium models, namely micromodels. The micromodels are designed to simulate the geometric and topological properties of real-world porous media while typically confining the foam flow to two-dimensional (2D) scenarios to enhance visualisation [24]. The unique design of micromodels, however, may have influenced the relative significance of different mechanisms in foam flow within a realistic porous medium, such as when determining whether Roof's snap-off (discussed in more detail later) serves as the primary mechanism for foam generation [21, 25].

Figure 2.2 (a) illustrates a micromodel crafted by etching a pore network onto one transparent silicon plate and sealing it with another plate. This micromodel exhibits symmetry about a midplane between the two covering plates, enabling a 2D representation of foam flow by projecting properties onto this midplane [19]. However, unlike an idealised purely 2D flow, the foam within the micromodel is influenced by the two covering plates, which apply viscous forces to the foam, thereby affecting its behaviour. The confinement of foam within the micromodel is akin to that within a Hele-Shaw cell [22] which only consists of two closely placed flat plates and two side walls, as shown in Figure 2.2(b). In micromodels or Hele-Shaw cells, horizontal Plateau borders attach to either of the two covering plates, whereas vertical Plateau borders connect both covering plates and may also adhere to the side walls of the irregular channels.

2.2 Foam generation in porous media

The configuration of foam undergoes changes through processes of foam generation and destruction. In the context of porous media, there are traditionally three established foam generation mechanisms: leave-behind, snap-off, and lamella division, as depicted in Figure 2.3. In contrast to these conventional mechanisms, yet another mechanism, pinch-off is a relatively recent discovery. It was initially observed in a smooth capillary microfluidic device with a constricted throat [26]. Foam formation through these mechanisms varies in terms of the locations where

foam is generated and their respective significance throughout the entire foam flow process.

2.2.1 Leave-behind

When gas initially infiltrates a porous medium saturated with liquid, it can leave behind liquid films or lenses that bridge the common throat between two adjacent pores. These lenses subsequently transform into thin films, often referred to as lamellae, which remain stable in the presence of a sufficiently high concentration of surfactants [28]. Although this mechanism can generate a substantial number of lamellae, these lamellae tend to align along the direction of gas flow, and the gas continues to flow through continuous paths across the porous medium. In this context, the gas mobility is not significantly reduced, and as a result, the leave-behind mechanism is generally considered an ineffective foaming method that primarily produces weak foams [27, 29].

2.2.2 Snap-off

The snap-off mechanism is a process wherein liquid drains through wetting films coating the walls of a porous medium under the influence of capillary pressure. This liquid accumulates near the pore throats of the porous medium and creates a bridge across the throat cross-sections. Roof [30] first introduced this mechanism to explain the formation of residual oil droplets in porous media. According to Roof's snap-off theory, the capillary pressure difference between the throat region and the downstream pore body drives the liquid drainage process, with the capillary pressure variation assumed to be quasi-static. Specifically, as the gas-liquid interface flows through a restricted throat and enters the following pore body, the capillary pressure in the confined region becomes higher than that in the pore body. This establishes a hydrodynamic pressure difference between the two regions. Consequently, the wetting phase flows back due to this pressure difference, leading to liquid accumulation and eventually the formation of a lamella.

To satisfy the geometric conditions required for Roof's snap-off to occur, the ratio of pore

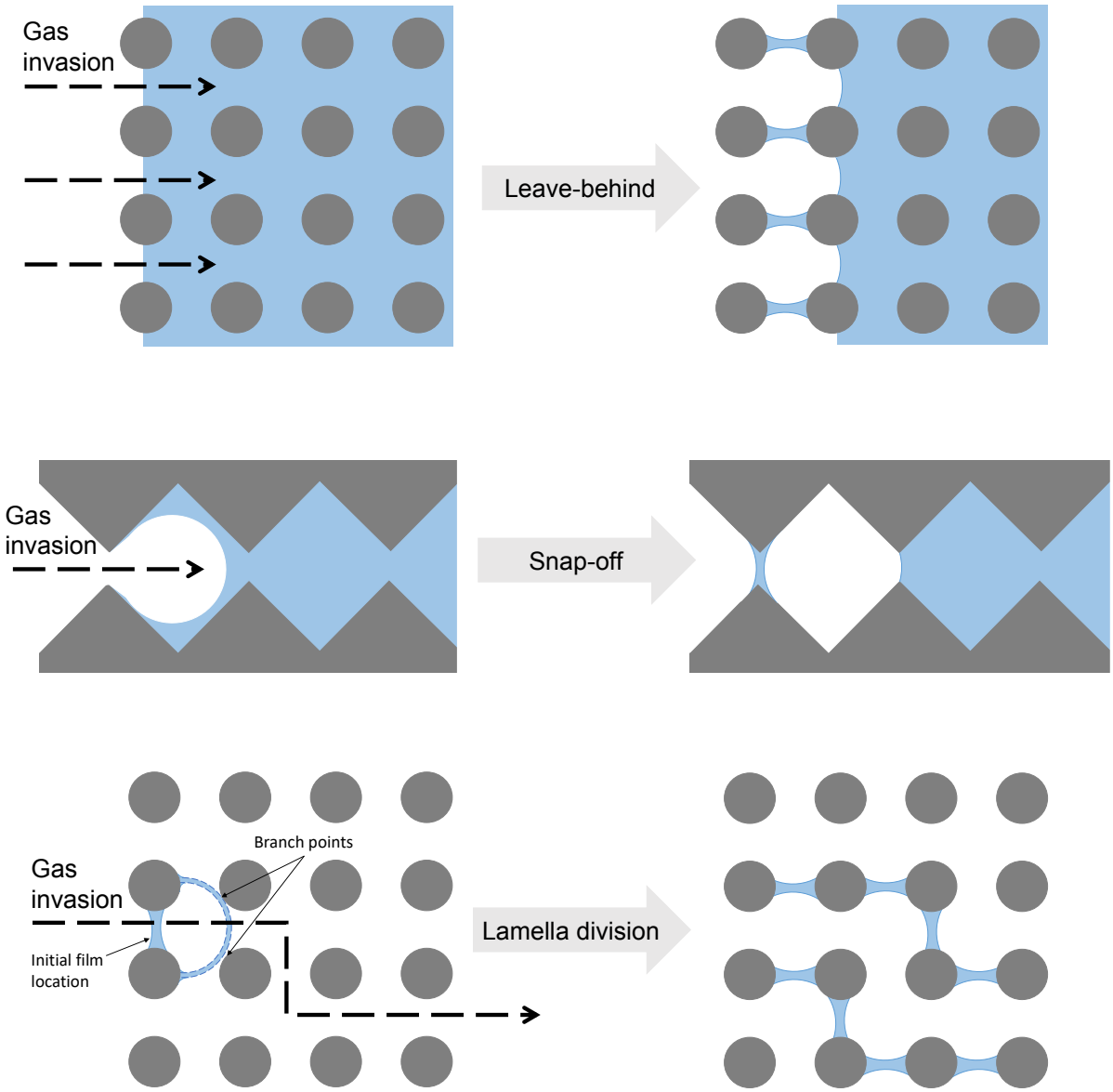


Figure 2.3: Schematic diagrams depicting foam generation mechanisms, including leave-behind, snap-off (Roof's mechanism), and lamella division within porous media. These diagrams are adapted from Chen et al. [27].

body to pore throat size should be greater than 3.0, and the pore surface should be sufficiently smooth to ensure that the transverse (along the pore) curvature of the gas-liquid interface is negligible in comparison to the cross-sectional curvature [21].

Roof's snap-off mechanism plays a crucial role in foam generation processes during the initial stages when the downstream pores are predominantly filled with liquid [31, 25]. As the process progresses, snap-off can still occur, but it differs from Roof's snap-off. Other snap-off mechanisms come into play, relying more on the throat radius and local fluctuations in capillary pressure. As films form and move downstream, the porous medium undergoes a drying process, leading to the eventual cessation of snap-off events. This happens because there is an insufficient amount of liquid present to accumulate and facilitate the snap-off process, as discussed in [32]. By contrast, if the liquid kept supplied during a foam flooding process, such as in co-injection of gas and liquid, snap-off would remain to generate foam films, as observed in micromodel experiments [21, 33].

2.2.3 Lamella division

The process of lamella division was first observed by Mast in an etched glass micromodel [34]. When a lamella traverses a pore body and approaches bifurcation points, it has the potential to split into multiple smaller lamellae. This mechanism relies on the presence of lamellae generated by other primary mechanisms. Notably, the likelihood of foam formation through the lamella division mechanism appears to be linked to the size of the "mother bubble". In micromodel experiments, it was observed that only relatively large bubbles, comparable in size to or larger than a pore, allowed for the occurrence of lamella division [35].

In situations where lamella division occurs within pores containing multiple pore throats that are not filled with liquid, a significant number of lamellae can be generated through this mechanism. Much like the snap-off mechanism, these newly formed lamellae serve to partition the gas into discontinuous phases along the flow direction, thereby increasing flow resistance and reducing gas mobility. The frequency of lamella division is influenced by several factors, including the number of branch points and the size of the bubble. Among these factors, bubble

size has a more pronounced impact on the occurrence of lamella division [36].

Cox [37] conducted numerical simulations to investigate lamella division during foam flow through a straight channel. These simulations highlighted the substantial influence of this mechanism on the rearrangement of foam configuration. The distribution of bubble sizes and the placement of branch points (obstacles within the channel) were found to have a significant impact on the resulting foam arrangement. Despite employing a relatively simple porous medium model and not accounting for effects such as viscous dissipation and liquid content, the final foam configuration was notably altered due to lamella division and associated topological changes.

After foam has been formed in porous media, lamella division could play an increasing role in foam generation and even become the dominant mechanism [38]. This proposition finds support in the concept of a critical velocity , above which the formation of strong foam is observed with a reduction of one to two orders of magnitude in total mobility [38]. The critical velocity is thought to correspond to a minimum pressure gradient that is required for static lamellae to start moving and for the process of lamella division to take place. However, it is worth noting that foam generation in porous media depends on various factors, some pertain to micro-structure of porous media, like pore-throat size, pore length, pore coordination number, permeability, and heterogeneity, and others associated with flow ratio of gas or liquid [33, 38]. Injection methods, such as gas-liquid co-injection and alternating slugs of gas and liquid, also have great impact on the effectiveness of foam generation. Therefore, it is not determined whether snap-off or lamella division dominates foam generation during foam flow in porous media.

2.2.4 Pinch-off

As illustrated in Figure 2.4, when a bubble traverses a narrow opening within a porous medium, it can undergo a process known as pinch-off, where it is divided into two separate bubbles due to the influence of neighbouring bubbles or the pore wall [26]. This phenomenon was also observed by Xiao et al. [39] in micromodel experiments, primarily within the wetter regions

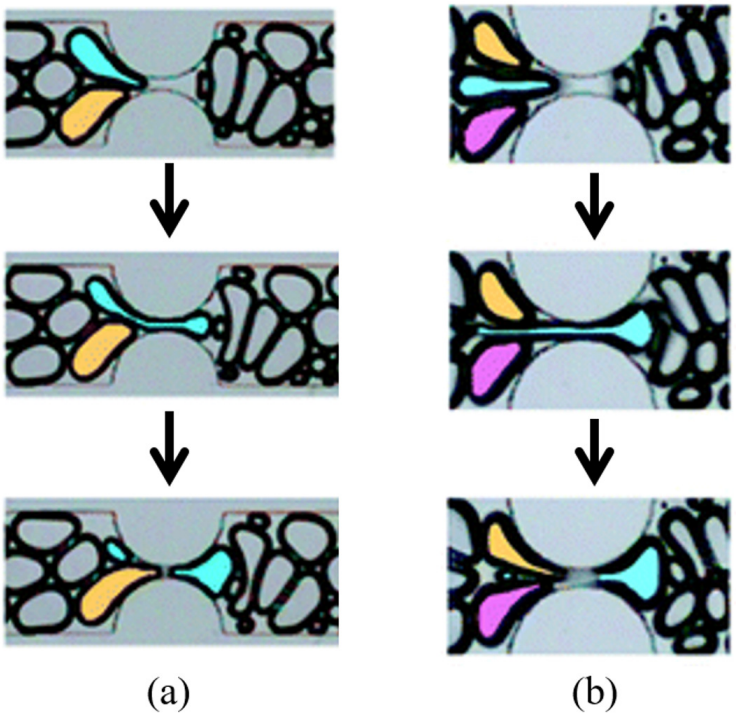


Figure 2.4: Pinch-off is a phenomenon that occurs when a bubble is subjected to compression as it moves through a localised constriction, typically due to the influence of neighbouring bubbles or the channel wall. There are two scenarios where pinch-off occurs: (a) neighbouring-wall pinch-off. One bubble (blue) is pinched off by its neighbouring bubble (yellow) and the wall of the constricted channel. (b) neighbouring-neighbouring pinch-off. One bubble (blue) is pinched off by its two neighbouring bubbles (yellow and red, respectively). From Liontas et al. [26].

of the porous medium. It was observed that pinch-off requires a substantial deformation of the bubble, and eventually, the bubble's boundary contacts itself, leading to its separation. Importantly, the newly formed bubbles may be smaller than the characteristic size of the pore, which sets this mechanism as being distinct from the three mechanisms discussed earlier.

2.3 Foam stability and coalescence in porous media

Foam exhibits thermodynamic instability [40]. As a result, the notion of foam stability is a relative concept, signifying a foam's capacity to maintain its physical structure for an extended period without undergoing significant changes or collapsing. Foams that can preserve their structural integrity for an extended period are classified as stable, whereas those prone to rapid deterioration or collapse are designated as unstable. The ageing of foam involves two principal

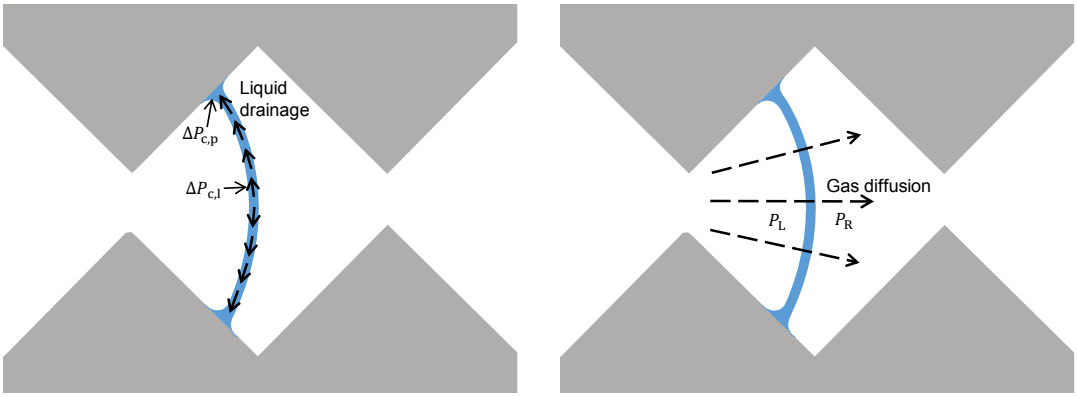


Figure 2.5: Schematic diagram illustrating two mechanisms that can lead to the collapse of foam: capillary suction (left) and gas diffusion (right). Due to the significant surface curvature near the Plateau borders, the capillary pressure, represented as ΔP_c, is higher at the Plateau borders than at the centers of the lamellae, i.e. $\Delta P_{c,p} > \Delta P_{c,l}$. This pressure difference drives the movement of liquid from the film centres toward the Plateau borders. Meanwhile, gas diffuses from the side with higher gas pressure, denoted as P_L, to the other side of the foam film with lower pressure, denoted as P_R.

mechanisms that contribute to its degradation: the rupture of foam films and the diffusion of gas across foam films. These are introduced as follows.

2.3.1 Capillary suction coalescence

Capillary suction coalescence refers to the process in which foam coalesces as a result of liquid drainage from the foam's thin films or lamellae. This drainage occurs due to the hydrodynamic pressure difference between the central film and the Plateau borders located at the boundaries of the film. As depicted in Figure 2.5, the capillary pressure at the Plateau borders, $\Delta P_{c,p}$, is larger than that in the film centre, $\Delta P_{c,l}$. Consequently, the hydrodynamic pressure of the liquid in the centre of the foam film becomes greater than that in the Plateau borders, resulting in a pressure difference between these two regions. In situations where a film remains stable and in a stationary state, this pressure difference is offset by a disjoining pressure Π [41]. This disjoining pressure emerges as a cumulative outcome of the interplay between repulsive and attractive forces exerted on the two gas-liquid interfaces on a foam film.

The Derjaguin, Landau, Vervey, and Overbeek (DLVO) theory represents a significant milestone in the understanding of disjoining pressure, as referenced in [41]. According to the DLVO

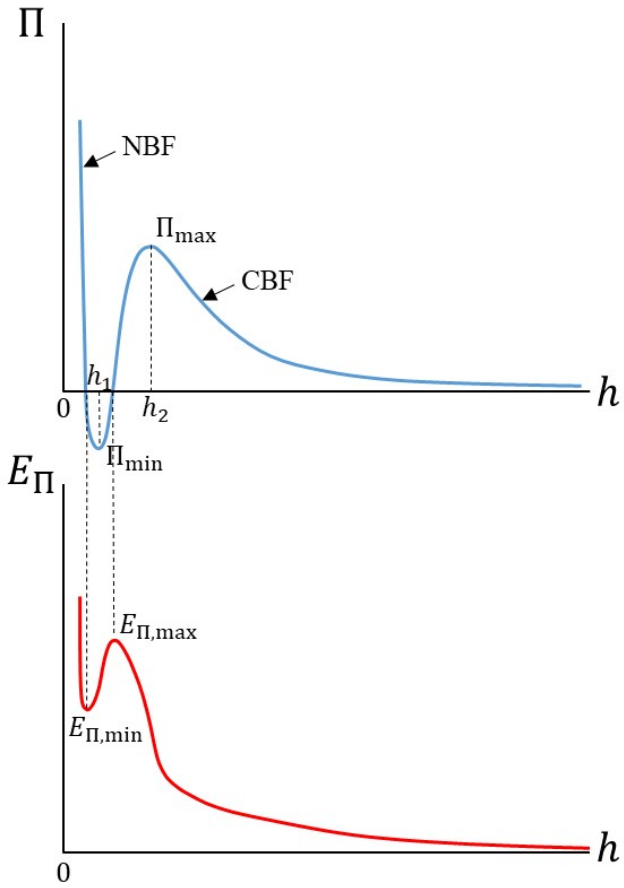


Figure 2.6: Schematic illustration of disjoining pressure Π and disjoining energy (per unit area) E_Π isotherms.

theory, the disjoining pressure arises from the interplay of two opposing forces: electrostatic forces and Van der Waals forces acting on the two gas-liquid interfaces on a film. The repulsive electrostatic force originates from charged surfactant molecules present on the two gas-liquid interfaces on a foam film. The strength of this force is influenced by the density of packing of surfactant molecules on each interface [42]. A higher packing density results in stronger repulsion, enhancing film stability. However, the salinity of the aqueous phase can reduce the charge separation of the surfactants on film surfaces, thus affecting the film's stability [43].

The second force, the Van der Waals force, is an attractive force that tends to destabilise a film. It arises from interactions between molecules, including gas-gas, gas-liquid, and liquid-liquid interactions, and its strength depends on the properties of these molecules [43]. In addition to the DLVO components, there are steric/hydration forces, which are repulsive in nature and contribute to stabilising foam films. These forces are categorised as non-DLVO components.

The disjoining pressure is a function of the film thickness, as illustrated in Figure 2.6. The disjoining pressure isotherm demonstrates a local minimum at a comparatively low thickness denoted as h_1 and a local maximum at a relatively greater thickness known as h_2. In the range of [0, h_1] and [h_2, ∞], the disjoining pressure increases as the film thickness decreases, and this has a stabilizing effect on foam films. For a stable film in equilibrium, its thickness is determined by the capillary pressure and its relative magnitude compared to the local maximum [44]. As the liquid drainage occurs within a film, the disjoining pressure increases as the film thickness decreases. If the capillary pressure is lower than the local maximum of the disjoining pressure, the drainage would cease and the film remains stable at a thickness in the range [h_2, ∞]. Otherwise, the film thickness jumps below h_1 once it reduces to h_2, and may remain stable. Stable foam films with thickness in the ranges of [0, h_1] and [h_2, ∞] are referred to as Newton black films (NBF) and common black films (CBF), respectively [45]. However, when the capillary pressure surpasses a critical threshold, as can happen at extremely high foam quality, films ultimately rupture. Figure 2.6 also illustrates the disjoining energy (per unit area) E_Π variation with the film thickness, linked to the disjoining pressure via $\Pi = -\mathrm{d}E_\Pi/\mathrm{dh}$. E_Π takes local minimum and maximum at zero disjoining pressure.

In porous media where a substantial number of foam films are present, the liquid films are interconnected rather than being isolated. Khatib et al. [46] introduced the concept of the limiting capillary pressure, which represents the maximum pressure that foam lamellae can endure before undergoing catastrophic coalescence. They proposed that the capillary pressure decreases continuously with increasing liquid saturation and identified a critical liquid saturation level. Beyond this critical level, the limiting capillary pressure is not exceeded, thereby ensuring the stability of the foam. It is worth noting that the limiting capillary pressure is distinct from the critical capillary pressure determined by the isotherm of the disjoining pressure, although its value may be close to the local capillary pressure at which lamellae rupture [44].

2.3.2 Bubble coarsening and coalescence

According to the Young-Laplace equation, Eq. 2.1, smaller gas bubbles are of higher pressure due to their larger curvature at the boundary. This pressure difference leads to gas diffusion from smaller bubbles through the foam film and into larger bubbles. This gas transfer process is illustrated in Figure 2.5, where gas moves from areas with higher gas pressure to areas with lower gas pressure. This gas diffusion has two primary effects. First, it equalises the curvature differences, resulting in flatter foam lamellae while preserving foam stability [44, 47]. Second, it causes the foam texture to coarsen by filling larger bubbles at the expense of smaller ones, ultimately leading to weaker and less textured foam.

Foam coarsening in porous media is influenced by pore size [48]. Jones et al. [47] conducted an experiment where they saturated a 2D micromodel with foam and observed the coarsening process. The final arrangement of foam, after convergence, showed most of the bubble films situated in the pore throats, resulting in a bimodal bubble size distribution. Large bubbles were found to occupy pore bodies, while numerous small bubbles were trapped in pore throats.

The absolute rate of gas diffusion from a smaller bubble to a larger neighbouring bubble is proportional to the area of the common film and the pressure difference between the two bubbles, with a proportional factor defined as the gas permeability coefficient. In bulk foam situations, von Neumann's law offers a suitable description of the coarsening rate [49]. Nevertheless, adjustments to this law become necessary when foam is confined within porous media and subjected to constraints imposed by the walls [50].

In physical terms, the coarsening rate of foam depends on both the type of gas involved and the transport mechanisms of these different gases [48]. For specific gases, such as N_2 or CO_2, the coarsening process involves a sequence where they first dissolve into the foam lamella and then penetrate into the neighboring bubble. Moreover, the permeability through the lamella varies for each gas type. For instance, CO_2 exhibits a higher solubility in surfactant solutions and faster diffusion through foam lamellae compared to N_2, leading to a more rapid coarsening rate [48]. Furthermore, a study by Zeng et al. [43] observed that a N_2-CO_2 mixture in an 8:2

mol ratio exhibits the same foam strength as pure N_2 foam, which is notably stronger than CO_2 foam, especially when the foam quality is high. This suggests that the inclusion of N_2, known for its lower diffusion rate, plays a stabilizing role in maintaining foam stability.

By contrast, the coarsening of steam foam can operate through a process involving steam condensation on one surface of a film and evaporation on the other surface. This process is predominantly governed by the presence of thin films and rapid heat conduction, resulting in a relatively fast coarsening process that can weaken foam stability [48]. Falls et al. [51] observed an enhancement in foam strength when a small amount of N_2 was introduced into steam foam. This improvement occurred because N_2 dissolved within the foam films and impeded the condensation and evaporation of water vapour. Consequently, coarsening may mainly occur through the slower process of water vapour diffusion through the films.

The rate at which foam coarsens can be modified in the presence of a porous medium. Unlike bulk foam confined within a container much larger than the bubble sizes, coarsening is hindered as the bubble size approaches a similar order of magnitude as the pore size [52]. The gas diffusion timescale for bubbles of the same size was found to be approximately an order of magnitude larger in porous media compared to that for foam in bulk [50]. Diffusion rates in the 2D micromodels, on the other hand, were observed to be lower than that in a core sample, possibly due to differences in pore sizes and pore connectivity [47].

2.4 Foam flow in porous media

In porous media exhibiting water-wetting characteristics, it is common for the surfactant solution to accumulate in tiny crevices and to form a coating film on the interior walls of the pores [14]. This process results in the creation of a continuous network of liquid that adheres to the surface of the solid matrix. Conversely, gas within bubbles, as the non-wetting phase, typically occupies the central regions of larger pores, and is separated by thin liquid films. This distribution of liquid within the pores supports certain assumptions regarding the connectivity of the liquid phase, including the maintenance of consistent hydrodynamic pressure within the

Plateau borders. Additionally, the presence of liquid coatings the pore surfaces serves as the fundamental basis for the generation of foam through snap-off.

When foam traverses porous media, it exhibits intricate localised behaviours that collectively contribute to a complex behaviour observed at larger scales, such as the pore network level. A notable example of this complexity is the transformation of foam flow into a gas-liquid two-phase flow when it passes through narrow channels within porous media, as demonstrated by experiments [53]. These experiments involved the injection of pre-generated foams with varying structures, ranging from low-quality foam with small spherical bubbles to high-quality foam with a bamboo-like structure, into a stratified heterogeneous porous medium. In low-permeability regions, characterised by the presence of very small pores, large bubbles tended to undergo complete disruption. Conversely, in high-permeability regions, bubbles of equivalent size displayed deforming rather than collapsing entirely.

In the subsequent discussion, the intricacies of foam flow in porous media are further explored from various perspectives. Another local complexity, namely the foam topological transformation, and overall behaviour of foam flow in porous media are reviewed.

2.4.1 T1 topological transformation

In the context of 2D foam flow within porous media, a phenomenon can occur where two bubbles that were initially not adjacent become neighbours, while the previous neighbouring pair becomes non-adjacent. This process is illustrated in Figure 2.7. The terminology "T1 transition", introduced by Weaire and Rivier [54], is employed to describe this phenomenon. It involves the contraction of a foam film and eventually vanishing, followed by the emergence of a new film that separates the two initially non-adjacent bubbles. Specifically, a foam film may gradually contract, eventually forming a fourfold vertex that is inherently unstable. This vertex then expands immediately, creating a new film that separates the new neighbouring bubbles. Alternatively, the T1 topological transformation could occur precisely when the foam film reaches a critical length. When a foam film shrinks to a size below this critical length, it becomes unable to sustain a stable configuration. This situation then necessitates a T1

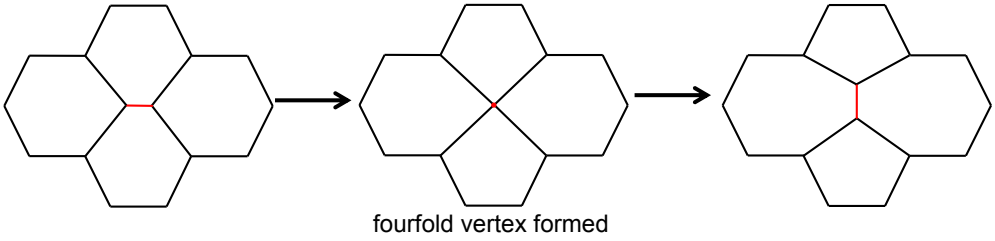


Figure 2.7: T1 topological transformation in 2D foams.

transition to occur, leading to the creation of a new film and the rearrangement of neighbouring bubbles.

In 3D foams, T1 transitions exhibit additional variations. There are three fundamental types of 3D T1 transitions: edge-to-triangle (ET), triangle-to-edge (TE), and quadrilateral-to-quadrilateral (QQ) transitions [55], as illustrated in Figure 2.8. For the ET transition, one Plateau border is initially shared by three bubbles, connecting with two end bubbles. During an ET transition, as the end bubbles approach each other, the Plateau border contracts, ultimately leading to the formation of a six-fold vertex, which then transforms into a triangle. Conversely, the TE transition is the logical reversal of the ET transition, involving the transformation of a triangle into an edge.

The QQ transition occurs in scenarios where the foam film has a high aspect ratio. As shown in Figure 2.8, two short Plateau borders simultaneously contract to zero length, resulting in the swapping of neighbouring bubbles. Besides, the QQ transition may also occur through a sequence of the ET and TE transition processes. These diverse 3D T1 transitions contribute to the intricate behaviour of foams in three dimensions.

2.4.2 Flow intermittency and bubble trapping

The migration of foam through porous media displays intermittent flow patterns and the entrapment of bubbles, which is influenced by factors such as foam quality, flow rate, and the microstructure of the porous media [56, 57, 58, 59]. The relationship between flow intermittency and bubble trapping underscores the dynamic nature of foam transport in porous media. As

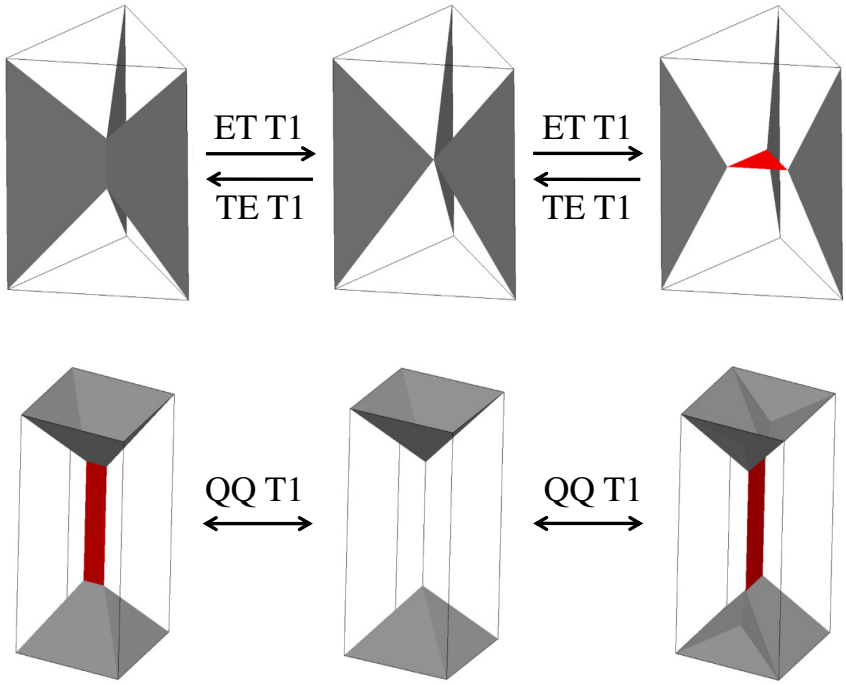


Figure 2.8: ET, TE, and QQ T1 transitions in 3D foams.

bubbles navigate through the flow channels, they may become trapped at specific locations, impeding the flow. Conversely, trapped bubbles may regain mobility and transform into actively flowing bubbles when there is a favourable pressure gradient. Experimental data demonstrate that the pathways for active flow change over time due to transitions in the status of bubbles, alternating between bubble trapping and moving [57].

Most of the gas contained within foam in porous media is present in the form of trapped bubbles. Radke and Gillis [60] documented trapped gas proportions ranging from 70% to 100% in their experiments, conducted at various flow rates and foam qualities. Friedman et al. [61] carried out experiments across a broad range of velocities and discovered gas trapped within bubbles at levels ranging from 75% to 90%. Despite potential experimental errors arising from flow intermittency, the fraction of gas that remains trapped is considered substantial.

The substantial proportion of trapped gas underscores the significance of foam coarsening within a porous medium, potentially contributing to flow intermittency. Specifically, foam coarsening has the potential to reconfigure the foam structure, thus modifying flow resistance. Experimental evidence suggests that foam coarsening typically involves the redistribution of foam films to

the pore throats, resulting in a reduction of the foam's surface energy within porous media [47]. Consequently, certain flow pathways may experience increased obstruction as the low-energy state of the foam demands a higher pressure gradient for displacement.

Further evidence can be found in the experimental study conducted by Jones et al. [56]. In their experiments, foam flow was examined in a 2D Hele-Shaw cell equipped with two parallel channels, one wide and the other narrow, both connecting to the inlet and outlet channels. They observed a transition in the foam structure from a stair-case configuration, consisting of both flat and zigzag films, to a bamboo-like configuration near the entrance of the narrow channel. When the lamellae of the bamboo foam exited the channel, they became immobilised, resulting in a blockage of the continuous flow within that particular channel. This observation suggests that the bamboo configuration, when interacting with the surrounding confined channels, has the potential to cause an increase in flow resistance.

A similar scenario could occur in porous media. As previously mentioned, foam films tend to occupy pore throats due to foam coarsening. This leads to a structure resembling the bamboo configuration, although the confined channels within porous media may exhibit more irregular shapes. When these lamellae interact with the confined flow channels, the resulting high flow resistance could impede lamella movement and, consequently, lead to the entrapment of bubbles.

Conversely, foam coarsening may also result in the development of a coarser-textured foam by eliminating smaller bubbles. In this scenario, flow resistance along certain pathways may decrease due to the coarser foam texture.

2.4.3 Increased sweep efficiency

Flooding a displacing fluid into porous media proves advantageous when its mobility is lower than that of the fluid being displaced. The reduced mobility is signified by increased pressure gradient applied to maintain the migration of displacing fluid in porous media. In foam flooding, where foam serves as the displacing agent, the applied pressure gradient increases as the foam invades a porous medium, blocks the flow paths by trapped bubbles, and redirects into unswept

regions [39]. The process of blocking and redirecting in foam flooding leads to the formation of a sharp and stable displacing front [39, 62]. For this reason, foam can effectively reach and sweep areas that may be otherwise inaccessible to gas or water flooding, thereby enhancing the sweep efficiency.

The higher pressure gradient, indicative of reduced gas mobility, primarily results from the presence of trapped bubbles. Lv et al. [58] conducted experiments and noticed a rise in the trapped gas fraction, accompanied by an increase in the pressure gradient, when using foam with various foam qualities, ranging from 50% to 94%. Nevertheless, they also observed that the trapped foam changes to a coarser texture when the foam quality surpasses 75%. This implies that, even though trapped bubbles may experience film rupture at higher foam qualities, the growing proportion of trapped bubbles could have dominated the behaviour of the applied pressure gradient, resulting in its increase and subsequently reduced gas mobility.

The stable foam front is sustained through a phenomenon known as flow intermittency. As show in Figure 2.9, foam first invades the high-permeability regions within the porous medium, and then it effectively blocks and redirects fluid flow towards areas with lower permeability [39]. The blocking and redirection of fluid is linked to the dynamic nature of the foam configuration. This dynamic foam configuration results in a decrease in relative permeability within the high-permeability regions where the foam initially prefers to invade [39, 53, 63].

Furthermore, experiments conducted with micromodels have demonstrated that the liquid phase in foams is the initial component to penetrate into low-permeability regions saturated with oil or surfactant solution, resulting in a drier foam state within the high-permeability region [39, 64]. As the liquid phase displaces a significant portion of the in-situ fluid in the micromodels, gas bubbles gradually enter the low-permeability region from the previously invaded high-permeability zone. This asynchrony in the process may stem from the high capillary entry pressure, initially impeding the gas phase from entering small pores [63].

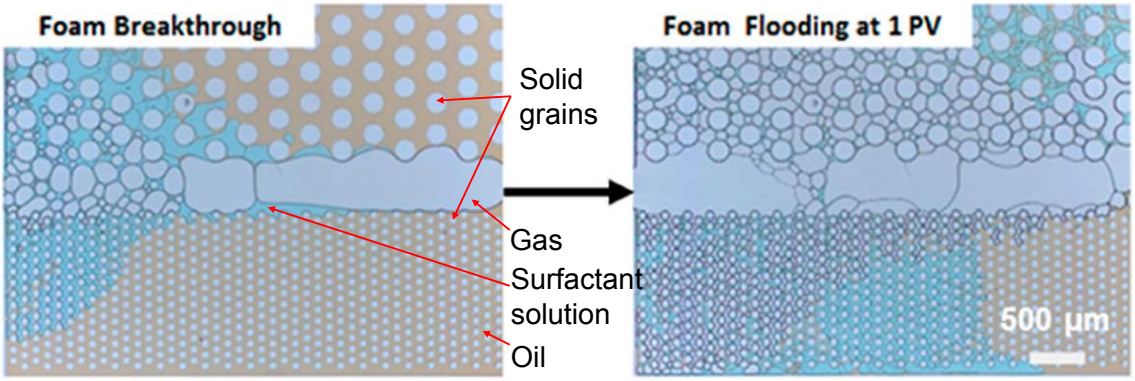


Figure 2.9: Foam displacing oil in a micromodel, from Xiao et al. [39]. This micromodel comprises three distinct sections: the upper section characterized by high permeability, a middle fracture, and the lower section characterized by low permeability. Foam is introduced into the micromodel from the left side of the fracture and exits from the right side. During the experiments, it was observed that as foam advanced, it initially invaded the fracture, then proceeded to invade the upper section, and finally reached the lower section. Notably, the liquid phase invaded the lower region before the gas phase. This sequential diversion of foam resulted in a high sweep efficiency. 1 PV refers to one volume of the void space within the micromodel, indicating the volume of fluid that has been injected equals the volume of the void space in the micromodel.

2.4.4 Non-Newtonian behaviour of foam

Foam behaves as a yield-stress fluid, which means that it requires a minimum pressure gradient to maintain the mobility of its lamellae [65]. This stands in contrast to Newtonian fluids, which can start flowing under even infinitesimal pressure gradients as predicted by the Navier-Stokes equation. The effective yield stress observed in foam is a consequence of the capillary behaviour of foam films when subjected to both volumetric and geometric constraints [66, 59]. These constraints, particularly local geometric restrictions commonly found in realistic porous media, can lead to the presence of a finite net pressure gradient even at extremely low flow rates, thereby giving rise to the concept of yield stress of foam. Conversely, certain geometries, such as a straight channel with a uniform circular or polygonal section, fail to induce the emergence of yield stress in foam [59, 67, 68, 69].

At finite flow rates, maintaining foam flow in porous media involves considering additional factors, such as the viscous resistance within the liquid slug between bubbles and the migration of surfactants from the front to the back of the bubbles [70]. These factors collectively con-

tribute to the pressure gradient necessary to maintain foam flow within porous media. Their influence depends on several variables, including the flow rate, foam quality, and the specific microstructure of the porous media.

In the context of foam flow in porous media, foam quality f_g can be redefined as the ratio of the gas flow rate (superficial velocity) to the total flow rate, expressed as $f_g = U_g/(U_g + U_l)$, where U_g represents the gas flow rate, and U_l represents the liquid flow rate. This definition in fact depicts the gas and liquid flows in porous media, with gas and liquid flow rates known in prior, and thus is distinct from that defined using gas and liquid volumes for formed foams. Foam may not form in a porous medium, though this is unlikely to occur in the presence of high-concentration surfactants. Note that this definition is also not linked to gas or liquid saturation, since it is not dependent on the void space volume in a porous medium. For steady-state foam flow in homogeneous porous media with varying foam qualities, researchers have observed two distinct regimes, known as the low-quality regime and the high-quality regime [71], as depicted in Figure 2.10(a). The pressure gradient in steady-state foam flow exhibits a dependence on foam quality, and this relationship serves as a distinguishing factor between these two regimes [72], as highlighted in Figure 2.10(b).

In the low-quality regime, the pressure gradient increases with increasing foam quality at a constant total flow rate. In contrast, in the high-quality regime, the pressure gradient decreases as foam quality rises. These phenomena can be attributed to the distinct dominant mechanisms that govern each regime. In the low-quality regime, foam flow behaviour is primarily controlled by processes such as bubble trapping and mobilisation. On the other hand, in the high-quality regime, foam experiences film destruction, and bubble sizes adjust by redistributing the liquid phase to alleviate the high capillary pressure which is above the limiting capillary pressure due to low water saturation [46, 72].

For a given foam quality, it is observed that the pressure gradient increases as the total flow rate rises. This variation in pressure gradient with flow rate reflects the effective or apparent viscosity of foam within porous media, and this relation is influenced by the foam quality. Notably, in the low-quality regime, the effective viscosity of foam flow exhibits a characteristic

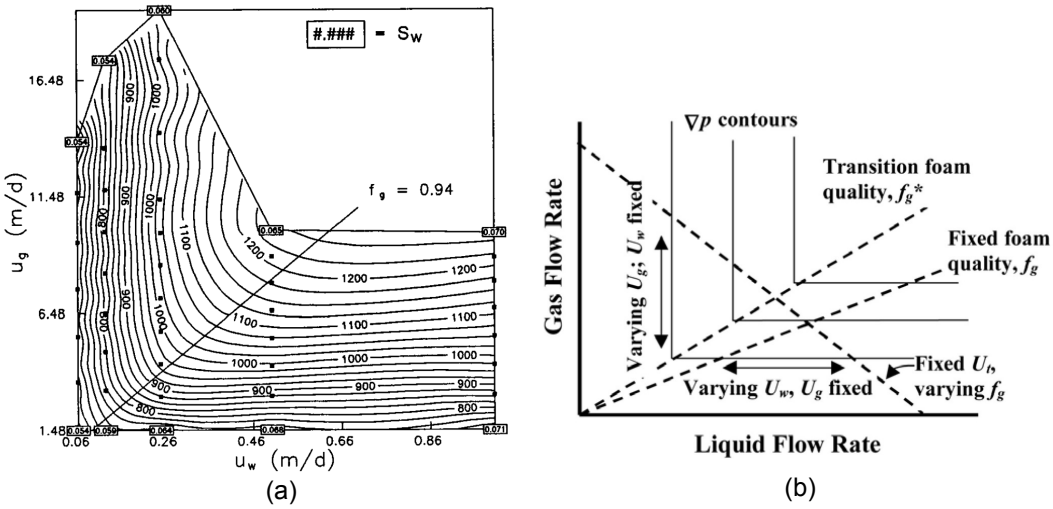


Figure 2.10: Two regimes of steady-state foam flow in homogeneous porous media. (a) Experimental results of the pressure drop at various gas and liquid flow rates, from Osterloh and Jante [71]. (b) The general distribution of the data presented in (a), from Alvarez et al. [72].

known as shear thinning, where the viscosity decreases as shear rate increases.

Theoretical studies support the shear-thinning behaviour, and propose that the pressure gradient across single or multiple bubbles follows a power-law relationship with the capillary number [67, 73]. The capillary number Ca is defined as the ratio of the product of liquid phase viscosity μ and gas flow rate V divided by the gas-liquid interfacial tension γ. This power-law relationship was substantiated through experiments conducted in Hele-Shaw cells [74, 75], where the measured pressure gradient data aligned well with the theoretical power-law formulation.

More recent research conducted in porous media has revealed a stronger shear-thinning behaviour of foam flow, particularly at very low capillary numbers [76, 57, 59]. An experimental study by Mauray et al. [59] highlighted contrasting results between foam flow in Hele-Shaw cells and in porous media. This research suggests that the yield stress of foam flow in porous media plays a substantial role in the overall flow resistance at low capillary numbers. Furthermore, it implies that it is the presence of the yield stress that gives rise to the strong shear-thinning behaviour observed at low capillary numbers.

2.5 Pore-scale modelling of foam flow

Practical applications involving the flow of multiphase fluids (such as foam) through porous media typically occur on a large scale, encompassing core and field scales [77, 78]. Predicting the displacement of foam at these scales is valuable for optimising the applications. This prediction relies on characterising multiphase flow at the representative elementary volume (REV) scale, where the microstructure of porous media and overall fluid behaviour are implicitly represented by phenomenological parameters, like porosity, pore size, tortuosity, permeability, and relative permeability [79]. In this framework, extensions of Darcy's law are utilised to more accurately capture momentum relationships, incorporating the effects of capillary pressure and relative permeability of each fluid phase [80]. Additionally, these parameters may be correlated with fluid saturation and specific interfacial area to close the system of governing equations used in macroscopic modelling of multiphase flows [81, 82, 83].

In foam systems, complexity escalates due to the abundance of films, leading to a significant interfacial area and intricate interplay among various phases. These interactions involve foam generation and coalescence, topological changes, and the capturing and mobilising of films, as detailed in earlier sections. To address this growing complexity, additional phenomenological parameters such as foam generation and coalescence functions are introduced [84]. In continuum-scale models, prior knowledge of phenomenological parameters is generally necessary. However, owing to the intricate microscale heterogeneity of porous media and diverse pore-scale phenomena, there remains uncertainty regarding the characterisation of foam at the REV scale using these parameters. It is unclear whether the currently available phenomenological parameters adequately capture foam behaviour and if the relationships between these parameters have been thoroughly elucidated [85]. One approach to overcoming these challenges is through pore-scale simulations of foam flow, where pore-scale models directly address the transport processes of foam within realistic porous structures at the pore scale [19].

This section is focused on pore-scale foam modelling techniques, with a specific emphasis on those that have been further explored or developed within the context of this thesis. Pore-scale modelling approaches involve the direct resolution of foam structure. Depending on

the simplifications made concerning fluid viscosity and inertia effect, these approaches can be categorised into three types: quasi-static foam modelling, force-equilibrium foam modelling, and modelling approaches that treat foam as a two-phase fluid system governed by the Navier-Stokes equations. Other methods, such as the phase-field model [86], are not within the scope of the discussion.

2.5.1 Quasi-static foam modelling

Plateau's law [20] is a fundamental principle that accurately describes the structure of a dry foam in a state of stationary equilibrium, as a result of foam's minimising its surface energy. When dealing with simple foam structures, like a single bubble on a flat wall, Plateau's law can be directly applied to determine the structure of propagating foam. This approach operates under the quasi-static assumption, where the foam remains in equilibrium at all times [65].

When working with more intricate foam structures containing numerous bubbles of varying sizes, predicting the static foam structure and its quasi-static movements using Plateau's law becomes challenging. In such scenarios, it is more effective to directly predict the foam configuration with the minimum total surface energy. The Surface Evolver [87] is a powerful tool designed for this purpose, which utilises the gradient descent method to minimise the foam's surface energy. When the surface tension remains constant, minimising the total surface energy of the foam is equivalent to minimising its surface area. This method is often called the soap film model [87].

In Surface Evolver, the foam films and solid walls are discretised and represented by triangular elements (in 3D) or line segments (in 2D). The fundamental geometric element representing the foam structure is the vertex. The foam configuration is evolved towards states with lower surface energy by adjusting the positions of the vertices that comprise the foam surface, ultimately leading to the attainment of a state characterised by the lowest surface energy. This resulting foam configuration is referred to as the minimal surface.

In cases where the gravity effect is disregarded, the pressure within each single phase of the

fluid is considered to be uniform. The pressure difference, ΔP, across the foam films can then be calculated using the Young-Laplace equation.

$$\Delta P = 2\gamma\left(\frac{1}{r_1} + \frac{1}{r_2}\right), \tag{2.1}$$

where γ is the gas-liquid interfacial tension. r_1 and r_2 are the two principal curvature radii. The factor of 2 takes into consideration the presence of two gas-liquid interfaces on a single film. The mean curvature of the film is denoted as k, defined as $k = 0.5(1/r_1 + 1/r_2)$.

The quasi-static method, while useful, has certain limitations primarily rooted in its assumption of quasi-static flow. This assumption treats foam flow as an exceptionally slow process and overlooks the impact of viscous dissipation [88]. At high foam qualities, viscous dissipation could be primarily dominated by the friction between the wall and the Plateau borders [74]. This dissipation, however, is ignored in the quasi-static approach. Consequently, the quasi-static approach cannot be used to capture the flow rate-dependent characteristics of foam flow in porous media.

In addition, in the quasi-static approach, topological transformations in foam flow are treated as discrete jumps rather than continuous processes under imposed strains [88, 89]. This leads to ambiguity regarding the sequence in which these topological transformations occur, particularly when a series of such transformations is triggered. The issue arises because the intermediate foam configurations, before converging to the minimal surface, are not physically valid. In cases where two or more lamellae simultaneously trigger topological transformations, it becomes unclear which changes in topology should occur first [88]. In contrast, realistic foam flow that accounts for viscous dissipation occurs continuously. The sequence of topological changes can be determined based on the process of foam structure evolution.

Moreover, topological changes can be induced in the presence of viscous effects at relatively large imposed strains, as observed in experiments where foam lamellae elongate to a greater extent than under slowly imposed strains [90]. This highlights the need to consider the role of fluid viscosity in the dynamic motion of foams.

2.5.2 Force-equilibrium modelling for dynamic foam motion

An extension beyond the quasi-static regime is to include the effect of fluid viscosity, but still ignore the inertial effect of the fluid. Despite the dynamic nature, the net force acting on any control volume within the flow field remains at equilibrium. In this dynamic regime, the key factors influencing foam flow are pressure, viscous stress, and film tension (twice the value of the gas-water interfacial tension). These factors govern the dynamic motion of foam, through the equilibrium of forces. It is worth noting again that "equilibrium" here means the balance of forces including the drag force.

One well-known dynamic model that relies on the force balance principle is the viscous froth model [91, 89]. This model is designed for the motion of 2D dry foam in Hele-Shall cells. In the viscous froth model, it is assumed that the pressure within each bubble is uniform. This model therefore only considers viscous forces within the liquid, ignoring that in the gas. The pressure difference across a lamella serves to drive the motion of the lamella. This pressure-driven motion is balanced by the film tension force and the viscous force acting on the lamella. The simplest version of the viscous froth model adopts a linear relation between the viscous force and the normal velocity of the lamella [89]

$$\Delta P - 2\gamma k = \zeta u_{\mathrm{n}}, \tag{2.2}$$

where ΔP is the pressure drop across the lamella from the concave side to the convex side, k the lamella curvature, u_{n} the normal velocity, and ζ the viscous drag coefficient. The default orientation of the normal velocity vector is directed toward the convex side of the film.

The viscous froth model, such as the linear one described by Eq. 2.2, is applied at interior points along a lamella. To determine the pressure within each bubble, Eq. 2.2 is integrated around the boundary of each bubble composed of a set of lamellae. This integration around each bubble is then linked to the volume change of the bubble, which results in a system of equations that can be solved to determine the unknown pressure within each bubble [89].

Once the pressure within each bubble is known, the normal velocity at any point on the lamellae can be calculated by further utilising Eq. 2.2. Subsequently, the positions of the lamellae or the overall foam configuration can be evolved by moving the points on the lamellae using the kinematic equation $d\boldsymbol{x}/dt = u_{\mathrm{n}}\boldsymbol{n}$, where $\boldsymbol{x}$ represents the position of points on the lamellae, and t represents time. $\boldsymbol{n}$ denotes the normal unit vector at a point on the lamellae.

Updating the position of a three-fold point can be achieved by considering the angles formed between the lamellae meeting at the point, as described by Kern et al. [89]. In a bulk foam, for instance, when three mobile lamellae meet at a three-fold point, they form an angle of 120 degrees. By contrast, one mobile lamella forms an angle of 90 degrees with the wetting films coating on the side walls. Note that this description assumes that the effect of viscous forces exerted by the side walls is ignored.

The boundary integral method for Stokes flow is another approach to foam modelling that falls within the category of force-equilibrium modelling. This method starts by employing the Stokes flow equation, which is derived by neglecting the inertia term in the Navier-Stokes equation. This simplification results in a linear momentum equation governing Stokes flow. In the context of a multi-phase fluid flow system, the linear momentum equation, in conjunction with the mass conservation equation, can be converted into an integral equation computed specifically over interfaces, such as the gas-liquid and liquid-solid interfaces [92].

The resulting boundary integral equation is applied to the interface points to determine unknown quantities, including the stress on the wall and the velocities of the gas-liquid interface. Subsequently, the equation is applied to other field points to solve for the entire flow field. the positions of the points on the interfaces can be updated using the same kinematic equation employed in the viscous froth model.

The boundary-integral method for multi-phase fluid flow has found extensive applications in the studies of liquid droplet flow [93, 94] and concentrated emulsions flow [95, 96]. The emulsions exhibit structural similarities with foams, where drops, functioning as bubbles, are densely packed, separated by a continuous liquid network. In these applications, the numerical solution of the boundary-integral equation for multi-phase fluid flow presents several challenges, such

as the high viscosity contrasts between the two fluid phases in some cases and the presence of singularity and near-singularity problems [97]. Addressing these challenges is essential to ensure numerical stability and accuracy.

Zinchenko and Davis [93] conducted a study on drops passing through interparticle constrictions, addressing various types of singularities and near-singularities. These included interactions between drops themselves, solids themselves, solids and drops, solids and solids, and drops and drops. In the case of foam-like emulsions with very low liquid volumetric fraction, the interfacial force term within the boundary integral equation must account for the disjoining pressure [98, 99]. The disjoining pressure plays a role in stabilizing the foam films and is sensitive to changes in film thickness [100]. This sensitivity can potentially lead to numerical instability and limit the time step that can be employed in simulations. For this reason, the consideration of extremely thin films may significantly increase computational costs, thereby restricting the applicability of the boundary integral method in large-scale foam flow problems.

2.5.3 Computational fluid dynamics for foam

Foam, as a two-phase fluid, can be analyzed using methods originally designed for multiphase fluid flow, including the level set method [101, 102], volume of fluid method [103], coupled level set and volume of fluid method [104], and lattice Boltzmann method [105, 106]. While these methods are generally applicable for predicting foam flow, they have primarily been employed to study the flow of single or multiple individual gas bubbles, where the liquid slug between bubbles typically has considerable thickness. Consequently, these studies do not address the unique characteristics of high-quality foams, which are characterized by polygonal bubbles.

The presence of thin liquid films in high-quality foams presents challenges for both mathematical modelling and numerical simulations [107]. Bazhlekov et al. [100] have demonstrated that the stability of these thin films is maintained by disjoining pressure, which introduces complexities into numerical simulations and may increase computational costs. Additionally, high-quality foams with thin films exhibit a multiscale nature, with various physical processes occurring at different timescales [107].

To address these challenges, Saye and Sethian [107] proposed a multi-scale foam model that utilises the concept of scale separation and coupling. In their approach, the gas dynamics of bubble gas, liquid drainage within both Plateau borders and foam lamellae, and film rupture are separated based on their distinct characteristic timescales. The spatial scale separation is reflected in the dry foam assumption, where finite-thickness foam lamellae are simplified into curved surfaces based on the contrast between the film thickness and bubble size. Furthermore, these separated processes are coupled in sequence to predict the integrated dynamic evolution of foam.

Kim et al. [49] employed the dry foam assumption and utilised the immersed boundary method to monitor the motion of foam lamellae. Their study focused on the simulation of diffusion coarsening in two-dimensional dry foams, and the results they obtained were consistent with the predictions of von Newmann's law. Later, they successfully extended the immersed boundary method to model three-dimensional foams [108].

In these methods [49, 107, 108], the governing equations for fluid dynamics encompass the influence of inertia, potentially enhancing the methods' capacity to accurately depict realistic foam behaviour, including those characterised by underdamping [19]. However, it is worth noting that their research solely considered bulk foams, and the scenarios involving foam in porous media were not explored.

2.6 Challenges and thesis objectives

The literature review above implies that the complexity of foam flow in a porous medium arises from a variety of factors. These factors encompass, but are not restricted to, the foam's structural characteristics, which can be influenced by its microscopic behaviours such as foam generation, destruction, and T1 topological transformation, as well as the foam's quality and the geometric attributes of the porous medium. Importantly, these factors are interconnected and interdependent. For example, when foam initially invades a porous medium's high-permeability region, it leads to blockage of this region and the redirection of fluids into areas with lower

permeability [39]. Also, the concept of Roof's snap-off implies that in certain locations within a porous medium, new foam films can be more readily formed, although this mechanism typically dominates foam generation only during the initial stages of foam flooding [31].

The physical properties of foam undergo changes over time as it flows through a porous medium. When examining a specific moment in time, the physical characteristics of the foam are primarily dominated by the foam's configuration, which exhibits a unique topology, and the distribution of liquid within the foam films. In the case of high-quality foam, characterised by a low liquid volumetric fraction, the behaviour of the foam is predominantly influenced by factors such as foam topology, the number of bubbles, and their sizes. To predict the physical quantities associated with given foam configurations and porous media, this work places emphasis on employing physics-based modelling approaches and numerical methods. Specifically, this work focuses on two key approaches: quasi-static modelling and force-equilibrium foam modelling. Within this scope, the study identifies research gaps and introduces innovative methods to address representative issues found in the existing literature. Research gaps and objectives of this thesis are outlined as follows.

The quasi-static foam modelling method, known as the soap film model, is a valuable tool for solving problems involving specified initial foam configurations and pore geometries [66]. However, conventionally, this method has been primarily applied at the pore scale, where the porous medium, if involved, is treated as an integrated confined geometry and directly discretised. An intriguing question arises as to whether this method can be more readily extended to larger scales, such as the pore-network scale. This specific issue is addressed within this study, which subsequently explores its application in investigating the yield stress of foam within porous medium models that incorporate interconnected pores. Furthermore, this study introduces a novel scenario where trapped foam films do not directly interact with the moving film. This particular case is discussed in Chapter 3 of the thesis.

The 2D viscous froth model is available for studying dynamic foam flow in situations where the rate at which the foam is driven along is comparable with the foam relaxation rate controlled by viscous dissipation [89]. This model is specifically designed for foam flow in Hele-Shaw cells

that consist of two closely spaced flat plates. This system is often referred to as 2D because of only one layer of foam confined within the channel. However, the foam films in this scenario are in fact not completely flat across the plates [23]. To further investigate the influence of the narrow yet finite size of the gap on foam flow within Hele-Shaw cells, this study examines a typical case known as a viscous froth lens in straight channels. The case has been studied using the 2D viscous froth model in literature [88], but in this work, it is reviewed in a 3D context. For this purpose, a 3D version of the viscous froth model is developed to address this specific scenario. These investigations are carried out in Chapter 4.

In the development of the 3D viscous froth model, the quasi-static modelling approach plays a crucial role as a fundamental component. The connection between these two modelling approaches stems from a common characteristic: the neglect of fluid viscosity within each bubble in both the viscous froth model and the quasi-static soap film model. Furthermore, due to this simplification, both methods are unable to predict the velocity field within individual bubbles. This challenge is addressed in the present work through the development of a boundary-integral approach. Conventionally, the boundary integral method has found applications in two-phase fluid flows such as the emulsions flow [95, 96, 93]. However, in this work, the potential of this method is explored in the context of dry foam. This exploration and its implications are detailed in Chapter 5.

The boundary-integral approach offers a novel tool for gaining new insights into typical problems, such as film motion in diverging-converging channels, which is considered in this study. By decomposing the film motion, it can be investigated how the film responds to external strains, as detailed in Chapter 5. Additionally, the energy consumption during the film motion, analysed through this motion decomposition, provides a fresh perspective on understanding the yield stress of foam flow in porous media, as elaborated in Chapter 6. In the same chapter, the study also provides a preliminary exploration of 2D foam flow in a Hele-Shaw cell within the framework of the boundary integral method for dry foam. Unlike the 2D viscous froth model, this approach takes into account the viscosity of the fluid within the bubbles, which could have a notable impact on the behaviour of the foam films.

Chapter 3

Quasi-static film motion in porous medium models with blocked throats

3.1 Introduction

When the flow rate of a foam decreases towards zero, the foam's behaviour becomes quasi-static. This implies that the structure of the foam remains the minimal surface, namely the configuration with the lowest surface energy. The minimal surface adapts to evolving constraints as the foam moves. To compute this minimal surface, a commonly employed approach involves using the Surface Evolver tool [87], which utilises the gradient descent method to minimize the overall surface energy. In Surface Evolver, the foam's geometry is discretised into a triangle mesh, represented by a network of vertices or material points, with edges and faces formed by their connections.

In situations where foam is present within a porous medium, it is possible to mesh the surface of the solid matrix. Since the solid matrix confines the motion of the foam, the vertices on the solid surface are constrained from moving normal to the surface, and instead, tangential movements are often necessary to maintain mesh quality. In this manner, the pore- or bubble-scale modelling approach for quasi-static foam flow, available in Surface Evolver, can be directly applied to investigate foam behaviour within a porous medium, even when dealing with a

large porous medium. However, when addressing the flow of multi-phase fluids, including foams, within a large-scale porous medium, the focus often shifts to the pore network of the medium [14]. This shift is primarily driven by the significant computational cost associated with applying a microscopic model to a macroscopic problem. Consequently, the development of a quasi-static foam modelling approach for foam within porous media at the pore-network scale remains a compelling endeavour.

This chapter begins by introducing the porous medium models that are used, in Section 3.2. Then, two methods for predicting the minimal surface of foam, as outlined in Section 3.3 and 3.4, respectively. The first method involves using Surface Evolver at the pore or bubble scale, whereas the second approach is a novel proposal tailored to the pore-network scale. In Section 3.5, the pore-network scale method is verified through a comparative analysis with the outcomes derived from the pore-scale method. In Section 3.6, quasi-static film motion in porous medium models with trapped pore throats is studied. Conclusions are presented in Section 3.7.

3.2 Porous medium models

The porous medium models used in this work are 2D models. One straightforward approach to constructing a porous medium is to replace each site in a lattice pore network model with a pore that has a specified shape. Simulations of percolation behaviour performed on lattices have suggested a reasonable size for such a pore network [109]. Chatzis and Dullien [109] conducted computational simulations of percolation behaviour of fluid in a 2D lattice, and they argued that a lattice with a width of 30 bonds and a length of 40 bonds is sufficient to represent an infinite 2D lattice. However, for the sake of simplicity, this work considers smaller geometric models. As will be demonstrated later, even in these simpler models, the presence of trapped lamellae has a significant impact on the movement of a lamella as it travels through a pore.

The present work employs several different geometric models, all of which are constructed based on the individual pores depicted in Figure 3.1. These pore shapes are derived from a diamond structure. To generate the pores, the corners of the diamond are adjusted so that each corner

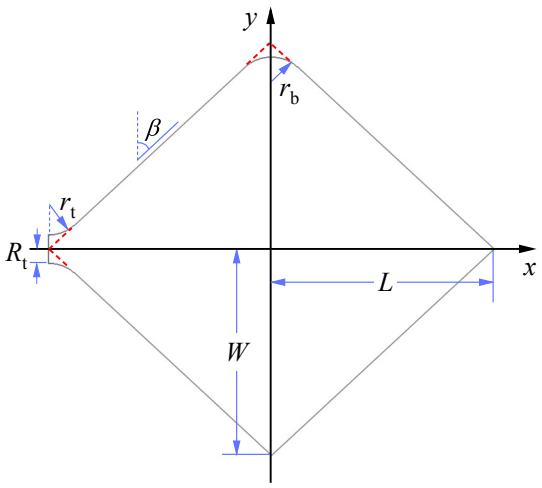


Figure 3.1: The pore geometry utilised in this study is derived from a diamond structure, whose corners are rounded or modified to throats. The geometry is characterised by several geometric parameters: L the half of pore length, W the half of pore width, R_t the half width of pore throat, r_b the rounding radius at corners in the pore body, r_t the rounding radius at the pore throats, and β the angle between the straight wall and the vertical. These parameters are not independent, which are related by $\tan\beta = L/W$ and $R_t = (1/\sin\beta - 1)r_t$. Different pores are obtained by changing different numbers of corners to throats. The types of pores used in this work include: a pore with two opposite pore throats, a pore with two neighbouring pore throats, and a pore with three pore throats.

represents either a pore throat or a pore corner within the broader pore body. A pore corner is obtained by rounding a diamond corner with a selected radius. A smaller rounding radius results in a sharper pore corner. Two types of pores are considered in the simulations: the two-throat pore and the three-throat pore.

Table 3.1 presents the dimensionless values chosen for the relevant geometric parameters in this study. The radius at the corner within the central pore body is set to 0.25 for sharp pores and 1.0 for rounded pores. The pore length ($2L$) and width ($2W$) are both set to 3.0. It is worth noting that the typical dimensional length of a real-world pore might be around 10 μm [39]. The corners are rounded in consideration of the fact that pore corners tend to be rounded due to the presence of a small amount of water occupying the corners. This water can be brought by the Plateau borders moving along the walls [110, 111]. Two different values for the radius at the corners within the pore body, r_b, are considered: 0.25 and 1.0. Additionally, three types of pores are utilised, distinguished by the number of throats and the relative positions of these throats. These types include the two-throat pore with opposite throats, the two-throat pore

Table 3.1: Pore dimensions used in the simulations

Geometric parameter	Value
L	1.5
W	1.5
R_t	0.1036
r_b	0.25, 1.0
r_t	0.25
β	$\pi/4$

with neighbouring throats, and the three-throat pore. A two-throat pore with opposite throats corresponds to a bi-conical pore, as previously employed in research [66, 112, 113]. A two-throat pore, whether with opposite or neighbouring throats, is characterised as a sharp pore when r_b is set to 0.25, and a rounded pore when r_b is set to 1.0.

The geometric models used in this chapter are summarised in Figure 3.2. In Section 3.5, the two-throat pore is used, shown in Figure 3.2(a), to verify the code conducting the pore-scale method discussed in Section 3.3. In the same section, a porous medium is constructed, composed of three pores as shown in Figure 3.2(b), including one upstream three-throat pore and two downstream two-throat pores with neighbouring throats, in order to verify the pore-network method proposed in Section 3.4. It is found that only one lamella would move forwards in the downstream pore with the other lamella trapped in the pore throats, which is discussed in detail in Section 3.5. In Section 3.6, the porous medium models shown in Figure 3.2(c)-(f) is considered. The number of pores with trapped lamellae varies from 0 to 3, and for each case the pore with a moving lamella is considered to be sharp and rounded, respectively.

3.3 Pore-scale method

In the pore-scale method, foam films or lamellae are divided into discrete material points, and the positions of these points dictate the foam's configuration within Surface Evolver [87]. The configuration evolution of the foam system towards the state of minimal surface is accomplished through iterations, where each iteration involves updating the positions of these material points by calculating displacements using the gradient descent method. Figure 3.3 illustrates the discretisation of foam lamellae, in 2D, and the categories of related geometric elements. It

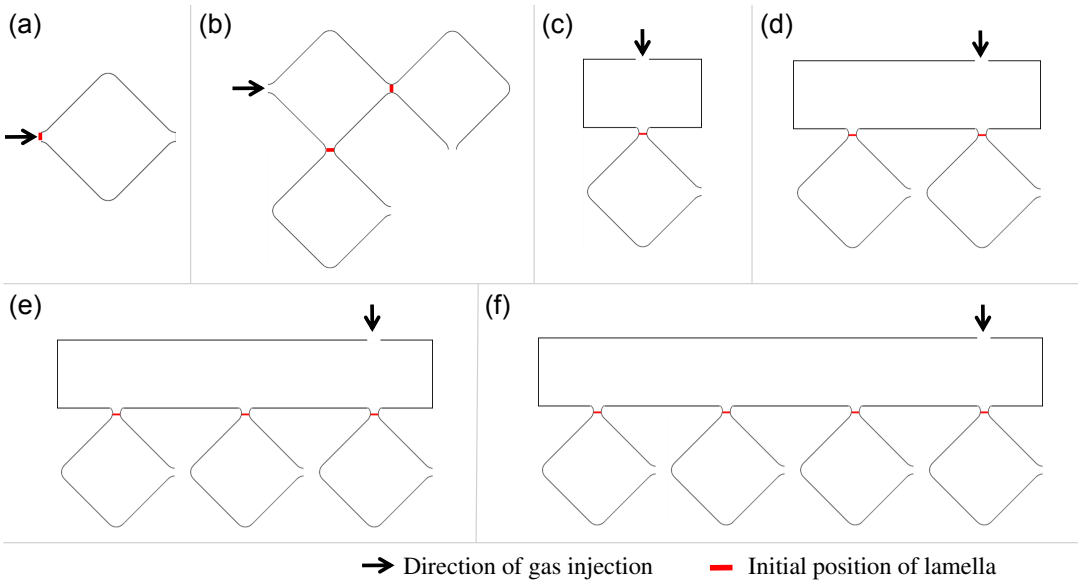


Figure 3.2: Porous medium models used in this chapter. (a) A single two-throat pore with opposite throats. (b) A porous medium composed of three pores. (c)-(f) Porous medium models with the number of downstream pores varying from 1 to 4. The arrows show the direction that gas is injected into the models, and the red line segments show the initial positions of lamellae in the models. Model (a) and (b) are used in Section 3.4. Model (c)-(f) are used in Section 3.5.

is important to acknowledge that some of the elements depicted in the schematic may not be directly relevant to the specific application under consideration in this chapter. The inclusion of all potential geometric elements serves the purpose of explaining the pore-scale method, which is applicable in a broad range of scenarios involving foam flow within confined geometries.

As shown in Figure 3.3, the linear interpolation is employed to approximate the curved foam lamellae. Each segment of a lamella between two adjacent material points is represented as a straight line segment connecting these points. These material points fall into two distinct categories based on the number of edges connecting to them: two-fold points and three-fold points. A two-fold point is situated within the interior of a film, while a three-fold point corresponds to the intersection of three foam lamellae, commonly referred to as the Plateau border. The Plateau border itself can be further categorised as either a bulk Plateau border or a wall Plateau border, depending on whether it is located within the bulk of the foam or right on the wall.

Furthermore, material points can be categorised into four distinct types based on their mobility: fixed points, mobile points, semi-mobile points, and constrained points. A material point is

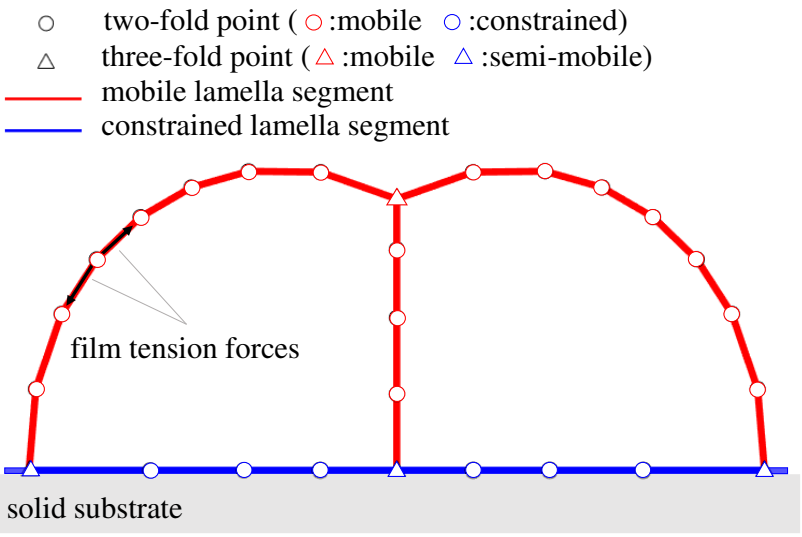


Figure 3.3: Schematic diagram of a foam configuration that includes two bubbles adhered to the surface of a solid substrate or wall. Within this configuration, segments of lamellae are discretised into two types: mobile lamella segments and constrained lamella segments. The constrained lamella segments represent the wetting film that coats the wall surface. Material points are categorised into either two-fold points or three-fold points, depending on the number of lamella segments they connect. A two-fold point can either be mobile, located on a mobile lamella, or constrained, attached to the wall. Meanwhile, a three-fold point can be either mobile or semi-mobile, with the former corresponding to a bulk Plateau border and the latter to a wall Plateau border. This schematic serves as a reference solely in the context of the pore-scale method discussion and may not precisely mirror a realistic foam configuration.

designated as fixed when it is positioned in a narrow section of the wall characterised by high curvature, which severely limits its capacity to move. A mobile point is identified as a two-fold point situated within a lamella located in the pore space, rather than being part of the wetting film on wall. A semi-mobile point is defined as a three-fold point on the wall that remains connected to a mobile lamella. Lastly, a constrained point refers to a two-fold point positioned on the constrained lamella which exactly is a coating film on the wall.

3.3.1 Film tension force

In a foam system, where the film tension (assumed to be unity) plays a critical role, it drives the surface to minimise its overall area, aiming for a state of minimal surface area. The overall film tension force, denoted as $\boldsymbol{F}_i$, acting on material point i, can be expressed as

$$\boldsymbol{F}_i = \sum_{k=1}^{K} \boldsymbol{f}_k, \tag{3.1}$$

where K is the number of edges connecting to point i, either 2 or 3 in 2D, and $\boldsymbol{f}_k$ is the tension force exerted by the kth connecting edge, which is a unit vector along the edge, pointing out of point i, as shown in Figure 3.3. The overall film tension force acting on a material point represents the steepest descent direction of the total surface energy with respect to the movement of the material point [87]. It is important to note that only mobile lamellae can exert a force on a material point, while constrained lamellae coating the wall and forming enclosed bubbles do not exert any force on associated material points.

To adhere to the constraints of conserving bubble volume (which exactly refers to the area of each bubble in 2D) and ensuring semi-mobile points move tangentially along the wall, adjustments are necessary in the movement direction of each material point. The wall constraint dictates that, for a semi-mobile point, the tension force should be projected onto the tangent direction of the wall at that specific point. This projection can be independently calculated for each material point. Conversely, the constraint related to bubble volume introduces a set of equations that need to be solved. This allows us to determine how the overall tension force

acting on each material point should be further modified.

One approach to constructing the system of equations for computing the modification is to utilise the gradient directions of bubble volumes, at each material point, where the bubble volume is theoretically represented as an integral across all material points on the boundary of a bubble. Specifically, denote $\boldsymbol{g}_{ij}^{\mathrm{p}}$ the gradient direction at point i due to the volume conservation in bubble j, where the superscript p indicates that, if point i is on the wall, the resultant gradient direction should be further projected onto the tangential plane of the wall. The adjustment of the tension force at each point can then be constructed as a linear combination of the gradient directions originating from all bubble volumes at that specific point, following the methodology outlined by Brakke [87]. With the adjustment, the modified movement direction at each material point, denoted by $\boldsymbol{F}_i^{\mathrm{v}}$, can be expressed as

$$\boldsymbol{F}_i^{\mathrm{v}} = \boldsymbol{F}_i^{\mathrm{p}} + \sum_{j=1}^{N} P_j \boldsymbol{g}_{ij}^{\mathrm{p}}, \tag{3.2}$$

where N is the number of bubbles, $\boldsymbol{F}_i^{\mathrm{p}}$ the projected film tension force, P_j the coefficient associated with the contribution of the jth bubble. As mentioned, $\boldsymbol{g}_{ij}^{\mathrm{p}}$ refers to the gradient direction at point i, computed using the expression of the volume of bubble j. It represents the steepest direction in changing the volume of bubble j as point i moves.

Because of the mass conservation (under the incompressible assumption, namely the volume conservation), the volume of each bubble remains as material points move along the directions given in Eq. 3.2, which leads to a linear system of equations for the unknown coefficients P_j

$$\sum_{i=1}^{N_j} \boldsymbol{F}_i^{\mathrm{v}} \cdot \boldsymbol{g}_{ij}^{\mathrm{p}} = 0, \quad j = 1, 2, ..., N, \tag{3.3}$$

where N_j is the number of material points of jth bubble. Solving this linear system of equations, the evolving direction of each material point can be determined. Furthermore, the displacement of each material point can be calculated as $\lambda \boldsymbol{F}_i^{\mathrm{v}}$, where λ is a small scaling factor. Employing a small scaling factor is critical because the directions utilised to update the positions of material

points provide merely a first-order accurate estimation of the descent direction for the total surface energy. Employing a small scaling factor ensures that the computed displacement ultimately leads to a decrease in the total surface energy once the foam configuration undergoes evolution.

On the other hand, even though Eq. 3.3 is designed to maintain bubble volumes, achieving precise conservation of bubble volume during the evolution of the foam configuration towards the minimal surface remains challenging. Specifically, the evolution of the foam configuration involves an iterative process in which material points undergo displacement guided by computed values at each iteration step. Despite the inclusion of a small scaling factor λ to aid in preserving bubble volume, numerical errors in bubble volumes may accumulate over time. These errors stem from two primary factors. Firstly, the adjustments made to the evolving directions rely on the gradient directions of the bubble volumes at each material point, resulting in a second-order error in bubble volume following the finite displacements of the material points. Secondly, due to the finite number of material points used for discretising the lamellae, a discretisation error further contributes to the deviation in bubble volume. To address these errors, it is recommended to integrate volume restoring motion into each iteration step, immediately following the adjustment of the foam configuration based on the computed displacements [87].

3.3.2 Volume restoring motion

The volume restoring motion, $\boldsymbol{F}_i^{\mathrm{r}}$, for each material point i, is expressed as a linear combination of the gradient direction of each bubble volume at the material point

$$\boldsymbol{F}_i^{\mathrm{r}} = \sum_{j=1}^{N} C_j \boldsymbol{g}_{ij}^{p}, \tag{3.4}$$

where C_j is the coefficient associated with the contribution of the jth bubble. The volume restoring motions of all material points work to restore the volume for each bubble j

$$\sum_{i=1}^{N_j} \Big(\sum_{j'=1}^{N} C_{j'} \boldsymbol{g}_{ij'}^{\mathrm{p}} \Big) \cdot \boldsymbol{g}_{ij}^{\mathrm{p}} = V_j^{\mathrm{t}} - V_j, \tag{3.5}$$

where V_j is the current volume of bubble j, and V_j^{t} is the target volume required to be restored. Eq. 3.5 can be written in a more convenient form for the unknown $C_{j'}$

$$\sum_{j'=1}^{N} C_{j'} \Big(\sum_{i=1}^{N_j} \boldsymbol{g}_{ij'}^{\mathrm{p}} \cdot \boldsymbol{g}_{ij}^{\mathrm{p}} \Big) = V_j^{\mathrm{t}} - V_j. \tag{3.6}$$

3.4 Pore network-scale method

In various practical applications of foam, such as in soil remediation and enhanced oil recovery, bubbles are often considered to be comparable in size to or even larger than the pores within the surrounding medium. They effectively bridge the cross-sections of the flow paths [114, 52]. In contrast to a bulk foam in a container, a pore throat typically does not contain multiple foam lamellae. Consequently, this leads to a uniform distribution of pressure throughout the pore throat. When foam lamellae are present within a pore body, pressure variations can arise among pore throats that connect to the same pore body.

Figure 3.4 illustrates the partitioning of a large porous medium into individual pores, which are interconnected through pore throats. Different colours are employed to distinguish one pore from its neighbouring pores, but it is crucial to emphasise that this division scheme is not fixed and can be adjusted during a simulation. For example, when certain throats have sufficient width to accommodate multiple lamellae simultaneously, the pores connected through these throats may merge into a single pore.

Focusing on the pink-marked pore located in the central region of the medium, it can be observed that changes in the total surface energy of the lamellae within the pore can be explained by two physical factors: the pressure differences among the throats connected to the pore and the gas flow moving through these throats. In contrast, in the pore-scale method, the alteration in total surface energy is linked to the displacements of the material points on the lamellae.

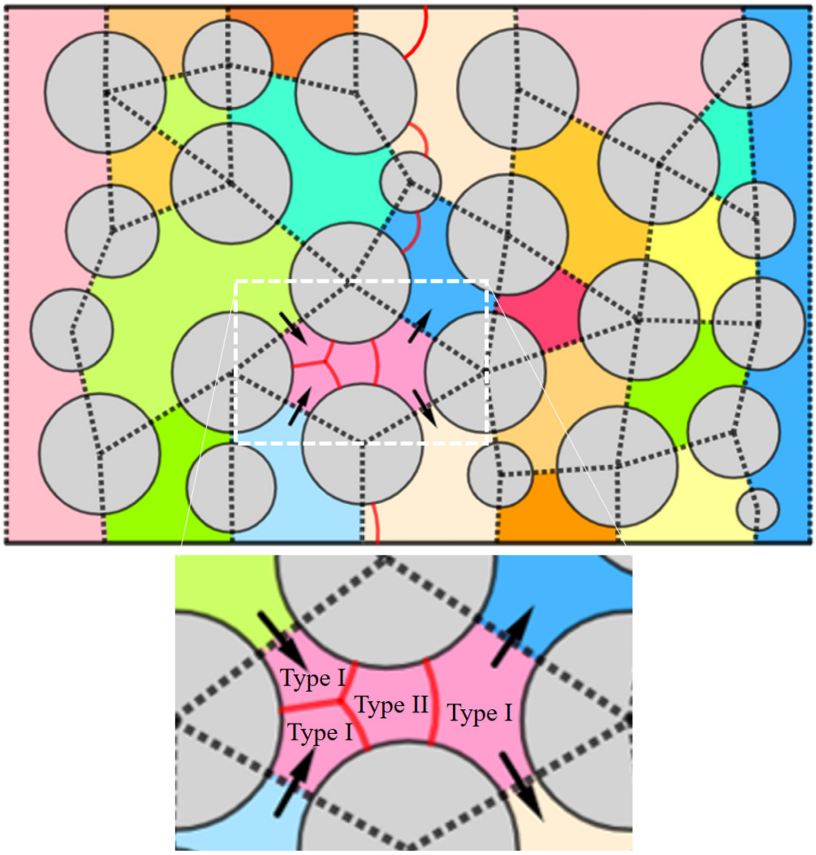


Figure 3.4: A schematic diagram illustrates a 2D porous medium, with solid grains depicted as grey circles. The void spaces consist of interconnected pores, connected by pore throats, and the pores are displayed in various colours. Foam lamellae within the porous medium are represented by red curves. Black arrows indicate the assumed directions of gas flow through the pore throats encircling the pink-colored pore situated in the centre of the medium. Gas areas or bubbles can be classified as either Type I or Type II. Type I bubbles are enclosed by pore throats, pore walls, and lamellae, while Type II bubbles are enclosed solely by pore walls and lamellae. The pore network-scale method aims to describe variations in the total surface energy within the pore by expressing it as a function of pressure differences among the pore throats and the gas flow through these throats.

3.4.1 Mass conservation in pores

In a porous medium, the amount of gas within a pore is conserved. Let δf_{pt} represent a small amount of gas flowing through a pore throat t of pore p. By convention, δf_{pt} is positive when gas enters pore p through the throat t, and negative when gas exits the pore through the same throat. The principle of mass conservation applies to the fluid flow through pore p, and can be expressed as follows

$$\sum_{t=1}^{N_p} \delta f_{pt} = 0, \tag{3.7}$$

where N_p is the number of throats of pore p. Thus, the gas flow through a particular throat of a pore can be expressed as the sum of the gas flow through all other throats of that pore. For example, the gas flow through pore throat $t = 1$ can be expressed as follows

$$\delta f_{p1} = -\sum_{t=2}^{N_p} \delta f_{pt}. \tag{3.8}$$

3.4.2 Gradient of system energy

As depicted in Figure 3.4, there are two distinct categories of gas areas, or referred to as bubbles, distinguished by the boundaries that enclose them. Type I bubbles are encircled by pore throats, pore walls, and lamellae, whereas Type II bubbles are solely enclosed by pore walls and lamellae. Type II bubbles are essentially individual bubbles that do not span multiple pores.

The volume of Type I gas area is denoted as V_{pt}, where p indicates the pore and t signifies the throat belonging to that particular pore. The pressure at pore throat t of pore p is represented as P_{pt}. The potential energy of the gas within the pore due to pressure, denoted as E_p, can be expressed as

$$E_p = \sum_{t=1}^{N_p} P_{pt} V_{pt} + \text{Const}, \tag{3.9}$$

The term Const accommodates the energy related to Type II bubbles. It is important to note that there are cases where a Type I bubble is surrounded by two or more throats. In such instances, the gas potential energy within that bubble might be counted multiple times in Eq. 3.9. However, this repetition does not impact the energy variation to be discussed shortly because the pressure at these throats linked to the same Type I bubble is identical, resulting in a pressure difference of zero among these throats.

In Eq. 3.9, we have implicitly assumed that P_{pt} is a constant coefficient, though the pressure can change as gas flows through a pore. In this case, the pressure potential energy is only affected by the change of bubble volumes. This is reasonable since it is the work of pressure that changes the surface energy. As shown in the following, the difference of Eq. 3.9 reflects the pressure work, and thus can be linked to the variation in surface energy.

Considering an infinitesimal gas flow, δf_{pt}, through pore throat t, the first-order approximation of the variation in the pressure potential energy in pore p is

$$\delta E_p = \sum_{t=1}^{N_p} P_{pt} \delta f_{pt}. \tag{3.10}$$

The change in energy described above corresponds to the net work done by pressure in pore p, which is subsequently stored as film surface energy. Substituting Eq. 3.8 into Eq. 3.10, the energy variation becomes

$$\delta E_p = 0 \delta f_{p1} + \sum_{t=2}^{N_p} (P_{pt} - P_{p1}) \delta f_{pt}, \tag{3.11}$$

where the first term, on the right hand side, is added for completeness.

The overall variation in surface energy, denoted as δE, for the entire porous medium can be calculated by adding up the energy changes for all the pores within the medium

$$\delta E = \sum_{p=1}^{M} 0\delta f_{p1} + \sum_{p=1}^{M}\sum_{t=2}^{N_p}(P_{pt} - P_{p1})\delta f_{pt}, \tag{3.12}$$

where M is the number of pores in the porous medium.

A simplified form of Eq. 3.12 can be obtained for a specific porous medium, where the total energy variation can be expressed as a linear function of the gas flow through the pore throats

$$\delta E = \sum_{t=1}^{M_{\mathrm{T}}} g_t(\Delta P)\delta f_t, \tag{3.13}$$

where M_{T} is the number of all the pore throats in the porous medium, g_t the coefficient of gas flow, which depends on the pressure difference term in Eq. 3.12, and δf_t the absolute value of gas flow through pore throat t. It is worth noting that the subscript t now denotes a global index, which refers to a specific pore throat in the entire porous medium, rather than a local index that represents throats of an individual pore.

To illustrate the transition from Eq. 3.12 to Eq. 3.13, consider the porous medium model depicted in Figure 3.5, which consists of three pores. For this model, the expression for Eq. 3.12 can be written as

$$\begin{aligned}\delta E =& 0\delta f_{11} + (P_{12} - P_{11})\delta f_{12} + (P_{13} - P_{11})\delta f_{13} + \\ & 0\delta f_{21} + (P_{22} - P_{21})\delta f_{22} + \\ & 0\delta f_{31} + (P_{32} - P_{31})\delta f_{32},\end{aligned} \tag{3.14}$$

which can be further combined into a form as in Eq. 3.13. To do so, it is known that

$$\begin{aligned}
\delta f_1 &= \delta f_{11}, \\
\delta f_2 &= -\delta f_{12}, \delta f_2 = \delta f_{21}, \\
\delta f_3 &= -\delta f_{13}, \delta f_3 = \delta f_{31}, \\
\delta f_4 &= -\delta f_{22}, \\
\delta f_5 &= -\delta f_{32}.
\end{aligned} \tag{3.15}$$

Substituting Eq. 3.15 into Eq. 3.14, we obtain

$$\delta E = 0\delta f_1 - (P_{12} - P_{11})\delta f_2 - (P_{13} - P_{11})\delta f_3 - (P_{22} - P_{21})\delta f_4 - (P_{32} - P_{31})\delta f_5. \tag{3.16}$$

The coefficients of δf_t in Eq. 3.16 have been denoted as $g_t(\Delta P)$ in Eq. 3.13. These coefficients represent the pressure differences among pore throats and can be obtained using the pore-scale method or, in simpler cases, by analytical solutions [112].

In Eq. 3.13, the gas flow through each pore throat is nominally given by $\delta f_t = -g_t(\Delta P)$, which represents the gradient descent direction of total surface energy in a porous medium. This allows us to simulate the evolution of the foam system based on the gas flow through pore throats. However, the gas flow determined by the gradient descent direction $-g_t(\Delta P)$ might not adhere to the principle of mass conservation. To address this issue, rewrite Eq. 3.7 in a form with respect to the absolute value of the gas flow through pore throats

$$\sum_{t=1}^{M_\mathrm{T}} k_{pt}\delta f_t = 0, \tag{3.17}$$

where k_{pt} is a coefficient, taking 0, 1, or -1. The coefficient arises because the absolute value of gas flow through pore throat t has been used for δf_t, and its direction has been predetermined for a given porous medium, as exemplified in Eq. 3.15. It is not important how directions in default for pore throats are specified, i.e. one may randomly set the directions at the beginning.

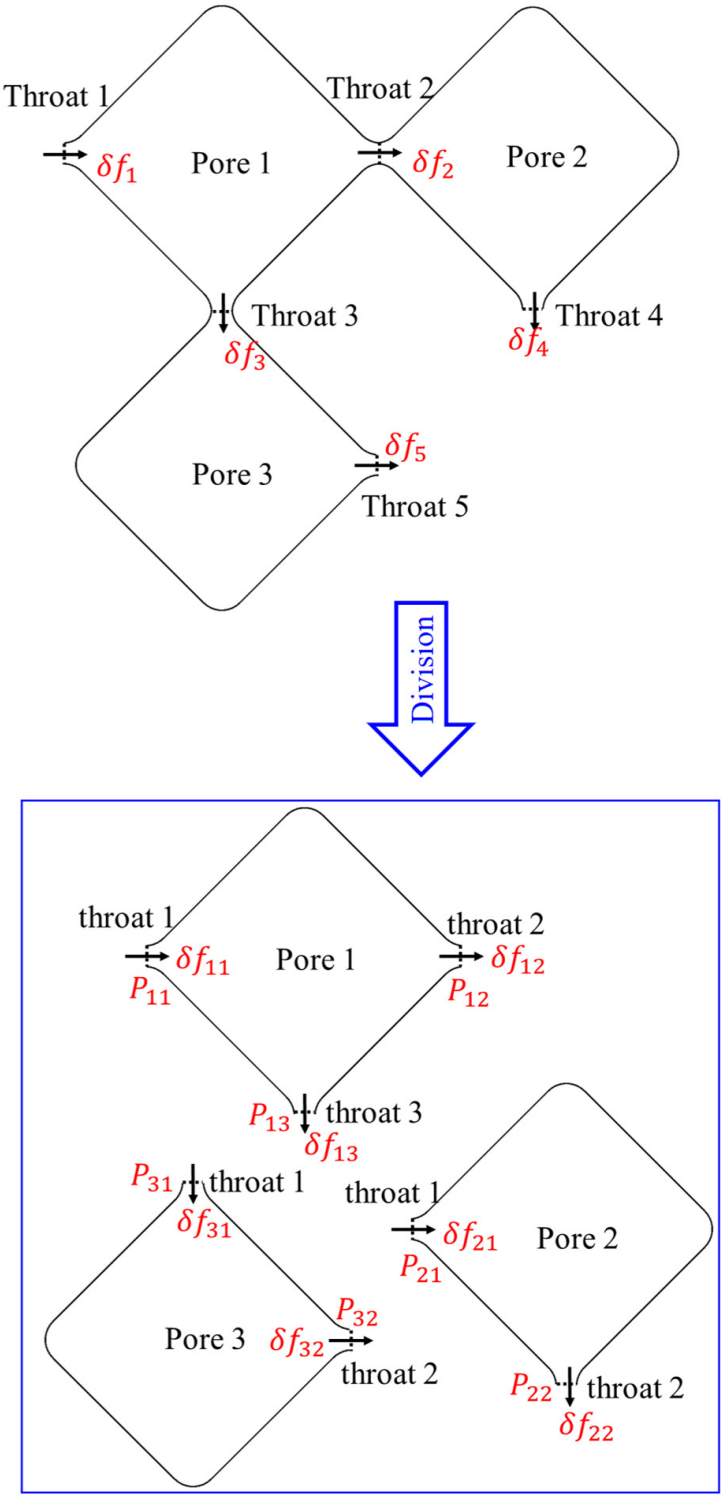


Figure 3.5: A porous medium model consisting of three pores, including a three-throat pore and two two-throat pores, whose indices p are 1, 2, 3, respectively. There are five throats in this model, whose global indices t are 1, 2, ..., 5. The black arrows indicate the assumed directions of gas flow. δf_t is the absolute value of the gas flow through throat t of the porous medium model. P_{pt} is the pressure at the throat of local index t of pore p. δf_{pt} is the gas flow through the throat t of pore p, which is either positive or negative, depending on whether the gas is flowing into or out of pore p. When referring to a specific pore, the local index t of a throat of the pore is up to 2 or 3.

The modification for each gradient component given in Eq. 3.13 then is assumed to be $-\sum_{p=1}^{M} K_p k_{pt}$ with K_p being the coefficient associated with the mass conservation in pore p. As a result, the gas flow through each pore throat, δf_t, is updated to $\delta f_t = -g_t(\Delta P) - \sum_{p=1}^{M} K_p k_{pt}$. To solve for the unknown coefficient K_p, the modified gas flow through each pore throat must satisfy the total M mass conservation equations. To do so, the modified expression for δf_t is substituted into Eq. 3.17, yielding

$$\sum_{t=1}^{M_\mathrm{T}} k_{pt}(g_t + \sum_{p=1}^{M} K_p k_{pt}) = 0, \tag{3.18}$$

which can be transformed into a more convenient expression

$$\sum_{p=1}^{M}(K_p \sum_{t=1}^{M_\mathrm{T}} k_{pt}) = -\sum_{t=1}^{M_\mathrm{T}} k_{pt} g_t. \tag{3.19}$$

Eq. 3.19 is a counterpart of Eq. 3.6 derived for the pore-scale method. An extra equation to consider when solving Eq. 3.19 is the total amount of gas that is injected into the porous medium model. For instance, in the previous example of the porous medium model shown in Figure 3.5, δf_1 equals δV, which is a small increment in gas volume specified in the simulations.

The final expression for the gas flow through each pore throat can be expressed as $\delta f_t = -\lambda\big(g_t + \sum_{p=1}^{M} K_p k_{pt}\big)$, where λ is a scaling factor that needs to be small. This is because the total surface energy exhibits a non-linear dependency on the gas flow through each pore throat. The presence of a small scaling factor guarantees the effectiveness of surface energy reduction, as it ensures slight alterations to the foam structure.

3.4.3 Algorithms for surface energy minimisation

Two algorithms are available for quasi-static simulations of foam flow within a porous medium. The first method involves employing the pore-scale approach within a confined geometry, such as a porous medium, without subdividing it into smaller components, as has been done in

various previous studies [66, 37, 115, 48, 116]. The second algorithm established in this work, named the two-level method, combines the pore-scale and pore network-scale methods. It is effective when gas bubbles are larger than the pore size. This is because the pore network-scale method relies on a uniform pressure distribution within the most constrained area of the local geometry, i.e. the pore throats.

The two-level method involves a process where a small gas volume, denoted as δV, is introduced into the geometric model. Iterations between the pore-scale and pore network-scale methods continue until a converged foam configuration is achieved. In each iteration step, the pore network-scale method determines the gas flow through each pore throat, which is subsequently injected into each pore. Then, the pore-scale method or the analytical method mentioned after Eq. 3.15 and 3.16 is used to calculate the pressure distribution within each pore. The resulting pressure differences among pore throats are employed as input for the pore network-scale method in the subsequent iteration. Notably, to simulate the gas injection process at each step, the total gas flow through the pore throats connected to the injection port is initially set to δV in the first iteration and then adjusted to zero in the following iterations until the foam configuration reaches convergence.

3.5 Verification of the two-level method

The verification of the pore-scale or sub-pore level method's implementation is conducted through simulations of a single lamella's motion through a pore with two opposite throats. The selection of the resolution for discrete representation of films can be achieved by a grid-independence study that the resolution is refined until converged numerical results are obtained. For a given grid resolution, the minimum-surface energy result is indicated by a positive definite Hessian matrix [87]. Qualitatively, this is suggested by that more iterations produce no change in the foam configuration. In the simulations throughout this chapter, the length of each discrete edge is controlled between 0.07 and 0.16, with averaged value roughly 0.1. Moreover, in each simulation, the iteration continues until the rate of the variation in total surface energy,

reflected by the length summation of all mobile films, with respect to the number of iterations below 10^{-8}. This resolution, as well as the iteration termination criterion, as shown in the following, are sufficient to resolve the problem, with results matched well with the analytical solution. The simulation results of the pressure drop across the lamella, denoted as ΔP, closely align with the analytical solution, as illustrated in Figure 3.6. The pressure drop varies with the volume, denoted by V, swept by the lamella since its entry into the pore. In the numerical simulations, both asymmetric and symmetric jumps of the two wall Plateau borders can be observed as the lamella progresses through the central pore body.

The symmetric jump is only observed when a relatively large volume increment is applied to propel the lamella forward within the pore, consistent with previous research findings [66]. In physical terms, when the lamella approaches the corners with a high velocity, the perturbations that lead to an asymmetric lamella shape remain small until the lamella reaches the converging pore section on both sides, resulting in a symmetric jump [113]. In the quasi-static limit, the asymmetric jump, as depicted in Figure 3.6(a), is consistently present in realistic movements, while the symmetric behaviour shown in Figure 3.6(b) is primarily presented to highlight the significant influence of asymmetry on the pressure profile as the lamella traverses the pore. Further discussion on the effects of the jump can be found in [66, 115].

To assess the effectiveness of the two-level method, a specific geometry is considered, which consists of three pores, including two with adjacent throats and one three-throat pore, as depicted in Figure 3.2(b) and 3.5. At the start of the simulation, both interior pore throats are blocked by flat lamellae with zero pressure drop, represented by the foam configuration a in Figure 3.7. Gas is then injected into the model through the top-left pore throat and allowed to exit the model through two other pore throats connected to the external space. Gas injection continues until one of the lamellae approaches one of the two outlets. The pressure drop across the geometric model and the gas flow through the two interior pore throats are predicted using the pore-scale method and the two-level method, respectively. The results are compared in Figure 3.8 and 3.9.

The results obtained using the two-level method align with those obtained from the pore-scale

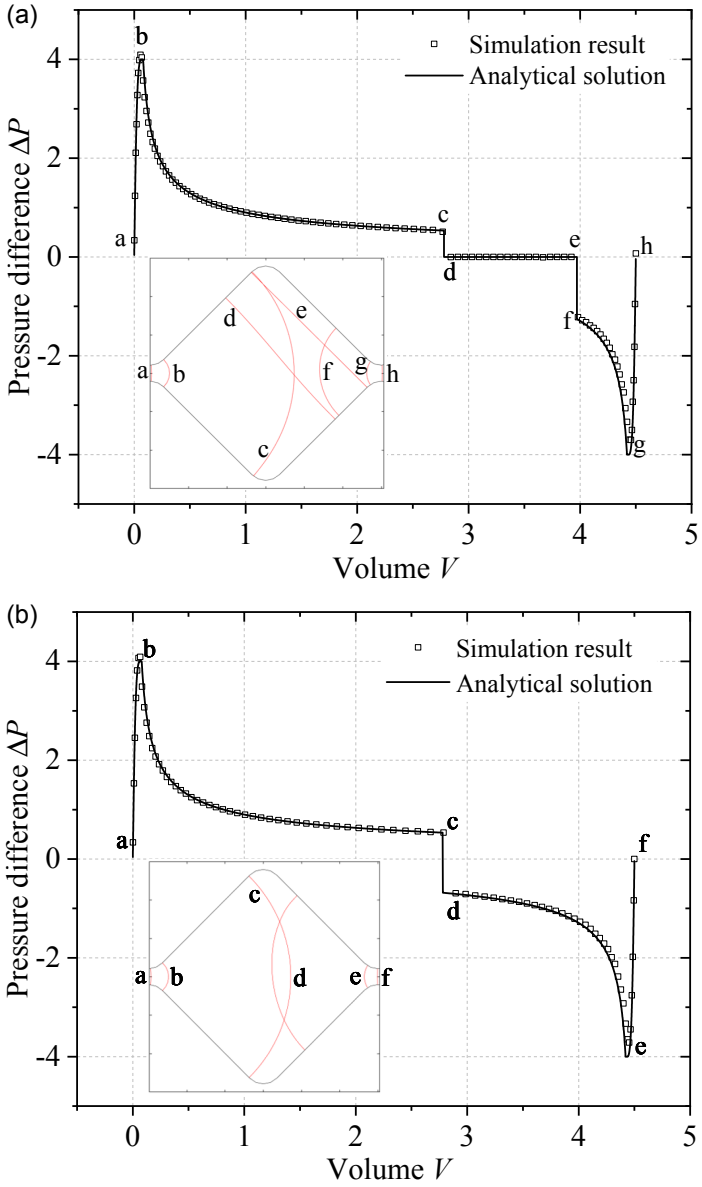


Figure 3.6: The passage of a lamella through a pore with two opposite throats. The results regarding the pressure drop across the lamella are compared with the analytical solution. The insert figures illustrate the shapes of the lamella, denoted by letters, in two scenarios: (a) the asymmetric jump, where the two Plateau borders become asymmetric about the horizontal axis of the pore after approaching the corners in the wide pore body, and (b) the symmetric jump, where the two Plateau borders remain symmetric about the horizontal axis of the pore during the lamella propagation. The analytical solution for both the symmetric and asymmetric jumps can be found in [112].

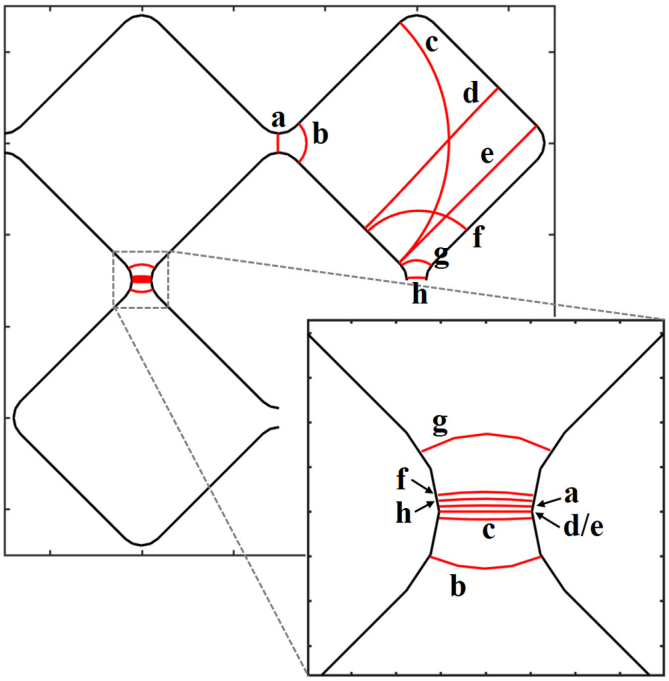


Figure 3.7: A geometry composed of a three-throat pore and two two-throat pores is employed to assess the effectiveness of the two-level method. The lamella configurations are identified by letters arranged in alphabetical order. Initially, two flat lamellae are located within the two interior pore throats. Despite the identical shapes of the downstream pores and the symmetric initial lamella configuration, the movements of the two lamellae exhibit asymmetry, as one lamella is trapped near the pore throat while the other progresses through the downstream pore.

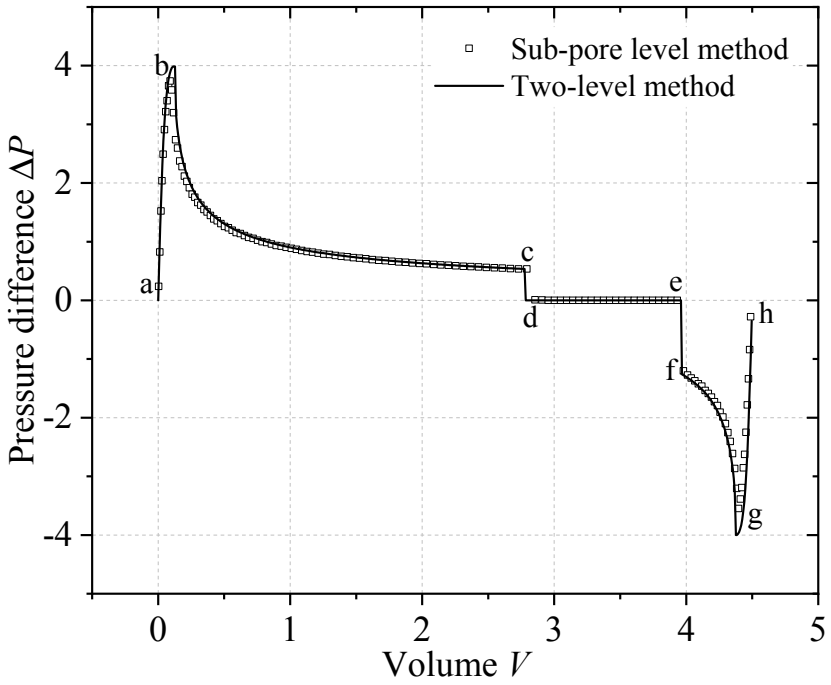


Figure 3.8: The pressure difference across the three-pore model, calculated using both the sub-pore level (i.e. pore-scale) method and the two-level method. For the positions and shapes of the lamellae identified by the letters, please refer to Figure 3.7.

method, confirming the validity of the two-level method. The pressure difference across the model exhibits an asymmetric jump due to the asymmetrical movements of the Plateau borders. Additionally, gas bubble trapping occurs in one of the pore throats, while the gas predominantly flows through the other pore throat. Although the two downstream pores are symmetrically positioned in the porous medium model, symmetric displacement of the two lamellae in these pores is unlikely to occur because this motion mode is unstable and can be transformed into the stable asymmetric displacement pattern under small perturbations.

The stable displacement pattern is consistently obtained with the pore-scale method, primarily due to the discretisation error of the foam system, which introduces disturbances to the positions of the two lamellae in the downstream pores. In contrast, the two-level method can reproduce the unstable displacement mode, but this mode becomes unstable itself when small perturbations in the gas flow through the pore throats are introduced during iterations. Therefore, the stable motion mode is achieved where there is only one moving lamella, while the other is trapped near the pore throat. This applies even when there are multiple downstream pores in the porous medium model, as discussed further in Section 3.6.

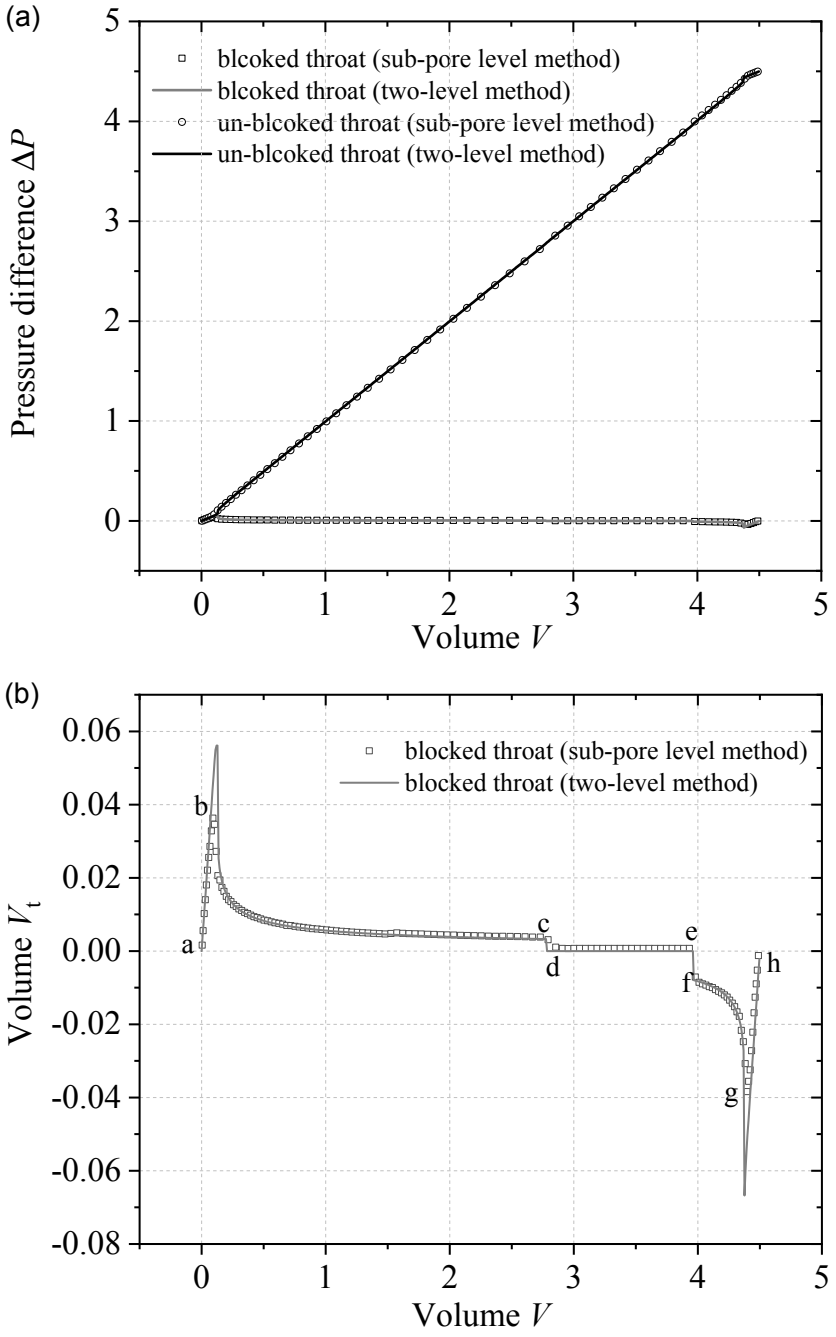


Figure 3.9: The gas flow through two interior throats as a function of the total amount of gas injected into the three-pore porous medium model is depicted. (a) Both the sub-pore level method and the two-level method provide consistent results for the gas flow through the two throats, denoted as V_{t}. The difference in magnitude of the gas flow through the two throats indicates that one pore throat is predominantly used for gas flow, while the other pore throat is blocked by the lamella. (b) A separate plot shows the gas flow specifically through the blocked throat. For the positions and shapes of the lamellae identified by the letters, please refer to Figure 3.7.

It is important to highlight that, in the two-level method, pore-scale simulations are usually required because the corresponding pressure differences among throats of each individual pore are needed as input in the pore-network level simulations. However, for relatively simple foam configurations, the pressure differences between throats can also be obtained by analytical solutions. In this study, the analytical solution for the pressure drop across the pore with two adjacent throats is used as the input in the implementation of the two-level method.

3.6 Numerical results

This section is focused on the motion of a moving lamella in the presence of trapped lamellae in porous medium models illustrated in Figure 3.2 (c)-(f). The number of downstream pores in these models varies from 1 to 4. Since all the throat geometries connecting the upstream pore and the downstream pores are the same, the expected stable motion mode, as discussed in the previous section, is that only one lamella moves through the downstream pore while all other lamellae are trapped in the pore throats. This leads to variations in the number of trapped lamellae from 0 to 3. When there is only one downstream pore, the problem simplifies to a single lamella moving through a single pore with two neighbouring throats, which is referred to as the "original" case. As defined in Section 3.2, the downstream pore that a lamella moves through is classified as either a sharp or rounded pore based on the rounding radius, r_{b}, at the central pore body being 1.0 or 0.25, respectively.

3.6.1 Film motion in sharp pores

Figure 3.10shows the pressure difference across the geometric model featuring sharp downstream pores ($r_{\mathrm{b}} = 0.25$). This visualisation reveals three distinct phenomena. To begin with, the positive and negative peaks of the pressure differential have shifted towards the midpoint of the horizontal axis when compared to the original scenario. In the original case, the upstream pore has only one downstream pore with two neighbouring throats. The delay in the occurrence of the positive peak can be attributed to a small quantity of gas passing through the trapped

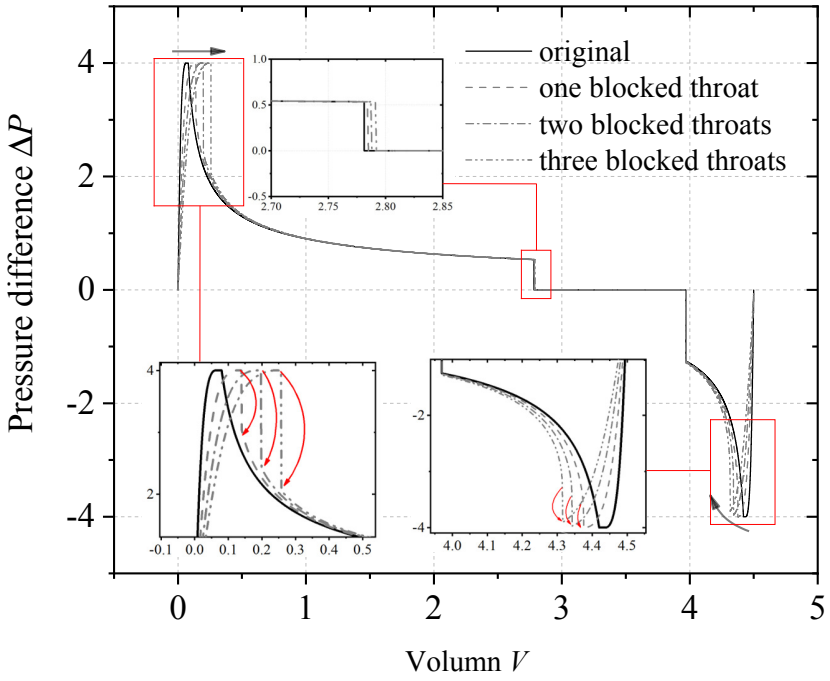


Figure 3.10: The pressure difference, which varies with the amount of gas injected into the porous medium model with sharp downstream pores (where $r_b = 0.25$), is influenced by the presence of trapped lamellae. When a lamella traverses the central pore body, there is a jump in the pressure difference. Similar jumps are observed when the lamella approaches the negative peak or departs from the positive peak, as indicated by the red arrows in the insert figures. The movements and magnitudes of these peaks are illustrated by the black arrows. Specifically, the positive peak experiences a delay in its occurrence but maintains its magnitude. Conversely, the negative peak occurs earlier than expected and diminishes in magnitude as more lamellae become trapped. Additionally, the central jump is slightly delayed.

pore throat and being retained in that region. This behaviour is illustrated in configurations a to b in Figure 3.7 and in the gas flow through each pore throat in Figure 3.9 (b). Conversely, the gas previously trapped in the throat is released later when the lamella moves through the second half of the pore, causing the negative peak to occur earlier than anticipated.

Secondly, there is an abrupt change in the pressure difference, either following the positive peak or preceding the negative peak. This jump becomes more pronounced as lamellae entrap a greater number of throats. Lastly, the magnitude of the negative peak decreases as more lamellae become trapped, whereas the positive peaks remain consistent and unaffected by the presence of trapped lamellae.

In the original scenario, where no lamellae is trapped, the symmetry of the pressure difference variation, denoted as ΔP, in relation to the injected gas volume, V, is disrupted solely by the

abrupt shifts in the wall Plateau borders within the central section of the pore body. However, the two peak areas remain symmetric with respect to the midpoint on the horizontal axis. By contrast, when trapped lamellae are present, the symmetry of the pressure difference variation is further compromised due to the three phenomena, especially the last two. Specifically, the symmetry of the two peak regions is further distorted because the magnitudes of the positive and negative peaks are no longer equal, and the shifts at both peaks are asymmetric. Moreover, we observe a superposition effect where the degree of symmetry disruption becomes more pronounced as the number of trapped lamellae increases.

To elucidate the described phenomena and their consequences, consider the scenario illustrated in Figure 3.1 (f), assuming that only one lamella is in motion through the pore while the others remain trapped. Two curves are utilised, which depict the pressure difference as it varies with gas volume for a single lamella moving through a single pore and for three lamellae trapped case, respectively. The former is exactly the original curve in Figure 3.10. The latter is obtained by tripling the horizontal direction of the initial increasing section of the original curve in Figure 3.10, and the maximum total gas volume injected into the three downstream pores reaches up to 0.177, three times the volume corresponding to the maximum pressure difference of the original curve in Figure 3.10. Furthermore, the curve needs to be extended into the negative domain of the horizontal axis. To do so, remember that the three trapped lamellae become convex toward the upstream pore when the pressure difference across the moving lamella becomes negative. The resultant curve of pressure difference versus the injected gas volume for lamellae trapped case is marked in blue in Figure 3.11.

In Figure 3.11, by setting the pressure difference as the control variable and considering it to be independent of flow paths, an interpolation curve can obtained from the two curves representing the pressure difference variations with gas volume for a moving lamella and three trapped lamellae, respectively. Specifically, the pressure difference, as a function of the injected gas volume, is represented by the red solid curve for a single lamella moving through a single pore and the blue solid curve for three lamellae trapped in throats. To create an interpolation between these two curves, the gas volumes corresponding to the same pressure difference are averaged, as shown by the grey dashed line segment and its midpoint. Note that the inter-

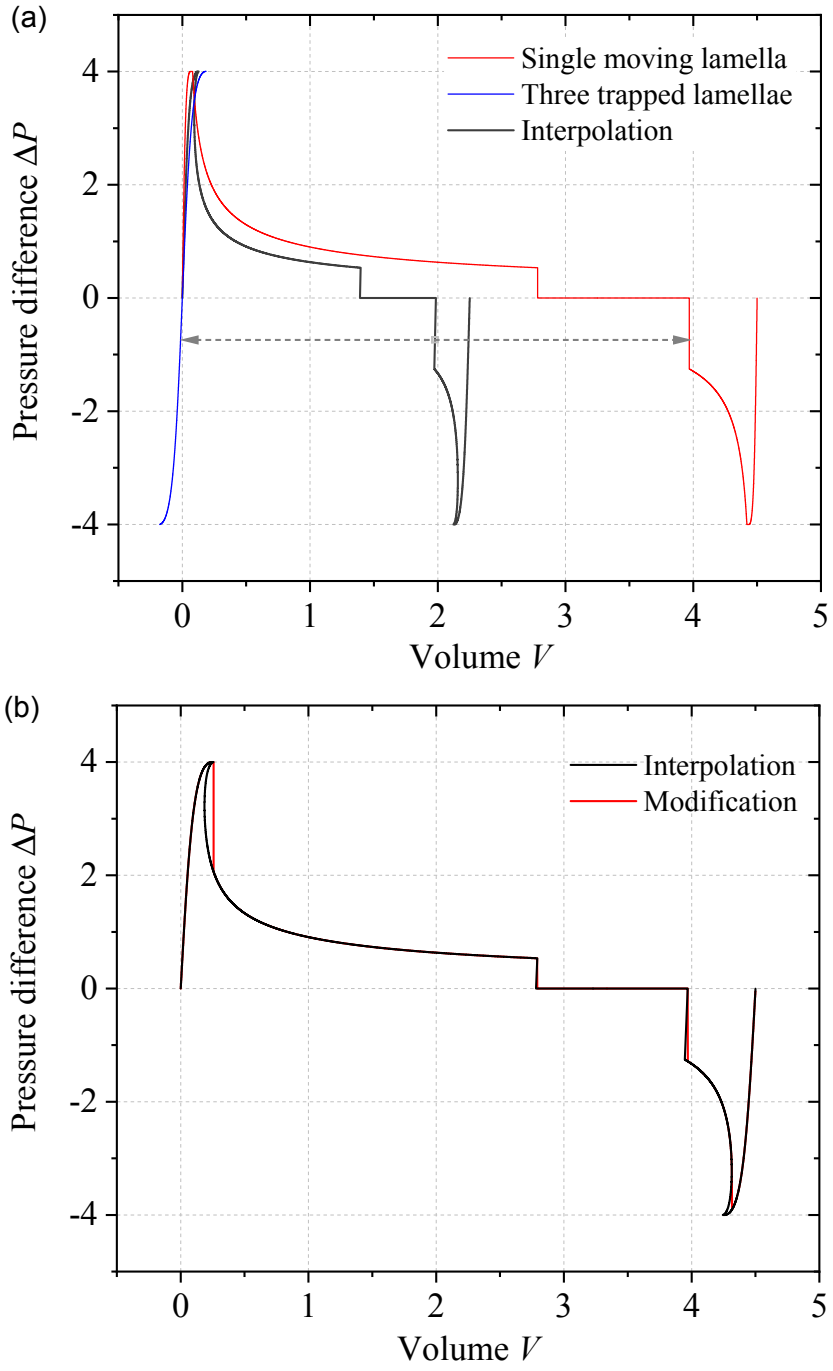


Figure 3.11: The pressure difference observed across the porous medium model in Figure 3.1(f) varies in response to the gas volume injected into the model. (a) The total volume of gas injected into the porous medium model equals the sum of the gas volumes entering all downstream pores. However, for better visualisation, an interpolation curve is first obtained, by averaging the volume values of the two curves at the same pressure difference value. (b) The interpolated solid curve in (a) is then doubled in terms of the horizontal coordinate to account for continuous gas injection. Modifications are made at the two peaks, as well as where jump in pressure difference occurs, and these modifications are asymmetric. The magnitude of the positive peak remains constant, whereas the magnitude of the negative peak decreases.

polation is conducted to avoid summation of the horizontal coordinates of the two curves for better visualisation in one figure; therefore, the horizontal coordinate of the interpolation curve represents half of the total gas volume injected into the porous medium model. As shown by the modification curve in Figure 3.11, this interpolated curve demonstrates that the quantity of gas volume injected into the porous medium model varies non-monotonically as the pressure difference continuously varies. This contradicts the nature of continuous gas injection into the model. To accommodate the continuous gas injection, a jump in the pressure difference becomes necessary, which further impacts the magnitude of the negative peak, causing it to decrease.

In addition to the previously described phenomena, it is worth noting that the presence of trapped lamellae has a relatively minor effect on delaying the central jump of the pressure difference compared to the original case, shown in Figure 3.10. This leads to a slight degradation of the symmetry in the relationship between the pressure difference and the injected gas volume. In comparison, the three phenomena discussed earlier remain the most significant effects caused by the presence of trapped lamellae on the motion of a single lamella. More importantly, these phenomena may also manifest when the moving lamella is situated in a rounded pore with a radius of $r_\mathrm{b} = 1.0$, as discussed in the next.

3.6.2 Film motion in rounded pores

The outcomes of simulations involving the motion of a single lamella through a bi-conical pore highlight differences in average flow resistance between pores with rounded corners, e.g. $r_\mathrm{b} = 1.0$, in the central pore body and those with sharp corners, e.g. $r_\mathrm{b} = 0.25$, as indicated in literature [66, 115]. Specifically, a rounded pore with larger-radius corners would result in zero average flow resistance for the lamella, because no jump in pressure difference occurs during the film motion.

In Figure 3.12, a schematic depicts a lamella within a pore featuring two neighbouring throats and a 90-degree angle between the pore walls and the lamella. It is important to note that the

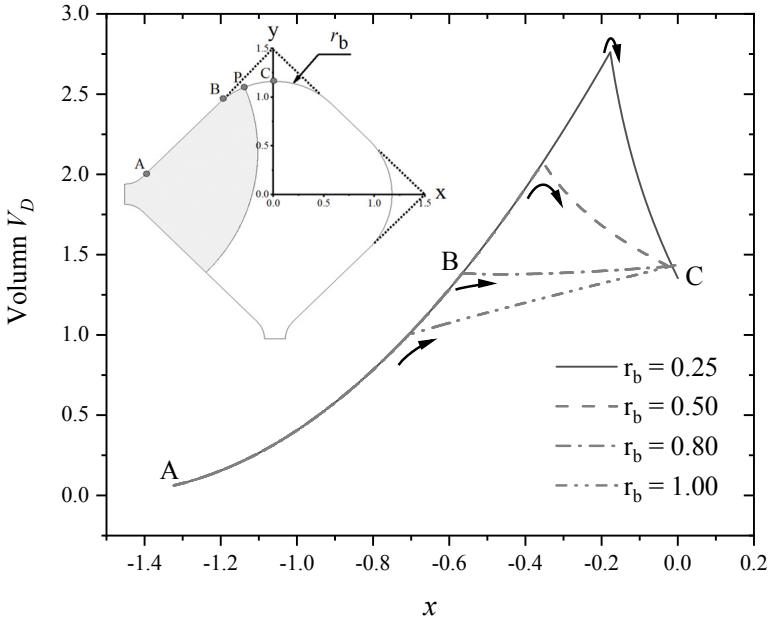


Figure 3.12: The relationship between the volume swept by a lamella and the horizontal coordinate of the Plateau border on the upper wall of the pore is crucial in understanding the behaviour of lamellae within the pore structure. The letter P in the insert figure is used to illustrate a Plateau border position on the upper wall. The region of the swept bubble volume is shaded in grey for clarity. The key factor influencing this behaviour is the sharpness of the corner within the pore, which is determined by the rounding radius, denoted as r_b. In cases where the corner is sharp, such as r_b equals 0.25 or 0.50, the volume would decrease after the upper Plateau border enters the corner, supposing the film does not jump. To avoid this decrease, the lamella typically jumps to a new position, leading to a corresponding jump in the pressure difference. Conversely, when the corner is rounded, for example, such as r_b equals 0.80 or 1.00, the volume increases continuously as the upper Plateau border moves along the upper pore wall. In these scenarios, the lamella's motion is smooth, and there are no abrupt volume changes or jumps in the pressure difference.

volume swept by the lamella may not increase continuously as a function of Plateau border location along the pore wall, depending on the sharpness of the corners within the pore body.

For small corner radii, such as r_b equals 0.25, an interesting phenomenon occurs. As the wall Plateau borders continue to move along the curved corner, the volume of the bubble appears to decrease. To ensure that the volume swept by the lamella increases continuously, the wall Plateau borders must jump to new positions. This jump in the Plateau borders' positions is necessary to avoid a discontinuity in the swept volume and results in a corresponding jump in the pressure difference. On the contrary, when the corner radius is large, as is the case when r_b equals 1.00, there is a guarantee of continuous increase in the swept volume as the lamella moves along the pore. In this scenario, no jump in terms of the locations of the wall Plateau borders is

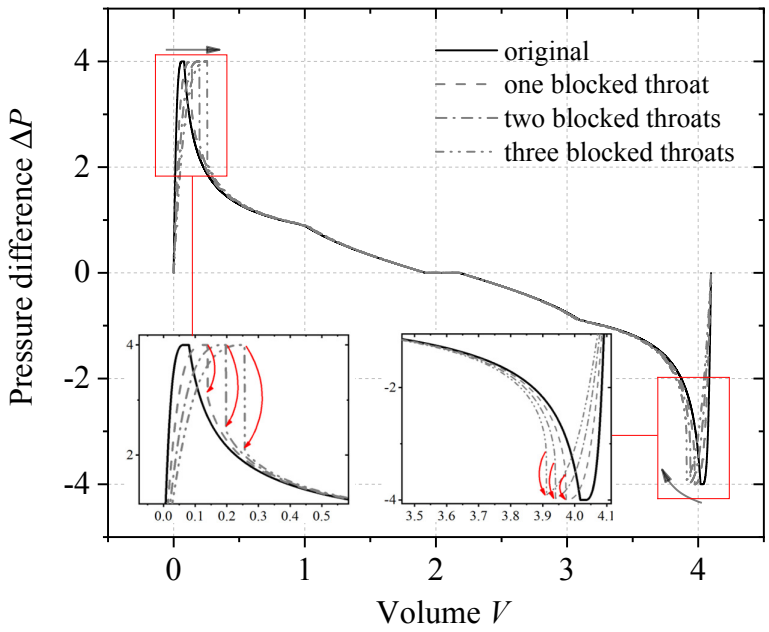


Figure 3.13: The pressure difference observed across the geometric model, with downstream pores featuring rounded corners (i.e. r_b equals 1.0), is influenced by the presence of trapped lamellae. In this scenario, there is no jump in the pressure difference as the moving lamella passes through the central pore body. However, jumps do occur at both peaks, as indicated by the red arrows in the insert figures. The changes in the positions and magnitudes of these peaks are illustrated by the black arrows. The positive peak experiences a delay in its occurrence, but its magnitude remains constant. On the other hand, the negative peak occurs earlier than expected, and its magnitude decreases as more lamellae become trapped.

expected because the rounded corner allows for smooth and continuous motion without abrupt changes in the swept volume or pressure difference.

The curve, denoted by original, in Figure 3.13, displays for a single pore the pressure difference as a function of the injected gas volume, for the rounded downstream pore with $r_{\mathrm{b}} = 1.0$. It exhibits purely central symmetric variation around the midpoint of the horizontal axis, indicating an average flow resistance of zero. However, the presence of trapped lamellae introduces the same effects observed in Figure 3.10, including shifted positions of both positive and negative peaks, jumps in the pressure difference at these peaks, and a decrease in the magnitude of the negative peak. Consequently, the averaged flow resistance or yield stress, which is represented by the volume-averaged pressure difference, can become non-zero. The introduction of trapped lamellae disrupts the initially symmetric film motion, leading to changes in the pressure difference curve and the overall flow resistance characteristics of the quasi-static film motion.

3.6.3 Yield stress of film motion

The yield stress of film motion within porous medium models is a crucial parameter that reflects the flow resistance in the quasi-static limit. It can be characterised by the volume-averaged pressure difference [16, 66], defined as $\Delta P^{\mathrm{avg}} = 1/V_{\mathrm{tot}} \int_0^{V_{\mathrm{tot}}} \Delta P dV$, where ΔP^{avg} is the volume-averaged pressure difference and V_{tot} is the total amount of gas injected into the medium. Figure 3.14 illustrates the impact of trapped lamellae on the volume-averaged pressure difference for both cases: the sharp downstream pore and the rounded downstream pore.

The results demonstrate that confined lamellae contribute to an elevation in the volume-averaged pressure difference when a lamella moves through a pore. This implies that foam flow resistance is influenced not only by the moving lamella but also by the immobile trapped lamellae. This phenomenon is especially noteworthy when a larger number of lamellae are present and confined in nearby pore throats. In situations involving pores with rounded configurations, this effect is amplified in relative terms, giving rise to noticeable flow resistance and subsequently reducing foam mobility.

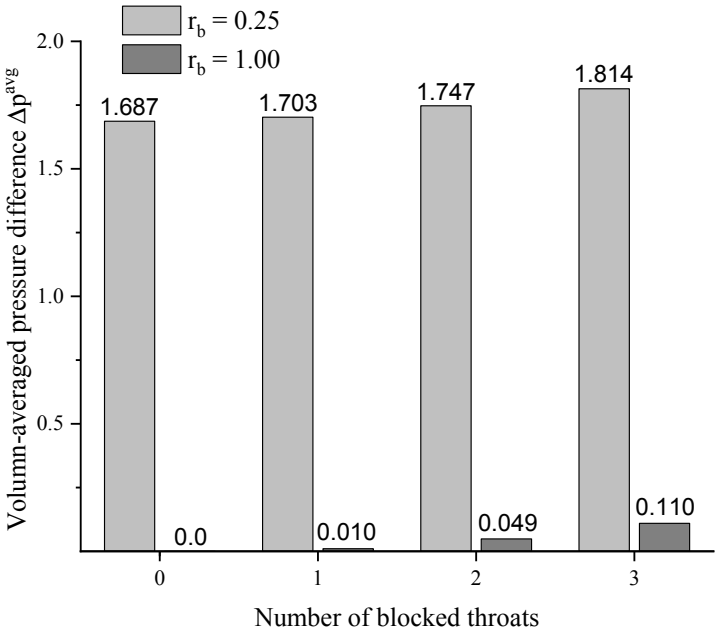


Figure 3.14: The volume-averaged pressure difference for two types of porous medium models with trapped lamellae: one with pores featuring sharp corners (r_b equals 0.25), and the other with pores having rounded corners (r_b equals 1.00). The influence of trapped lamellae is relatively more apparent in cases with rounded pores, since it results in non-zero flow resistance. However, the absolute increase in the volume-averaged pressure difference is similar for both cases.

3.7 Conclusions

In this chapter, the impact of bubble trapping on the yield stress of foam in porous media is further investigated, by numerical simulations conducted in the quasi-static limit. To this end, a two-level method has been presented, which utilises the connectivity of pores in a porous medium to minimise the total surface energy at the pore-network level. The simulation results reveal that, within the porous medium models considered in this study, the only stable mode of propagation for films involves a single lamella moving through the system, while the remaining lamellae become trapped within pore throats. Despite these trapped lamellae not directly interacting with the moving lamella, the average flow resistance for the lamella progressing through the downstream pore increases with the number of trapped lamellae. This occurs because the trapped lamellae can influence gas flow along different pathways and alter the pressure distribution within the porous medium. Furthermore, the investigation reveals that the average flow resistance escalates due to the further disruption of the symmetry in the pressure difference across the porous medium models. This is mainly attributed to three specific

phenomena: the shifted positions of both positive and negative pressure peaks, abrupt changes in the pressure difference at these peaks, and a reduction in the magnitude of the negative peak.

Chapter 4

Foam flow through confined straight channels

4.1 Introduction

In various applications [16, 112, 117, 111, 66] conducted within the quasi-static regime, the effect of viscous dissipation of fluid is often neglected. In this context, additional constraints pertaining to the surface Plateau borders (or wall Plateau borders), where foam films meet the solid surfaces, are excluded in the computations. Consequently, the foam films remain perpendicular to the solid surfaces, aligning with the assumption that there are no tangential viscous forces exerted on the films by the solid surfaces. However, at relatively high flow rates, this assumption becomes invalid, and the concentrated viscous dissipation within the Plateau borders leads to deviations from the 90-degree angles between the films and solid surfaces [113, 118, 23]. Xu and Rossen [113] noticed this problem and introduced additional modelling to account for the viscous motion of the surface Plateau borders, while still assuming that foams maintain minimal surfaces. This improvement can be seen as an extension of the soap film model [113, 119], incorporating extra constraints specific to the surface Plateau borders.

The 2D viscous froth model is an alternative approach for foam modelling that incorporates the effects of viscous forces acting on the surface Plateau borders [89, 19]. This model was

specifically proposed to predict the dynamic motion of dry foams in Hele-Shaw cells consisting of two side walls and two closely positioned covering plates. In mathematical terms, the model is formulated by considering the equilibrium of the pressure differential across the films, the interfacial force resulting from surface tension, and the viscous resistance applied to the films by the covering plates. Additionally, the viscous resistance is commonly assumed to be associated with the normal film velocity through power-law nonlinear relationships, though a linear relationship is often utilised for simplicity [23, 120]. The inclusion of viscous forces in the viscous froth model, unlike the 2D soap film model [66], permits the continuous deformation of the foam configuration [88, 121, 122, 123, 124]. As the foam flow rate increases, the shearing effect happens on the time scale comparable to that of the relaxation of foam structure [89]. In this case, the foam configurations could be deviated significantly from the minimal surface states in stationary equilibrium. Particularly, a T1 topological transformation may be initiated at sufficiently high flow rates, leading to the detachment of bubbles from adjacent films. This phenomenon is observed in scenarios like the flow of a viscous froth lens [88] or a three-bubble cluster [122, 123, 124] in straight channels.

In research employing the 2D viscous froth model, unlike the drag force from the covering plates, which is integrated into the model using the drag force term, the drag force originating from the side walls demands extra attention [23]. This drag force was discovered to have a significant impact on the dynamic arrangements of foam within Hele-Shaw cells because the contact lines between the films and the side walls tend to lag behind the interior of the films [23, 120]. Cox et al. [120] provided analytical solutions for the 2D viscous froth model. These solutions are valuable for predicting stable configurations in foam flow scenarios that take into account the drag forces originating from both the covering plates and the side walls. In more recent years, the model has undergone improvements from various perspectives to incorporate additional physical phenomena observed in realistic foam flow. Notable advancements include accounting for the effect of finite liquid content [125] and incorporating the Marangoni effect [126]. These advancements have enhanced the model's ability to capture a wider range of phenomena involved in foam flow problems.

While the viscous froth model has primarily been used as a 2D representation thus far, re-

searchers have recognised the potential influence of the third dimension (across the gap) present in realistic foam flow systems [118, 23]. One significant observation, for instance, is that the foam films are curved across the gap, which imposes an upper limit on the film migration velocity. Beyond this limit, the foam films start to lie along the confining plates and cannot reach a steady configuration, and the applicability of the viscous froth model is questionable. Despite its potential impact on foam dynamics, the third dimension has not been explicitly incorporated into the viscous froth model. Consequently, there is still a lack of quantitative characterisation of the effects of this third dimension, which is essential for evaluating the extent to which the 2D viscous froth model accurately approximates real-world 3D scenarios.

In this chapter, the goal is to construct a 3D version of viscous froth model for viscous foam that explicitly incorporates the third dimension. This endeavour is inspired by the work of Xu and Rossen [113], where they investigated the impact of viscous forces exerted by the solid surfaces on the time-averaged flow resistance of a single film traversing a bi-conical pore. This concept has been subsequently implemented in Surface Evolver [119]. It will be illustrated how this approach allows us to create a 3D viscous froth model that can be linked to the 2D viscous froth model by reducing the number of dimensions. A typical foam structure, known as the viscous froth lens, is focused in this chapter, which has been examined in previous applications of the 2D viscous froth model [88, 126]. The covering plates are assumed to have rough surfaces, imposing drag forces on foam films. This effect is crucial since the aspect ratio of the cross-section of Hele-Shaw cells is typically far away from unity, and thus the length of the contact line between a film and the covering plates is sufficiently larger than that on side walls. For the same reason, the side walls can be assumed to remain smooth for simplicity, hence the omission of drag forces generated by the side walls.

This chapter is structured as follows. In Section 4.2, an overview of the geometric characteristics of the viscous froth lens is provided. Section 4.3 details the methodology, which encompasses both the 2D viscous froth model and the components of the 3D viscous froth model. The 2D viscous froth model is derived from the Young-Laplace equation, and an approximate relationship between the drag coefficients needed in 2D and 3D models is established, building upon prior research [23]. These equations are then rendered dimensionless to prepare them for subse-

quent numerical simulations. In Section 4.4, the numerical methods are presented for the use in simulations of the dynamic motion of the viscous froth lens with the 3D model and predictions of the steady-state configurations of the viscous froth lens using the 2D model. Section 4.5 is dedicated to presenting the numerical results. The selection of the drag coefficient in 2D and its dependence on locations along films are analysed. Discussion and conclusions are offered in Section 4.6 and 4.7, respectively.

4.2 Viscous froth lens in straight channels

The viscous froth lens flows within a straight channel with a rectangular cross-section, as depicted in Figure 4.1. A Cartesian coordinate system with axes labelled as xyz is referenced, where the y-axis corresponds to the flow direction. The channel consists of two closely spaced covering plates that lie parallel to the y-z plane and two side walls that are oriented parallel to the x-y plane.

The viscous froth lens consists of a bubble partly occupying the straight channel, with a film spanning between the bubble and the opposite side wall. The region within the channel, extending from the rearward side of the so called trailing and spanning films to the inlet of the channel, is referred to as bubble B1. The lens bubble is denoted as B2. In the simulations, B2's volume remains constant, while the volume of B1 progressively grows over time, to mimic the gas injection process. The films intersect the two covering plates at surface Plateau borders (spb), and they encounter each other at the bulk Plateau border. These Plateau borders converge at four-fold nodes.

The Parameters involved in Figure 4.1 include: U the velocity of the gas injected into the channel, namely the driving velocity, W the width of the channel, H the height of the channel or the size of the gap between the two covering plates, L the initial length of the spanning film, θ the angle between films and covering plates, f_{3D} the drag force acting on unit length of the surface Plateau border, whose direction is opposite to the normal velocity of the surface Plateau border u_n, γ the film tension (roughly twice the value of the surface tension of a single

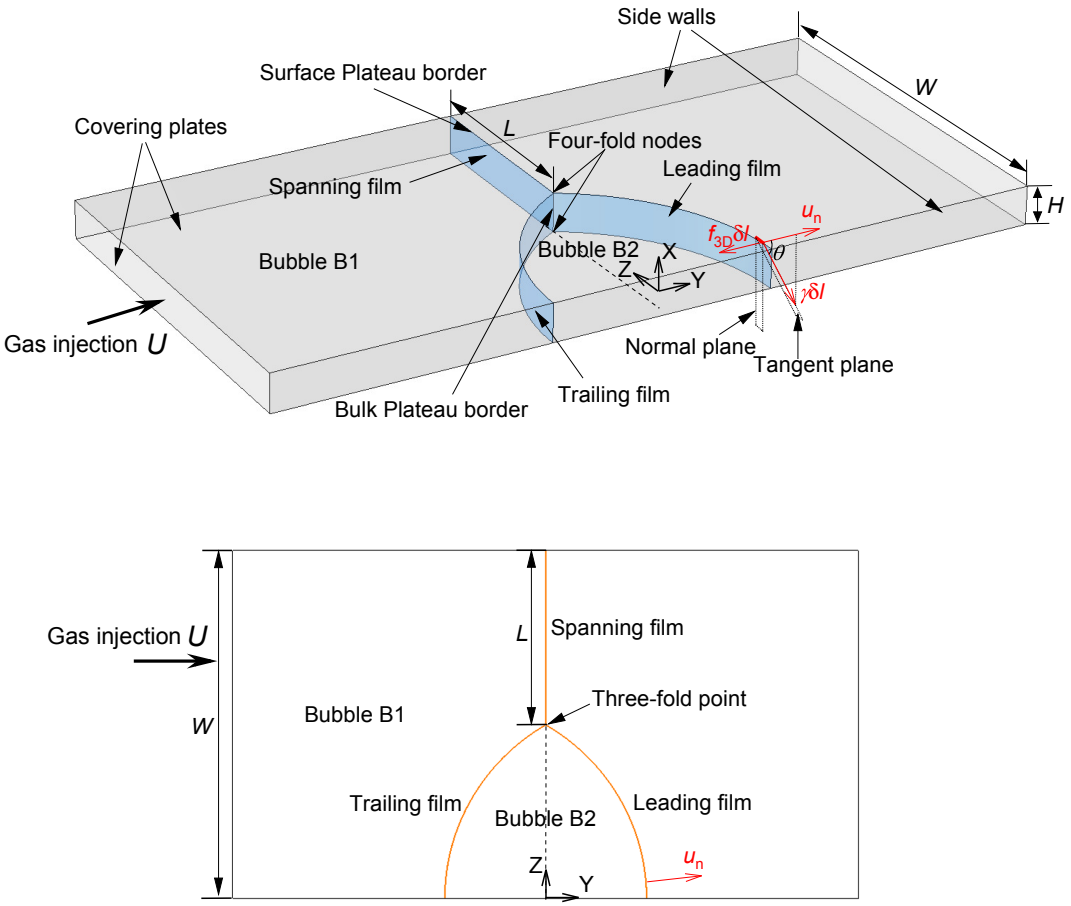


Figure 4.1: Geometry of a viscous froth lens confined in a straight channel with uniform rectangle cross-sections in 3D (top), as well as the perspective observed from above the covering plates (bottom).

gas-liquid interface), δl the length of a short edge along the surface Plateau border. The local force equilibrium requires $f_{3D}\,\delta l = \cos\theta\,\gamma\,\delta l$.

When the channel height H is considerably narrow, it is possible to represent the flow system as a 2D problem by observing the situation from above the covering plates. From this perspective, films (1D curves) are essentially surface Plateau borders seen from above, and what appears to be a three-fold point is actually a four-fold node seen from above.

4.3 Viscous froth model

In this section, the methods used in this study are presented, structured as follows. In Section 4.3.1, the 2D viscous froth model is reviewed. In Section 4.3.2, the 2D viscous froth model is derived from the Young-Laplace equation applied to the foam confined in straight channels in a 3D context. In Section 4.3.3, the 3D version of viscous froth model is introduced, which can be used to predict the foam in the straight channels. In Section 4.3.4, the 2D and 3D viscous froth models are made dimensionless for use in numerical simulations.

4.3.1 2D viscous froth model

As previously mentioned, the 2D viscous froth model was initially developed for analyzing 2D dry foam flow within straight rectangular channels or Hele-Shaw cells. The simplest version of the 2D viscous froth model is a linear version that adopts a linear resistance force term. The linear 2D viscous froth model is expressed as

$$\Delta P - \gamma k = \zeta u_{\mathrm{n}} \tag{4.1}$$

where ΔP [Pa] represents the pressure drop across the film from the concave side to the convex side, γ [$\mathrm{N\,m^{-1}}$] the film tension, k [$\mathrm{m^{-1}}$] is the film curvature, u_{n} [$\mathrm{m\,s^{-1}}$] the velocity component along the local normal to the films, or normal velocity of films (positive values implying its direction also towards the convex side of the film), and ζ [$\mathrm{N\,s\,m^{-3}}$] the viscous drag coefficient. Note that the definitions of normal velocity differ slightly between 2D and 3D but exhibit similarities. In 3D, the analogue would presumably be the velocity component of the surface Plateau borders along the plates but normal to the surface Plateau border itself.

Additionally, k within Eq. 4.1 refers to the curvature of films in 2D, which are essentially 1D curves embedded in 2D. Given that these 2D films exist within a 3D context, we can interpret k as the curvature of the films along the covering plates. The curvature of the film across the gap, on the other hand, is not directly incorporated into the 2D viscous froth model. The impact of

curved films across the gap is only represented through the drag force term and is not formally accounted for geometrically within the model.

The application of the 2D viscous froth model in simulating the dynamic behavior of foams is explained as follows. For a given initial configuration of 2D foam confined in Hele-Shaw cells, the film curvature can be calculated. By relating the line integral of the velocity vector along the bubble boundaries to the changes in bubble volumes [89], which are already known, we can determine the pressure within the bubbles. Consequently, we can solve for the pressure difference between the bubbles. Using this pressure difference across the bubble boundaries, we can compute the film normal velocities by applying Eq. 4.1. With these film normal velocities, we can then carry out the dynamic evolution of the foam configuration.

4.3.2 Young-Laplace equation to 2D viscous froth model

An inherent assumption within the viscous froth model is the neglect of fluid viscosity within the bubbles away from any confining plates. In this scenario, the behavior of a film, with the exception of its borders, is governed by the film tension force. As a result, the pressure difference ΔP across the film is balanced by the film tension force, as described by the Young-Laplace equation

$$\Delta P = \gamma(k_1 + k_2), \tag{4.2}$$

where k_1 [m^{-1}] and k_2 [m^{-1}] are the two principal curvatures of the film. Eq. 4.2 is equivalent to Eq. 2.1, albeit expressed in a distinct manner.

In the case of foams in a state of stationary equilibrium within Hele-Shaw cells, the films remain flat across the gap while typically exhibiting curvature along the covering plates. In this scenario, the curvature k_1 across the gap is zero, while the curvature k_2 along the covering plates is nonzero. This situation contrasts with the case of a single film moving within straight channels [23], where the viscous force exerted by the covering plates is considered, and the

viscous force from the side walls is neglected. For the latter, the curvature k_1 across the gap is nonzero, while the curvature k_2 along the covering plates is zero.

In more general situations involving moving foams within Hele-Shaw cells, the films exhibit curvature both along the covering plates and across the gap. Moreover, the two principal curvatures might not align precisely with the covering plates or across the gap, respectively. However, in cases where there is a significant contrast in the scales of film curvatures along the plates and across the gap, it is possible to make an assumption that one principal curvature is approximately oriented across the gap, while the other is roughly along the covering plate. Such situations can arise when the film migration velocity approaches zero, and the films become nearly flat across the gap, or at high migration velocities where the curvature across the gap can be considerably larger than that along the covering plates, primarily due to the thin gap. This approximation, concerning the orientations of the two principal curvatures, is employed when deriving the 2D viscous froth model from the Young-Laplace equation.

Another necessary assumption is that the shape of the Plateau border along the confining plates serves as a valid representation for the shape along the film at all points across the gap. This includes the profile where the film intersects the mid-plane between the two covering plates. With this added assumption, the curvature k_2 along the plate is presumed to vary along the films but not across the gap. Additionally, since the sum of k_1 and k_2 remains constant over a film, k_1 across the gap is also assumed to vary along the films but not across the gap. Consequently, k_1 can be determined by the angle formed between the film and the covering plate. Specifically, by definition $k_1 = d\theta_s/ds$ where s denotes arc length across the gap, and θ_s is the local orientation angle between the film tangent and the horizontal. We can determine k_1 by computing the integral $\int k_1\, dx$ along the film across the gap, starting from the mid-plane. This integral can be re-wirtten as integral $\int (dx/ds)\, d\theta_s$, where dx/ds is $\sin(\theta_s)$, and then we integrate from $\theta_s = \pi/2$ in the mid-plane of the gap to $\theta_s = \theta$ on the plate. This results in $k_1(H/2) = \cos\theta$ and hence $k_1 = \cos\theta/(\mathrm{H}/2)$. Consequently, the term $\gamma\, k_1$ in Eq. 4.2 can be represented as $\gamma\, k_1 = \gamma \cos\theta/(\mathrm{H}/2)$, where $\gamma \cos\theta$ denotes the tangential component of the film tension force at the surface Plateau borders.

The tangent component of the film tension force is balanced by the viscous drag force, namely $\gamma \cos\theta = f_{3D}$, where f_{3D} is linked to the normal velocity of film through $f_{3D} = \xi\, u_n$. $\xi[\mathrm{N\,s\,m^{-2}}]$ is the drag coefficient in 3D scenarios. We can substitute this formula into the Young-Laplace equation, Eq. 4.2, resulting in $\Delta P = \gamma\, k_2 + (2/H)\, \xi\, u_n$. It can be found that the resultant equation is exactly the 2D viscous forth model, given the assumption that k_2 varies only along the films but not across them. Moreover, by the same token k_1 is assumed to varying only along the films but not across them, as $k_1 + k_2$ is necessarily spatially uniform. Note that, the resultant formula implies that the drag coefficient in 2D is linked to the drag coefficient in 3D through a factor $2/H$, namely $\zeta = (2/H)\, \xi$ [88, 23].

The above derivation from the Young-Laplace equation to the 2D viscous froth model relies on the assumptions that the two principal curvatures are oriented along the plates and across the gap, respectively, and that they only vary along the films. Consequently, the 2D viscous froth model serves as an approximate representation of realistic foam behaviour within Hele-Shaw cells, and the relationship between the drag coefficient in 3D, denoted as ξ, and the drag coefficient in 2D, denoted as ζ, is also approximate.

When the underlying assumptions are not maintained, the 2D viscous froth model may not accurately depict the actual behaviour of foam confined in Hele-Shaw cells. For instance, at high film migration velocities, the 2D viscous froth model predicts that the films will become flat with significant curvature primarily only at their upstream end [88, 120]. In this scenario, the film curvatures along the plates (near the upstream end) and across the gap are not distinctly separated in their magnitudes. As a result, the principal curvatures may not necessarily align with the respective directions across the gap and along the plates, respectively. Another example pertains to situations involving moving films in wide gaps. In such cases, there is no longer a distinct separation of scales in terms of curvature across the gap and along the plates. Furthermore, the shape formed by the Plateau border along the confining plates might no longer accurately represent the shape of the film away from the confining plates, including the profile where the films intersect with the mid-plane.

Note that the challenges when the 2D viscous froth model may not accurately represent 3D

scenarios can potentially be mitigated by relaxing some of the constraints mentioned earlier. One approach is to treat the drag coefficient ζ as a fitting parameter, rather than a value directly linked to the drag coefficient ξ through the factor $2/H$. This aspect will be further analysed in Section 4.5.

4.3.3 Viscous froth model in 3D

The modelling of foam flow within Hele-Shaw cells can be enhanced by introducing a 3D version of the viscous froth model. In doing so, it is important to recognise that the 2D viscous froth model is grounded on two key assumptions: (1) uniform pressure throughout each bubble and (2) the presence of viscous dissipation occurring solely at the surface Plateau borders. The first assumption remains valid when the impacts of fluid viscosity and bulk inertia within each bubble and each film away from confining plates, are negligible. Under such circumstances, the dominant factor is the film tension, which seeks to minimise the surface energy of the film. The second assumption is associated with the motion of the surface Plateau borders that is influenced by the viscous force exerted on them by the covering plates [113].

By extending these principles to three dimensions, a 3D viscous froth model, namely a soap film model with additional constraints on the motion of the surface Plateau borders, can be developed. In the 3D viscous froth model, the dynamic effect is also introduced by the relationship between the normal velocity of the surface Plateau border and the drag force acting upon it.

Specifically, the 3D viscous froth model comprises three main components. The first component pertains to the foam maintaining a minimal surface (subject to constraints on bubble volumes and specified Plateau border locations), meaning that the pressure difference across any foam film is determined by the Young-Laplace equation, i.e. Eq. 4.2. The second component is the equation for the dynamic motion of surface Plateau borders. As mentioned previously, on the surface Plateau borders, the viscous drag force and the film tension force are in equilibrium. This can be expressed as

$$\gamma \cos\theta = \xi u_{\mathrm{n}}, \tag{4.3}$$

where θ represents the angle between the covering plate and the tangent plane of the foam film at a specific point on the surface Plateau border, as shown in Figure 4.1. Here, u_{n} denotes the normal component of the velocity at that point on the surface Plateau border. The direction of u_{n} is tangential to the covering plate plane since the surface Plateau border adheres to the covering plate. It can be found from Eq. 4.3 that there exists an upper limit to the projected tension force, corresponding to the case that films become parallel along the plates, and hence an upper limit to the film migration velocity, resulted as γ/ξ, beyond which Eq. 4.3 is not applicable [23]. The final aspect of the 3D viscous froth model involves determining the motion of the four-fold node, where three surface Plateau borders and one bulk Plateau border intersect. In this study, the angles between surface Plateau borders are fixed to 120 degrees.

4.3.4 Dimensionless viscous froth model

In numerical simulations, it is preferable to work with the dimensionless form of the 3D viscous froth model. To achieve this, the width of the Hele-Shaw cell, denoted as W, is established as the characteristic length. The characteristic pressure is defined as γ/W, and the characteristic velocity is γ/ξ, which corresponds precisely to the upper limit of the film migration velocity when the film becomes tangent with the covering plates. Correspondingly, the characteristic time is $W\xi/\gamma$. With these parameters in place, the dimensionless form of the Young-Laplace equation can be represented as

$$\Delta P^* = k_1^* + k_2^*. \tag{4.4}$$

where ΔP^* is the dimensionless pressure, defined as $\Delta P^* = \Delta P W/\gamma$. The dimensionless principal curvatures k_1^* and k_2^* are defined as $k_1^* = k_1 W$ and $k_2^* = k_2 W$, respectively. The dimensionless form of Eq. 4.3 is

$$\cos\theta = u_{\mathrm{n}}^{*}. \tag{4.5}$$

where the dimensionless normal velocity is defined as $u_{\mathrm{n}}^{*} = u_{\mathrm{n}}\xi/\gamma$.

The 2D viscous froth model can also be made dimensionless as

$$\Delta P^{*} - k^{*} = \zeta^{*} u_{\mathrm{n}}^{*}. \tag{4.6}$$

where k^{*} is the dimensionless curvature, defined as $k^{*} = kW$. ζ^{*} is the dimensionless drag coefficient for 2D viscous froth model, defined as $\zeta^{*} = W\zeta/\xi$. Recall that $\xi = H\zeta/2$ under the specific assumptions made in Section 4.3.2, in which case the dimensionless 2D viscous froth model is

$$\Delta P^{*} - k^{*} = \frac{2}{H^{*}} u_{\mathrm{n}}^{*}. \tag{4.7}$$

where H^{*} is the dimensionless gap size, i.e. an aspect ratio. In the following, the superscript $*$ denoting the dimensionless quantities is dropped for simplicity.

Eq. 4.7 provides a reliable approximation of the 3D viscous froth model under the specified assumptions made in Section 4.3.2. As revealed later in this study, these assumptions remain valid as the ratio U/H remains small compared to unity, where U represents the dimensionless driving velocity (which is dimensional driving velocity multiplied by ξ/γ) and H stands for the dimensionless gap size: effectively Eq. 4.7 behaves as a quasi-static system in that limit. However, as U/H increases, the outcomes based on Eq. 4.7 may exhibit increasing deviations from those produced by the 3D viscous froth model. In such scenarios, the drag coefficient ζ in the 2D viscous froth model should be considered as a fitting parameter, and its value can be adjusted away from the default $2/H$ to bring the results of the 2D model closer to those of the 3D model.

Additionally, this study introduces in 3D the concept of "apparent drag force", denoted as f_{D}.

This force is defined as

$$f_{\mathrm{D}} = \Delta P - k_{\mathrm{spb}}, \tag{4.8}$$

which is the difference between the pressure difference across films, ΔP, and the curvature of the surface Plateau borders, designated as k_{spb}. The idea underlying this concept is that if the 2D viscous froth model accurately captures the behaviour of a viscous froth lens in 3D scenarios, particularly with regard to the dynamic motion of the surface Plateau borders, the apparent drag force is expected to exhibit a linear relationship with the normal velocity of the surface Plateau borders.

4.4 Numerical methods

In this section, a comprehensive explanation of the numerical method for the 3D viscous froth model is provided. Also, a new approach is introduced for predicting the steady-state configuration of 2D viscous froth lens. The outcomes from the 2D viscous froth models are employed for comparison with the results of the 3D viscous froth model. Throughout this section, reference is made to the geometry of the viscous froth lens in Figure 4.1.

4.4.1 Numerical method for 3D viscous froth model

The process of simulating the dynamic motion of the viscous froth lens in 3D, taking into account the viscous forces at surface Plateau borders, is elucidated as follows. Eq. 4.4 and 4.5 are employed for this purpose. Eq. 4.4 means that a foam remains the minimal total surface energy state given the position of the surface Plateau borders and nodes, the conserved volume of the lens bubble, and the specified volume upstream of the lens structure. To predict the foam configuration at this state, the gradient descent method-based surface energy minimisation approach embedded in Surface Evolver can be utilised [119].

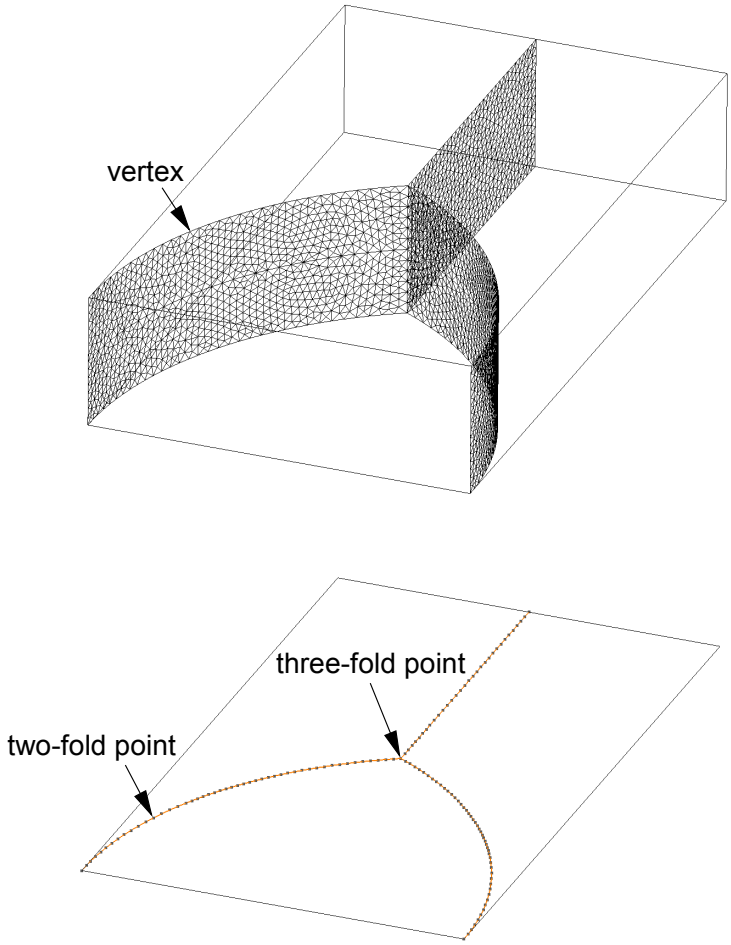


Figure 4.2: Discrete representations of films in 3D (top) and 2D (bottom). In 3D, films are 2D surfaces embedded in 3D, discretised into triangular elements. Each element is characterised by three vertices and edges. In 2D, films are 1D curves embedded in 2D. Discrete films in 2D are represented by points connected via short edges. The classification of a discrete point as either a two-fold or three-fold point is determined by the number of edges connected to that discrete point.

Surface Evolver [87] discretises foam films into a triangle mesh, as shown in Figure 4.2, and iteratively minimises the surface energy of the foam system by adjusting the positions of the mesh vertices. In the simulations, the foam configuration is eventually deemed as converged when the rate of the relative change in surface energy with respect to iterations falls below 10^{-9}. The number of iterations required to achieve the converged configuration with the minimal surface energy (subject to constraints) is case dependent. For instance, in this investigation, 15000 iterations are conducted to attain the initial viscous froth lens, whereas 900 iterations are executed for each subsequent time step once the viscous froth lens is in motion. As the iteration proceeds, the vertices of the foam system's mesh undergo gradual adjustments in

directions that result in a reduction of the total surface energy of foam films. Simultaneously, large mesh elements are subdivided, and small elements are removed to uphold approximately uniform element sizes along the foam films. The motion direction for each vertex is determined by several factors, including the local film mean curvature, gradient of each bubble volume, and local constraints such as the forced contact between films and solid surfaces that include the covering plates and the side walls.

Two types of constraints are considered in the implementation of the approach: one pertaining to bubble volumes and the other concerning the interaction between the films and the solid surfaces. For the 3D viscous froth lens, there are two identified bubbles, namely B1 and B2, as shown in Figure 4.1. B1 refers to the volumetric space rearward of the trailing and spanning films until the inlet of the channel, while B2 corresponds to the lens bubble itself. The gas injection into the channel is simulated by progressively increasing the volume of B1, while keeping the volume of B2 constant throughout the simulations. The geometric constraints involve two covering plates and two side walls. The constraint imposed by the covering plates on the films varies at different stages of the simulation. Initially, when computing the stationary equilibrium of the viscous froth lens, the covering plates only need to establish contact with the films, but the films configure their shape to minimise surface energy. However, as the viscous froth lens begins to move, the positions of the surface Plateau borders are determined using Eq. 4.3. In contrast, the side walls do not account for viscous resistance. As a result, the films and side walls consistently maintain contact throughout the simulations, and tend to meet at right angles [88].

The dynamic simulations using the 3D viscous froth model commence from an equilibrium state of the viscous froth lens. To predict this initial configuration, the inlet of the channel is held fixed at $x = -1.0$, while the two side walls are anchored at $z = 0.0$ and $z = 1.0$, respectively. The initial volume target of B1 is set to $0.4882H$, and the volume target of B2 remains constant at $0.10236H$ throughout the simulations, where 0.4882 and 0.10236 are the areas of B1 and B2, observing from the top above y-z plane. In fact, 0.10236 is exactly the constant area of the lens bubble in a 2D viscous froth lens in stationary equilibrium, when the length of spanning film L is fixed to 0.5, i.e. half the width of the channel. Employing these parameters and the

aforementioned solid surface-imposed constraints in Surface Evolver, we can obtain the initial viscous froth lens configuration in stationary equilibrium, where the spanning film lies flat and is positioned at $x = -0.4$, and the viscous froth lens is symmetric about the spanning film. For the 3D viscous froth lens in stationary equilibrium, the z-coordinate of the four-fold node on the covering plate is 0.5 as expected, because the volume of B2 is set to $0.10236H$.

The dynamic evolution of the viscous froth lens involves two procedures for each time step of the simulation. The first procedure entails computing the angles between the films and the covering plates. The angle at each vertex situated on the surface Plateau borders is determined by calculating the mean vector of the unit normal vectors of all the triangle elements to which the vertex is connected. Using these angles, we can calculate the normal velocities of the surface Plateau borders on the covering plates using Eq. 4.3. With these computed velocities, we can update the positions of the surface Plateau borders and subsequently the position of the four-fold nodes via the 120-degree rule by one time step, denoted as ΔT, using the forward Euler method. The second procedure involves increasing the volume of B1 by an amount of $UH\Delta T$, since the volumetric flux of gas through the inlet is UH. For instance, with $U = 0.1$, $H = 0.2$, and ΔT fixed to 0.01, the volume increment for each time step is set to 0.0002. After adjusting the volume of B1, the configuration of the viscous froth lens is evolved to the state of minimal surface energy subject to constraints. With the updated film surface, we then can proceed to conduct the first procedure for the next time step, and this process continues as the simulation progresses in time.

4.4.2 Steady-state configuration of 2D viscous froth lens

For comparison, the steady-state configurations (i.e. steadily propagating configurations) of the 2D viscous froth lens under different driving velocities are predicted. In this work, a new approach to predict the steady states is used, which transforms the problem into an equivalent surface energy minimisation problem with a varying (and driving velocity-dependent) de facto tension along the films. To do so, notice that Eq. 4.6 can be transformed to a form in a manner analogous to the 2D Young-Laplace equation

$$\Delta P = \zeta u_{\mathrm{n}} + k. \tag{4.9}$$

In Eq. 4.9, the quantity $\zeta u_{\mathrm{n}} + k$ can be interpreted as an effective tension force or curvature that influences the viscous froth lens' equilibrium configuration. The presence of the viscous term $\zeta\, u_{\mathrm{n}}$ leads to a distinction between the effective curvature and the geometric curvature. This difference is position-dependent along films, and also relies on the driving velocity.

To predict the steady-state configuration of the viscous froth lens, one can again utilise the surface energy minimisation approach depicted in Surface Evolver [87]. Particularly, the 2D algorithm detailed in Section 3.3 is used, where films (1D curves embedded in 2D) are represented using a series of discrete points connected by short straight edges. Similar to the process described for minimising the surface energy of foam in 3D, a 2D foam is also evolved toward its stationary equilibrium state, by adjusting the positions of discrete points in directions that result in a reduction of surface energy. Moreover, the evolving direction is mainly determined by the net film tension force acting on each discrete points by all the neighbouring edges. Throughout the foam configuration's evolution, extended edges undergo subdivision, while short edges are removed to sustain approximately uniform edge sizes. To apply this method for an equivalent surface energy minimisation problem, specifically for achieving the steady state of a 2D viscous froth lens within the context of this work, the only required modification to the algorithm [127] is to change the film tension force $\boldsymbol{f}_{\mathrm{o}}$, which denotes the net film tension force acting on each discrete point, to the corresponding effective film tension force $\boldsymbol{f}_{\mathrm{e}}$ at each discrete point except for the three-fold ones, as shown in Figure 4.3. The original film tension force and the effective film tension force are linked through $\boldsymbol{f}_{\mathrm{e}} = \boldsymbol{f}_{\mathrm{o}} + \boldsymbol{f}_{\mathrm{m}}$, where $\boldsymbol{f}_{\mathrm{m}}$ is the correction term associated with the viscous drag force.

The effective tension forces acting on a discrete point located on the so called trailing film, leading film, or spanning film of the viscous froth lens are depicted in Figure 4.3. The modification added to the original film tension force at any two-fold point on the films is given as $\boldsymbol{f}_{\mathrm{m}} = -\delta l\big(\boldsymbol{U} \cdot \boldsymbol{n}\big)\boldsymbol{n}$, where δl is the length of the film segment associated with the two-fold point, $\boldsymbol{U}$ the vector of the driving velocity, and $\boldsymbol{n}$ the unit normal vector on the film. δl is

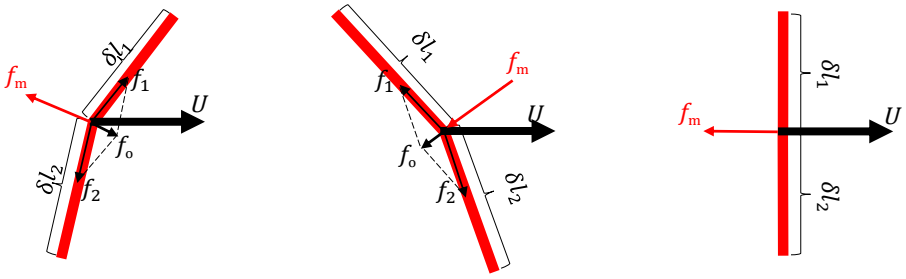


Figure 4.3: As has been mentioned, the original film tension forces, used in surface energy minimisation processes, are changed for predicting the steady-state configurations of the 2D viscous froth lens. From left to right, the modifications of the film tension force at two-fold points are as follows: first, for a film that is convex backward, similar to the trailing film; second, for a film that is convex forward, resembling the leading film; and third, for a straight film, such like the initial spanning film.

calculated as $\delta l = 0.5(\delta l_1 + \delta l_2)$, with δl_1 and δl_2 representing the lengths of two neighbouring edges connecting to the two-fold point.

4.4.3 Scheme of numerical simulations

Given the dimensionless 3D viscous froth model depicted in Section 4.3.4, and that the initial length of the spanning film is fixed at 0.5, the behaviour of the 3D viscous froth lens is influenced by two key independent variables: the driving velocity U and the gap size H. As indicated by Eq. 4.7 (with values of u_n^* up to U), the velocity and gap size affect the viscous froth lens behaviour, at least when steady states reached, in a coupled manner through the combined parameter U/H, denoted by η. In 3D, this ratio may also play a crucial role in determining the motion of the viscous froth lens. This is because the value of U provides information about the angle through which the film turns across the height of the gap to ensure that Eq. 4.5 is satisfied. Thus, η denotes the curvature of the film across the gap, serving as an indicator of whether the film curvature across the gap dominates over the curvature along the plates. Under this assumption, the driving velocity U and the driving velocity-to-gap size ratio η are selected as the independent variables in the simulations.

Specifically, H takes values within [0.1, 0.2, 0.3, 0.4], while η is set to values within [0.5, 0.75, 1.0, 1.25, 1.5, 1.75, 1.875, 2.0]. Note that the upper limit for the parameter U is set at 1.0, as this

dimensionless velocity tends to cause films to lie along the confining plates, which corresponds to the upper limit of the film migration velocity. Beyond this limit, the viscous froth model ceases to be applicable. Even so, the selected values for U encompass a broad range of driving velocities. In addition, the gap size H is typically assumed to be much smaller than the width of the channel, and consequently, H is also reasonably constrained to values less than 1.0 in the simulations. In this study, the maximum value of H is set to 0.4.

The regulation of the element size is determined by a specified reference range $[L_{\min},\ L_{\max}]$, denoted as R_1, with $L_{\min}$ and $L_{\max}$ defined as 0.00396 and 0.0099, respectively. In a 2D context, the element size corresponds to the length of edges in the discrete representation of foam films, whereas in a 3D context, it pertains to the length of edges for individual triangle elements. In the simulations for steady states of 2D viscous froth lens, as well as in the series of simulations for 3D viscous froth lens where $H = 0.1$, the element size is constrained to fall within the range R_1.

In other simulations involving the movement of the 3D viscous froth lens, where H takes values of 0.2, 0.3, and 0.4, the employed element resolutions may be comparatively coarser. For instance, R_2: $[2L_{\min},\ 2L_{\max}]$, R_3: $[3L_{\min},\ 3L_{\max}]$, and R_4: $[4L_{\min},\ 4L_{\max}]$, are utilised correspondingly. The selected element size range in each scenario is tailored to meet the criterion that the resolution of the discrete representation of each film is sufficiently addressed in both directions, along the covering plates and across the gap, respectively.

To ensure a more equitable comparison of results for the 3D viscous froth lens at the same η but different H values, a finer resolution for each set of simulations with the same H is additionally employed. Specifically, R_1 is considered in cases where $H = 0.2$. Similarly, R_2 and R_3 are employed in instances where $H = 0.3$ and 0.4, respectively. The values of H and η as well as the mesh resolutions used in the simulations, are summarised in the Table. 5.1. One last parameter that is assigned in the simulation is the time step ΔT, which is fixed to 0.01 in this study. The use of this small time step is essential for maintaining the stability of the numerical simulations, as it ensures that the displacement of each vertex within a time step remains smaller than the size of the smallest mesh element.

Table 4.1: Values of H and η and mesh resolutions employed in 3D simulations

H \ η	0.5	0.75	1.0	1.25	1.5	1.75	1.875	2.0
0.1	R_1	R_1	R_1	R_1	R_1	R_1	R_1	R_1
0.2	R_2, R_1	R_2, R_1	R_2, R_1	R_2, R_1	R_2, R_1	R_2, R_1	R_2, R_1	R_2, R_1
0.3	R_3, R_2	R_3, R_2	R_3, R_2	R_3, R_2	R_3, R_2	R_3, R_2	R_3, R_2	R_3, R_2
0.4	R_4, R_3	R_4, R_3	R_4, R_3	R_4, R_3	R_4, R_3	R_4, R_3	R_4, R_3	R_4, R_3

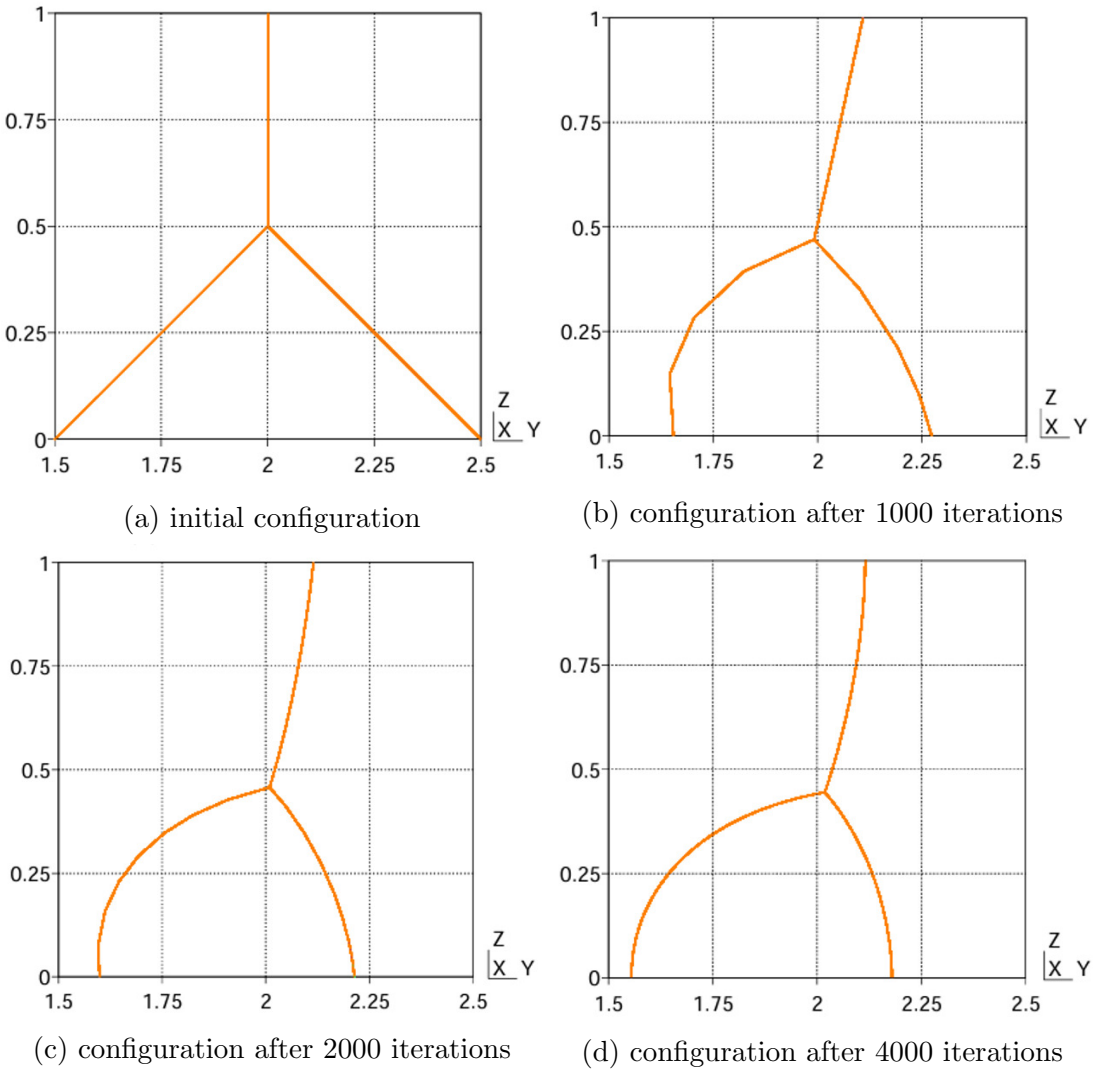
4.5 Numerical results

In this section, the numerical results for each simulation outlined in Section 4.4.3 are presented. The section is structured as follows. In Section 4.5.1, the steady states of the 2D viscous froth lens are presented. These results serve as a foundation for subsequent comparisons with the outcomes of the 3D viscous froth model. In Section 4.5.2, the evolution of the 3D viscous froth lens is predicted and analysed. In Section 4.5.3, the results obtained from the 2D and 3D simulations are compared, providing a general guideline for the selection of the drag coefficient needed in the 2D viscous froth model. In Section 4.5.4, the results of the 3D viscous froth model are utilised to further analyse whether an effective drag coefficient in the 2D viscous froth model might actually vary with position along the films.

4.5.1 Steady state of 2D viscous froth lens

For each set of values of H and η, the steady state of the 2D viscous froth lens is predicted by the method presented in Section 4.3.2. In the simulations, the drag coefficient is set to $2/H$. The edge size is kept within the range R_1, by removing edges shorter than $L_{\min}$ and subdividing edges longer than $L_{\max}$. As implied by Eq. 4.7, the only determining factor of the result is driving velocity-to-gap size ratio η. For this reason, all the 32 cases, where $H \in [0.1, 0.2, 0.3, 0.4]$ and $\eta \in [0.5, 0.75, 1.0, 1.25, 1.5, 1.75, 1.875, 2.0]$, only yield 8 different results.

The process predicting a steady-state configuration of the 2D viscous froth lens is exemplified in Figure 4.4, with η set to 1.875 and the small factor λ required in the algorithm (referring back to Section 3.3) is set to 0.005. In the process, the configuration of the 2D viscous froth



(a) initial configuration

(b) configuration after 1000 iterations

(c) configuration after 2000 iterations

(d) configuration after 4000 iterations

Figure 4.4: The method outlined in Section 4.4.2 is employed to forecast the steady state of a 2D viscous froth lens at $\eta = 1.875$. The iterative process, depicted in (a) to (d), progressively refines the edge sizes to fall within R_1.

lens is adjusted iteratively, progressively converging towards the steady state. In the initial phase of the iterations, a relatively large edge size is used for swift configuration adjustments. Subsequently, the longer edges are subdivided to enhance mesh refinement until the specified size range R_1 is met. For the refined discrete representation of the 2D viscous froth lens, iterations are implemented until the steady state is reached. The approaching steady state of the viscous froth lens in 2D can be reflected via the convergence history of the z-coordinate of the three-fold point, as presented in Figure 4.5.

To quantify the degree of deformation in a given steady-state viscous froth lens relative to its initial state, one can assess the change in the z-coordinate of the three-fold point. At

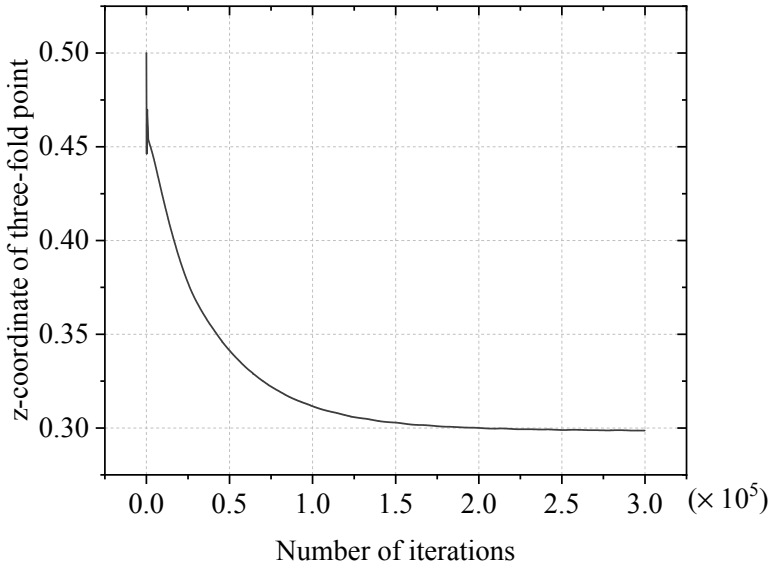
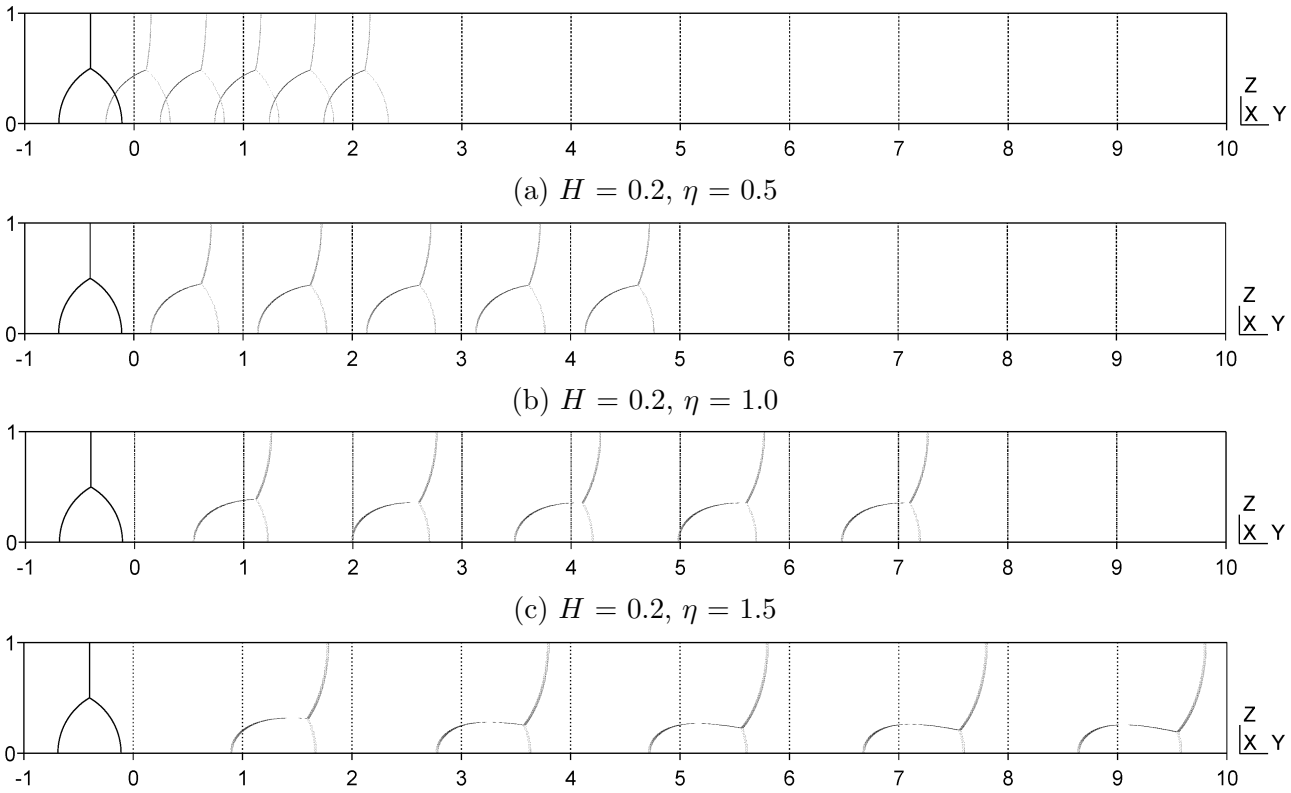


Figure 4.5: The convergence of the z-coordinate of the three-fold point, as the iteration proceeds.

relatively small values of η, such as 0.5, 1.0, and 2.0, there exists steady-state configurations of 2D viscous froth lens, whose three-fold points tend to approach a constant z-coordinates, as latter shown in Figure 4.8. By contrast, tests were also conducted at higher values of η, such as 4.0 and 8.0, the 2D viscous froth lens cannot approach a steady state without the occurrence of topology transformation [88]. Here, the topology transformation refers to the T1 topology transformation that is initiated by the leading film continuously shrinking towards zero length, under sufficiently high driving velocities [88].

4.5.2 Evolution of 3D viscous froth lens

The dynamic evolution of the viscous froth lens in 3D is predicted using the method introduced in Section 4.3.1. During the motion of the viscous froth lens, its structural deformation can be characterized by the change in the z-coordinate of the four-fold node. For instance, consider H set to 0.2 while η set to 0.5, 1.0, 1.5, and 2.0, respectively. In the numerical simulations, the edge size for triangle elements is maintained within the range R_2, resulting in a mesh resolution of approximately 16 elements across the gap. The outcomes of the dynamic motion for these four cases are depicted in Figure 4.6. At low driving velocities, such as $U = 0.1$ at $\eta = 0.5$, the froth lens deviates only gradually from its initial configuration as it moves downstream. In contrast, high driving velocities, like $U = 0.4$ at $\eta = 2.0$, result in more rapid deformation of



(a) $H = 0.2$, $\eta = 0.5$

(b) $H = 0.2$, $\eta = 1.0$

(c) $H = 0.2$, $\eta = 1.5$

(d) $H = 0.2$, $\eta = 2.0$

Figure 4.6: Configurations of the viscous froth lens in 3D at different time $T = 0.0$, 5.0, 10.0, 15.0, 20.0, and 25.0.

the viscous froth lens, measured by the variation in the z-coordinate of the four-fold node.

As the viscous froth lens moves downstream, the four-fold node may approach steady states in terms of its z-coordinate, as suggested in Figure 4.7. Once the rate of change in the z-coordinate of the four-fold node on the covering plate drops below 0.001, it is regarded as being constant over time. This signifies the attainment of a steady state for the viscous froth lens in 3D. Remembering $H = 0.2$ here, the cases with relatively high driving velocities, such as $U = 0.2$ at $\eta = 1.0$ or $U = 0.3$ at $\eta = 1.5$, take longer to reach the steady state compared to the case with lower driving velocities, such as $U = 0.1$ at $\eta = 0.5$. Moreover, the final deformation at steady states is more pronounced in cases under high driving velocities. At sufficiently high driving velocities, such as $U = 0.4$ at $\eta = 2.0$, the viscous froth lens would experience a T1 topological transformation, because the length of the leading film eventually shrinks towards zero as the z-coordinate of the four-fold node approaches zero, as shown in Figure 4.7. These observations from the results of the 3D viscous froth model align with findings from simulation

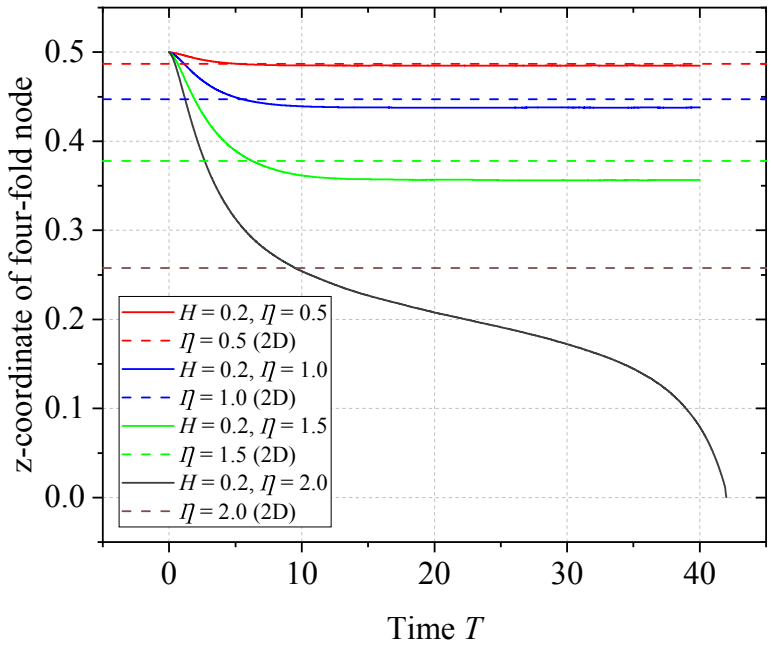


Figure 4.7: The dynamic evolution of the z-coordinate of the four-fold node of the viscous froth lens in 3D. H is set to 0.2, and η is set to 0.5, 1.0, 1.5, and 2.0, respectively. For comparison, the dashed lines represent the 2D results at the same driving velocities. In the 2D computations, ζ is set to $2/H$.

studies employing the 2D viscous froth model [88]. On the other hand, the results of the 3D model do exhibit quantitative distinctions from those obtained with the 2D model, as discussed later.

The outcomes of the 2D viscous froth lens across varying η values in the range [0.5, 2.0] are displayed and compared with the results extracted from figures 5 and 7 of the literature [88] in Figure 4.8. It is noteworthy that refining the 2D results obtained through the approach outlined in Section 4.4.2 can bring them even closer to those from the literature, achieved by using a smaller element resolution (finer than R_1) and more iterations. Nevertheless, such refinement can be unnecessary as the current mesh resolution proves computationally efficient and has been able to capture the behaviour of the viscous froth lens in both 2D and 3D. Additionally, the element resolution employed in 2D matches that used in the 3D cases with $H = 0.1$. Comparisons based on similar mesh resolutions are therefore more justifiable.

As depicted in Figure 4.8, for all considered values of H in this study, $H = 0.1$, 0.2, 0.3, and 0.4, the z-coordinates of the four-fold node at various η values within the range [0.5, 1.5] exhibit remarkable proximity. This suggests that, for η values in the range [0.5, 1.5], the primary factor

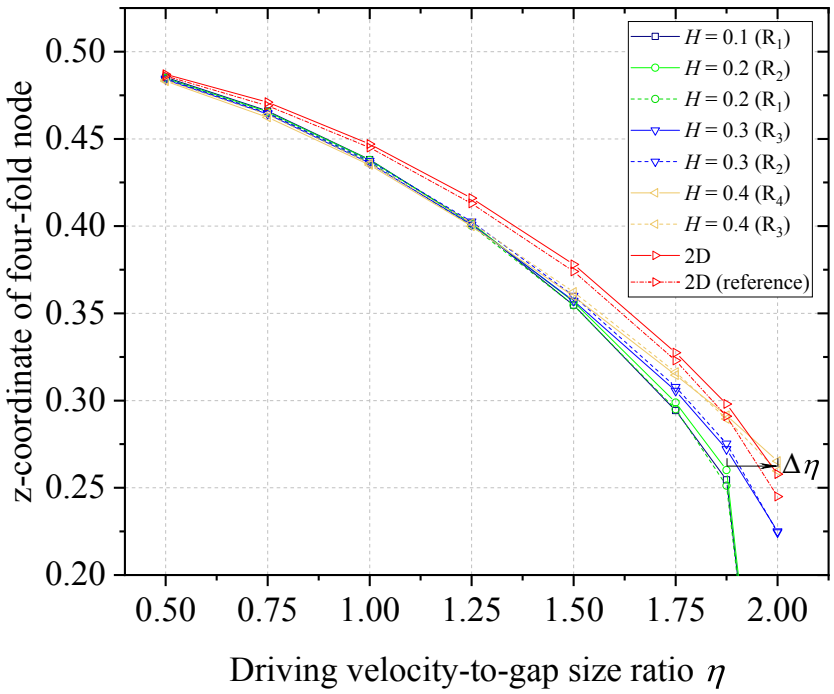


Figure 4.8: The z-coordinate of the four-fold node of viscous froth lens in 3D or the three-fold point of 2D viscous froth lens at steady states, varying with the driving velocity-to-gap size ratio η. For $H = 0.1$ and 0.2, the z-coordinates are zero and the data points are not shown in the present figure. A z-coordinate of zero indicates the occurrence of a T1 topological transformation. $\Delta\eta$ represents the increment of η required to make the 2D viscous froth model's result match that of the 3D viscous froth model. In the present example, this increment is measured between the curves labelled by "$H = 0.2$ (R_2)" and "2D". The 2D results are compared with those available in the literature [88], with the latter denoted by "reference".

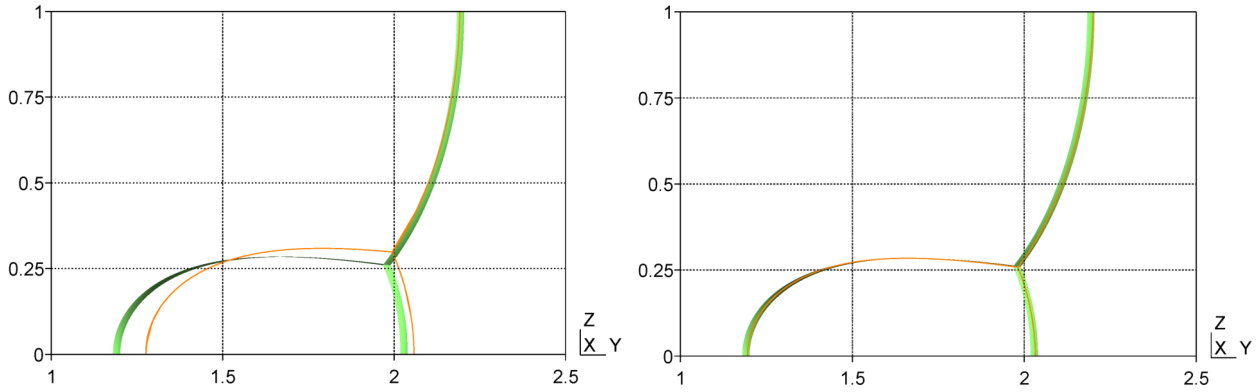
influencing the steady-state configuration of the 3D viscous froth lens is the η ratio. In contrast, the secondary influencing factor, H, assumes a non-negligible role in shaping the behaviour of the viscous froth lens at higher η values, particularly within the range [1.5, 2.0]. In this interval, the deformation of the 3D viscous froth lens, quantified by the z-coordinate of the four-fold node, becomes more pronounced with decreasing H. This distinction is particularly evident at $\eta = 2.0$.

For $H = 0.1$, 0.2, and 0.3, the deformation of the 2D viscous froth lens is less pronounced compared to that of the 3D viscous froth lens, as η varies within the investigated range of 0.5 to 2.0. Conversely, in scenarios with $H = 0.4$, the deformation in 2D can become more prominent than that in 3D, particularly at larger values of η, such as 2.0. In this case, the viscous froth lens in 3D reaches a steady state without undergoing topology transformation, and the driving velocity U reaches as high as 0.8. In contrast, at $H = 0.1$ and 0.2, the viscous froth lens undergoes topology transformations at smaller driving velocities of $U = 0.2$ and 0.4, respectively. This observation suggests that a specified foam configuration, such as a viscous froth lens, may exhibit increased resistance to topology transformations as the gap size H expands. This is because the foam structure may avoid undergo topology transformations at higher driving velocities in channels with larger gap sizes.

4.5.3 Drag coefficient as fitting parameter

In Section 4.5.1, it has been highlighted that the 2D results are obtained with ζ set to $2/H$. This relation is analytically accurate under the two underlying assumptions: the two principal curvatures are oriented along the plates and across the gap, respectively, and that they only vary along the films. In general circumstances, however, this relation can only be approximate, which could have led to the deviation of the results in 2D and 3D. An interesting question that arises is whether the 2D results can be made closer to those of 3D. The answer hinges on the concept of considering the drag coefficient as an adjustable fitting parameter. A suitable value of ζ results in roughly the same z-coordinate of the three-fold point in the 2D simulations as that of the four-fold node in the 3D simulations.

The selection of a suitable value of ζ can be analysed as follows. Referencing the example shown in Figure 4.8, assume that a change of $\Delta\eta$ leads to roughly the same z-coordinate by the 2D viscous froth model as that by the 3D viscous froth model (at $H = 0.2$ and $\eta = 1.875$ in the case). This suggests that the η used in the 2D simulations should be updated to $\eta + \Delta\eta$. Then, the drag coefficient used in 2D viscous froth model can be computed as $\zeta = 2(\eta + \Delta\eta)/U$, namely $\zeta = (1 + \Delta\eta/\eta)(2/H)$. Figure 4.8 shows that, as η varies within the range [0.5, 1.875], $\Delta\eta$ is positive for $H = 0.1$, 0.2, and 0.3, and increases as η increases. By contrast, at $H = 0.4$, $\Delta\eta$ first increases with η, and then reduces and eventually could take negative values. Within most of the range of η considered in this study, $\Delta\eta$ is positive, whereas it can be negative at high values of η such as 2.0.



(a) $U = 0.375$, $H = 0.2$, $\zeta = 10.0$ (b) $U = 0.375$, $H = 0.2$, $\zeta = 10.667$

Figure 4.9: Comparison between the steady-state configurations of the viscous froth lens in 2D and 3D, at $H = 0.2$ and 0.375. The viscous froth lens in 2D and 3D are represented in orange and green, respectively. (a) In the 2D computation, ζ is computed using $2/H$ and set to 10.0. (b) In the 2D computation, ζ is computed using $(1 + \Delta\eta/\eta)(2/H)$, where $\Delta\eta \approx 0.125$, and set to 10.667.

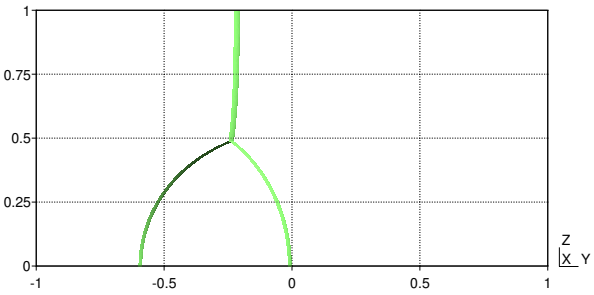
For the specific example adjusting ζ shown in Figure 4.8, where $H = 0.2$ and $\eta = 1.875$, $\Delta\eta$ is approximately 0.125, and thus ζ should be adjusted from $2/H = 10.0$ to $(1 + \Delta\eta/\eta)(2/H) \approx 10.667$. In Figure 4.9, the steady-state viscous froth lens in 3D, at $U = 0.375$ and $H = 0.2$, is compared with the steady-state 2D viscous froth lens, at $U = 0.375$, and $\zeta = 10.0$ and 10.667, respectively. It can be observed that, after adjusting the drag coefficient ζ needed in the 2D viscous froth model, the steady-state configuration of the 3D viscous froth lens can be more accurately represented by the configuration predicted by the 2D viscous froth model.

4.5.4 Dependence of drag coefficient on position along film

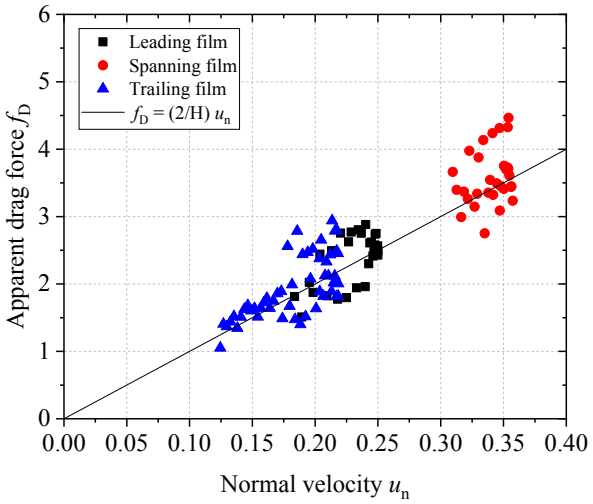
One scenario where the assumptions underlying the relation $\zeta = 2/H$ are exactly satisfied is the quasi-static limit that the film migration velocity at any position along films approaches zero. In fact, as long as the normal velocity of any part of a film is low, the 2D viscous froth model can be locally valid in that part. For example, a steadily propagating system has, for all locations in the structure, a uniform apparent velocity along the channel. However the actual normal velocity of points varies: film elements that happen to have their normal directions pointing along the propagation direction require higher normal velocities than film elements that have their normal directions pointing obliquely. Since the level of agreement or otherwise between 3D and 2D models is likely dependent on normal velocity, there is a possibility that some parts of the structure will see better agreement between 3D and 2D models than others. This implies that at locations where the normal velocity remains low, the relationship between the apparent drag force, defined in Eq. 4.8, and the normal velocity should closely resemble the linear relation assumed in the 2D viscous froth model.

Consider the specific case where $H = 0.2$ and $\eta = 1.5$. The apparent forces at mesh vertices along surface Plateau borders of the trailing, spanning, and leading films are computed, at two distinct time moments. One is at $T = 1.0$, representing the early stage of the dynamic motion of the viscous froth lens, and the other at $T = 40.0$, representing the steady state of the viscous froth lens. The corresponding configurations and the relationship between the apparent drag force and the normal velocity are illustrated in Figure 4.10. At $T = 1.0$, during the initial stage of deformation of the viscous froth lens, it is observed that the averaged normal velocity along the spanning film exceeds that along the trailing and leading films. This is because the normal to the spanning film is almost along the channel, whereas the other two films contain oblique sections. The data points are discretely scattered around the line $f_a = (2/H)u_{\mathrm{n}}$ with a significant portion of them falling above this line. This observation aligns with the analysis presented in the previous section, where the drag coefficient in the 2D viscous froth model is treated as a fitting parameter, and its value in this case is expected to be greater than $2/H$.

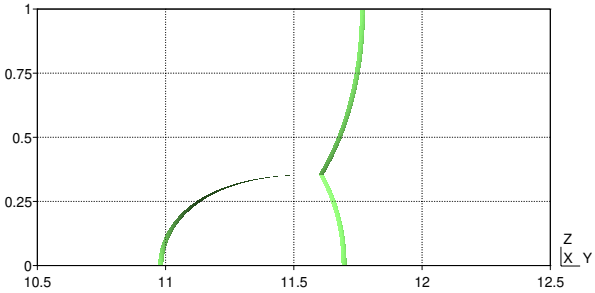
As the viscous froth lens approaches a steady-state condition, the trailing and spanning films



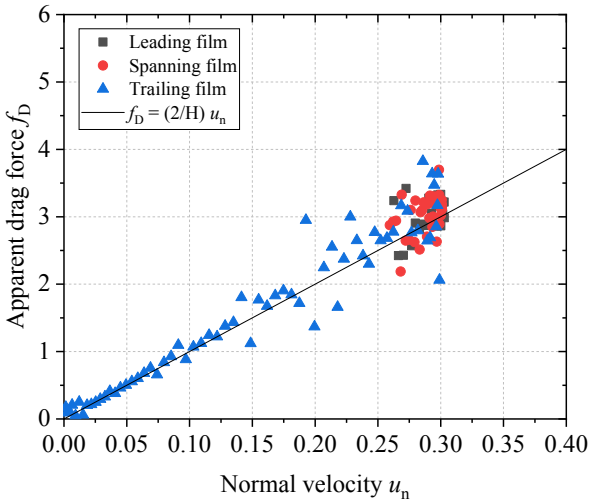
(a) $U = 0.3$, $H = 0.2$, $T = 1.0$



(b) $U = 0.3$, $H = 0.2$, $T = 1.0$

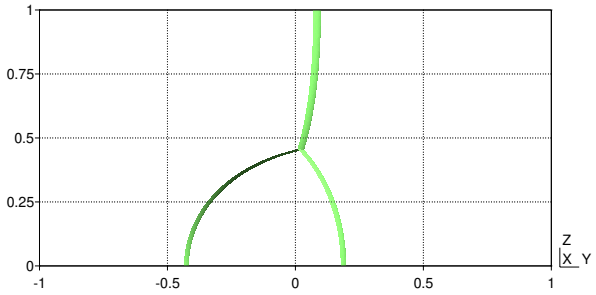


(c) $U = 0.3$, $H = 0.2$, $T = 40.0$ (steady-state)

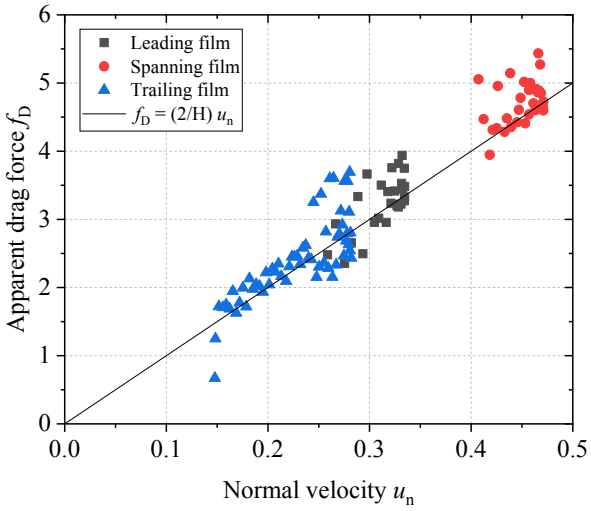


(d) $U = 0.3$, $H = 0.2$, $T = 40.0$ (steady-state)

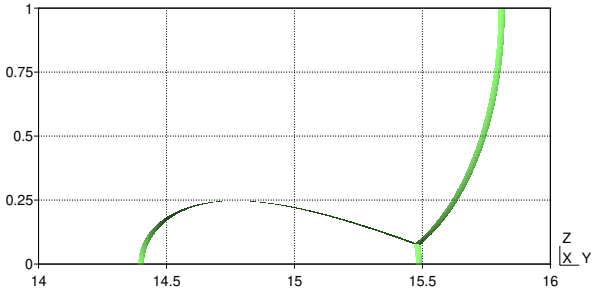
Figure 4.10: The configurations and the relation between the apparent drag force and the normal velocity of surface Plateau border, for the case $U = 0.3$ and $H = 0.2$ ($\eta = 1.5$), at different moments of time: (a) and (b) for $T = 1.0$, and (c) and (d) for $T = 40.0$ when the viscous froth lens approaches steady state.



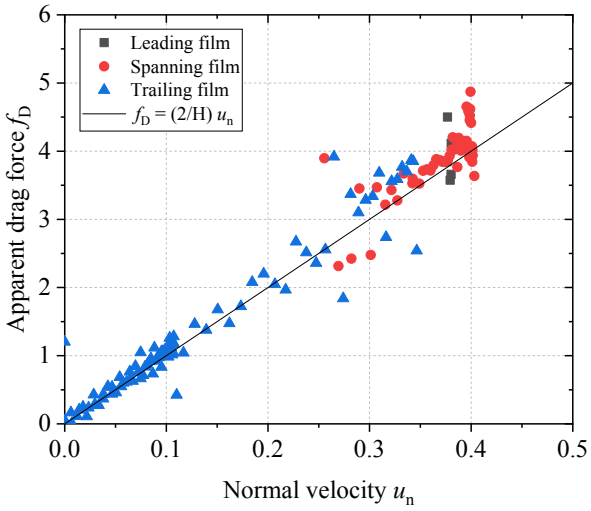
(a) $U = 0.4$, $H = 0.2$, $T = 1.0$



(b) $U = 0.4$, $H = 0.2$, $T = 1.0$



(c) $U = 0.4$, $H = 0.2$, $T = 40.0$



(d) $U = 0.4$, $H = 0.2$, $T = 40.0$

Figure 4.11: The configurations and the relation between the apparent drag force and the normal velocity of surface Plateau border, for the case $U = 0.4$ and $H = 0.2$ ($\eta = 2.0$), at different moments of time: (a) and (b) for $T = 1.0$, and (c) and (d) for $T = 40.0$.

elongate, while the leading film shrinks. The normal velocity of the surface Plateau border along the trailing film now exhibits a wider distribution compared to the early deformation stage. The minimum value of the normal velocity approaches zero, particularly when the trailing film becomes nearly flat near the bulk Plateau border. This happens because normal velocities on parts of the trailing film can now become quite low, especially on those parts of the film that are quite flat close to the node. It becomes evident that the relationship between the apparent drag force and the normal velocity closely approximates the line $f_a = (2/H)u_n$ as the normal velocity approaches zero.

Similar behaviour is observed in another case where $H = 0.2$ and $\eta = 2.0$, albeit with topology transformations now eventually happening. The film configurations and the relationship between the apparent drag force and the normal velocity at two time points, $T = 1.0$ and $T = 40.0$ are presented in Figure 4.11. The observations at $T = 1.0$ are approximately consistent with those in Figure 4.10. By contrast, at $T = 40.0$, near zero normal velocity occurs at a position within the middle section of the trailing film, further away from the bulk Plateau border than the position in Figure 4.10. Nevertheless, the data points are in close proximity to the line $f_a = (2/H)u_{\mathrm{n}}$ as the normal velocity tends to zero, which is consistent with the findings in Figure 4.10.

In both Figure 4.10 and 4.11, at least some data points tend to approach the line $f_a = (2/H)u_{\mathrm{n}}$, during the later stage of deformation of the viscous froth lens. Moreover, most of the data points are positioned slightly above the line, as previously mentioned for data points during the early stage of deformation. However, Figure 4.10 and 4.11 also suggest that the relationship between the apparent drag force and the normal velocity may not be accurately represented by a single linear function, even though the drag force and the normal velocity are assumed to be linearly related in a 3D context. Furthermore, it can be found that this relationship is position-dependent, because it varies along the films. Moreover, the film configuration evolves over time, and thus this relationship is also time-dependent. Consequently, when attempting to predict the motion of the viscous froth lens using the 2D viscous froth model, the drag coefficient needed in the 2D viscous froth model may be both position- and time-dependent.

4.6 Discussion

The 2D viscous froth model offers a notable improvement over the quasi-static soap film model, particularly in its ability to predict the continuous deformation of foam configurations and drive topology transformations in an ordered manner [88]. In physical terms, this enhancement can be primarily attributed to the inclusion of the viscous drag force in the model, which is connected to the normal velocity of the foam films. By allowing a determination of velocity, the 2D viscous

froth model becomes capable of reproducing the dynamic motion of a foam. Nonetheless, it must be remembered that the continuous deformation observed in 2D viscous froth is actually a 2D representation of an underlying 3D phenomenon. Specifically the viscous froth represents a foam flow that occurs within Hele-Shaw cells with uniform rectangular cross-section.

The 2D viscous froth model may necessitate additional adjustments when applied to a channel with non-uniform cross-sections. Consider, for instance, a channel characterised by non-uniform rectangle cross-sections, featuring flat side walls and curved covering plates along the channel. The width of the cross-sections remains constant along the channel, whereas the gap size undergoes variations. When a film flows within such a channel, the perspective observed from the direction normal to the side walls would resemble the scenario studied by Xu and Rossen [113]. As the film moves through the location where the cross-sectional area begins to decrease along the channel, the motion of the film in this specific region may occur at a faster rate when compared to the motion of the film in other areas. To accommodate this alteration, it might be imperative to introduce a modification to the viscous froth model that considers the varying cross-sectional area along the channel [126].

By contrast, in scenarios where the 2D viscous froth model may not perform well, the 3D viscous froth model could still be applicable. The results obtained from the 3D model can, in turn, contribute to enhancing the 2D viscous froth model by exploring how real-world flow conditions impact the parameters within the 2D model.

4.7 Conclusions

In this research, a comparative analysis of the motion of a viscous froth lens has been carried out, using both 2D and 3D viscous froth models. Theoretical analysis reveals that the 2D viscous froth model can be derived from the Young-Laplace equation, under assumptions that the two principal curvatures of the bulk films align with the plates and the gap, respectively, and only vary along the plates. It suggests that the drag coefficient needed in the 2D viscous froth model is connected to the drag coefficient in 3D by a factor that is twice the reciprocal of

the normalised gap size. This concept remains valid when the aforementioned assumptions are met. In this case, the 2D viscous froth model suggests that the steady-state configurations of the viscous froth lens are determined by the ratio of the driving velocity to the gap size. This influence of these two parameters in an interdependent manner also extends to the steady-state behaviour of the viscous froth lens in 3D, even though the assumptions may not be entirely accurate as the driving velocity-to-gap size ratio increases. The numerical results suggest that, at relatively small values of the driving velocity-to-gap size ratio, the dominant factor is the ratio itself. However, at relatively large values of the driving velocity-to-gap size ratio, the gap size also significantly influences the behaviour of the viscous froth lens in 3D.

The quantitative comparison of the steady-state viscous froth lens in both 2D and 3D indicates that the drag coefficient in the 2D viscous froth model should be treated as an adjustable fitting parameter to achieve better alignment with the results obtained from the 3D viscous froth model. The formula for this adjustment is provided in this study. Further investigation of the 2D viscous froth model, particularly in terms of whether the drag coefficient can be treated as a uniform constant for the entire structure of the viscous froth lens, suggests that the drag coefficient needed in the 2D viscous froth model may also exhibit a dependency on the local position along the foam films. As a result, it may not simply be regarded as a uniform value.

Chapter 5

Boundary-integral modelling for dry foam in three dimensions

5.1 Introduction

Beyond the quasi-static regime, as indicated by Chapter 4, the viscous effect plays an important role in affecting the dynamic motion of foam in porous media. The viscous effect not only contributes to the overall resistance of foam flow, but also may stimulate the occurrence of topology changes, which in turn influences the foam's subsequent behaviour [88]. Additionally, at finite but relatively low flow rates, the inertia force is much less important than pressure and viscous stress. In this case, the foam flow system, like that depicted by the 2D viscous froth model [89], behaves as an overdamped system [19].

The viscous froth model's sensitivity to flow rate allows it to capture dynamic foam behaviour that would not occur in the absence of viscous dissipation, such as significant deformation and subsequently resulting topology changes at higher flow rates [66, 89, 121]. However, it is worth noting that the viscous forces concentrate at Plateau borders, with no consideration given to the fluid's viscosity within bubbles. This source of viscous dissipation can be taken into account by an alternative approach to foam modelling, namely the boundary integral method which incorporates the fluid viscosity within bubbles. Similar to the viscous froth model, the inertia

effect of fluid is also ignored in the boundary integral method.

In this chapter, the dry foam assumption is introduced into the foam modelling process using the boundary integral method. The dry limit is a reasonable simplification for high-quality foams due to their multi-scale nature [107], and has been used in the original viscous froth model [89] and other fluid-dynamics modelling approaches [49, 107]. In the dry limit, the finite thickness of films in a realistic foam is simplified to curves in 2D or surfaces in 3D. Plateau borders are then represented by points in 2D or curves in 3D. In 3D foams, nodes at which Plateau borders meet are represented by points, but they are not treated as a geometric element in 2D foams. Note that, the modelling approach presented in this chapter also excludes other complexities, such as fluid drainage in foam films, gas coarsening between neighbouring bubbles, and surfactants redistribution along films.

5.2 Mathematical formulation

In this section, the boundary integral equation for dry foam in the presence of solid walls is derived, using the boundary integral representation of the Stokes flow equations. To elucidate the mathematical formulation, Figure 5.1 illustrates a scenario wherein a foam adheres to a solid surface. This schematic diagram involves most structural elements that could exist in a realistic 3D foam, and is referenced in the following sections. The key aspects involved in the formula derivation are the categorization of different types of interfaces and the boundary condition applied on the solid surfaces.

5.2.1 Stokes flow equations

As shown in Figure 5.1, a foam (in the first instance though, not necessarily a dry foam) is composed of concentrated gas bubbles separated by a continuous liquid phase (surfactant solution), placed on the upper surface of a solid plate. It has been assumed that the solid surface is water-wetting and thus the continuous liquid phase forms a wetting film coating on

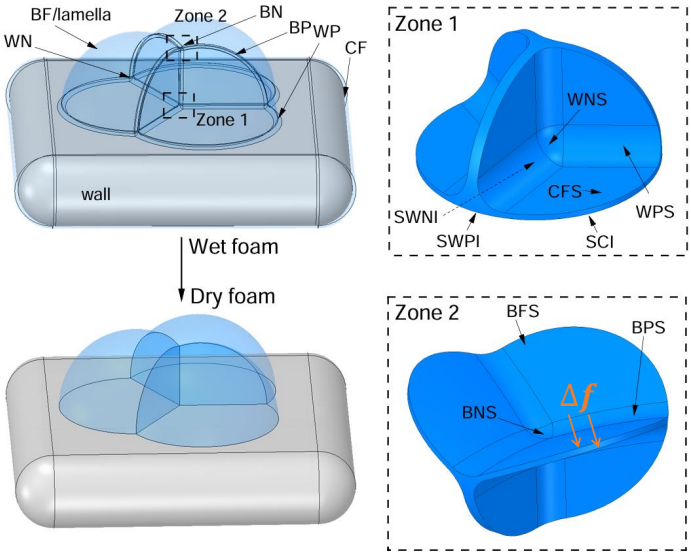


Figure 5.1: Schematic diagram of a foam consisting of three bubbles attached on the surface of a solid plate. In the extreme case of dry foam, the thin films reduce to non-thickness 2D surfaces embedded in 3D. The Plateau borders reduce to curves embedded in 3D. The nodes reduce to four-fold points. Geometric elements of the foam include bulk films (BF) or lamellae, wetting films coating on the wall (CF), bulk Plateau borders (BP), wall Plateau borders (WP), nodes on the wall (WN), nodes in bulk (BN). The gas-liquid and solid-liquid interfaces are categorized into nine types: wall Plateau border surfaces (WPS), wall node surfaces (WNS), coating film surfaces (CFS), solid-wall node interfaces (SWNI), solid-coating film intefaces (SCI), solid-wall Plateau border interfaces (SWPI), bulk film surfaces (BFS), bulk Plateau border surfaces (BPS) and bulk node surfaces (NBS). The arrows in orange illustrate the interfacial force on gas-liquid interface.

the solid surface. The gas-liquid surface tension is γ, and the gas viscosity is $\lambda\mu$, where μ is the viscosity of continuous liquid phase and λ is the ratio between the gas viscosity and the liquid viscosity.

Assume that there are $N-1$ bubbles, and the foam as well as the solid plate are immersed in an unbounded gas domain. Use D_0 to refer to the domain of the liquid region and D_K the domain of the Kth gas region, where $K = 1, 2, ..., N-1$. Use D_N to denote the outermost unbounded gas area. In the schematic diagram shown in Figure 5.1, for instance, N equals 4, i.e. three bubbles and one unbounded gas area.

At low Reynolds numbers and ignoring the buoyant force, foam flow is governed by the incompressible Stokes flow equations, which can be written as [100]

$$\nabla \cdot \Pi^K = \mathbf{0}, \quad \nabla \cdot \boldsymbol{u}^K = 0, \quad \boldsymbol{x} \in D_K, \quad \text{for } K = 0, 1..., N, \tag{5.1}$$

where Π^K is the stress tensor and K is the index of each fluid domain. The stress tensor is a term combining pressure and viscous stress

$$\Pi^K = -p^K \mathrm{I} + \lambda^K \mu \big(\nabla \boldsymbol{u}^K + (\nabla \boldsymbol{u}^K)^T\big), \tag{5.2}$$

where $\lambda^0 = 1.0$ and $\lambda^K = \lambda$ for $K = 1, 2, ..., N$. The dispersed gas domains are separated from the liquid domain by the interfaces $\{\Gamma_K\}_{K=1}^N$.

Across each interface Γ_K, the velocity is continuous, but the normal stress component undergoes a discontinuity arising from the surface tension and the disjoining pressure [100]

$$(\Pi^0 - \Pi^K) \cdot \boldsymbol{n} = \Delta \boldsymbol{f}, \quad \boldsymbol{u}^0 = \boldsymbol{u}^K, \quad K = 1, 2, ..., N, \tag{5.3}$$

where $\boldsymbol{n}$ is the unit vector normal to Γ_K and $\Delta \boldsymbol{f}$ is the interfacial force (per unit area). $\Delta \boldsymbol{f}$ is defined as $\Delta \boldsymbol{f}_\mathrm{t} + \Delta \boldsymbol{f}_\mathrm{d}$, where $\Delta \boldsymbol{f}_\mathrm{t}$ is the surface tension-induced component of the interfacial

force and $\Delta \boldsymbol{f}_{\mathrm{d}}$ is the disjoining pressure-induced component. $\Delta \boldsymbol{f}_{\mathrm{t}}$ is calculated as $\Delta \boldsymbol{f}_{\mathrm{t}} = 2\gamma k \boldsymbol{n}$, where k is the mean curvature at a point on the gas-liquid interfaces. The curvature k is positive when the interface is convex along the unit normal vector $\boldsymbol{n}$, and negative otherwise. Equivalently, one may assume that k is always positive and the value of the force is calculated as $-2\gamma k$, such that the direction of the force always points into the concave side of a gas-liquid interface.

In some cases, e.g. the flow velocity being finite and uniform in the far field, the far field flow does not vanish at infinity. For these cases, the flow in the outermost domain is decomposed into two components, namely $\boldsymbol{u}(\boldsymbol{x}) = \boldsymbol{u}^{\infty}(\boldsymbol{x}) + \boldsymbol{u}^{d}(\boldsymbol{x})$, where $\boldsymbol{u}^{\infty}$ is the background flow and $\boldsymbol{u}^{d}$ is the disturbed flow. The latter vanishes at infinity while the former does not. Both flows satisfy the Stokes flow equations. In addition, the imposed flow is nonsingular in the whole space while the disturbed flow is nonsigular only in the outermost region.

5.2.2 Boundary integral equations

Place a point $\boldsymbol{x}_0$, named the source point, inside a bubble domain D_m, $m \in \{1, 2, ..., N-1\}$, and use the boundary integral representation of Stokes flow in fluid domains $\{D_K\}_{K=1}^{N-1}$. Depending on whether or not $K = m$, we have [92]

$$\begin{aligned}
&\int_{\Gamma_m} \Pi_{ik}(\boldsymbol{x}) G_{ij}(\boldsymbol{x}, \boldsymbol{x}_0) n_k(\boldsymbol{x}) dS(\boldsymbol{x}) - \lambda\mu \int_{\Gamma_m} u_i(\boldsymbol{x}) T_{ijk}(\boldsymbol{x}, \boldsymbol{x}_0) n_k(\boldsymbol{x}) dS(\boldsymbol{x}) = 8\pi\lambda\mu u_j(\boldsymbol{x}_0), \\
&\int_{\substack{\Gamma_K \\ K \neq m}} \Pi_{ik}(\boldsymbol{x}) G_{ij}(\boldsymbol{x}, \boldsymbol{x}_0) n_k(\boldsymbol{x}) dS(\boldsymbol{x}) - \lambda\mu \int_{\substack{\Gamma_K \\ K \neq m}} u_i(\boldsymbol{x}) T_{ijk}(\boldsymbol{x}, \boldsymbol{x}_0) n_k(\boldsymbol{x}) dS(\boldsymbol{x}) = 0,
\end{aligned} \tag{5.4}$$

with G and T the Stokeslet and stresslet, respectively, which in 3D are defined as

$$G_{ij}(\boldsymbol{r}) = \frac{\delta_{ij}}{|\boldsymbol{r}|} + \frac{r_i r_j}{|\boldsymbol{r}|^3}, \quad T_{ijk}(\boldsymbol{r}) = -6\frac{\boldsymbol{r}_i \boldsymbol{r}_j \boldsymbol{r}_k}{|\boldsymbol{r}|^5}, \tag{5.5}$$

where $\boldsymbol{r} = \boldsymbol{x} - \boldsymbol{x}_0$. The indices i, j, and for the stresslet k also, ranging from 1 to 3, denote

the components of vectors or tensors within a 3D Cartesian coordinate framework.

Then, decompose the Stokes flow in the outermost gas domain and notice that the imposed flow is nonsingular in the whole space [92], leading to

$$\int_{\Gamma_N} \Pi_{ik}(\boldsymbol{x}) G_{ij}(\boldsymbol{x}, \boldsymbol{x}_0) n_k(\boldsymbol{x}) dS(\boldsymbol{x}) - \lambda\mu \int_{\Gamma_N} u_i(\boldsymbol{x}) T_{ijk}(\boldsymbol{x}, \boldsymbol{x}_0) n_k(\boldsymbol{x}) dS(\boldsymbol{x}) = -8\pi\lambda\mu u_j^{\infty}(\boldsymbol{x}_0). \tag{5.6}$$

In addition, the boundary integral representation of the Stokes flow in the continuous liquid network is

$$\int_{\Gamma_0} \Pi_{ik}(\boldsymbol{x}) G_{ij}(\boldsymbol{x}, \boldsymbol{x}_0) n_k(\boldsymbol{x}) dS(\boldsymbol{x}) - \mu \int_{\Gamma_0} u_i(\boldsymbol{x}) T_{ijk}(\boldsymbol{x}, \boldsymbol{x}_0) n_k(\boldsymbol{x}) dS(\boldsymbol{x}) = 0. \tag{5.7}$$

Subtracting Eq. 5.4 and Eq. 5.6 from Eq. 5.7, and substituting Eq. 5.3 into the resultant formula, we find a boundary integral equation for the velocity at the source point $\boldsymbol{x}_0$

$$\begin{aligned} u_j(\boldsymbol{x}_0) =& u_j^{\infty}(\boldsymbol{x}_0) - \frac{1}{8\pi\lambda\mu} \int_{\Gamma_s} \Pi_{ik}(\boldsymbol{x}) G_{ij}(\boldsymbol{x}, \boldsymbol{x}_0) n_k(\boldsymbol{x}) dS(\boldsymbol{x}) \\ &+ \frac{1}{8\pi\lambda} \int_{\Gamma_s} u_i(\boldsymbol{x}) T_{ijk}(\boldsymbol{x}, \boldsymbol{x}_0) n_k(\boldsymbol{x}) dS(\boldsymbol{x}) \\ &- \frac{1}{8\pi\lambda\mu} \int_{\Gamma_0 - \Gamma_s} \Delta f_i(\boldsymbol{x}) G_{ij}(\boldsymbol{x}, \boldsymbol{x}_0) dS(\boldsymbol{x}) \\ &+ \frac{1-\lambda}{8\pi\lambda} \int_{\Gamma_0 - \Gamma_s} u_i(\boldsymbol{x}) T_{ijk}(\boldsymbol{x}, \boldsymbol{x}_0) n_k(\boldsymbol{x}) dS(\boldsymbol{x}), \end{aligned} \tag{5.8}$$

where Γ_s refers to the solid surface and $\Gamma_0 - \Gamma_s$ is the boundary of the liquid phase excluding the solid surface, i.e. all the gas-liquid interfaces. On the right-hand side of Eq. 5.8, the first and third integrals are called the single-layer potentials and the second and last integrals are called the double-layer potentials [92]. Each integral can be further decomposed into several terms in the form of integrals over multiple panels of the gas-liquid interfaces or the solid surface.

As shown in Figure 5.1, the foam structure is composed of six different geometric elements, including the films in bulk (BF) or lamellae, coating films (CF), Plateau borders in bulk (BP),

Plateau borders on the wall (WP), nodes on the wall (WN), and nodes in bulk (BN). Based on these different elements, the boundaries involved in this system can be categorised into nine types in addition to the boundary at infinity: (1) Interface between the nodes on the wall and the wall surface (SWNI); (2) Interfaces between the solid wall and the coating films (Solid-CF interface/SCI); (3) Interfaces between the solid wall and the wall Plateau borders (Solid-WPB interface/SWPI); (4) Surfaces of bulk films (BFS); (5) Surfaces of bulk Plateau borders (BPS); (6) Surfaces of nodes in bulk (BNS); (7) Surfaces of wall Plateau borders (WPS); (8) Surfaces of nodes on the wall (WNS); (9) Surfaces of coating films (CFS). With these different types of interface panels, Eq. 5.8 can be written as

$$\begin{aligned} u_j(\boldsymbol{x}_0) =& u_j^{\infty}(\boldsymbol{x}_0) + I_{\mathrm{SWNI}} + I_{\mathrm{SCI}} + I_{\mathrm{SWPI}} \\ &+ I_{\mathrm{BFS}} + I_{\mathrm{BPS}} + I_{\mathrm{BNS}} + I_{\mathrm{WPS}} + I_{\mathrm{WNS}} + I_{\mathrm{CFS}}, \end{aligned} \tag{5.9}$$

where I denotes the integral over each boundary section (bs). Specifically, the integrals over SWNI, SCI and SWPI are

$$I_{bs} = -\frac{1}{8\pi\lambda\mu}\int_{bs}\Pi_{ik}(\boldsymbol{x})G_{ij}(\boldsymbol{x},\boldsymbol{x}_0)n_k(\boldsymbol{x})dS(\boldsymbol{x}) + \frac{1}{8\pi\lambda}\int_{bs}u_i(\boldsymbol{x})T_{ijk}(\boldsymbol{x},\boldsymbol{x}_0)n_k(\boldsymbol{x})dS(\boldsymbol{x}), \tag{5.10}$$

and, over BFS, BPS, BNS, WPS, WNS and CFS, the integrals are defined as

$$I_{bs} = -\frac{1}{8\pi\lambda\mu}\int_{bs}\Delta f_i(\boldsymbol{x})G_{ij}(\boldsymbol{x},\boldsymbol{x}_0)dS(\boldsymbol{x}) + \frac{1-\lambda}{8\pi\lambda}\int_{bs}u_i(\boldsymbol{x})T_{ijk}(\boldsymbol{x},\boldsymbol{x}_0)n_k(\boldsymbol{x})dS(\boldsymbol{x}), \tag{5.11}$$

where Δf_i is the interfacial force across the gas-liquid interface. As mentioned, it is calculated as $\Delta f_i = -2\gamma k(\boldsymbol{x})$, pointing towards the concave side of the gas-liquid interface. In Eq. 5.10, the single-layer potential involves an unknown stress Π_{ik}, due to the presence of solid walls.

5.2.3 The extreme case of dry foam

Under the assumption of dry foam, the double-layer potential over BFS is zero because of the opposite normal directions at the two overlapping gas-liquid interfaces of films. Besides, the infinitesimal volume of the Plateau borders and nodes lead to the double-layer potentials over BPS, WPS, SWPI, BNS, SWNI and WNS being zero. By contrast, the double-layer potential over SCI cannot be cancelled from the double-layer potential over CFS, resulting in a remaining term $-1/(8\pi)\int_s u_i(\boldsymbol{x})T_{ijk}(\boldsymbol{x},\boldsymbol{x}_0)n_k(\boldsymbol{x})dS(\boldsymbol{x})$, where the normal vector $n_k(\boldsymbol{x})$ points into the solid domain.

As for the limit values of single-layer potentials, they can be considered from three aspects. Firstly, the single-layer potential over BNS is zero, because $||\Delta f|| \sim 1/R_{\mathrm{BNS}}$ and $S_{\mathrm{BNS}} \sim R_{\mathrm{BNS}}^2$, where R_{BNS} and S_{BNS} are the curvature radius and the surface area of BNS, lead to $\int_{bs}\Delta f_i(\boldsymbol{x})G_{ij}(\boldsymbol{x},\boldsymbol{x}_0)dS(\boldsymbol{x}) \sim R_{\mathrm{BNS}}$ that tends to zero as R_{BNS} approaches zero. Similarly, the single-layer potentials over WNS and SWNI are also zero because the areas of WNS or SWNI decreases much faster than the interfacial force across WNS or the stress on SWNI increases, respectively. Secondly, the summation of single-layer potentials over BPS is zero because the angles between the films remain 120 degrees. Otherwise, there exists singular forces act on the bulk Plateau borders, which immediately leads to the films restoring the states that forming 120-degree between each pair of the three meeting bulk films. Similarly, the summation of single-layer potentials over WPS and SWPI are also zero because of the force balance at wall Plateau borders.

Other single-layer potentials, including those over SCI, CFS and BFS are non-zero in the dry limit. Furthermore, the single-layer potential over SCI and CFS can be combined as an integral over the solid wall, and the single-layer potential over BFS can be transferred into an integral over films with the interfacial force being doubled that of one single gas-liquid interface.

The resultant boundary integral equation for the velocity at a source point inside a gas area is written as

$$u_j(\boldsymbol{x}_0) = u_j^{\infty}(\boldsymbol{x}_0) - \frac{1}{8\pi\lambda\mu}\Big(\int_{S_\mathrm{l}} -\Delta F_i(\boldsymbol{x}) G_{ij}(\boldsymbol{x}, \boldsymbol{x}_0) dS(\boldsymbol{x}) + \int_{S_\mathrm{s}} q_i(\boldsymbol{x}) G_{ij}(\boldsymbol{x}, \boldsymbol{x}_0) dS(\boldsymbol{x}) \Big) - \frac{1}{8\pi} \int_{S_\mathrm{s}} u_i(\boldsymbol{x}) T_{ijk}(\boldsymbol{x}, \boldsymbol{x}_0) n_k(\boldsymbol{x}) dS(\boldsymbol{x}), \tag{5.12}$$

where S_l represents the film or lamella surface and S_s is the surface of solid wall. $\boldsymbol{q}$ is the unknown normal stress projected onto the normal direction acting on the separated phase of fluid by the wall. The value of the interfacial force ΔF_i is defined as $-2\Delta f_i$ and thus is calculated as $4\gamma k\, n_i$. In default, the interfacial force points into the concave side of the lamella.

Denote as the characteristic length L_0, characteristic velocity U_0 and characteristic time $T_0 = L_0/U_0$. Using these characteristic quantities, Eq. 5.12 can be written in the dimensionless form

$$u_j^*(\boldsymbol{x}_0^*) = u_j^{\infty,*}(\boldsymbol{x}_0^*) - \frac{1}{8\pi}\Big(\int_{S_\mathrm{l}} -\frac{1}{Ca} k^*(\boldsymbol{x}^*) \boldsymbol{n}_i(\boldsymbol{x}^*) G_{ij}(\boldsymbol{x}^*, \boldsymbol{x}_0^*) dS^*(\boldsymbol{x}^*) + \int_{S_\mathrm{s}} q_i^*(\boldsymbol{x}^*) G_{ij}(\boldsymbol{x}^*, \boldsymbol{x}_0^*) dS^*(\boldsymbol{x}^*) \Big) - \frac{1}{8\pi} \int_{S_\mathrm{s}} u_i^*(\boldsymbol{x}^*) T_{ijk}(\boldsymbol{x}^*, \boldsymbol{x}_0^*) n_k(\boldsymbol{x}^*) dS^*(\boldsymbol{x}^*), \tag{5.13}$$

where $Ca = \lambda\mu L_0/(4\gamma T_0)$, $k^* = kL_0$, and $q_i^* = q_i T_0/(\lambda\mu)$. In order to simplify the notations, the superscript * will be ignored in the following.

The value of Ca can be estimated given that the flow is at low Reynolds numbers ($Re << 1$). The Reynolds number is defined as $Re = \rho L_0^2/(\lambda\mu T_0)$ and can be reformulated using Ca as $Re = 4\gamma\rho L_0 Ca/(\lambda\mu)^2$. This can be simplified as $Re = Ca/Oh^2$ where Oh is the Ohnesorge number defined as $Oh = \lambda\mu/(2\sqrt{\gamma\rho L_0})$. Thus the low Reynolds number condition requires $Ca << Oh^2$. Apparently, Ca should be rather small if the fluid in bubbles is of low viscosity, and the characteristic length and the surface tension are large. In addition, when converting the quantities in dimensionless form back to the realistic physical quantities, it has been implicitly assumed that the actual velocity is not much larger than the adopted characteristic velocity. In other words, the calculated dimensionless velocity should scale as $O(1)$ or smaller if the numerical results can be reproduced in the realistic world.

5.2.4 Boundary condition on the wall

As shown in Eq. 5.13, the velocity is a continuous quantity, which means that the velocity of the foam films is zero on the wall if the no-slip boundary condition is used. In other words, the no-slip boundary condition is not directly compatible with Eq. 5.13, since it is reasonable that foam films are mobile and can move on the wall surface. As an alternate choice, the slip boundary condition is considered in this work.

The viscous force between the fluid and the wall is ignored under the slip boundary condition. One major effect of this simplification could be the ignorance of the viscous force imposed on the wall Plateau borders by the wall (which by contrast is a crucial factor involved in the viscous froth model). This limitation, however, might be released through specified angles between the wall and the foam films.

The slip boundary condition requires that the fluid cannot penetrate the wall and thus the normal velocities of fluid on the wall are known quantities equal to the normal velocities of the wall itself. The shear stress on the wall surface is zero such that the fluid is assumed free to move tangentially along the wall surface. Consequently, the unknown quantities on the wall are composed of the normal stress and the two tangential velocity components. Adopting the slip boundary condition may be justified by the work in [67] that there can be a transition region near the front and back of bubbles along which velocity decays from velocity of the bubble itself at the front to no slip at the back. Moreover, there is no shear stress in the film away from the transition region, only shear stress in the transition region, but even in the transition region there is no shear stress at the gas-liquid interface.

5.2.5 Singularity and near-singularity subtraction

The integrals in Eq. 5.13 cannot be directly used in general numerical calculation because the kernels, i.e. Stokeslet and stresslet, are singular and near-singular when $\boldsymbol{x}$ is located right at $\boldsymbol{x}_0$ and $\boldsymbol{x}$ approaches $\boldsymbol{x}_0$, respectively. To address the singularity or near-singularity, following properties of the Stokeslet and stresslet are utilised [92]

$$\int_S G_{ij}(\boldsymbol{x},\boldsymbol{x}_0)n_i dS(\boldsymbol{x}) = 0, \quad \int_S T_{ijk}(\boldsymbol{x},\boldsymbol{x}_0)n_k dS(\boldsymbol{x}) = 0, \tag{5.14}$$

where the source point $\boldsymbol{x}_0$ is located exterior to an enclosed surface S, such as the solid plate surface.

solid-self singularity and solid-induced near-singularity

When solving Eq. 5.13 for the unknown pressure and tangential velocity components on solid surfaces, the source point $\boldsymbol{x}_0$ is placed right on the solid surfaces, leading to the singularity occurring in the single-layer and double-layer potentials over the solid surfaces. To address this singularity, following identities are derived based on Eq. 5.14

$$\int_{S_\mathrm{s}} q(\boldsymbol{x}_0)G_{ij}(\boldsymbol{x},\boldsymbol{x}_0)n_i dS(\boldsymbol{x}) = 0, \quad \int_{S_\mathrm{s}} u_i(\boldsymbol{x}_0)T_{ijk}(\boldsymbol{x},\boldsymbol{x}_0)n_k dS(\boldsymbol{x}) = 0, \tag{5.15}$$

where initially the source point $\boldsymbol{x}_0$ is situated exterior to the solid surface S_s. $q(\boldsymbol{x}_0)$ gains significance through its definition employing $q_i(\boldsymbol{x}_0) = q(\boldsymbol{x}_0)n_i(\boldsymbol{x}_0)$ when $\boldsymbol{x}_0$ is precisely positioned on the solid surface. Subtract Eq. 5.15 from Eq. 5.12 and then place the source point right on the wall, leading to

$$\begin{aligned} u_j(\boldsymbol{x}_0) = u_j^\infty(\boldsymbol{x}_0) - \frac{1}{8\pi}\Big(&\int_{S_\mathrm{l}} -\frac{1}{Ca}k(\boldsymbol{x})n_i(\boldsymbol{x})G_{ij}(\boldsymbol{x},\boldsymbol{x}_0)dS(\boldsymbol{x}) \\ &+ \int_{S_\mathrm{s}} \big(q(\boldsymbol{x}) - q(\boldsymbol{x}_0)\big)G_{ij}(\boldsymbol{x},\boldsymbol{x}_0)n_i(\boldsymbol{x})dS(\boldsymbol{x})\Big) \\ &- \frac{1}{8\pi}\int_{S_\mathrm{s}} \big(u_i(\boldsymbol{x}) - u_i(\boldsymbol{x}_0)\big)T_{ijk}(\boldsymbol{x},\boldsymbol{x}_0)n_k(\boldsymbol{x})dS(\boldsymbol{x}). \end{aligned} \tag{5.16}$$

When calculating the velocity at a field point $\boldsymbol{x}_f$ that is close to the wall, the single-layer and double-layer potentials associated with the flow on the wall become near singular. This near-singularity can also be cancelled using Eq. 5.15, in which $\boldsymbol{x}_0$ is selected as the point on the wall that is closest to the field point.

lamella-self singularity and lamella-induced near-singularity

When the source point is placed right on or close to a lamella, the single-layer potential, in Eq. 5.16, over films or lamellae become singular or near-singular. It is possible to construct identities similar to Eq. 5.15 to subtract the singularity and near-singularity, but may not be a convenient choice in the case of dry foam, where each film forms one side of an enclosed bubble boundary and thus is non-closed itself. Moreover, a film could be a common boundary of two neighbouring bubbles. These issues lead to the inconvenience utilising identities as in Eq. 5.15 to subtract the singularity or near-singularity.

As an alternate method, a non-singular contour-integral representation of single-layer potential is utilised, which can be used to calculate the single-layer potential over a non-closed surface [100]

$$\begin{aligned} &\int_{S'} -\frac{1}{Ca} k(\boldsymbol{x}) G_{ij}(\boldsymbol{x}, \boldsymbol{x}_0) n_i(\boldsymbol{x}) dS(\boldsymbol{x}) \approx -\frac{1}{Ca} k_{S'}^{\text{avg}} \int_{S'} G_{ij}(\boldsymbol{x}, \boldsymbol{x}_0) n_i dS(\boldsymbol{x}), \\ &\int_{S'} G_{ij}(\boldsymbol{x}, \boldsymbol{x}_0) n_i dS(\boldsymbol{x}) = \oint_{\Gamma_{S'}} \frac{d\boldsymbol{r} \times \boldsymbol{r}}{|\boldsymbol{r}|}, \end{aligned} \tag{5.17}$$

where S' is a non-closed surface and $\Gamma_{S'}$ is the contour of S'. For S' being a small surface area, such as the area represented by a basic element that will be introduced in Section 5.3.1, the averaged value $k_{S'}^{\text{avg}}$ can be approximated as $k_{\boldsymbol{x}_c}$, where $\boldsymbol{x}_c$ usually is set to the centre point of the small surface area. The direction of the curve integral is given by the unit vector $\boldsymbol{t}$ along the contour. $\boldsymbol{t}$ is defined as $\boldsymbol{t} = \boldsymbol{n} \times \boldsymbol{n}_{\Gamma_{S'}}$, where $\boldsymbol{n}_{\Gamma_{S'}}$ is the unit outward vector tangent to the surface S' and perpendicular to the contour $\Gamma_{S'}$.

5.2.6 Singular forces on bulk Plateau borders

In the derivation of Eq. 5.13, the condition of the force balance at Plateau borders on walls or in bulk has been used. For wall Plateau borders, the no-slip boundary condition leads to that the normal gradient of the tangent velocity is zero on wall. In other words, the velocity field maintains that the films are perpendicular to the walls. Thus, the forces are always balanced

at wall Plateau borders.

In contrast, the angles between films in bulk may in principle deviate from 120 degrees due to the shearing effect of the fluid. As mentioned, once the forces acting on a bulk Plateau border leads to net non-zero force, this singular force should restore the 120-degree angles between films in bulk. For this reason, an additional motion for Plateau borders in bulk and nodes should be considered to maintain the 120-degree angles between films in bulk, which is detailed in Section 5.3.5. Note that the singular force applies only prior to any additional motion being introduced. After the additional motion is applied and Plateau borders are restored to 120 degree angles, presumably there should no longer be a singular force.

One issue arising from the additional motion of bulk Plateau borders, however, is the accumulation of errors in bubble volumes. This is because the additional motion is locally introduced to maintain the force balance at bulk Plateau borders, while its effect on the motion of other parts of the foam is not considered. To solve this problem, the contribution of the singular unbalanced force at bulk Plateau borders should be modelled in the boundary integral method.

Use $\boldsymbol{F}$ to denote the density of singular force along the bulk Plateau borders. the contribution of the motion of bulk Plateau borders to the whole flow field is approximated as $1/(8\pi Ca)\int_{L_{\mathrm{BP}}} F_i(\boldsymbol{x})G_{ij}(\boldsymbol{x},\boldsymbol{x}_0)dl(\boldsymbol{x})$. This integral is computed along bulk Plateau borders, denoted as L_{BP}, and should be added to the right-hand side of Eq. 5.13. This treatment is found to alleviate the volume deviations during simulations, as demonstrated later in Section 5.4.1.

By contrast, an alternate method accounting for the effect of the singular force is available in the literature. Bajlekov [128] defined an "equivalent capillary pressure" in the context of three-phase flow problem, based on the equilibrium of forces including those due to capillary pressure and the tangent film tension forces, in a Plateau border vicinity. This method could also be applied in the present case, assuming that the singular forces at Plateau borders are balanced by the equivalent capillary pressure over film areas nearby the Plateau borders. One main advantage of this method then is that the singularity of the Plateau border's motion is avoided, and thus the angle between films is not implemented as a boundary condition. In

addition, because of no singular forces involved, we can directly use Eq. 5.13 to compute the velocity of any points on foam films, including those on Plateau borders. The implementation of this method is later discussed in Section 5.3.5.

5.3 Numerical methods

In this section, numerical techniques for modelling foam motion using Eq. 5.16 are discussed. These include the triangulation of the geometries including the surfaces of films and walls, the numerical approximations of the quantities involved in Eq. 5.16, such as the mean curvature and unit normal vector of a film, and the discretisation of Eq. 5.16. In addition, the modelling of the motion of the bulk Plateau borders and its impact on the rest of the foam is explained.

5.3.1 Surface representation and mesh refinement

All surfaces, including films and walls, are triangulated in simulations. For films, an auxiliary mesh composed of so-called basic elements is constructed from the original triangle mesh, which is needed in the calculation of the single-layer potential over films [100], as shown in Figure 5.2.

The mesh should be sufficiently fine to resolve the details of the geometry, while the size distribution can be non-uniform in order to reduce the total number of mesh vertices and thus the computational cost [129]. Moreover, element distortion should be avoided for the benefit to the accurate discretisation in terms of the curvature calculation and obtaining a well conditioned linear system.

In order to maintain the favourable mesh properties during the simulations, three mesh refinement processes are applied. These operations include: (1) Element size optimisation, (2) Subtraction and addition of edges and (3) Mesh topology adjustment.

Operation (1) is achieved by a physical analogy between the mesh and a truss structure [129]. Under this analogy, each mesh vertex or material point is attracted [130] or repulsed [129]

by neighbouring vertices. The attractive or repulsive force is proportional or inversely proportional to the length of the edge between each vertex and its neighbours, with weighting factors accounting for the geometric properties, such as the local mean curvature. For instance, the following expression presents the tangent displacement $\boldsymbol{X}_{\mathrm{t}}$ of a vertex $\boldsymbol{x}_c$ attracted by its neighbouring vertices $\boldsymbol{x}_{c'}$ [130]

$$\boldsymbol{X}_{\mathrm{t}} = \epsilon(I - \boldsymbol{n}_c\boldsymbol{n}_c)\sum_i (k_{c'})^{3/2}\Delta S_{c'}(\boldsymbol{x}_{c'} - \boldsymbol{x}_c), \tag{5.18}$$

where the subscript c and c' here are indices used to denote the vertices, $\boldsymbol{n}_c$ unit normal vector at $\boldsymbol{x}_c$, $k_{c'}$ film mean curvature at $\boldsymbol{x}_{c'}$, and $\Delta S_{c'}$ area of the basic element at $\boldsymbol{x}_{c'}$. The summation is over all the vertices $\boldsymbol{x}_{c'}$ that directly connect to the vertex $\boldsymbol{x}_c$. The factor ϵ is chosen so that the tangential displacements of points by a time step can improve the mesh properties, instead of distorting the mesh. For vertices on wall Plateau borders, the displacement should be further projected onto the tangent plane of the wall, since these vertices consistently maintain contact with the surface of the wall.

Operation (2) enhances mesh quality by removing short edges and subdividing excessively long edges. The length of each edge between two neighbouring vertices is compared with two global length scales, $l_{\max}$ and $l_{\min}$. As the length of an edge becomes less than $l_{\min}$, the edge is deleted. In contrast, an edge, whose length is larger than $l_{\max}$, is subdivided by adding a middle vertex on the edge. For subdivided edges on the wall, the middle point is simply projected to the wall surface. For subdivided edges on foam films, the added vertex is projected onto a high-order approximation of the surface proposed by Bazhlekov et al. [100].

Finally, operation (3) is achieved by reconnecting the vertices of two neighbouring triangles if the two triangles form a sharp quadrilateral. This operation can help to maintain favourable coordination numbers for most vertices in the mesh.

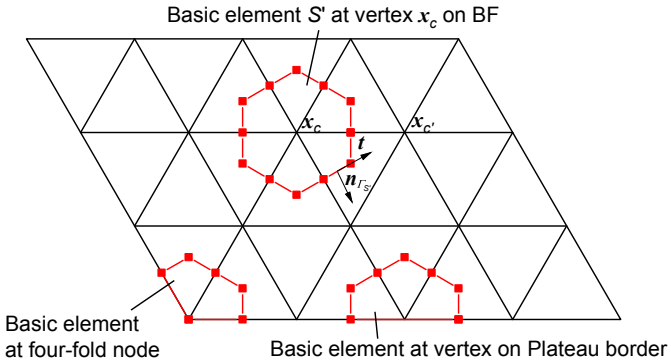


Figure 5.2: Two grids are employed to discretise the foam film. The triangle elements of black contour are used to represent the film geometry. The basic elements of red contour, which are constructed from the centre points of the triangle elements and the middle points of their edges, are needed in the calculation of the mean curvature and the single-layer potential over the film. There are three types of basic elements, at four-fold nodes, vertices on Plateau borders, and interior vertices on bulk films, respectively. The contour of the basic element S' at vertex $\boldsymbol{x}_c$, where c is the index of the vertex, is denoted as $\Gamma_{S'}$. The neighbouring vertices of $\boldsymbol{x}_c$ are denoted by $\boldsymbol{x}_{c'}$. Two distinct unit vectors are defined: the first being the unit normal vector $\boldsymbol{n}_{\Gamma_{S'}}$ situated within the plane of the triangle element and extending outward from the basic element, while the second is the unit tangent vector $\boldsymbol{t}$ aligned with the contour of the element. In this schematic diagram, the unit normal vector $\boldsymbol{n}$ of the basic element is assumed to point out of the page, and $\boldsymbol{t}$ obeys the definition $\boldsymbol{t} = \boldsymbol{n} \times \boldsymbol{n}_{\Gamma_D}$.

5.3.2 Calculation of the film mean curvature and normal vector

There are two methods for the calculation of the film mean curvature, as well as the normal vector of the film. The first choice is the contour integral method that utilises the relation between the mean curvature and the gradient of the surface energy [87]. The mean curvature at a vertex $\boldsymbol{x}_c$ on films is approximated as the magnitude of the gradient of surface energy at the vertex divided by the surface area $\Delta S_{S'}$ associated with the vertex, namely the area of the basic element S' at the vertex $\boldsymbol{x}_c$ [87]

$$k(\boldsymbol{x}_c)\boldsymbol{n}(\boldsymbol{x}_c) \approx (1/\Delta S_{S'}) \oint \boldsymbol{n}_{\Gamma_{S'}} d\Gamma_{S'}, \tag{5.19}$$

where $\boldsymbol{n}(\boldsymbol{x}_c)$ is the unit normal vector [100]. Since k is taken positive, the normal vector always points into the concave side of the film. By contrast, the other method for the computation of the mean curvature and normal vector at a vertex is through a local paraboloid fitting using the positions of the vertex and its neighbouring vertices [131].

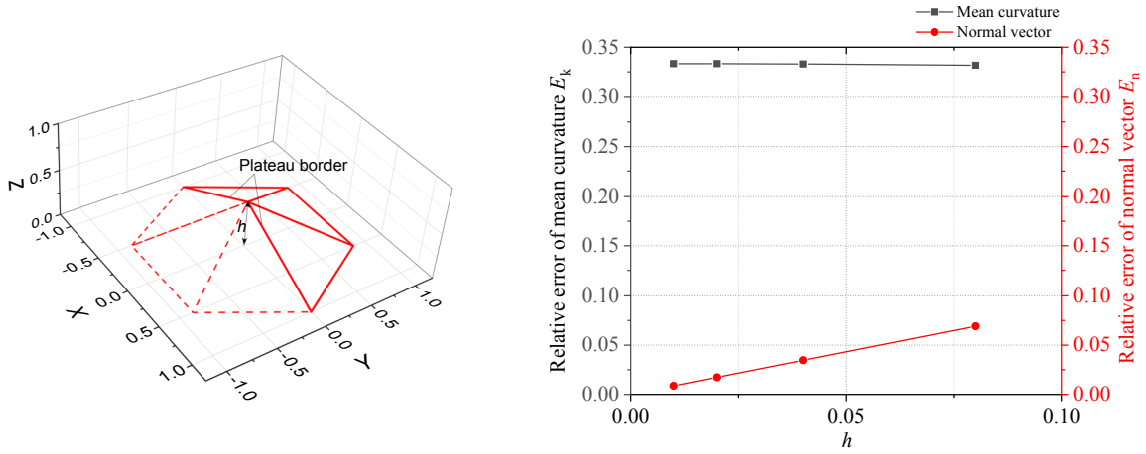
The accuracy of each method in approximating the mean curvature of films depends on how the initial foam configuration is obtained [128]. For instance, if the relaxation process of a bubble is predicted using the boundary integral method and the mean curvature is computed using the contour integral method, the final mean curvature of the bubble can be accurately estimated by the contour integral method [128]. On the other hand, in the case of an initial bubble that conforms to a perfect sphere, with all vertices positioned on its spherical surface, utilising paraboloid fitting presents a more accurate method for estimating the mean curvature.

Both approaches encounter difficulties in approximating the mean curvature at a vertex on the border of a film, such as when applied to basic elements at four-fold nodes or vertices on Plateau borders. The contour integral method tends to underestimate the magnitude of the mean curvature. This phenomenon is illustrated in Figure 5.3, where a basic element on film border is derived by subdividing a regular basic element that encompasses its contour with six edges of equal length. The central vertex of the regular basic element is vertically offset by a small distance h from the plane defined by its contour. Using the contour integral method, the mean curvature and unit normal vector of the basic element on film border are calculated and then compared to those of the unaltered regular basic element.

It is found that the error in mean curvature maintains at a high level across the range of h, while the error in normal vector is relatively small, especially when the basic element approaches flat. This implies that even with the utilisation of extremely refined element sizes for film discretisation, the contour integral method struggles to yield a precise approximation of mean curvature at a vertex located along the film border.

In addition, further tests indicate that the error in film mean curvature tends to increase as the coordination number of the target vertex decreases. For these reasons, the mean curvature at vertices on film borders is instead approximated through interpolation. Specifically, the mean curvature at a vertex along the film border is estimated, by calculating the arithmetic mean value of the mean curvature values from adjacent vertices located on the same film.

Regarding the paraboloid fitting technique for a vertex on film border, it necessitates the presence of auxiliary vertices in close proximity to the vertex. These auxiliary vertices are



(a) (b)

Figure 5.3: The accuracy of the mean curvature and unit normal vector at the border of a film, computed by the contour integral method. (a) Schematic diagram of a basic element on the border of a film, denoted by the red solid line segments. This basic element constitutes half of a standard basic element possessing a regular hexagonal contour, with the complementary half represented by the dashed red line segments. To mimic a curved surface, the centre vertex of the regular basic element is vertically offset by a small distance, h. The curvature and unit normal vector of the regular basic element, as computed through the contour integral method, serve as the benchmarks referred to as k_{ref} and $\boldsymbol{n}_{\mathrm{ref}}$, respectively. (b) The errors in mean curvature and unit normal vector of the basic element on the film border are presented as functions of h, denoted as E_k and E_n, respectively. The errors are defined as $E_k = |k - k_{\mathrm{ref}}|/k_{\mathrm{ref}}$ and $E_n = ||\boldsymbol{n} - \boldsymbol{n}_{\mathrm{ref}}||$, respectively.

essentially mirror images of the interior vertices on the films, and they are positioned with respect to a specific plane passing through the target vertex. Acquiring these auxiliary vertices for vertices located along the wall Plateau borders is straightforward, as the bisecting plane or mirror plane coincides precisely with the wall's tangent plane. Nonetheless, when addressing a vertex positioned along the bulk Plateau borders, a more complex situation emerges. In this particular context, the vertex necessitates three separate bisecting planes, all of which must be estimated.

5.3.3 Calculation of the double-layer and single-layer potentials

The double-layer potentials are only computed over each element on walls. Since the singularity of double-layer potential in Eq. 5.16 has been removed, the double-layer integral over each triangle element can be calculated using the one-point trapezoidal rule [93]

$$\int_{S''} (\phi(\boldsymbol{x}) - \phi(\boldsymbol{x}_0)) dS(x) \approx (\phi(\boldsymbol{x}_c) - \phi(\boldsymbol{x}_0)) \Delta S_{S''}, \tag{5.20}$$

where ϕ is a general scalar function of position $\boldsymbol{x}$. $\boldsymbol{x}_c$ is the centre point of each triangle element S'' and $\Delta S_{S''}$ is the area of the element. S'' is used to denote triangle elements on walls, to distinguish them from the basic elements S' on films. Note that, when $\boldsymbol{x}_c = \boldsymbol{x}_0$, namely the source point is right on the element over which the integral is calculated, the approximate integral value is zero, and thus this calculation is simply ignored in simulations [93].

The single-layer potential over each element on walls, in Eq. 5.16, may be also computed using Eq. 5.20, because the associated singularity has been removed. In the simulations, however, the nonsingular contour integral, Eq. 5.17, is used to compute the single-layer potential over each element on walls, because this ensures accurate solution of the boundary integral equation. The singularity-free form of the single-layer potential on walls is used in the numerical simulations, for its facilitating the programming.

The single-layer potential over foam films is also computed using the nonsingular contour inte-

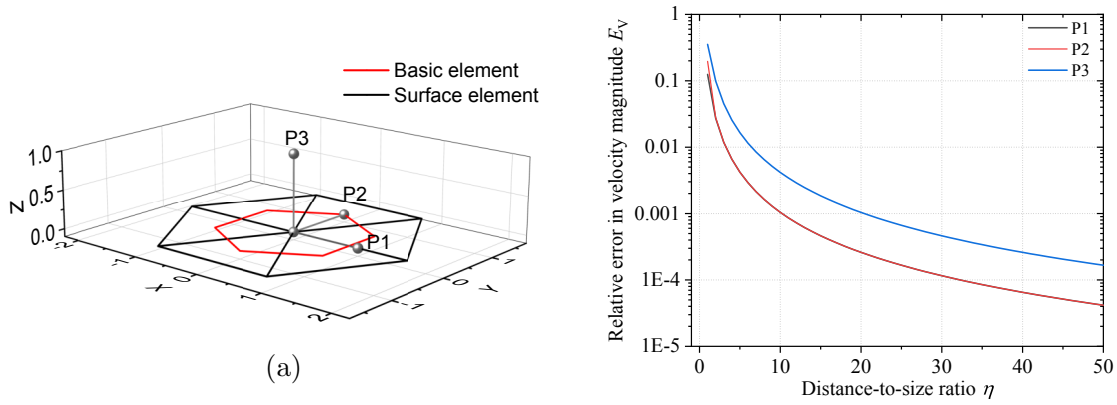


Figure 5.4: Comparison between the velocity magnitudes at given field points, computed using the nonsingular contour integral method and the one-point trapezoidal rule, respectively. (a) The velocity is induced by a flat basic element whose contour is a regular hexagon on the OXY plane and centred at the origin. The edge length of the basic element is set to unity. Despite its planar nature, the basic element is assumed to possess a unit mean curvature, i.e. assuming a unit normal stress on the basic element. The field points, P1, P2, and P3, are aligned with along X, Y, and Z axis, respectively. The distance of the field points to the origin changes from 1 to 50. (2) The relative error E_V of the velocity magnitudes calculated using the one-point trapezoidal rule, compared with the result by the nonsingular formula, is presented as a function of the ratio η between the distance from field point to the origin and the edge size of the basic element.

gral namely Eq. 5.17. The numerical calculation of the nonsingular contour integral has been explained in detail in the original work [100]. Note that, this nonsingular contour integral can be applied no matter the source point is close to or far from the basic element. When the source point is far from the basic element, the single-layer integral is nonsingular itself. In this case, the one-point trapezoidal rule similar to Eq. 5.20 is more favourable due to its lower computational cost compared with that of calculating the nonsingular contour integral [100].

To establish the proper criterion for identifying the source point as being significantly distant from a basic element, a regular hexagon basic element is considered. This element is located on OXY plane and centred at the origin. Despite the element's flat nature, its mean curvature is assumed to be unity, i.e. assuming a unit normal stress on the basic element. The velocities' magnitudes at field points positioned along the X, Y, and Z axes, induced by the basic element, are computed. Both the nonsingular contour integral method and the one-point trapezoidal rule are employed for this purpose. The outcomes obtained through the nonsingular formula serve as the exact solutions, against which the relative errors arising from the one-point trapezoidal rule is gauged.

The behaviour of these errors is illustrated in Figure 5.4, where the relative error E_v exhibits a reduction in value as η increases, where η is the ratio between the distance, from the field point to the central vertex of the basic element, and the edge size of the basic element. The results suggest that when the separation between the source point and the fundamental element surpasses 20 times the size of the basic element, the error introduced by the one-point trapezoidal rule remains below 0.1%.

5.3.4 Discrete linear system of equations

The unknown stress exerted by the wall on the fluid in the bubbles is normal to the wall and thus can be expressed as $q_i = qn_i$, as has been utilised in Eq. 5.15, where q is the magnitude of the unknown normal stress projected in the direction of the normal to be solved. The normal velocity of fluid on the wall is known to be the same as the normal velocity of the wall, while the two tangential velocity components are unknown.

To represent the two tangential velocities, the local unit normal vector $\boldsymbol{n}$ and the global unit normal vector $\boldsymbol{k}$ along Z axis are utilised to construct two unit tangential vectors $\boldsymbol{b}$ and $\boldsymbol{c}$, i.e. $\boldsymbol{b} = (\boldsymbol{n} \times \boldsymbol{k})/|\boldsymbol{n} \times \boldsymbol{k}|$ and $\boldsymbol{c} = (\boldsymbol{n} \times \boldsymbol{b})/|\boldsymbol{n} \times \boldsymbol{b}|$, where $\boldsymbol{n}$ is assumed to be unequal to $\boldsymbol{k}$; otherwise, $\boldsymbol{b}$ and $\boldsymbol{c}$ are simply set to the two unit vectors along X and Y axis, respectively.

Using the newly defined local unit tangential vectors, the velocity of fluid on the wall can be expressed as $\boldsymbol{u} = A\boldsymbol{n} + B\boldsymbol{b} + C\boldsymbol{c}$, where A, B and C are the magnitudes of the normal and two tangential velocity components. Note that the form of the equation can be simplified, though the current one is used for clarity. Using this decomposition and the numerical methods for computing the integrals as outlined earlier, the discrete form of Eq. 5.16 can be obtained

$$
\begin{aligned}
& v_j \Big(8\pi \big(B(\boldsymbol{x}_0) b_j(\boldsymbol{x}_0) + C(\boldsymbol{x}_0) c_j(\boldsymbol{x}_0) \big) \\
& + \sum_{\substack{s \\ \boldsymbol{x}_0 \notin S_s''}} (q(\boldsymbol{x}_c) n_i(\boldsymbol{x}_c) - q(\boldsymbol{x}_0) n_i(\boldsymbol{x}_c)) G_{ij}(\boldsymbol{x}_c, \boldsymbol{x}_0) \Delta S_s \\
& + \sum_{\substack{s \\ \boldsymbol{x}_0 \notin S_s''}} (B(\boldsymbol{x}_c) b_i(\boldsymbol{x}_c) - B(\boldsymbol{x}_0) b_i(\boldsymbol{x}_0)) T_{ijk}(\boldsymbol{x}_c, \boldsymbol{x}_0) n_k(\boldsymbol{x}_c) \Delta S_s \\
& + \sum_{\substack{s \\ \boldsymbol{x}_0 \notin S_s''}} (C(\boldsymbol{x}_c) c_i(\boldsymbol{x}_c) - C(\boldsymbol{x}_0) c_i(\boldsymbol{x}_0)) T_{ijk}(\boldsymbol{x}_c, \boldsymbol{x}_0) n_k(\boldsymbol{x}_c) \Delta S_s \Big) = v_j \Big(R_\mathrm{b} + R_\mathrm{i} + R_\mathrm{r} \Big),
\end{aligned}
\tag{5.21}
$$

with R_b, R_i, and R_r three source terms, defined as

$$
\begin{aligned}
R_\mathrm{b} &= 8\pi u_j^\infty(\boldsymbol{x}_0), \\
R_\mathrm{i} &= -8\pi A(\boldsymbol{x}_0) n_j(\boldsymbol{x}_0) - \sum_{\substack{s \\ \boldsymbol{x}_0 \notin S_s''}} (A(\boldsymbol{x}_c) n_i(\boldsymbol{x}_c) - A(\boldsymbol{x}_0) n_i(\boldsymbol{x}_0)) T_{ijk}(\boldsymbol{x}_c, \boldsymbol{x}_0) n_k(\boldsymbol{x}_c) \Delta S_s, \\
R_\mathrm{r} &= -\sum_l I_l,
\end{aligned}
\tag{5.22}
$$

where s denotes the wall and simultaneously serves as the index for each individual element S_s'' on the wall, and ΔS_s is the area of the triangle element S_s''. v_j is a unit vector, taken as

n_j, b_j and c_j, respectively. I_l is the contribution of the single-layer potential over the lth lamella or film and can be calculated using Eq. 5.17. In Eq. 5.21, a projection to three orthogonal directions has been conducted for the velocity u_j by an additional inner product with the unit vector v_j, which is found to result in a well-conditioned linear system.

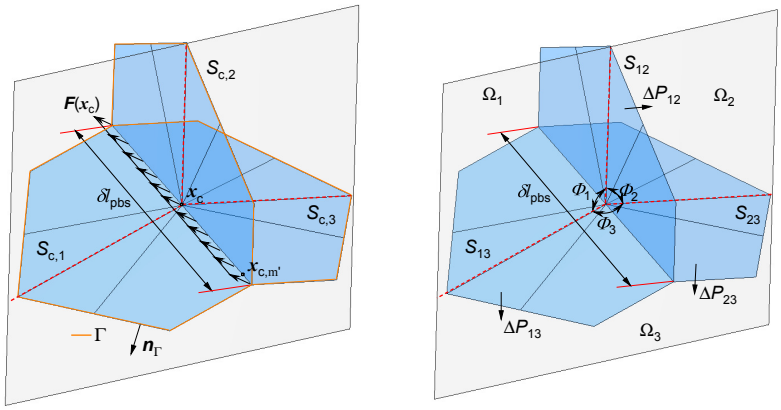
Eq. 5.21 illustrates that the motion of foam films results from a linear combination of three distinct movements: the background flow induced by R_b, the flow stemming from wall deformation caused by R_i, and the relaxation of the film induced by R_r. Consequently, the motion within a foam flow system can be deconstructed into three separate flow systems. These include the isolated background flow when foams or solid walls are absent, the exclusive wall deformation in the absence of both background flow and foams, and the foam relaxation exclusive of wall deformation and background flow.

Depending on whether the background flow or walls are present, this decomposition can be further simplified. For instance, two specific applications of the boundary integral method are explored in this chapter. The first application involves examining the evolution of a foam in a simple shear flow. In this context, the foam's motion comprises two elements: the background flow and the relaxation of the foam film. The second application centres on the motion of foam films within confined geometries, specifically within a diverging-converging channel. For this specific scenario, the foam's motion can be decomposed into two fundamental constituents: the flow induced by wall deformation and the relaxation of the foam film.

5.3.5 Motion of bulk Plateau borders

As detailed in Section 5.2.6, there exists a singular tension force exerted on bulk Plateau borders due to the departure from local equilibrium in the tension forces exerted by individual films. This singular tension force, operative on the bulk Plateau borders, shares the same dimensional characteristics as film tension, but its direction is perpendicular to the bulk Plateau borders. The disruption of local equilibrium arises from the shearing impact of the flow field, which imparts a dual influence on foam motion.

Firstly, the singular tension force acts to reinstate local equilibrium, resulting in 120-degree angles formed among the three films converging at a bulk Plateau border. Besides, the restoring motion of these bulk Plateau borders contributes to the overall motion of the remaining foam structure. To account for these dual effects, first address the estimation of the singular tension force acting on the bulk Plateau borders.



(a) (b)

Figure 5.5: Schematic diagram of three basic elements attached to a bulk Plateau border. The light grey reference plane is perpendicular to the Plateau border. (a) Reference for the method considering the singularity of the Plateau border's motion. The central vertex on the Plateau border is marked as $\boldsymbol{x}_c$, and the areas of its three adjacent basic elements are denoted as $S_{c,1}$, $S_{c,2}$, and $S_{c,3}$, respectively. The length of the Plateau border is denoted as δl_{pbs}. A singular force, uniformly distributed along the Plateau border, is represented as $\boldsymbol{F}(\boldsymbol{x}_c)$. The contour Γ, encompassing the combination of the three basic elements, is highlighted in orange. Its outward unit normal vector is denoted as $\boldsymbol{n}_\Gamma$. (b) Reference for the method involving the equivalent capillary pressure. The space is divided into three domains, denoted as Ω_1, Ω_2, and Ω_3. The angles formed between each pair of the basic elements in $\{\Omega\}_{i=1}^3$ are indicated as $\{\Phi\}_{i=1}^3$. In contrast to (a), the areas of the three basic elements are now referred to as S_{12}, S_{23}, and S_{13}, respectively. The equivalent capillary pressures for the three films are denoted as ΔP_{13}, ΔP_{12}, and ΔP_{23}, respectively.

The evaluation of the total tension force exerted on a basic element is achieved through the contour integral, Eq. 5.19, conducted around a vertex $\boldsymbol{x}_c$. Similarly, by computing this contour integral across all basic elements associated with a vertex situated along the bulk Plateau borders, the resulting vector encapsulates the overall tension forces affecting these interconnected basic elements. It comprises two constituents of film tension forces: the component normal to each individual basic element and the singular tension force along the bulk Plateau borders. As a result, the singular tension force at the vertex $\boldsymbol{x}_c$ on the Plateau border, denoted as $\boldsymbol{F}(\boldsymbol{x}_c)$, can be evaluated as

$$\boldsymbol{F}(\boldsymbol{x}_c) \approx \frac{1}{\delta l_{bps}}\Big(\oint \boldsymbol{n}_\Gamma d\Gamma - \sum_{m=1}^{M} \Delta S_{c,m} k(\boldsymbol{x}_{c,m}) \boldsymbol{n}(\boldsymbol{x}_{c,m}) \Big), \tag{5.23}$$

where the contour Γ refers to that of the combination of three basic element around an interior vertex on bulk Plateau borders or four basic elements around a four-fold node. δl_{bps} is the short length of the bulk Plateau border encompassed by the combination of the basic elements. M is the number of neighbouring basic elements, either 3 or 4, depending on the vertex $\boldsymbol{x}_c$ lies within the interior of the bulk Plateau borders or at their termination points. For the latter, the vertex precisely corresponds to a four-fold node. m is the index of the basic element at the vertex $\boldsymbol{x}_c$.

With the singular film tension force $\boldsymbol{F}(\boldsymbol{x}_c)$, the effects of the singular force on bulk Plateau borders are modelled as follows. The restoring motion of bulk Plateau borders, as well as the four-fold nodes, is achieved by a series of iteration using the computed $\boldsymbol{F}(\boldsymbol{x}_c)$ that is updated at each iteration step. For each step of iteration, each vertex $\boldsymbol{x}_c$ on bulk Plateau border is moved by a small displacement $\psi \boldsymbol{F}(\boldsymbol{x}_c)$, where ψ is small factor stabilising the iteration process. Notably, all other vertices, except for those on bulk Plateau borders, are fixed during the iteration process.

On the other hand, the effect of the motion of bulk Plateau borders on the remaining part of the foam is modelled by considering the velocity induced by the singular film tension force on bulk Plateau borders. The value of singular film tension force is set to the initial value for the restoring motion. the multiple-point trapezoidal rule is used to compute the singular film tension force-induced velocity at a source point $\boldsymbol{x}_0$ that is not located on the Plateau borders

$$u_j(\boldsymbol{x}_0) \approx \frac{\delta l_{bps} F_j(\boldsymbol{x}_{c,m'})}{M'} \sum_{m'=1}^{M'} G_{ij}(\boldsymbol{x}_{c,m'}, \boldsymbol{x}_0), \tag{5.24}$$

where each short bulk Plateau border segment of length δl_{bps} is divided into M' uniform segments. m' is the index for each segment. $\boldsymbol{x}_{c,m'}$ refers to the centre point of each short segment. $F_j(\boldsymbol{x}_{c,m'})$ remains equal to $F_j(\boldsymbol{x}_c)$ that has been computed using Eq. 5.23.

As mentioned in Section 5.2.6, another method that can be used to handle the motion of Plateau border, as outlined in [128], employs the concept of an equivalent capillary pressure. The implementation of this method is explained as follows. The equilibrium of three forces in the vicinity of a bulk Plateau border is illustrated in Figure 5.5 (b). The equivalent capillary pressure, referred to as ΔP_{eq}, acting on each basic element, is determined by various factors, including the length of the bulk Plateau border (δl_{bps}), the angles formed between each pair of basic elements ($\{\Phi_i\}_{i=1}^3$), and the areas of the individual basic elements, specifically S_{12}, S_{23}, and S_{13}. According to the findings in [128], the equivalent pressure can be computed as

$$\Delta P_{ij} = \frac{\delta l_{bps}}{2S_{ij}}\big(\cot(\frac{\Phi_i}{2}) - \cot(\frac{\Phi_j}{2})\big), \tag{5.25}$$

where ΔP_{ij} $(i \neq j)$, in the specific case illustrated in Figure 5.5 (b), is the equivalent capillary pressure ΔP_{eq} across the film separating domain Ω_i and Ω_j. S_{ij} denotes the area of the basic element between Ω_i and Ω_j. $\{\Phi_i\}_{i=1}^3$ refer to the angles formed between basic elements in domain $\{\Omega_i\}_{i=1}^3$.

Accordingly, an equivalent mean curvature denoted as k_{eq} can be defined, where $k_{\text{eq}} = 0.5\,\Delta P_{\text{eq}}$. The sign of k_{eq}, which can be either 1 or -1, should be reversed if the default orientation across the film, as illustrated in Figure 5.5 (b), does not align with the normal vector specified in Eq. 5.13. Substituting k in Eq. 5.13 with $k + k_{\text{eq}}$ allows the resulting equation to be employed at any point within the flow field. It is important to note that k_{eq} should be set to zero when the integration concerns interior basic elements on films.

When working with basic elements situated at four-fold vertices, the two approaches mentioned earlier can be easily extended and applied. It is important to observe that in the approach addressing the singular motion of bulk Plateau border, the singular force should be concentrated at a four-fold node. In the alternative method involving equivalent capillary pressure, each basic element surrounding a four-fold node connects to two pairs of basic elements, as opposed to just one pair (e.g. in Figure 5.5 (b)).

5.3.6 Evolution of the foam configuration

After solving the velocities at vertices on foam films, the foam configuration is evolved by a first-order ordinary differential equation named the kinematic equation, i.e. $d\boldsymbol{x}/dt = \boldsymbol{u}(\boldsymbol{x})$, where $\boldsymbol{x}$ is the position of a vertex on films. Using the forward Euler method, the kinematic equation can be approximated as $\boldsymbol{x}^{h+1} - \boldsymbol{x}^{h} = \boldsymbol{u}^{h}(\boldsymbol{x})\Delta t$, where h and $h+1$ denote the current and next moments of time, respectively, and Δt is the time step. Note that in the first method for modelling the effect of singular forces on bulk Plateau borders, i.e. treating the bulk Plateau border motion as singular, the positions of vertices on bulk Plateau borders are adjusted via the restoring motion.

5.4 Numerical results

This section presents the numerical results of applying the boundary integral equation for dry foam in two distinct scenarios. These scenarios are outlined in Table 5.1, which provides information about the geometric elements involved and the simulation platforms employed in each specific application.

Table 5.1: Two applications of the boundary integral method for dry foam

Application	Geometric element	Simulation platform
Five-bubble foam in a simple shear flow	BF BN BP	Surface Evolver
Foam film in a diverging-converging channel	BF CF WP	Visual Studio 19.0 (C++)

5.4.1 Foam evolving in a simple shear flow

Foam deformation in a simple shear flow is considered in this section to exemplify the application of the method proposed in this work to dry foams in bulk. Particularly, a foam comprising five bubbles is considered, as depicted in Figure 5.6. These bubbles consist of three larger ones, each with a volume of 0.2, positioned centrally and dividing in opposing directions two smaller bubbles with volumes of 0.1. The initial configuration of the foam is established in a state of

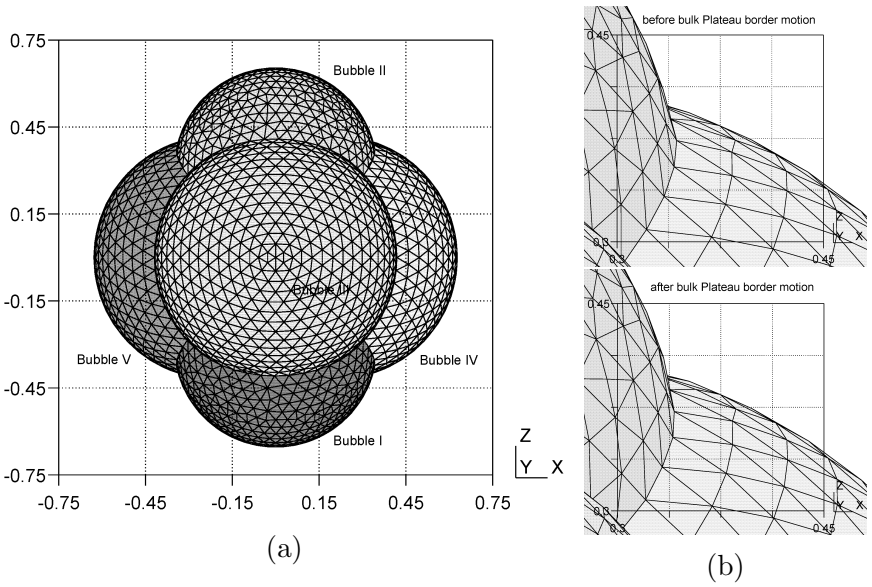
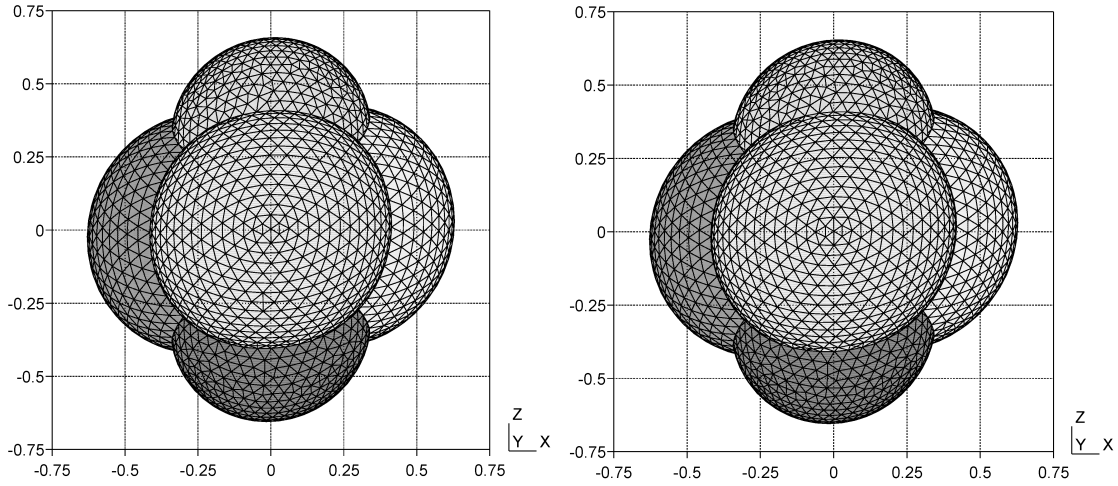


Figure 5.6: The initial equilibrium configuration of a five-bubble foam. (a) The initial foam composed of five bubbles was generated by minimising surface energy, using Surface Evolver. These bubbles are designated as I to V, with Bubble I and II having a volume of 0.1, while the remaining bubbles possess a volume of 0.2. The foam exhibits symmetry across the OYZ plane. (b) The enlarged illustrations display the vicinity of the bulk Plateau borders both before (top) and after (bottom) repositioning them to establish a local equilibrium among the three film tension forces.

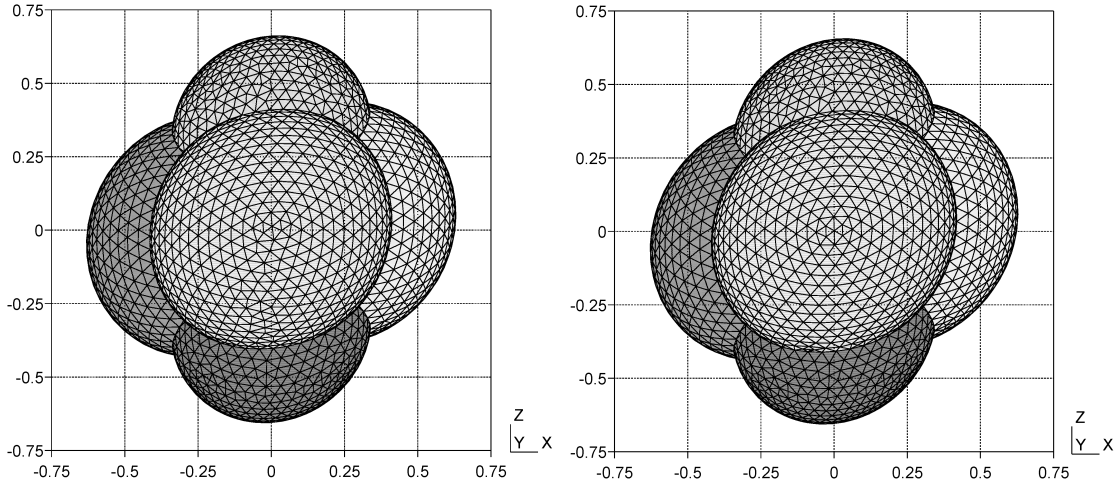
stationary equilibrium, achieved through the minimisation of surface energy utilising Surface Evolver [87]. This initial foam formation exhibits symmetry with respect to the OYZ plane, and the alignment of the Z-axis coincides with the centres of the two smaller bubbles. Figure 5.6 also shows the change in foam configuration after the singular motion of bulk Plateau borders.

A simple shear flow, $\boldsymbol{u}_0(x, y, z) = [0.0, 0.0, 0.1x]$, is imposed. The boundary-integral simulations of the foam evolving in the simple shear flow are conducted in Surface Evolver, where the associated mean curvature is computed using the contour integral method. The time step ΔT is fixed to 0.01, and the elements size ΔX is kept within 0.040 to 0.090 in the simulations.

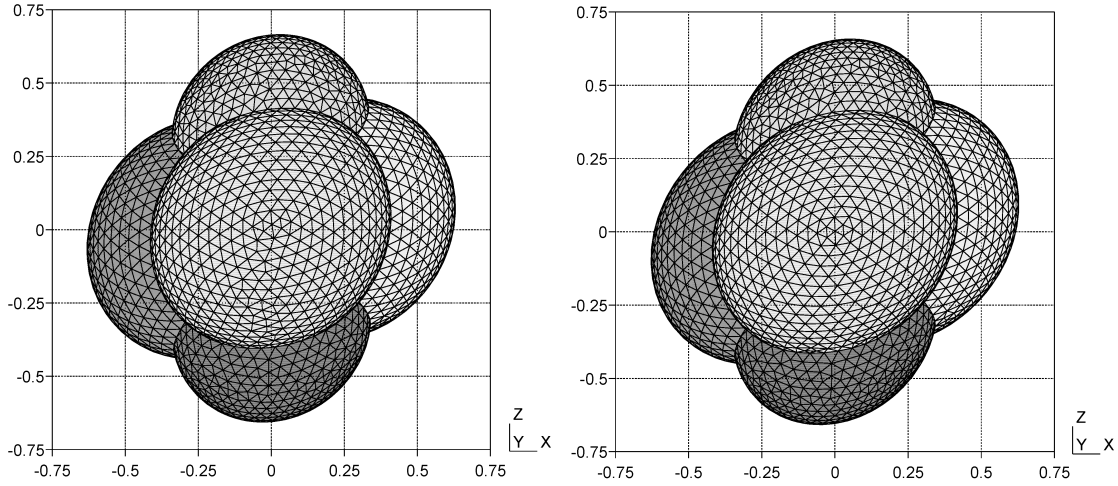
Figure 5.7 presents the dynamic motion of the foam at $Ca = 1.0$. The foam deforms under the imposed strains by the shear flow, while attempting to restore the minimal surface due to the film tension. Therefore, the evolution of the foam configuration is in contrast to the result at $Ca \to \infty$ namely at zero film tension, where the foam configuration is purely advected by the background shear flow. Note that the impact of the motion of the bulk Plateau border has been considered in the simulations, which is important to limit the errors in bubble volumes.



(a) $Ca = 1.0,\ T = 0.5$ (b) $Ca \to \infty,\ T = 0.5$



(c) $Ca = 1.0,\ T = 1.0$ (d) $Ca \to \infty,\ T = 1.0$



(e) $Ca = 1.0,\ T = 1.5$ (f) $Ca \to \infty,\ T = 1.5$

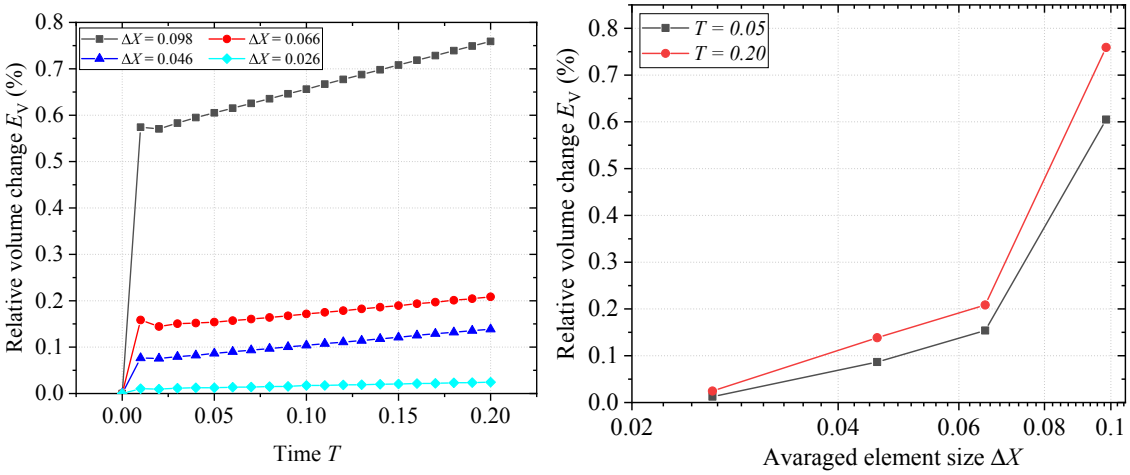
Figure 5.7: The evolution of the five-bubble foam in a simple shear flow. The left column shows results at time $T = 0.5$, 1.0, and 1.5, where Ca is set to unity. The right column shows the pure advection of the foam, namely Ca tends to infinity. At finite Ca, the surface tension tends to minimise the surface energy and maintain the shape of the foam. The difference in foam configuration between the two cases will become increasingly drastic with time.

During the simulations, close attention is paid to the bubble volumes, which must adhere to the principle of mass conservation. However, owing to discretisation errors and, notably, the additional motion introduced to maintain force equilibrium at the bulk Plateau borders, a gradual accumulation of discrepancies in bubble volumes is observed over time. The subsequent section focuses on investigating the impact of bulk Plateau border motion on bubble volume conservation. To achieve this, two distinct sets of numerical experiments, denoted as Group 1 and Group 2, are conducted.

In Group 1, the influence of bulk Plateau border motion on foam film dynamics is excluded, whereas this effect is incorporated in Group 2. Each group encompasses four varying ranges of element sizes, specifically $\Delta X \in [0.0178, 0.04]$, $[0.0267, 0.06]$, $[0.044, 0.099]$, and $[0.06, 0.135]$. Within each simulation belonging to the four cases in each group, continuous monitoring of bubble volumes occurs throughout the time interval T from 0 to 0.2.

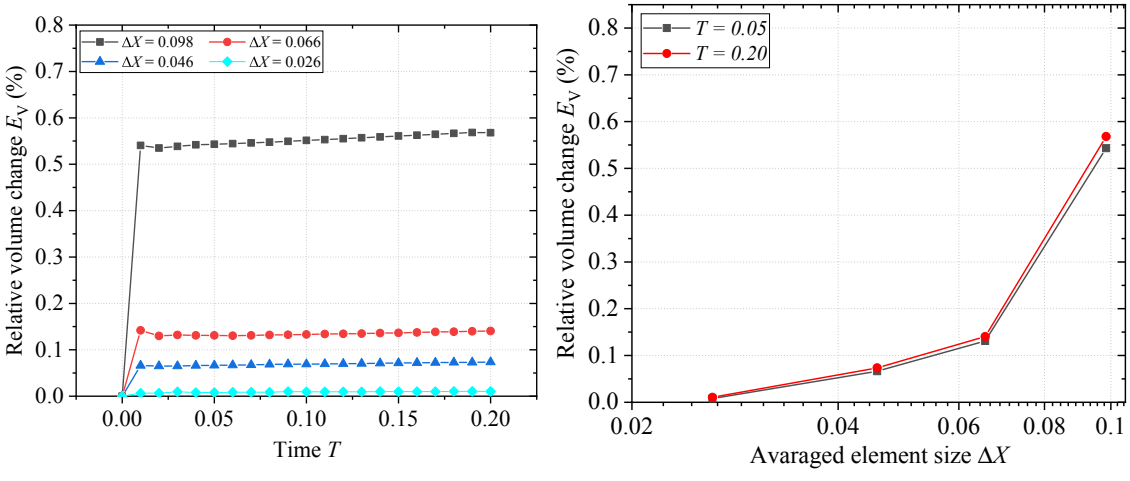
Since the volume deviation over time exhibits a similar trend for each bubble, only the findings concerning bubble V are presented hereafter. In Figure 5.8 (a), which corresponds to Group 1, the temporal evolution of bubble volume deviation, characterised by the absolute magnitude of the relative change in actual volume relative to the initial value of 0.2, is displayed with the average element size serving as the parameter. The average element size remains relatively stable throughout the simulations, measuring 0.026, 0.046, 0.066, and 0.098 for the respective element size ranges. Figure 5.8 (b) illustrates the variation in bubble V's volume concerning the average element size, with time as the parameter. The outcomes for Group 2 are depicted in Figure 5.9.

In both Figure 5.8 and 5.9, an abrupt escalation in error is observed at the initial time point, which can be explained as follows. Initially, the force distribution in the foam configuration, as predicted by Surface Evolver, lacks optimal balance. This discrepancy arises because the surface energy minimisation algorithm in Surface Evolver assumes that the film tension force of a vertex's basic element acts precisely on the vertex. However, for vertices situated on the bulk Plateau borders, the applied force encompasses not only the film tension force tangential to the vertex's basic element along the Plateau borders but also includes a component normal



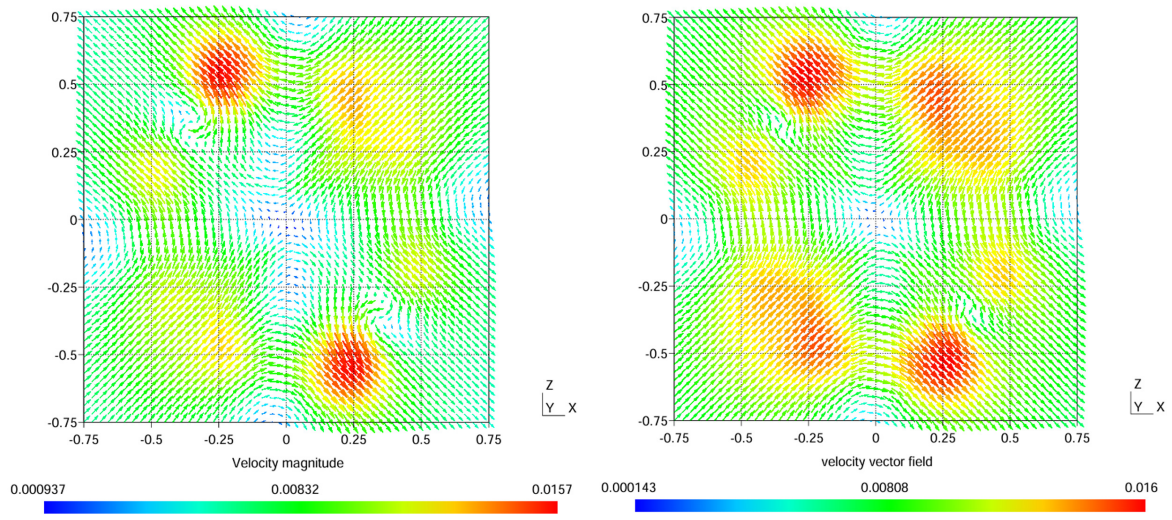
(a) (b)

Figure 5.8: The change in volume of bubble V during simulations excluding the effect of the motion of bulk Plateau borders on the motion of the remaining part of the foam. (a) The evolution of Bubble V's volume over time is showcased for four average element sizes, specifically $\Delta X = 0.098$, 0.066, 0.046, and 0.026. (b) The variation in Bubble V's volume is explored concerning the average element size. Comparisons of volumes are made at two distinct time instances: $T = 0.05$ and 0.20, respectively.



(a) (b)

Figure 5.9: The change in volume of bubble V during simulations incorporating the effect of the motion of bulk Plateau borders on the motion of the remaining part of the foam. (a) The evolution of Bubble V's volume over time is showcased for four average element sizes, specifically $\Delta X = 0.098$, 0.066, 0.046, and 0.026. (b) The variation in Bubble V's volume is explored concerning the average element size. Comparisons of volumes are made at two distinct time instances: $T = 0.05$ and 0.20, respectively.



(a) (b)

Figure 5.10: Vector field of velocity within the $y = 0$ plane. (a) Result by the method involving the singular motion of the Plateau border. (b) Result obtained through the method utilising the equivalent capillary pressure.

to the basic element, as suggested in a more complex scenario shown in Figure 5.5(a). For this reason, the initial evolution driven by the motion of bulk Plateau borders to establish force equilibrium leads to a relatively large variation in bubble volumes.

From Figure 5.8 and 5.9, it can also be observed that the initial abrupt volume deviation is alleviated as the averaged element size deceases, because the displacement of bulk Plateau borders during its motion decreases with the decreasing of the averaged element size. After the initial sharp increment of error in bubble volume, the error still accumulates with time. However, the accumulation of the error also becomes slower as the averaged element size decreases.

Notably, by comparing Figure 5.8 and 5.9, it can be found that the incorporation of the effect of the motion of bulk Plateau borders on the motion of the rest part of foam is found to be rather important in terms of conserving bubble volumes. The error accumulation rate with time at a given averaged element size decreases by an order of magnitude in Group 2 which involves the effect, than in Group 1 excluding the effect.

In the above numerical tests, the element size is roughly uniform throughout the foam during simulations. This approach leads to a rapid escalation in the foam's element number as the element size decreases, though reducing the element size proves advantageous for minimising

errors in volume conservation. Furthermore, the computational expenditure experiences a significant rise with an increase in the number of elements, given that the computational cost typically follows a quadratic scaling in relation to the element number within the framework of the boundary integral method.

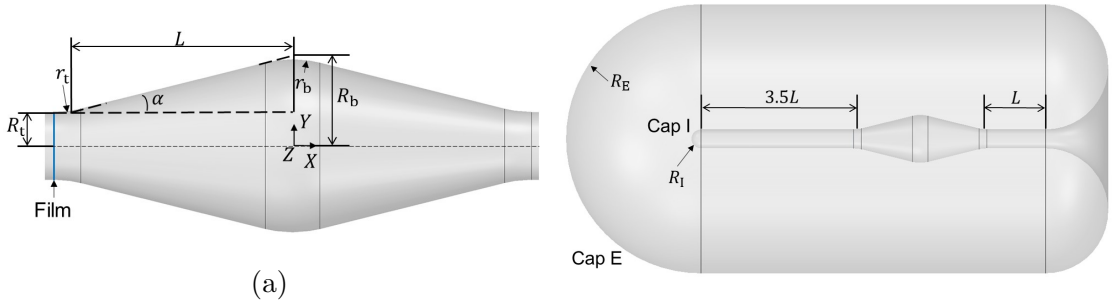
A more effective approach to representing foam configurations could involve the adoption of a non-uniform mesh. This scheme would entail refining the mesh in the vicinity of Plateau borders while maintaining coarser elements in other regions, thereby reducing the overall element number in simulations.

In the subsequent part of this section, the other method accounting for the singular forces on bulk Plateau borders, i.e. Eq. 5.25, is evaluated by examining a scenario in which the initial state is considered as the foam configuration shown in Figure 5.7 (d), employing a finer mesh with element sizes within the range of [0.0178, 0.04]. The foam is then allowed to relax in the absence of background flow. The velocity field within the plane at $y = 0$, passing through the geometric center of the foam configuration, is calculated utilising Eq. 5.25 for the basic elements situated on the film borders.

For comparison, the result of velocity field by the method where the movement of the bulk Plateau border is treated as singular is also presented. In this case, the position of the bulk Plateau border is adjusted, following the procedure outlined in Section 5.3.5, so that the angles between films at Plateau borders and between Plateau borders at nodes return to their static values. Subsequently, Eq. 5.16 is employed to compute the velocity field within the same region. The obtained results are presented in Figure 5.10. It is evident that both methods yield similar patterns in the distribution of velocity, encompassing both the direction and magnitude of the velocity.

5.4.2 Film motion in a diverging-converging channel

For foam flow in porous media, the geometry of flow channels plays an important role in determining foam's special properties, such as the yield stress that is reflected by the minimum



(a) (b)

Figure 5.11: Geometries of a foam film in a diverging-converging channel, in the context of the boundary integral method. (a) Geometry of the diverging-converging channel. Several dimensions are fixed, including $L = 2.0$, $R_t = 0.3$, $r_b = 0.35$ and $r_t = 1.0$, in the simulations. Other dimensions, including α and R_b, are not independent, and are related through $R_b = R_t + L\tan\alpha$. α is one half of the diverging angle of the channel. The initial position of the film is at the inlet of the pore, marked by the blue line segment. (b) The channel wall is extended to a complete enclosed surface built for boundary-integral simulations. Two hemispherical caps on the left side of the surface are denoted by Cap I and Cap E, respectively. The radius of Cap I equals the radius of the inlet of the pore, i.e. $R_{\mathrm{I}} = 0.3$. The radius of Cap E is set to $R_{\mathrm{E}} = 4.3$.

pressure gradient required to initiate foam motion in porous media. To characterise foam flow in porous media, a typical scenario considered in literature is the motion of a single film in a diverging-converging channel or pore [66, 59]. The diverging-converging channel refers to a channel consisting of two sections, one diverging section connected to the converging section through the corner in the central pore body. A single foam film moves from one side of the channel, called the inlet port, to the other side namely the outlet port, during which the film behaviour is confined by the varying cross-sectional channel and affected by the capillary number Ca.

To explore this scenario within the framework of the boundary integral method outlined in this study, the initial step involves extending the channel surface into a complete closed surface characterised by a smoothly varying unit normal vector across its entirety, as shown in Figure 5.11. The displacement of the film, initially situated at the channel inlet, is initiated through the deformation of the channel surface. This deformation specifically corresponds to the rightward motion of Cap I in Figure 5.11. The dimensionless velocity of Cap I is denoted as U, which exactly equals unity as the actual velocity of Cap I is selected as the characteristic velocity. In order to the maintain the volume of the space enclosed by the surface, the large hemispherical

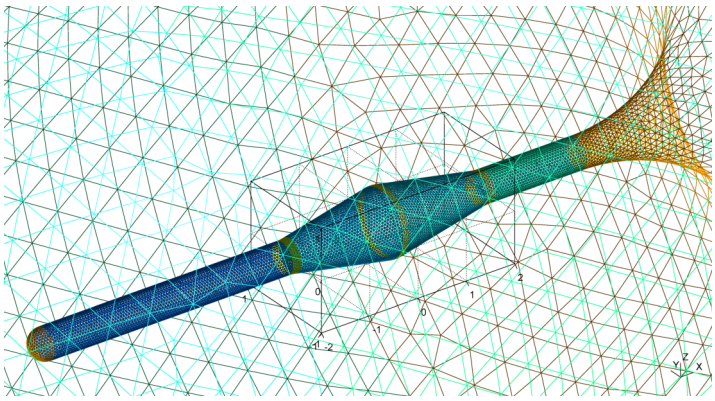


Figure 5.12: Triangulated wall surface, with a mesh configuration that exhibits finer elements within the inner region of the wall surface, transitioning to coarser elements on the outer side. The entirety of this mesh comprises a total of 28642 triangle elements.

surface, denoted as Cap E, also undergoes rightward movement. However, this motion occurs at a relatively reduced velocity of $R_{\mathrm{I}}^2/R_{\mathrm{E}}^2$, where R_{I} and R_{E} signify the radii of Cap I and Cap E, respectively.

As indicated in Eq. 5.21 and mentioned in Section 5.3.4, the film's movement in this context comprises two distinct components originating from R_{i} and R_{r}. The investigation begins by examining the induced flow resulting from the deformation of the wall, followed by an analysis of the film's relaxation motion within the channel. It is important to note that this study does not attempt a comprehensive parameter analysis of the problem.

Imposed flow field due to wall deformation

The imposed flow plays a key role in the foam film motion since it acts to deviate the foam film away from the equilibrium status, which further induces the film relaxation and its interaction with the imposed flow. The imposed flow is independent of the film presence, and thus is a constant steady flow in the channel. For this reason, in simulations of film motion in the channel, the imposed flow only needs to be solved once, and, at each moment of time, the imposed component of the velocity at each field point can be simply evaluated through interpolation.

Consider the diverging-converging pore, whose diverging angle is set to 20 degrees and α is set to 10 degrees accordingly. In the simulation, the imposed flow in the pore happens because of the deformation of the wall surface. The boundary of the solid particle is triangulated into

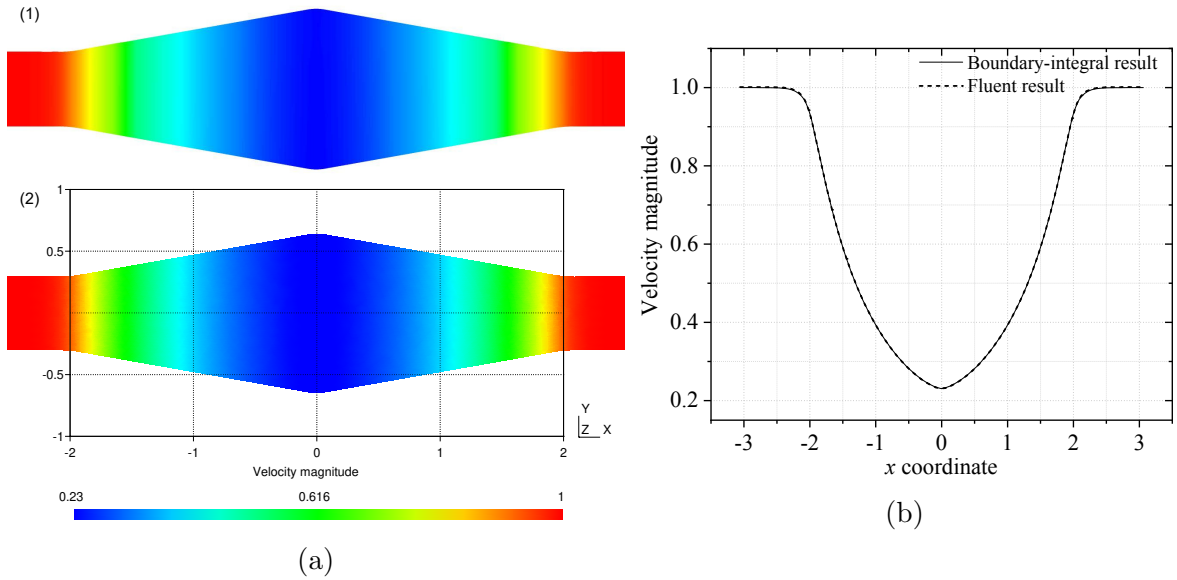


Figure 5.13: Comparison between the results of the imposed flow by the boundary integral method and the finite volume method. (a) Comparison of the results of the velocity magnitude on the channel surface by (1) the finite volume method and (2) the boundary integral method. (b) Quantitative comparison of the velocities along the intersection curve of the OXY plane and the channel surface by the two methods.

discrete elements, shown in Figure 5.12, using GMSH [132], an open-source mesh generator. Mesh independence study suggested that the numerical results are less sensitive to the element size of the outer surface than that of the inner surface. The current selection of the mean element size for the inner surface set in GMSH is 0.05 which is fine sufficiently to ensure mesh-independent results. With the triangulated wall surface, coefficients and sources terms in Eq. 5.21 can be computed, which is then solved using GMRES with restart [133].

For comparison, the imposed flow is also predicted using the finite volume method (FVM) in Fluent, a commercial software package. In this method, the Navier-Stokes equations for incompressible fluid are solved in a 3D fluid domain, where the inertial term is incorporated. In order to reproduce behaviour of fluid in Stokes flow or diminish the inertial effect, the Reynolds number of the problem is set to 3.0×10^{-4}, much less than unity. Boundary conditions set in Fluent include: uniform unity velocity at the inlet, zero pressure at the outlet, and slip boundary condition (zero tangent projection of the stress tension) at pore surface.

The numerical results of the velocity magnitude on the pore surface and its intersection with OXY plane, computed using the boundary-integral model and the FVM, are compared in

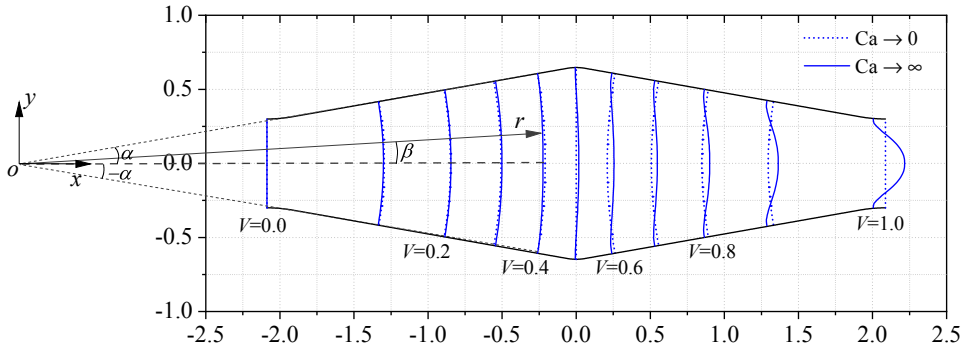


Figure 5.14: Film advection by the imposed flow, in contrast to the quasi-static film motion. From the left to the right side, the film profiles correspond to the swept volume 0.0, 0.1, $\cdots$, 1.0, respectively, with a constant volume gap 0.1. The volume is normalised by the pore volume namely the volume of the space between the inlet and the outlet. An auxiliary coordinate system oxy is established, based on which the polar coordinates β and r are defined. The film profile can be represented using x as a function of y, for the calculation of the mean curvature of the film. Furthermore, the mean curvature of the film can be depicted as a function of the the polar coordinate β.

Figure 5.13, and show good agreement. It can be found that the velocity decreases along the flow direction in the diverging section of the pore, while increasing in the converging section of the pore, due to the mass conservation of the flow field.

Advection of film by the imposed flow

With the known imposed flow field solved in the last section, the pure advection of the film by the imposed flow, corresponding to the film behaviour at Ca tending to infinity, can be simulated. A series of film profiles on the OXY plane are shown in Figure 5.14. For comparison, at Ca tending to zero, the quasi-static motion of the film in the same pore is also presented. It can be found that, as the film transverses in the pore, the film configurations gradually deviate from those in quasi-static motion. This deviation becomes noticeable when the film arrives in the converging section of the pore, that the film is mainly convex towards downstream, in the opposite to the orientation of quasi-static film profiles in the converging section. This is because in the converging section the leading edge of the $Ca \to \infty$ film is running ahead into a region where the advection is even faster than further upstream. Consequently, there is a net increment of the film area after the film sweeps one pore volume.

For finite Ca numbers, the film profiles exhibit deviations from both those resulting purely from

film advection and those seen in quasi-static states. Nonetheless, practical Ca values can often be quite small [134], implying that film profiles during motion might closely resemble those in quasi-static conditions. Within this context, the deformation of the film shape occurring within the diverging section of the pore could provide a more accurate characterisation of the film's actual deformation behaviour. Subsequent to the deformation initiated by film advection due to the imposed flow, immediate film relaxation takes place as the film configuration diverges from its equilibrium state.

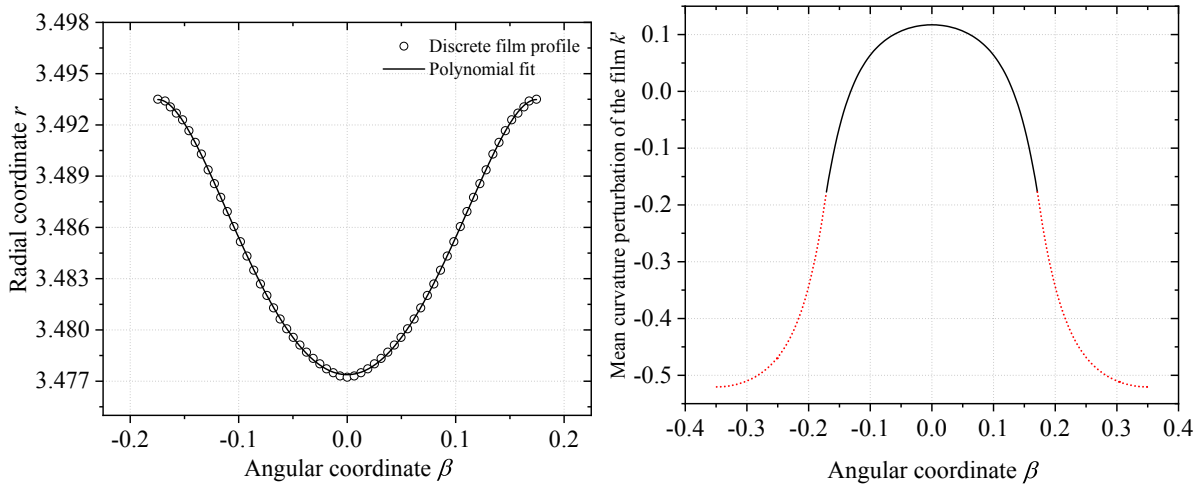
To illustrate the perturbation effect induced by the imposed flow on the film's shape, the film configuration corresponding to the swept volume $V = 0.4$ is examined, as indicated in Figure 5.14. This choice is motivated by the film's location within the diverging section of the pore, where the configuration closely approximates the equilibrium state while the accumulated strain on the film has reached a sufficient level. The film's position is denoted using a Cartesian coordinate system oxy as referenced in Figure 5.14, and this system is employed in the computation of the film's mean curvature. It is important to clarify that the mean curvature of the film does not equate to the curvature of the 2D film profile.

In Figure 5.15 (a), discrete vertex positions on the film profile are depicted, with the film profile being approximated through a polynomial fit. Since adding or subtracting a constant from the film's mean curvature does not affect the velocity field (derived from Eq. 5.16 and 5.17), the concept of the perturbation of the film's mean curvature is introduced, denoted as k'. This perturbation is defined as the actual value of the film's mean curvature k, subtracted by the area-weighted mean curvature of the film

$$k'(\boldsymbol{x}) = k(\boldsymbol{x}) - \frac{1}{\Delta S_{\text{film}}} \int_{\text{film}} k dS(\boldsymbol{x}), \tag{5.26}$$

where $\boldsymbol{x}$ denotes the position of vertices on the film, and ΔS_{film} is the film area. Eq. 5.26 is subsequently applied to the polynomial fit in Figure 5.15 (a). The perturbation of the film's mean curvature is illustrated in Figure 5.15 (b).

Furthermore, the fast Fourier transform (know as FFT) is performed for this perturbation



(a) (b)

Figure 5.15: The mean curvature perturbation of the film, computed with the polynomial fit of the film profile, the swept volume of which is 0.4, normalised using the pore volume. (a) The lamella profile is depicted utilising the radial coordinate r in relation to the angular coordinate β. The original discrete data corresponding to various vertices on the film is subject to polynomial fitting, enabling the computation of the mean curvature of film. Both radial and angular coordinates are established within a Cartesian coordinate system, where the y axis aligns with the pore axis, as indicated in Figure 5.14. (b) The perturbation of the mean curvature of film, k', is represented as a function of the angular coordinate β varying from $-\alpha$ to α, where $\alpha = \pi/18$. The curve is then extended to a full period (4α), shown by the dotted sections in red.

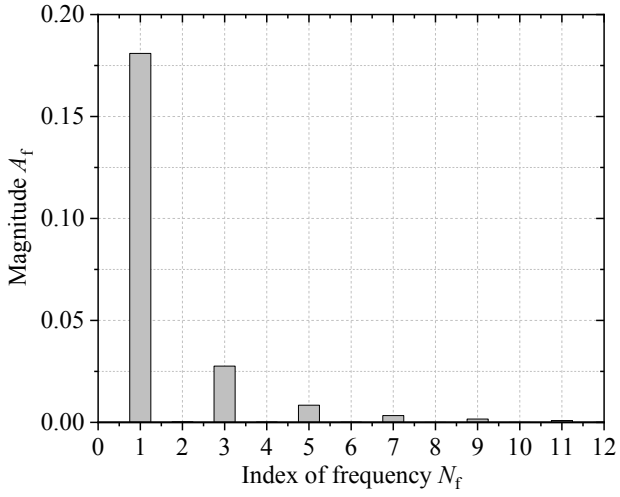


Figure 5.16: The perturbation of the film's mean curvature is analysed through Fourier expansion. The first-frequency component emerges as the prominent element within the curvature perturbation. This primary component aligns with a cosine-wave perturbation characterised by a wavelength identical to twice the length of the film profile.

(extended curve in Figure 5.15) with respect to the polar coordinate β. The sample interval is $\Delta\beta = \alpha/250$, and thus 1001 sample points are extracted from Figure 5.15(b). The magnitude of each frequency resulted from this Fourier expansion is presented in Figure 5.16. Notably, the dominant component of the mean curvature perturbation corresponds to the first-frequency component that is a cosine-wave perturbation characterised by a wavelength identical to twice the length of film profile. The magnitudes of even-order frequency components are sufficiently lower than those of odd-order ones, and for odd-order frequency components the magnitude decreases as the frequency increases. Particularly, the magnitude of the dominant component, i.e. the first frequency, greatly exceeds others. This observation implies that the relationship between film relaxation-induced velocity and the mean curvature of film in the film's motion is primarily influenced by the first-frequency mean curvature perturbation-induced flow.

Film motion under perturbed curvature

This section focuses on examining how the film responds to the mean curvature perturbation due to the imposed flow, where the capillary number Ca is set to unity. Given that the film's mean curvature serves as a linear source term in determining the flow field, as indicated in Eq. 5.16, the velocity arising from film relaxation can be expressed as a summation of velocities induced by individual frequency components derived from the Fourier expansion of the film's mean curvature perturbation. The mean curvature perturbation's frequency components, denoted as $\{k'_{N_\mathrm{f}}\}_{N_\mathrm{f}=1}^{\infty}$, can be expressed as

$$k'_{N_\mathrm{f}} = I A_\mathrm{f} \cos\Big(\frac{N_\mathrm{f}\pi\beta}{2\alpha}\Big), \tag{5.27}$$

where I is either 1 or -1, A_f represents the magnitude of each film mean curvature perturbation component resulted by FFT, and N_f is the index of frequency. Notably, owing to the inherent linearity of the boundary integral method, the value of A_f solely influences the scaling of the resultant velocity magnitude, without altering the fundamental characteristics of the relationship between the film relaxation-induced velocity and the film's mean curvature. Sub-

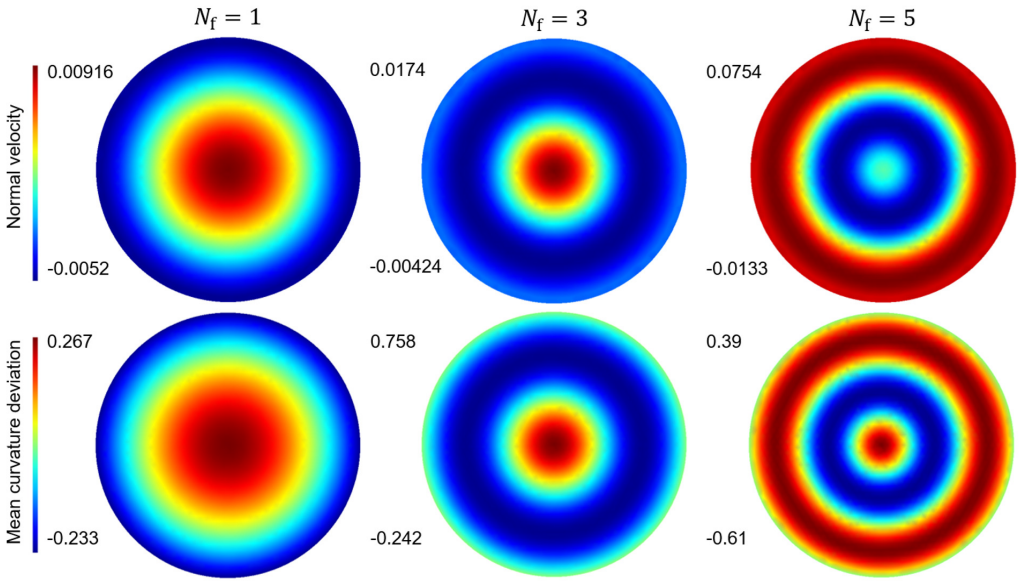


Figure 5.17: The first-, third-, and fifth-frequency (left to right) curvature perturbation-induced film normal velocity (top), and the distribution of the mean curvature deviation (bottom).

sequently, IA_f is fixed to unity, and the velocity induced by film relaxation is explored. Three odd-frequency components are considered, including $N_f = 1$, 3, and 5, for their relatively large actual magnitude.

These perturbation components of mean curvature are introduced to the film in an equilibrium state, with its horizontal position characterised by the X-coordinate of the Plateau border, which varies within the channel. Several distinct horizontal positions are tested, revealing a similar pattern in the relationship between the film velocity, particularly its normal component, and the deviation in mean curvature. Here, the term "mean curvature deviation" refers to the result obtained by substituting Eq. 5.27 into Eq. 5.26. As an example, the results of the case where the film intersects with the X-axis at x = -0.5 L (referring Figure 5.11(a) for the origin of X-axis) are presented. Figure 5.17 shows the mean curvature deviation on the film surface and the normal component of the induced velocity, for $N_f = 1$, 3, and 5. Figure 5.18 presents the normal velocity component as functions of the mean curvature deviation.

Figure 5.17 and 5.18 illustrates that the film motion induced by the first-frequency mean curvature perturbation results in a one-to-one mapping relation between the local mean curvature deviation and the local normal velocity. In contrast, the relationship between local mean curvature deviation and normal velocity becomes more intricate at higher frequencies, as a single

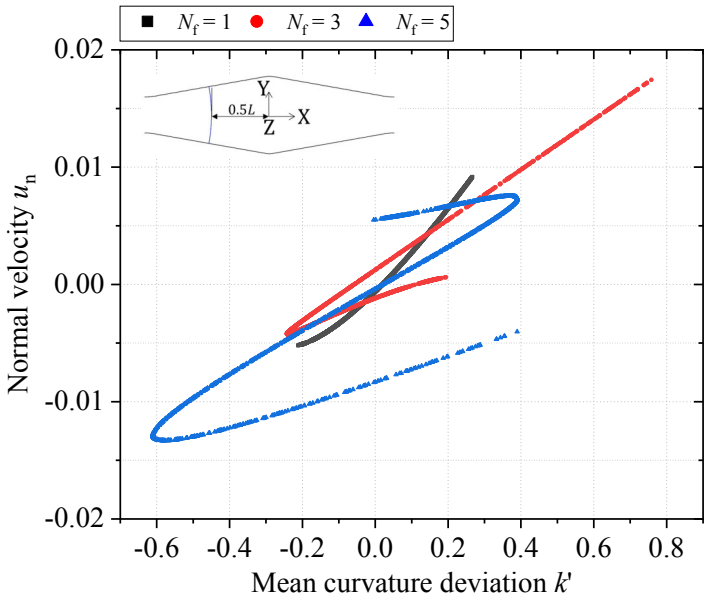


Figure 5.18: The correlation between the normal velocity u_n and the mean curvature deviation k' is investigated. The curvature deviation k' is computed using Eq. 5.26 for perturbation components of the mean curvature, as defined in Eq. 5.27, for $N_f = 1$, 3, and 5. The film is situated within the diverging section of the pore, and intersects with the X-axis at x = -0.5 L.

curvature value corresponds to multiple velocity values. This observation implies a lack of a straightforward relationship between local mean curvature and normal velocity in general. This is because the effect on the relaxation velocity depends on how each Fourier term, in Eq. 5.27, interacts with the Stokeslet in Eq. 5.16.

5.5 Conclusions

Utilisation of the boundary integral method to address the dynamic response of dry foams at low Reynolds numbers is explored in this chapter. The method holds applicability in contexts involving foams in bulk or in confined geometries. For the latter scenarios, the slip wall boundary condition is taken into account, resulting in the exclusion of the viscous forces exerted by walls on foams. To address the singularity challenges inherent in the resultant boundary integral equation for dry foams, two techniques are employed: the singularity subtraction method and the incorporation of a nonsingular contour integral.

These approaches are utilised to transform the boundary integral equations into a form devoid

of singularities. Subsequently, in the numerical simulations, the resultant nonsingular boundary integral equation undergoes further discretisation based on the mesh representation of the geometries, including both foam films and walls. In cases involving pure foams in bulk, the discrete equation yields an explicit expression for calculating velocities at field points. Conversely, when walls are present, the discrete equation takes the form of a linear system that can be solved through GMRES with restart [133].

The method is assessed through two applications within this study. One application involves examining the motion of a foam composed of five bubbles subject to a simple shear flow. The findings reveal that film tension operates to counteract the deformation induced by the shear flow. This occurs because the film tension introduces a relaxation velocity aimed at minimising the foam's surface energy. The movement of bulk Plateau borders significantly influences the overall foam motion by altering the mean curvature of films adjacent to these borders. Significantly, the outcomes underscore the necessity of integrating the effect of bulk Plateau border motion on the overall motion of the foam into computations. This incorporation proves beneficial for maintaining conserved bubble volumes.

The second application examines a prototypical scenario for foam flow within confined geometries, specifically focusing on a single film traversing a diverging-converging channel. In this context, gas injection into the channel is simulated by deforming the walls. The motion of the film is deconstructed into two distinct components: one arising from the flow induced by wall deformation and the other stemming from film relaxation. The flow due to wall deformation causes deviations in the film's configuration from its stationary equilibrium state characterised by a constant mean curvature.

Employing Fourier expansion, it is demonstrated that the nonuniform mean curvature predominantly exhibits a main perturbation component shaped as a cosine function. The wavelength of this perturbation, measured in terms of the polar coordinate, coincides with twice the diverging angle of the channel. Furthermore, the analysis reveals that the normal component of the film's relaxation velocity, induced by the primary curvature perturbation, exhibits a one-to-one mapping relation to the primary curvature perturbation itself. In contrast, higher-order curvature

perturbations yield relation behaviours characterised by multi-value functions. The number of branches in these functions increases with the order of the curvature perturbation.

Chapter 6

Other applications of the boundary-integral approach for dry foam

6.1 Introduction

The utilization of the boundary integral method in the analysis of dry foam represents a novel tool for comprehending the dynamics of foam flow, particularly in confined geometries such as porous media, where foam flow is typically at low Reynolds numbers. This method operates within the dynamic regime of foam flow, relying on the governing equations of fluid dynamics, thus advancing our capabilities in modelling foam flow within porous media. Importantly, when compared with existing quasi-static soap film mode and 2D viscous froth model, the boundary integral method offers the potential for fresh insights when addressing typical problems, since the viscosity effect of fluid in bulk is now considered in the method.

In this chapter, two extensions of the boundary integral modelling approach applied to dry foam are explored. Firstly, the motion decomposition derived from the boundary integral equation for dry foam is linked to the energy consumption during foam flow, yielding novel perspectives

on energy transport during foam flow within confined channels. Secondly, the boundary integral approach within a 2D framework is implemented, particularly for predicting foam motion in a Hele-Shaw cell, akin to the 2D viscous froth model. These extensions are detailed in Section 6.2 and 6.3, respectively.

6.2 Energy consumption during film motion in channels

Consider a single foam film in a diverging-converging channel, as shown in 5.11 (a), whose behaviour is governed by Eq. 5.13. This equation is presented again below for reference, with the superscript * dropped.

$$\begin{aligned} u_j(\boldsymbol{x}_0) = u_j^{\infty}(\boldsymbol{x}_0) - \frac{1}{8\pi}\Big(\int_{S_\mathrm{l}} -\frac{1}{Ca} k(\boldsymbol{x}) \boldsymbol{n}_i(\boldsymbol{x}) G_{ij}(\boldsymbol{x}, \boldsymbol{x}_0) dS(\boldsymbol{x}) \\ + \int_{S_\mathrm{s}} q_i(\boldsymbol{x}) G_{ij}(\boldsymbol{x}, \boldsymbol{x}_0) dS(\boldsymbol{x}) \Big) - \frac{1}{8\pi} \int_{S_\mathrm{s}} u_i(\boldsymbol{x}) T_{ijk}(\boldsymbol{x}, \boldsymbol{x}_0) n_k(\boldsymbol{x}) dS(\boldsymbol{x}). \end{aligned} \tag{6.1}$$

Since the flow is assumed to be steady-state, the energy input into the flow system is purely consumed through the variation in surface energy and the viscous dissipation. This energy consumption is analysed in this section. Note that all variables, e.g. energy, pressure, channel radius, time, and film area, are considered to be dimensionless.

6.2.1 Overall energy consumption

The total energy consumption rate can be quantified by assessing the energy consumed, denoted as ΔE, over a short time interval Δt centred around a particular moment in time. There are two approaches to represent this energy consumption. The first approach involves considering the external work performed by the pressure drop across the channel

$$\Delta E = (\Delta P_\mathrm{i} + \Delta P_\mathrm{r}) \Delta V, \tag{6.2}$$

where ΔP_{i} and ΔP_{r} are the pressure difference components due to imposed flow and film relaxation, respectively. ΔV is the volume of gas injected into the pore within time Δt. This volume is determined solely by the imposed flow, i.e. $\Delta V = \pi R_{\mathrm{t}}^2 \Delta t$, given that the (dimensionless) velocity of gas into the channel is unity. The subscripts i and r are used to denote the imposed flow and the film relaxation motion-induced components, respectively.

The other approach to represent the energy consumption is to consider the distinct sources consuming energy, under the assumption of constant film tension

$$\Delta E = \Delta E_{\mathrm{v}} + \frac{1}{Ca}\Delta S, \tag{6.3}$$

where ΔE_{v} refers to the viscous dissipation due to the fluid viscosity, and ΔS refers to the area change of the film. Utilizing the film motion decomposition discussed in Section 5.3.4, ΔE can be expressed as

$$\Delta E = \Delta E_{\mathrm{v,i}} + \Delta E_{\mathrm{v,r}} + \Delta E_{\mathrm{v,i-r}} + \frac{1}{Ca}\Delta S_{\mathrm{i}} + \frac{1}{Ca}\Delta S_{\mathrm{r}}, \tag{6.4}$$

where $\Delta E_{\mathrm{v,i}}$ is the viscous dissipation due to the imposed flow, $\Delta E_{\mathrm{v,r}}$ the viscous dissipation due to the film relaxation, and $\Delta E_{\mathrm{v,i-r}}$ the viscosity-associated energy consumption due to the interplay between the imposed flow and the relaxation motion (imposed flow-relaxation interaction), which appears due to the fact that the viscous dissipation rate is non-linear, and scales as the strain rate squared. ΔS_{i} and ΔS_{r} are the area change due to imposed flow and film relaxation, respectively.

6.2.2 Energy consumption of individual components of film motion

Consider the case of pure imposed flow. The viscous dissipation of the imposed flow is balanced by the work done by the pressure drop across the pore, i.e.

$$\Delta E_{\mathrm{v,i}} = \Delta P_{\mathrm{i}} \Delta V. \tag{6.5}$$

The energy consumption rate of the imposed flow is a constant since the imposed flow is a constant steady-state flow and ΔP_{i} is a constant independent of the film presence.

Then consider the film relaxation process. Since the macroscopic directional flow flux through the pore cross-section is zero for film relaxation process, the only energy source is the film surface energy, and the only energy consumption is due to the viscous dissipation. This suggests that the film surface energy, which is proportional to the film surface area given a constant film tension, is dissipated through the fluid viscosity

$$\Delta E_{\mathrm{v,r}} = -\frac{1}{Ca} \Delta S_{\mathrm{r}}. \tag{6.6}$$

where the minus sign before the term on the right-hand side accounts for the fact that film relaxation always tends to minimise the film surface energy and thus ΔS_{r} has a negative value. Eq. 6.6 indicates that the second and fifth terms on the right hand side of Eq. 6.4 cancel each other. It should be noted that Eq. 6.6 is based on the constant film tension assumption. If film tension ever became rate dependent (e.g. due to interfacial viscosity) then it could consume more energy in film stretching than the energy recovered in film contraction.

6.2.3 Energy consumption due to imposed flow-relaxation interaction

Apart from the energy consumed by the imposed flow and the film relaxation in isolation, the remaining energy consumption is attributed to the interaction between these two processes. This energy consumption consists of two terms: one is the viscosity-associated energy consumption, and the other is the film surface energy change due to the imposed flow. Combining Eq. 6.2, 6.4, 6.5, and 6.6 leads to

$$\Delta E_{\mathrm{v,i-r}} + \frac{1}{Ca}\Delta S_{\mathrm{i}} = \Delta P_{\mathrm{r}}\Delta V. \tag{6.7}$$

Unlike the relaxation-induced viscous dissipation and the energy stored in the form of film surface energy, the viscosity-associated energy consumption $\Delta E_{\mathrm{v,i-r}}$ cannot be linked to the change in film surface area. However, in cases where the the viscosity-associated energy consumption is zero, the total energy consumption, and thus the flow resistance, can be directly linked to the film surface area change. This means that the work done is stored as surface energy. It is possible that a film could suddenly reconfigure after traversing a certain amount of distance along a pore, and so not all the work done would be recovered [16]. As discussed later in Section 6.2.5, this provides us with a fresh energetic perspective on comprehending the yield stress of foam flow within porous media. The yield stress has been already explored in Chapter 3, utilising the concept of volumetric-averaged pressure difference.

6.2.4 Energy transport trajectories

Eq. 6.6 and 6.7 demonstrate how the additional energy consumption due to the existence of the film appears, which includes those due to the film relaxation and the interplay between the film relaxation and the imposed flow. Eq. 6.6 implies that the reduction of the film surface energy due to the film relaxation is totally dissipated by the fluid viscosity (neglecting interfacial viscosity here). It also suggests that the external work done by the relaxation-induced pressure drop leads to the film surface energy change and also contributes to a viscosity-associated energy consumption. Specifically, when the imposed flow stretches the film, part of the external work increases the film surface energy. On the contrary, when the imposed flow shrinks the film, part of the film surface energy acts to push the fluid flow through the pore. Figure 6.1 illustrates the energy transport via the film surface energy during the film stretching and shrinking due to the imposed flow.

The key factor affecting the total energy consumption during the film motion in the pore is the capillary number Ca, which is the ratio between the characteristic velocities of the imposed flow

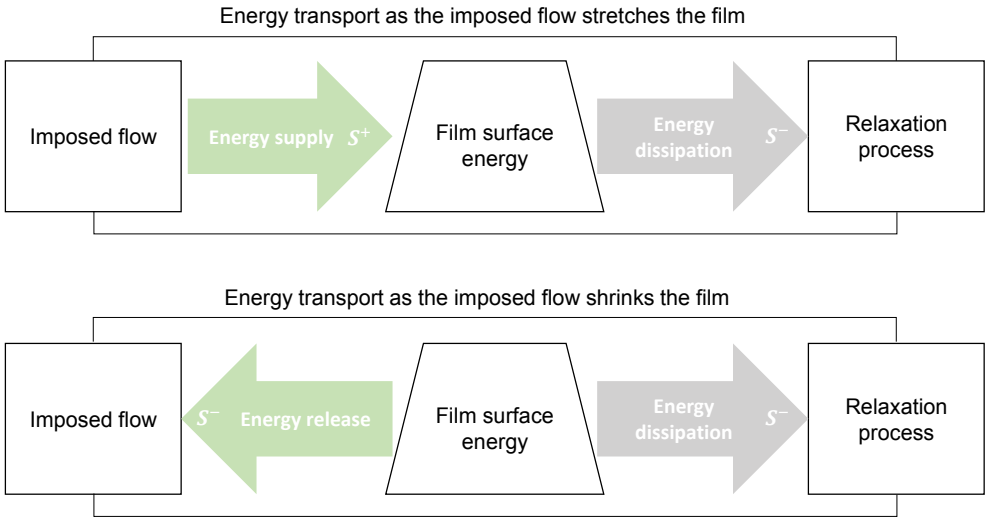


Figure 6.1: Energy transport via the surface energy. When the imposed flow stretches the film, the film surface energy increases due to the input energy from the imposed flow, and, synchronously, the surface energy partially dissipates through the relaxation process. When the imposed flow leads to the film shrinking, the film surface energy is released into the background imposed flow and also dissipates through the relaxation process.

and the relaxation process. At different values of Ca, the relaxation process minimising the film surface energy happens faster or slower than the film deformation imposed by the background flow. At small Ca, most of the work done is associated with deforming films, whereas at larger Ca, work done is balanced by viscous losses. Consequently, the proportions of energy transport via different movements and their interplay, as well as the net energy consumption and the resultant averaged flow resistance, vary with Ca, which ultimately contributes to the non-Newtonian behaviour of film flow.

6.2.5 Yield stress of film motion

In the quasi-static limit, namely Ca approaching zero, the film maintains the minimal surface configuration as the film transverses a diverging-converging pore or channel, which has been utilised in previous work to study the yield stress of foam flow [16, 66], as also discussed in Chapter 3. It has been shown that the yield stress arises from the front-to-back non-symmetry of the film movements along the axis of the pore [66]. Moreover, the occurrence of this non-symmetry is due to the existing of a sharp corner in the central pore body, which connects

the diverging and converging sections of the pore. When a foam film enters the corner, it spontaneously jumps to a new position in the converging section of the pore. This jump leads to a finite volumetric averaged pressure drop across the pore during the film movement, and thus the occurrence of non-zero yield stress.

In order to further understand the occurrence of the yield stress, this section first presents the results of the pressure drop across the diverging-converging pore, shown in Figure 5.11 (a), for the quasi-static film motion, which varies with the volume swept by the film in the pore. The angle α is set to a variable parameter. In addition to the pressure drop across the pore that has been considered in previous work [112, 66], the surface area change during the film motion is also monitored. Then, the arising of the yield stress is explained from the perspective of energy consumption during the quasi-static film motion.

Pressure drop and film area evolution

The quasi-static film motion can be predicted using the pore-scale method available in Chapter 3. For the pore geometry shown in Figure 5.11 (a), the analytical solution of the pressure difference is available. Figure 6.2 shows the results of the pressure drop and the surface area as functions of the volume swept by the film, during the quasi-static motion of the film in pores with different diverging angles. It is found that, for relative small diverging angles, e.g. $\alpha = 10$, 15, 20, 25, and 30 degrees, both the pressure drop across the pore and the film area exhibit continuous variations with respect to the swept volume. Conversely, pores with large diverging angles, e.g. $\alpha = 35$, 40, and 45 degrees, experience discontinuities in both pressure drop and film area. Note that the quantities here are still dimensionless ones, while they are made by some different characteristic quantities from those adopted in Eq. 6.1. In the quasi-static limit, i.e. $Ca \to 0$, the characteristic length L_0 is comparable to the actual pore size, leading to $R_t = 0.3$. The characteristic energy is the surface energy of film with area L_0^2, i.e. $4\gamma L_0^2$. The characteristic pressure is $4\gamma/L_0$, which is not related to the fluid viscosity.

In Figure 6.3, the integral of the pressure drop with respect to the swept volume, which reflects the flow resistance, is shown as a function of the jump of the film area during the film motion,

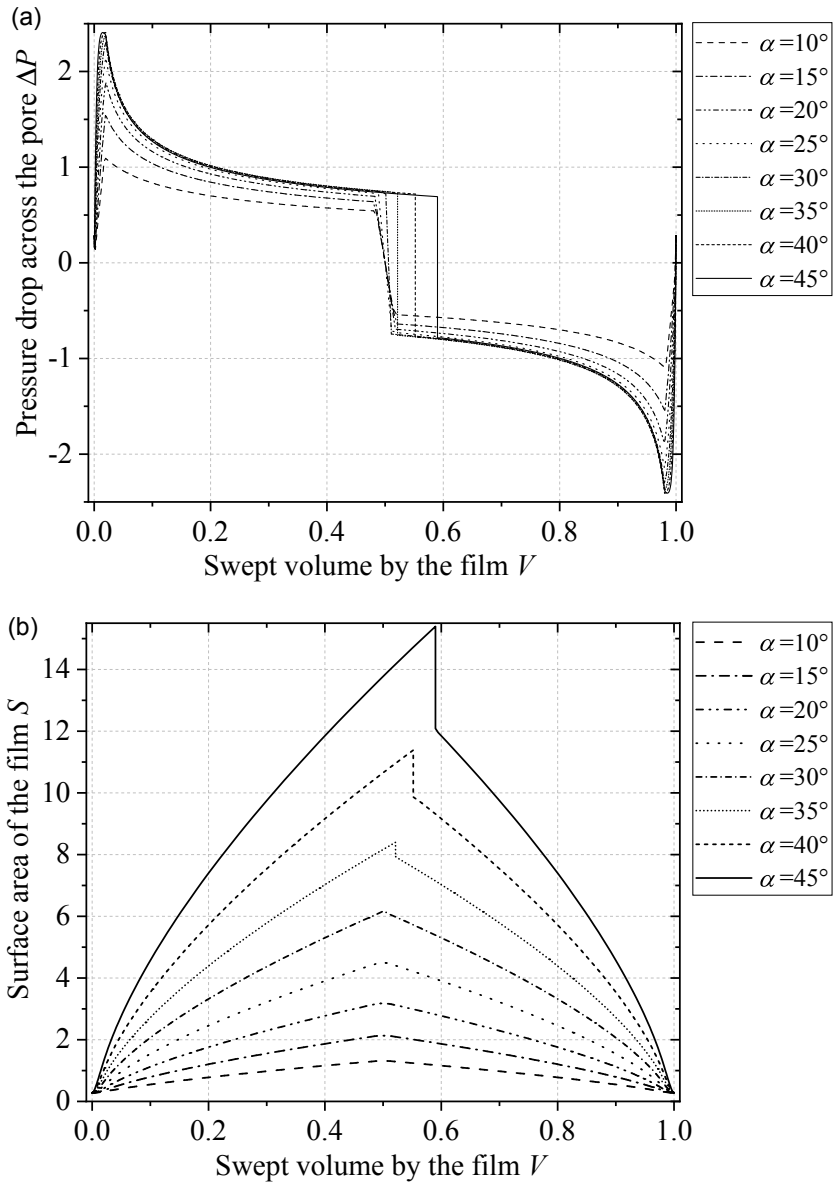


Figure 6.2: Quasi-static film motion in diverging-converging pores with different diverging angles. (a) Pressure drop ΔP as a function of the volume V swept by the film during the quasi-static film motion in pores with different diverging angles α. (b) Surface area S of the film as a function of V during the quasi-static film motion in pores with different diverging angles α. V is normalised using the absolute volume of the pore, $V_0(\alpha)$.

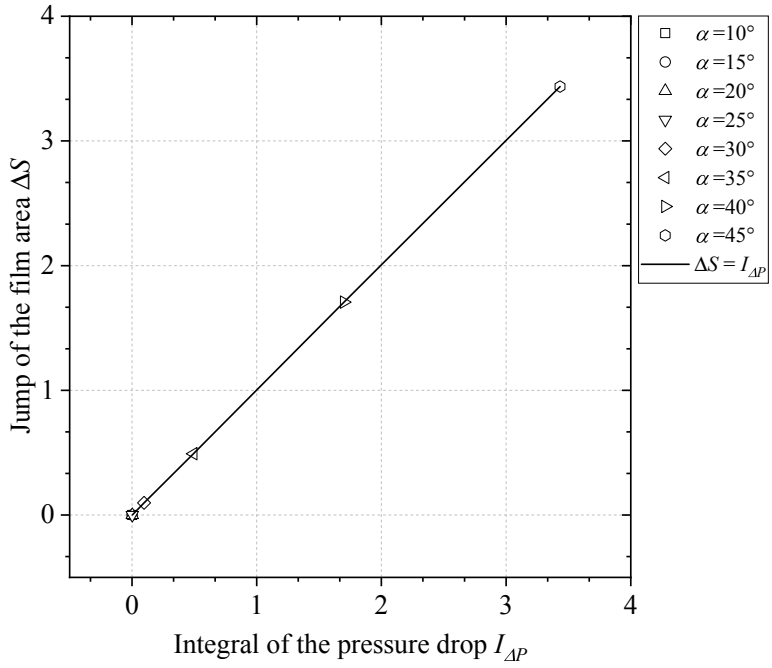


Figure 6.3: The integral I_P of the pressure drop with respect to the swept volume, which is calculated as $I_{\Delta P} = V_0 \int_0^1 \Delta P dV$, as a function of the jump of the film area during the film motion.

which shows both quantities are of the same value. This relation can be proved using the Young-Laplace equation. However, this problem is instead considered from the perspective of energy consumption in the following section.

Energy consumption during the quasi-static film motion

During the quasi-static film motion, viscous dissipation occurs during the fast film jump (if any) in the central pore body, while the film areas are the same at the inlet and outlet of the pore. Apart from the jump (if any) of the film in the central pore body, the remaining of the film motion should consist of both motion components (i.e. imposed flow and film relaxation) in principle, and the relaxation motion should always dissipate energy and lead to flow resistance. However, this part of the energy dissipation tends to zero in the quasi-static limit, because the imposed motion is much slower than the relaxation and thus the film configuration maintains the equilibrium status. In this case, both the viscosity dissipation due to the relaxation and its interaction with the imposed flow are zero. This means that the only energy consumption is the relaxation-induced viscous dissipation during the film jump (if any), and thus the jump

of the film area should equal the associated integral of the pressure drop across the pore, as indicated in Figure 6.3.

This observation provides us with a new insight into understanding the arising of the yield stress of foam flow in porous media, compared to the existing theory that the film spends more time in the diverging section of a sharp pore than in the converging section, and thus the net external work is non-zero, resulting in a non-zero yield stress [65, 66]. For a sharp pore, the external work totally transfers to the film surface energy during the film motion in the diverging section of the pore. As the film arrives at the pore corner in the central pore body, the film spontaneously relaxes into a new equilibrium position, which happens instantaneously and dissipates energy solely through fluid viscosity. Since there is a finite difference in the area of the thin film before and after the jump, the energy dissipated is also of a finite value. It is, therefore, this finite viscous dissipation that leads to the arising of the yield stress.

By decomposing the data from Figure 6.2(b) into a step area change and a continuous contribution, Figure 6.4 illustrates the variations in film area induced by both the imposed flow and relaxation for two different diverging angles, specifically $\alpha = 10$ and 40 degrees. The total change in film area throughout the film motion is simply the sum of the changes caused by the imposed flow and relaxation. Remarkably, it is observed that the net change in film area when the film reaches the pore outlet is zero during quasi-static film motion. Furthermore, Figure 6.4 shows that, in the case of the sharp pore ($\alpha = 40$ degrees), viscous dissipation only occurs when the swept volume corresponds to the film jump.

6.3 Boundary integral method in 2D

A boundary integral equation for 2D dry foam can be derived following a similar procedure as the one discussed in Chapter 5. Particularly, for 2D dry foam in bulk, the resultant boundary integral equation (dimensionless) is

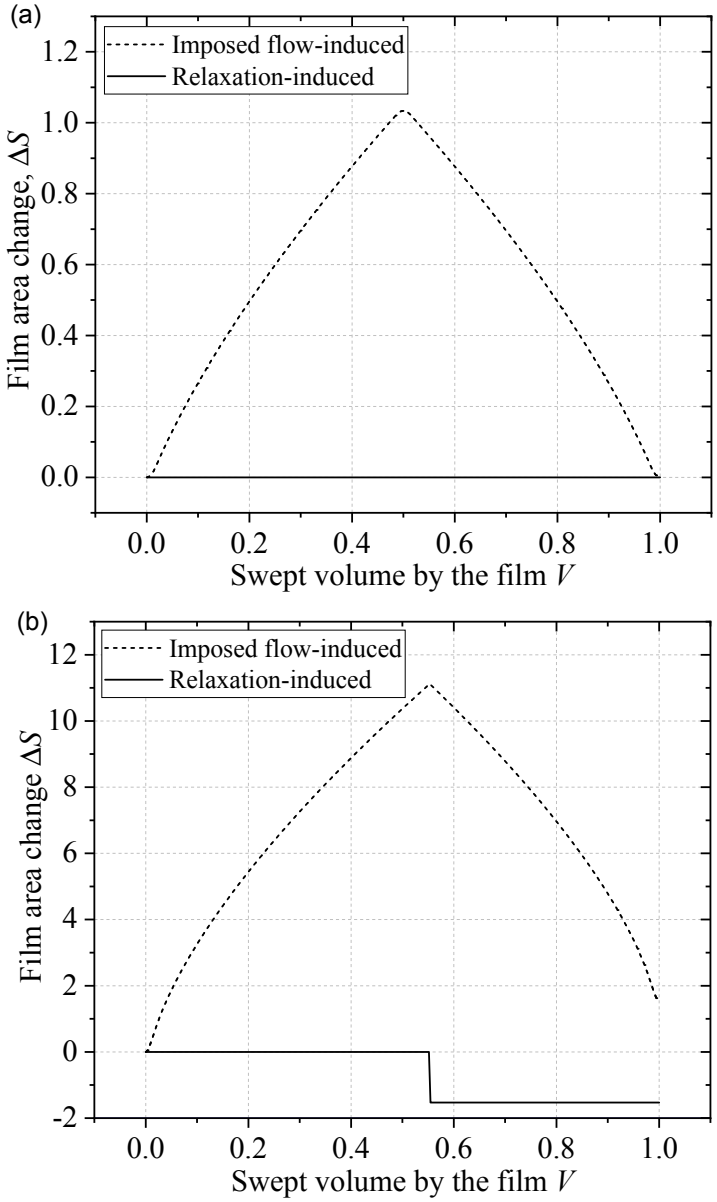


Figure 6.4: The film area change due to the imposed flow and the relaxation process during the quasi-static film motion. (a) α equals 10 degrees. (b) α equals 40 degrees.

$$u_j(\boldsymbol{x}_0) = u_j^{\infty}(\boldsymbol{x}_0) - \frac{1}{4\pi}\int_{\Gamma_l} \Delta F_i G_{ij}(\boldsymbol{x}, \boldsymbol{x}_0) dl(\boldsymbol{x}), \tag{6.8}$$

where, in 2D, the Stokeslet is defined as $G_{ij}(\boldsymbol{r}) = -1/(4\pi)(-\delta_{ij}\log(|\boldsymbol{r}|) + r_i r_j/|\boldsymbol{r}|^2)$ with $\boldsymbol{r} = \boldsymbol{x} - \boldsymbol{x}_0$. The interfacial force term, denoted as ΔF_i, is defined as $\Delta F_i = -(1/Ca)n_i k(\boldsymbol{x})$, where $Ca = (\lambda\mu L_0)/(2\gamma T_0)$ is capillary number. The physical interpretations of other variables in the equation remain consistent with the 3D formulation Eq. 5.16, but are now confined to a 2D context. For instance, $u_j^{\infty}(\boldsymbol{x}_0)$ is the known background flow, such as a simple shear flow.

In the scenario of foam flow confined in Hele-Shaw cells, both film tension and viscous forces play roles in contributing to the pressure difference across foam films, as implied by Eq. 4.9. In order to incorporate the impact of viscous forces on the interface force, a modification is made to the interfacial force term. This modification includes the contribution of the viscous force and results in the following expression $\Delta F_i = -(1/Ca)n_i k(\boldsymbol{x}) - \lambda_d n_i n_k u_k(\boldsymbol{x})$, where λ_d is the dimensionless drag coefficient (made dimensionless by multiplying $L_0/(\lambda\mu)$).

The numerical method for solving Eq. 6.8 is introduced in Section 6.3.1. Then the discrete form of Eq. 6.8 is presented in Section 6.3.2. The application of Eq. 6.8 in a simple scenario, namely a single bubble's relaxation when confined in Hele-Shaw cells, is explored in Section 6.3.3.

6.3.1 Nyström method

To numerically solve Eq. 6.8, the Nyström method is employed, with the Gauss-Legendre quadrature rule as the underlying quadrature [135, 136]. To elucidate this approach, consider an integral equation expressed in the following form [137]

$$\sigma(\tau) + \int_{T_0}^{T_1} w(\tau, \tau')\sigma(\tau')d\tau' = f(\tau), \quad \tau \in [T_0, T_1], \tag{6.9}$$

where w is the kernel function exhibiting a logarithmic singularity as $\tau' \to \tau$, f a known

function, and σ the unknown function to solve. Consider N collocation points, $\{\tau_i\}_{i=1}^{N} \in [T_0, T_1]$, and apply Eq. 6.9 at each collocation point τ_i

$$\sigma(\tau_i) + \int_{T_0}^{T_1} w(\tau_i, \tau')\sigma(\tau')d\tau' = f(\tau_i), \quad i = 1, ..., N. \tag{6.10}$$

The Nyström method approximates the integral in Eq. 6.10 using the values of the integrand at each of the collocation points [137]

$$\int_{T_0}^{T_1} w(\tau_i, \tau')\sigma(\tau')d\tau' \approx \sum_{j=1}^{N} a_{i,j}\sigma(\tau_j), \tag{6.11}$$

where $a_{i,j}$ is the coefficient depending on the underlying quadrature. Substituting Eq. 6.11 into Eq. 6.10, a linear system of equations is obtained

$$\sigma(\tau_i) + \sum_{j=1}^{N} a_{i,j}\sigma(\tau_j) = f(\tau_i), \quad i = 1, ..., N. \tag{6.12}$$

In order to determine the coefficient $a_{i,j}$ in Eq. 6.11 and 6.12, the panel-based Gaussian quadrature rule [137] is used. This involves dividing the integral interval into multiple non-overlapping panels, i.e. $[T_0, T_1] = \bigcup_{t=1}^{N_t} \Omega_t$, in order to accurately approximate the integral. Consequently, the integral over the original interval can be expressed as the sum of the integrals over each of the individual panels

$$\int_{T_0}^{T_1} w(\tau_i, \tau')\sigma(\tau')d\tau' = \sum_{t=1}^{N_t} \int_{\Omega_t} w(\tau_i, \tau')\sigma(\tau')d\tau'. \tag{6.13}$$

If a given collocation point τ_i, which is also the singularity point of the kernel function, is sufficiently distant from a panel Ω_t, the integral over Ω_t in Eq. 6.13 can be computed using the standard Gaussian quadrature rule

$$\int_{\Omega_t} w(\tau_i, \tau')\sigma(\tau')d\tau' \approx \sum_{j:\tau_j \in \Omega_t} \omega_j w(\tau_i, \tau_j)\sigma(\tau_j), \tag{6.14}$$

where ω_j is the weight associated with Gaussian node τ_j on panel Ω_t. However, when τ_i belongs to the panel Ω_t, the standard Gaussian quadrature method becomes inappropriate because of the singularity present in the kernel function [137, 138]. To address this issue, Kolm and Rokhlin [138] proposed an alternative approach involving a modified Gaussian quadrature with J nodes. This modified method allows for the approximation of the integral with a precision level up to $J-2$ (the method can exactly integrate a11 polynomials up to degree $J-2$)

$$\int_{-1}^{1} \log(|\tau-\tau_0|)\sigma(\tau)d\tau \approx \sum_{j=1}^{J} v_j\sigma(\tau_j), \quad \tau_0 \in (-1,1), \tag{6.15}$$

where $\{v_j\}_{j=1}^{J}$ are the weights dependent on the location of the singularity, and are computed as [138]

$$\begin{aligned} v_j =& \omega_j\Big((P_0(\tau_j)-P_1(\tau_j))R_0(\tau_0) + \sum_{n=1}^{J-2}(P_{n-1}(\tau_j)-P_{n+1}(\tau_j))R_n(\tau_0) \\ &+ P_{J-2}(\tau_j)R_{J-1}(\tau_0) + P_{J-1}(\tau_j)R_J(\tau_0)\Big), \quad j=1,2,...,J, \end{aligned} \tag{6.16}$$

where $\{\tau_j\}_{j=1}^{J}$ and $\{\omega_j\}_{j=1}^{J}$ denote the J nodes and weights of the Gaussian quadrature on the interval $[-1,1]$, respectively. $P_n(\tau)$ and $Q_n(\tau_0)$ are the nth Legendre polynomial and Legendre function of the second kind, respectively, and R_n is defined as [138]

$$R_n(\tau) = Q_n(\tau) + \frac{1}{2}\log(|\tau-1|). \tag{6.17}$$

The integral in Eq. 6.15 is computed within the interval $\tau \in$ [-1 1] which should be projected to the range [T_0 T_1], when applied to Eq. 6.13.

6.3.2 discretisation of the 2D boundary integral equation

In simulations employing the Nyström method, two types of grids are utilised [136]: an equidistant grid and a Gauss-Legendre grid. The equidistant grid serves as the representation for foam

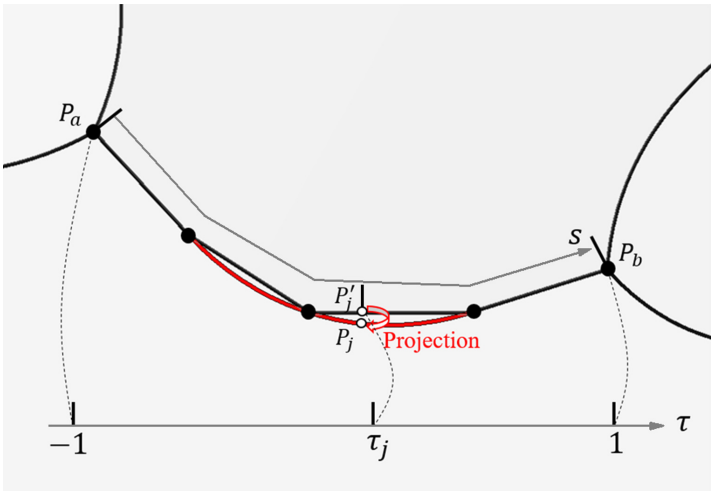


Figure 6.5: Two types of grids are utilised. The first one, referred to as the equidistant grid, is denoted by solid black circles. The second one, known as the Gauss-Legendre grid, is required to implement Gaussian quadrature. The latter is constructed by adding new points, which are indicated by hollow black circles, onto the equidistant grid. To calculate the coordinates of the new points along the curved lamella, the lamella length is mapped onto [-1,1]. Additionally, for each new point, a further projection onto an arc is implemented to preserve the curvature. This arc is constructed from the nearest three points on the equidistant grid.

lamellae, where the spacing between adjacent grid points is approximately constant. Conversely, the Gauss-Legendre grid is employed for integral calculations and is composed of nodes specified by the Gaussian quadrature rule. The velocity field is computed on the Gauss-Legendre grid, and subsequently, interpolation is performed to transfer these values back to the equidistant grid prior to the evolution of the foam configuration [135, 136].

As depicted in Figure 6.5, the discretisation of each lamella involves dividing it into a finite number of equidistant points. The line segment between each pair of adjacent points is approximated as a straight line. To estimate the total length along the lamella, the lengths of each individual line segment are summed up [88]. Each lamella is then treated as a panel denoted by Ω_l, with its start and end points designated as P_a and P_b, respectively. To map the length of the lamella along its arc-length, starting from P_a onto $\tau : [-1, 1]$, the following projection is employed: $\tau = (2s - L_{\Omega_l})/L_{\Omega_l}$ for $s \in [0, L_{\Omega_l}]$. Here, s denotes the coordinate along the curve of the lamella, and L_{Ω_l} represents the total length of the lamella.

The Gauss-Legendre grid is generated by introducing J nodes from the Gaussian quadrature, which are represented as $\{\tau_j\}_{j=1}^{J}$, onto the equidistant grid. The curve coordinates for each

of these nodes, denoted as $\{s_j\}_{j=1}^{J}$, are determined using the previously explained projection method. These nodes are located along the straight line segments connecting the equidistant grid points. In order to preserve the curvature of the lamella at each Gaussian node, a curved arc is constructed. This is achieved through interpolation with the three nearest points on the equidistant grid [88]. Subsequently, each newly generated node is projected onto this curved arc.

Consider a 2D dry foam composed of N_l lamellae, denoted as $\{\Omega_l\}_{l=1}^{N_l}$. Here, each lamella is considered as a panel. For each lamella Ω_l, let $\{s_{l,j}\}_{j=1}^{J_l}$ represent the Gaussian nodes on the Gauss-Legendre grid, and let $\{\omega_{l,j}\}_{j=1}^{J_l}$ and $\{v_{l,j}\}_{j=1}^{J_l}$ denote the coefficients for the original and modified Gaussian quadrature, respectively. The Nyström method is then used to discretise Eq. 6.8 and approximate the involved integral with Gaussian quadrature. This process results in a linear system of equations with $\sum_{l=1}^{N_l} 2J_l$ unknown velocity components

$$
\begin{aligned}
&u_\beta(\boldsymbol{x}_{l,i}) = u_\beta^\infty(\boldsymbol{x}_{l,i}) + \frac{1}{16\pi^2}\Bigg(\\
&\frac{L_{\Omega_l}}{2}\sum_{j=1}^{J_l}\Big(\big(-v_{l,j}+\omega_{l,j}\log\frac{2}{L_{\Omega_l}}\big)\delta_{\alpha,\beta}\frac{\log(|\boldsymbol{x}_{l,j}-\boldsymbol{x}_{l,i}|)}{\log(|s_{l,j}-s_{l,i}|)} + \omega_{l,j}\frac{(x_{l,j}^\alpha - x_{l,i}^\alpha)(x_{l,j}^\beta - x_{l,i}^\beta)}{|\boldsymbol{x}_{l,j}-\boldsymbol{x}_{l,i}|^2}\Big) \\
&\Big(-\frac{1}{Ca}|\boldsymbol{f}_{l,j}| - \lambda_d\sum_{\gamma=1}^{2}\hat{f}_\gamma(x_{l,j})u_\gamma(x_{l,j})\Big)\hat{f}_\alpha(x_{l,j}) + \\
&\sum_{\substack{L\in\{1,2,\dots,N_l\}\\ L\neq l}}\frac{L_{\Omega_L}}{2}\sum_{j=1}^{J_L}\omega_{L,j}\Big(-\delta_{\alpha,\beta}\log(|\boldsymbol{x}_{L,j}-\boldsymbol{x}_{l,i}|) + \frac{(x_{L,j}^\alpha - x_{l,i}^\alpha)(x_{L,j}^\beta - x_{l,i}^\beta)}{|\boldsymbol{x}_{L,j}-\boldsymbol{x}_{l,i}|^2}\Big) \\
&\Big(-\frac{1}{Ca}|\boldsymbol{f}_{L,j}| - \lambda_d\sum_{\gamma=1}^{2}\hat{f}_\gamma(x_{L,j})u_\gamma(x_{L,j})\Big)\hat{f}_\alpha(x_{L,j})\Bigg),
\end{aligned}
\tag{6.18}
$$

where x_j^α and x_j^β are the αth and βth coordinate at the jth node, respectively. The tension force $\boldsymbol{f}$, which is associated with the local curvature, and the unit normal $\hat{\boldsymbol{f}}$ pointing to the concave side to the boundary are approximated as $\boldsymbol{f} = 1/R\hat{\boldsymbol{f}}$ and $\hat{\boldsymbol{f}} = (\boldsymbol{x}_j - \boldsymbol{x}_c)/|\boldsymbol{x}_j - \boldsymbol{x}_c|$, respectively, where $\boldsymbol{x}_c$ and R denote the centre and radius of the arc onto which the Gaussian node $\boldsymbol{x}_j$ is projected. In Eq. 6.18, the scaling factor $L_{\Omega_l}/2$ is necessary due to the lack of scale invariance in the integrand and one unit of τ corresponds to $L_{\Omega_l}/2$ units of film length [135].

6.3.3 Single bubble in Hele-Shaw cells

To illustrate the boundary integral method for 2D dry foam, the structural relaxation of a single bubble is considered. The focus is on the normal velocity of the bubble boundary at the initial moment of time. The drag coefficient λ_d is allowed to vary, while the capillary number Ca is fixed to unity.

The bubble's initial boundary is obtained by smoothing the corners of a square with a side length of one unit, as shown in Figure 6.6. The smoothing is done with a rounding radius set to 0.25. Given the symmetry of the bubble relaxation process, only one quadrant of the bubble's boundary is utilised in the simulations, and it is represented as a panel. This panel is discretised using an equidistant grid consisting of 33 nodes. Additionally, a 16-node Gauss-Legendre quadrature rule is applied, which necessitates the placement of 16 Gauss-Legendre grid nodes along the equidistant grid. Note that the current selection of the grid resolution is only to demonstrate the effectiveness of the method proposed in this chapter, and the results are compared with those by the 2D viscous froth model under the same resolution. The element size used in simulations should be subject to grid-independent criterion in future applications of the method.

Figure 6.7 depicts the variation in the normal velocity of the boundary under different drag coefficients. When $\lambda_\mathrm{d} = 0$, the result corresponds to the pure 2D scenario (in contrast to the 2D scenario confined in Hele-Shaw cells), where the reduced surface energy dissipates solely through fluid viscosity, as explained in Section 6.2. This would be unstable to a Rayleigh-Plateau instability in the third dimension [139]. At $\lambda_\mathrm{d} = 1$, a slight deviation from the pure 2D case can be observed in the boundary velocity, with the magnitude of the normal velocity remaining on the order of 0.01. As λ_d increases, the influence of viscous drag force on the boundary velocity becomes more significant. The magnitude of the boundary velocity decreases as λ_d increases. For instance, when λ_d changes from unity to 100, the maximum absolute value of the normal velocity decreases from 0.0098 to 0.0086. Note that in a realistic case, λ_d can be quite large due to the low internal fluid viscosity which has been further assumed to be negligible in the viscous froth model. However, the results at different λ_d from zero to large ones can

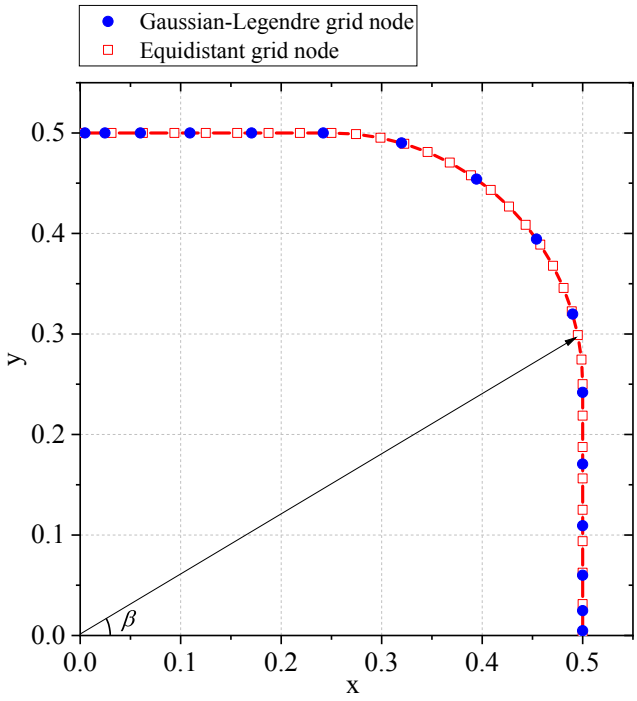


Figure 6.6: A bubble adopts a square shape with smoothed corners. The boundary of the bubble is approximated by the equidistant grid nodes, which are depicted as red squares. Furthermore, 16 Gauss-Legendre nodes are positioned along the equidistant grid. The angular coordinate β is measured in relation to the x axis.

qualitatively indicate the effect of the internal viscosity on the motion of bubble boundary.

The relationship between the normal velocity of the bubble boundary and $1/\lambda_\mathrm{d}$ is non-linear. This non-linearity arises because a part of energy dissipation originates from the viscosity of fluid in the entire flow field, rather than just from viscous dissipation due to the drag force on the boundary. This contrasts with the assumptions of the viscous froth model, which implicitly assumes that all energy consumption comes from viscous dissipation on the boundary. In the viscous froth model, the normal velocity of the bubble boundary is simply calculated as $u_n = (2\pi/L_\mathrm{boundary} - k)/\lambda_\mathrm{d}$, where L_boundary represents the circumferential length of the bubble boundary. It is clear that u_n exhibits a linear proportionality to $1/\lambda_\mathrm{d}$.

Figure 6.8 illustrates the normal velocity of bubble boundary at $\lambda_\mathrm{d} = 100$, predicted by the viscous froth model. The obtained result shows that the boundary velocity is greater than that obtained through the boundary-integral method for the same λ_d. This discrepancy arises because the energy consumption in the viscous froth model is solely attributed to the viscous dissipation on bubble boundary. In contrast, the boundary-integral method incorporates ad-

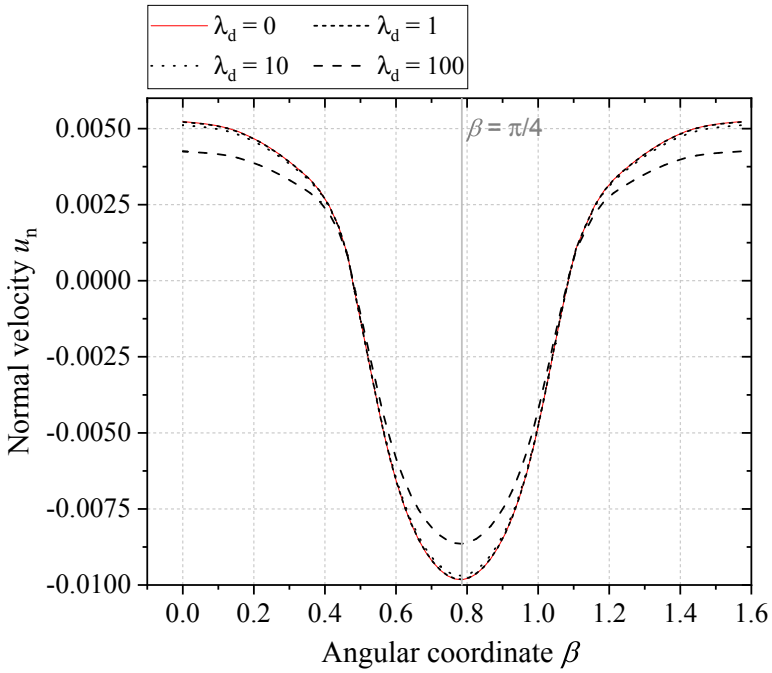


Figure 6.7: The boundary-integral results depict the normal velocities at equidistant grid nodes along the bubble boundary as a function of their angular coordinates. The drag coefficient is set to 0, 1, 10, and 100, respectively. Positive values of the normal velocity indicate the movement of the bubble boundary outward, while negative values indicate movement in the opposite direction.

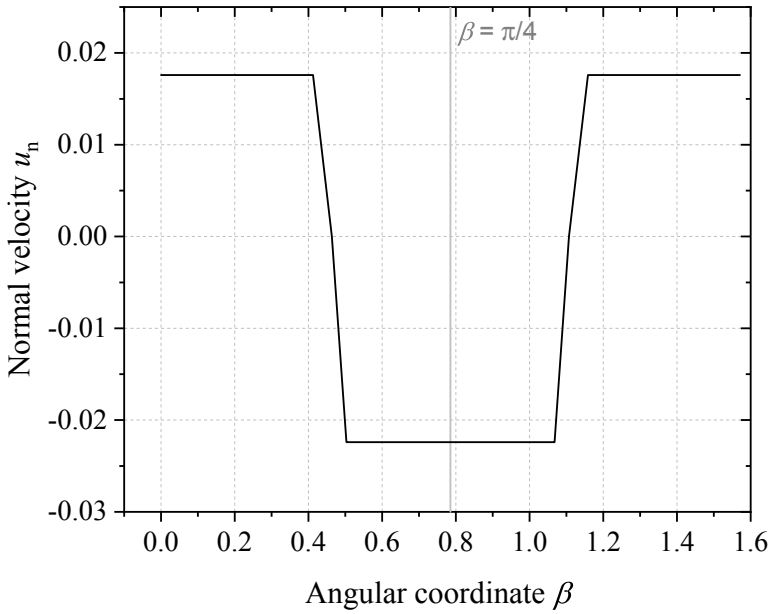


Figure 6.8: The results from the viscous froth model show the normal velocities at equidistant grid nodes along the bubble boundary as a function of their angular coordinates. The drag coefficient λ is set to 100. Positive values of the normal velocity indicate movement of the bubble boundary outward, while negative values indicate movement in the opposite direction.

ditional viscous dissipation of energy in other regions of the flow field (with Ca set to unity). Consequently, the bubble boundary might exhibit higher mobility in the viscous froth model due to the absence of this additional energy-consuming factor, though this part of energy consumption can be relatively small in realistic cases.

6.4 Conclusions

This chapter primarily focuses on exploring the extended applications of the boundary-integral approach for dry foam. The boundary integral equation for dry foam implies that the motion of foam in confined geometries can be considered as a linear combination of the background flow, the imposed flow, and the foam relaxation. Specifically, when examining the motion of foam films in diverging-converging channels, the motion can be decomposed into two components: the imposed flow and the relaxation motion. Consequently, the energy consumption during the film motion, which is associated with the average flow resistance, can also be divided into at least two terms, each linked to one of these motion components. However, because the rate of viscous dissipation is a non-linear function of strain, there is an additional energy consumption related to viscosity arising from the interaction between these two film motion components. This additional energy consumption cannot be attributed to changes in the area of the foam film, which complicates the analysis of flow resistance. In the extreme case, such as in quasi-static film motion, the viscosity-associated energy consumption becomes zero. In other words, work done on the system is stored as surface energy, except during abrupt jumps during which surface energy is dissipated. This allows for new insights into understanding average flow resistance, or the yield stress, to be gained.

In the context of quasi-static film motion within diverging-converging channels, a novel explanation for the emergence of yield stress centres on the change in the film area. This change occurs exclusively when the channel features a sharp configuration, particularly when it possesses a sharp corner within the central pore body. Remarkably, this area change represents the only source of energy consumption through viscous dissipation. Consequently, this new

perspective suggests that the yield stress of foam arises from the viscous dissipation induced by relaxation, which consumes finite energy and consequently results in a non-zero yield stress.

The second extension of this study applied the boundary integral method to dry foam in 2D scenarios, specifically within Hele-Shaw cells. In this approach, the viscosity of the fluid contained within the bubbles is taken into account as a factor affecting the foam's motion within Hele-Shaw cells. The study focuses on a simple test case involving a single bubble within a Hele-Shaw cell. The results reveal that fluid viscosity contributes to energy consumption during the bubble relaxation process, thus slowing down the motion of the bubble boundary compared to what is expected according to the 2D viscous froth model. However, the extent of this effect depends on the magnitude of the fluid viscosity, and the amount of slow down is expected to decrease as the fluid viscosity itself decreases.

Chapter 7

Conclusions and future work

The exploration of foam flow in porous media is an intriguing area of study, as foam serves as an effective agent for displacing substances due to its exceptional volumetric sweeping efficiency. In practical applications, such as enhanced oil recovery processes, employing foam flooding techniques can significantly enhance the rate of oil production. To provide a strong foundation for understanding the topic, a review of foam flow in porous media is conducted in Chapter 2 in this work. Basic concepts, such as geometric elements related to foam structure, and topology transformation, were explained. Fundamental generation and destruction mechanisms for foam in porous media were also introduced.

In terms of morphology, foam flow within porous media exhibits distinctive characteristics, marked by intermittent flow and the entrapment of bubbles. It is noteworthy that a significant portion of the gas in a foam is contained within these trapped bubbles. When confined within porous media, foam demonstrates quantitatively distinct behaviour as a yield-stress shear-thinning fluid. To predict both the configuration and physical properties of foam, various modelling techniques can be employed. These include methods like analysing soap film motion for quasi-static foam motion, employing a 2D viscous froth model for foam flow within Hele-Shaw cells, and utilising more advanced approaches such as the boundary integral method for analysing the Stokes flow of two-phase fluids, as well as computational fluid dynamics methods based on the Navier-Stokes equations.

One key insight from the literature is that the dynamics of high-quality foam exhibit a multi-scale nature [107]. For high-quality foams, the liquid can drain over tens or hundreds of seconds in thin films of micrometers thickness, while the films themselves can rupture within several milliseconds [140]. In this context, a common simplification used in foam modelling is the assumption of dry foam, which maintains the structure of the liquid network while disregarding the liquid phase content. This fundamental assumption serves as a basis for the modelling approaches employed in this work.

The main contribution of this thesis centres around the physics-based modelling and numerical simulations of microscopic foam flow behaviour. In Chapter 3, an expansion of the pore-scale quasi-static foam modelling approach is presented, to the pore-network scale. Within this pore-network level methodology, it is observed that the pressure difference among pore throats serves the same role in minimising surface energy as film tension does in the pore-scale approach. Since the pore network-scale necessitates the pressure difference as an input, it often requires integration with the pore-scale method or, in simpler cases, analytical methods to determine the pressure difference. This combined approach is referred to as the two-level method.

The verification of the two-level method is conducted by predicting the movement of two films within a three-pore porous medium model, employing both the pore-scale method and the two-level method. One significant discovery is that one of the films remains mobile and can traverse the downstream pore, while the other becomes trapped in the throat, though the porous medium exhibits symmetry concerning the shapes of the pores and the positions of the two downstream pores. From a quantitative perspective, it is observed that the pressure difference across the downstream pore differs from that observed when a single film is present within an isolated pore. This difference can be attributed to various phenomena, detailed in Chapter 3, which arise from the necessity for continuous gas injection and the capacity of the blocked throats to either store or release gas. The impact of these phenomena becomes more pronounced when multiple trapped films are present, as is the case when dealing with three or four downstream pores.

One implication of the findings is that the yield stress, a crucial input parameter in continuum-

scale models for macroscopic foam flow simulations [8], may be associated with the proportion of trapped gas within porous media. As detailed in Chapter 2, a significant portion of gas present during foam flow in porous media exists in the form of trapped bubbles. In such instances, the yield stress could experience significant augmentation due to the interconnected pores and the abundance of trapped films. This observation also implies that the strong shear-thinning behaviour [59] of foam at low capillary numbers might indirectly stem from bubble entrapment.

In Chapter 4, it is revealed that there is a connection between the pore-scale soap film model and the viscous froth model. This connection manifests in two distinct ways. Firstly, the steady states of foam within Hele-Shaw cells, as described by the 2D viscous froth model, can also be predicted using the pore-scale soap film model. This is accomplished by transforming the problem into an equivalent surface energy minimisation problem, which involves varying film tension along the foam films. Secondly, this work introduces a 3D version of the viscous froth model, which includes one of its constituents—the soap film model. In this 3D version, the viscous froth model effectively becomes a 3D soap film model with a boundary that dynamically evolves over time. The motion of this boundary is determined by the equilibrium between the film tension force and the drag force.

The 3D viscous froth model is employed to investigate a typical scenario where a viscous froth lens moves within a straight channel. Theoretical analysis indicates that the 2D viscous froth model can be deduced from the Young-Laplace equation, assuming that the two principal curvatures of the bulk film surface align with directions along the plates and across the gap, respectively, maintaining a constant value across the gap. This also suggests a connection between the drag coefficient in 2D, denoted as ζ, and the drag coefficient in 3D, denoted as ξ, via an estimate $\zeta = (2/H)\xi$, where H represents the gap size. However, it is important to note that this relationship holds true only under the previously mentioned assumptions. Due to these assumptions, the numerical results for the steady-state viscous froth lens in 2D and 3D reveal disparities in terms of the deformation of the viscous froth lens, where ζ is set to $(2/H)\xi$ in the 2D viscous froth model. This deformation is quantified by the change in vertical position of the three-fold vertex in 2D or the four-fold node in 3D. Additionally, assuming that the 2D viscous froth model can effectively capture the motion of the wall Plateau borders, the

results suggest that ζ is not a constant value but exhibits dependency on the position along foam films. However, it is possible to reconcile the 2D results with the 2D model's outcomes by treating ζ as an adjustable parameter. A formula is offered in this thesis, for selecting an appropriate value of ζ.

The significance of the research detailed in Chapter 4 lies in the correlation between foam behaviour and its initial configurations, as well as the necessity of modelling foam flow in micromodels. Prior work by Cox [37] has suggested a variety of foam configurations arising from slightly altered initial conditions, albeit within the quasi-static regime. This sensitivity may become more pronounced during pore-scale events occurring closely in time, where the dynamic 2D viscous froth model can be used to determine the sequence of events [88]. However, within Chapter 4, the 3D viscous froth model has demonstrated easier occurrence of topological transitions compared to 2D simulations, potentially exerting significant influence on subsequent foam behaviour within porous media, particularly in scenarios involving numerous foam films. Consequently, employing the 3D model for simulating foam flow in micromodels may offer enhanced effectiveness.

In Chapter 5, the boundary integral method is explored within the context of dry foam. What sets this method apart from the soap film model or the viscous froth model is its consideration of the viscosity of the fluid within the bubbles. However, it is important to note that the method assumes a slip boundary condition, meaning that it neglects the viscous forces acting along the wall surface, including those at the wall Plateau borders. To address the singularity or near-singularity that can arise in the resulting boundary integral equation, a combination approach is employed. This combines singularity subtraction [93] and the nonsingular contour integral [100] techniques. The outcome is a nonsingular form of the boundary integral equation, which is then discretised based on the discrete surfaces, including the wall surfaces and the films. In cases where foams exist in a bulk, this discretisation yields an explicit expression for the velocities of the films. However, when dealing with foams near solid surfaces, a linear system of equations is formed. To solve this system, the GMRES method with restart [133] is employed.

Chapter 5 also presents two significant applications. In the first, a cluster of five bubbles is

analysed within a simple shear flow environment. This application underscores the importance of considering the effect of the motion of bulk Plateau borders and nodes within the foam cluster on the motion of the rest of the foam. Neglecting this influence can lead to errors in bubble volumes that accumulate over time. The second application examines a 3D channel scenario akin to the one discussed in Chapter 3. Here, the study delves into how a foam film behaves when subjected to an imposed flow resulting from wall deformation. This investigation leverages the concept of motion decomposition derived from the boundary integral equation for dry foam. Notably, it reveals that the primary effect of the imposed strains manifests as a mean curvature perturbation on the film, with a wavelength matching twice the length of the film profile. Moreover, the study demonstrates one-to-one mapping relation between the normal velocity of the film and this primary mean curvature perturbation. In contrast, for higher-order mean curvature perturbations, the relationship exhibits as multi-valued functions.

Chapter 6 further explores the boundary integral method for dry foam from two distinct angles. Firstly, it examines the energy consumption during the motion of a single film within a diverging-converging channel, employing the principle of motion decomposition for the film. In the quasi-static limit, the sole source of energy consumption is found to be viscous dissipation, measured by the loss of surface energy, particularly during the film's jump within the central pore body. This finding provides a novel perspective on understanding the yield stress observed in foam flow within porous media. It suggests that the emergence of yield stress is attributed to viscous dissipation, which consumes a finite amount of surface energy. Importantly, this consumption of surface energy occurs only when the film encounters a sharp corner within the central body of a pore.

The other contribution from Chapter 6 is that the effect of the fluid viscosity within bubbles is further considered, building upon the foundation of the 2D viscous froth model. This extension is preliminarily explored in this work, where the boundary integral equation in 2D is discretised through the Nyström method. A single bubble in a Hele-Shaw is considered, taking into account several factors including film tension, the viscosity of the fluid within the bubbles, and the viscous forces acting on the bubble boundary. It is found that the additional source of energy consumption, namely the viscous dissipation within bubbles, leads to a slower motion of the

bubble boundary compared to the predictions made by the 2D viscous froth model.

Potential avenues of future work are as follows. Future work in this area should further address the challenges and limitations identified in the course of this research. For the boundary integral method applied to 3D dry foam, it is crucial to tackle the issue arising from the slip condition, specifically the neglect of the viscous forces acting on wall Plateau borders. This is particularly important for foam flow in porous media at relatively high flow rates, where the viscous force on wall Plateau borders becomes non-negligible. It is worth noting that this issue also occurs when applying the boundary integral method to emulsions flow, where viscosity in droplets is likely to be even more important than viscosity in bubbles.

In addition, improvements to the boundary-integral modelling of 2D foam within Hele-Shaw cells can be considered, especially when incorporating solid surfaces. Appropriate modelling of the motion of Plateau borders and their impact on the overall foam behaviour is also an important aspect for further research.

Future work could also involve applying the 3D viscous froth model to more complex scenarios, such as the case of three-bubble foams in straight channels that have been recently explored [141, 142, 124]. These endeavours would help expand the applicability of foam modelling techniques and further enhance our understanding of foam behaviour in a variety of settings.

Bibliography

[1] C Hill and J Eastoe. Foams: From nature to industry. *Advances in colloid and interface science*, 247:496–513, 2017.

[2] S Omirbekov, H Davarzani, B Sabyrbay, S Colombano, and A Ahmadi-Senichault. Experimental study of rheological behavior of foam flow in capillary tubes. *Journal of Non-Newtonian Fluid Mechanics*, 302:104774, 2022.

[3] AH Alagorni, ZB Yaacob, and AH Nour. An overview of oil production stages: enhanced oil recovery techniques and nitrogen injection. *International Journal of Environmental Science and Development*, 6(9):693, 2015.

[4] AC Payatakes. Dynamics of oil ganglia during immiscible displacement in water-wet porous media. *Annual Review of Fluid Mechanics*, 14(1):365–393, 1982.

[5] S Thomas. Enhanced oil recovery-an overview. *Oil & Gas Science and Technology-Revue de l'IFP*, 63(1):9–19, 2008.

[6] LW Holm. Carbon dioxide solvent flooding for increased oil recovery. *Transactions of the AIME*, 216(01):225–231, 1959.

[7] LW Holm and VA Josendal. Mechanisms of oil displacement by carbon dioxide. *Journal of petroleum Technology*, 26(12):1427–1438, 1974.

[8] H Hematpur, SM Mahmood, NH Nasr, and KA Elraies. Foam flow in porous media: Concepts, models and challenges. *Journal of Natural Gas Science and Engineering*, 53:163–180, 2018.

[9] H Rahnema, M Barrufet, and DD Mamora. Combustion assisted gravity drainage–experimental and simulation results of a promising in-situ combustion technology to recover extra-heavy oil. *Journal of Petroleum Science and Engineering*, 154:513–520, 2017.

[10] LW Lake and PB Venuto. A niche for enhanced oil recovery in the 1990s. *Oil & Gas Journal*, 88(17):62–67, 1990.

[11] Qiang X. *Theoretical and experimental study of foam for enhanced oil recovery and acid diversion*. The University of Texas at Austin, 2003.

[12] C Wang and HA Li. Stability and mobility of foam generated by gas-solvent/surfactant mixtures under reservoir conditions. *Journal of Natural Gas Science and Engineering*, 34:366–375, 2016.

[13] Q Li. *Foam generation and propagation in homogeneous and heterogeneous porous media*. The University of Texas at Austin, 2006.

[14] MJ Blunt. *Multiphase flow in permeable media: A pore-scale perspective*. Cambridge university press, 2017.

[15] I Fatt. The network model of porous media. *Transactions of the AIME*, 207(01):144–181, 1956.

[16] WR Rossen. Minimum pressure gradient for foam flow in porous media: effect of interactions with stationary lamellae. *Journal of colloid and interface science*, 139(2):457–468, 1990.

[17] W Drenckhan and S Hutzler. Structure and energy of liquid foams. *Advances in colloid and interface science*, 224:1–16, 2015.

[18] D Langevin. Aqueous foams and foam films stabilised by surfactants. gravity-free studies. *Comptes Rendus Mécanique*, 345(1):47–55, 2017.

[19] PS Stewart and S Hilgenfeldt. Gas-liquid foam dynamics: From structural elements to continuum descriptions. *Annual Review of Fluid Mechanics*, 55:323–350, 2023.

[20] J Plateau. Experimental and theoretical statics of liquids subject to molecular forces only. 1873.

[21] AR Kovscek, G Tang, and CJ Radke. Verification of roof snap off as a foam-generation mechanism in porous media at steady state. *Colloids and Surfaces A: Physicochemical and Engineering Aspects*, 302(1-3):251–260, 2007.

[22] S Arif, JC Tsai, and S Hilgenfeldt. Speed of crack propagation in dry aqueous foam. *Europhysics Letters*, 92(3):38001, 2010.

[23] P Grassia, G Montes-Atenas, L Lue, and TE Green. A foam film propagating in a confined geometry: Analysis via the viscous froth model. *The European Physical Journal E*, 25:39–49, 2008.

[24] A Anbari, H-T Chien, SS Datta, W Deng, DA Weitz, and J Fan. Microfluidic model porous media: Fabrication and applications. *Small*, 14(18):1703575, 2018.

[25] WR Rossen. Comment on "verification of roof snap-off as a foam-generation mechanism in porous media at steady state". *Colloids and Surfaces A: Physicochemical and Engineering Aspects*, 322(1-3):261–269, 2008.

[26] R Liontas, K Ma, GJ Hirasaki, and SL Biswal. Neighbor-induced bubble pinch-off: novel mechanisms of in situ foam generation in microfluidic channels. *Soft Matter*, 9(46):10971–10984, 2013.

[27] M Chen, YC Yortsos, and WR Rossen. Insights on foam generation in porous media from pore-network studies. *Colloids and Surfaces A: Physicochemical and Engineering Aspects*, 256(2-3):181–189, 2005.

[28] OS Owete and WE Brigham. Flow behavior of foam: a porous micromodel study. *SPE Reservoir Engineering*, 2(03):315–323, 1987.

[29] TC Ransohoff and CJ Radke. Mechanisms of foam generation in glass-bead packs. *SPE reservoir engineering*, 3(02):573–585, 1988.

[30] JG Roof. Snap-off of oil droplets in water-wet pores. *Society of Petroleum Engineers Journal*, 10(01):85–90, 1970.

[31] WR Rossen. Snap-off in constricted tubes and porous media. *Colloids and Surfaces A: Physicochemical and Engineering Aspects*, 166(1-3):101–107, 2000.

[32] AR Kovscek and CJ Radke. Gas bubble snap-off under pressure-driven flow in constricted noncircular capillaries. *Colloids and Surfaces A: Physicochemical and Engineering Aspects*, 117(1-2):55–76, 1996.

[33] J Gauteplass, K Chaudhary, AR Kovscek, and MA Fernø. Pore-level foam generation and flow for mobility control in fractured systems. *Colloids and Surfaces A: Physicochemical and Engineering Aspects*, 468:184–192, 2015.

[34] RF Mast. Microscopic behavior of foam in porous media. In *Fall Meeting of the Society of Petroleum Engineers of AIME*. OnePetro, 1972.

[35] MM Almajid and AR Kovscek. Pore-level mechanics of foam generation and coalescence in the presence of oil. *Advances in colloid and interface science*, 233:65–82, 2016.

[36] AR Kovscek and CJ Radke. Fundamentals of foam transport in porous media. Technical report, Lawrence Berkeley Lab., CA (United States), 1993.

[37] SJ Cox. Simulations of bubble division in the flow of a foam past an obstacle in a narrow channel. *Colloids and Surfaces A: Physicochemical and Engineering Aspects*, 473:104–108, 2015.

[38] PA Gauglitz, F Friedmann, SI Kam, and WR Rossen. Foam generation in porous media. In *SPE/DOE Improved Oil Recovery Symposium*. OnePetro, 2002.

[39] S Xiao, Y Zeng, ED Vavra, P He, M Puerto, GJ Hirasaki, and SL Biswal. Destabilization, propagation, and generation of surfactant-stabilized foam during crude oil displacement in heterogeneous model porous media. *Langmuir*, 34(3):739–749, 2018.

[40] M Rashed Rohani, C Ghotbi, and A Badakhshan. Foam stability and foam-oil interactions. *Petroleum science and technology*, 32(15):1843–1850, 2014.

[41] R Sedev and D Exerowa. Dlvo and non-dlvo surface forces in foam films from amphiphilic block copolymers. *Advances in colloid and interface science*, 83(1-3):111–136, 1999.

[42] R Farajzadeh, R Krastev, and PLJ Zitha. Foam films stabilized with alpha olefin sulfonate (aos). *Colloids and Surfaces A: Physicochemical and Engineering Aspects*, 324(1-3):35–40, 2008.

[43] Y Zeng, R Farajzadeh, AA Eftekhari, S Vincent-Bonnieu, A Muthuswamy, WR Rossen, GJ Hirasaki, and SL Biswal. Role of gas type on foam transport in porous media. *Langmuir*, 32(25):6239–6245, 2016.

[44] AS Aronson, V Bergeron, ME Fagan, and CJ Radke. The influence of disjoining pressure on foam stability and flow in porous media. *Colloids and Surfaces A: Physicochemical and Engineering Aspects*, 83(2):109–120, 1994.

[45] C Hédreul and G Frens. Foam stability. *Colloids and Surfaces A: Physicochemical and Engineering Aspects*, 186(1-2):73–82, 2001.

[46] ZI Khatib, GJ Hirasaki, and AH Falls. Effects of capillary pressure on coalescence and phase mobilities in foams flowing through porous media. *SPE reservoir engineering*, 3(03):919–926, 1988.

[47] SA Jones, N Getrouw, and S Vincent-Bonnieu. Foam flow in a model porous medium: I. the effect of foam coarsening. *Soft matter*, 14(18):3490–3496, 2018.

[48] LE Nonnekes, SJ Cox, and WR Rossen. Effect of gas diffusion on mobility of foam for enhanced oil recovery. *Transport in Porous Media*, 106(3):669–689, 2015.

[49] Y Kim, M Lai, and CS Peskin. Numerical simulations of two-dimensional foam by the immersed boundary method. *Journal of Computational Physics*, 229(13):5194–5207, 2010.

[50] D Cohen, TW Patzek, and CJ Radke. Two-dimensional network simulation of diffusion-driven coarsening of foam inside a porous medium. *Journal of colloid and interface science*, 179(2):357–373, 1996.

[51] AH Falls, JB Lawson, and GJ Hirasaki. The role of noncondensable gas in steam foams. *Journal of petroleum technology*, 40(01):95–104, 1988.

[52] WR Rossen. Foams in enhanced oil recovery, chapter 12 in foams: Theory, measurements and applications, prud'homme, rk and khan, s, 1996.

[53] K Ma, R Liontas, CA Conn, GJ Hirasaki, and SL Biswal. Visualization of improved sweep with foam in heterogeneous porous media using microfluidics. *Soft Matter*, 8(41):10669–10675, 2012.

[54] D Weaire and N Rivier. Soap, cells and statistics—random patterns in two dimensions. *Contemporary Physics*, 25(1):59–99, 1984.

[55] DA Reinelt and AM Kraynik. Simple shearing flow of dry soap foams with tetrahedrally close-packed structure. *Journal of Rheology*, 44(3):453–471, 2000.

[56] SA Jones, B Dollet, Y Méheust, SJ Cox, and I Cantat. Structure-dependent mobility of a dry aqueous foam flowing along two parallel channels. *Physics of Fluids*, 25(6):063101, 2013.

[57] SA Jones, N Getrouw, and S Vincent-Bonnieu. Foam flow in a model porous medium: Ii. the effect of trapped gas. *Soft matter*, 14(18):3497–3503, 2018.

[58] M Lv, Z Liu, C Ji, L Jia, and Y Jiang. Investigation of pore-scale behaviors of foam flow in a polydimethylsiloxane micromodel. *Industrial & Engineering Chemistry Research*, 57(44):15172–15180, 2018.

[59] A Mauray, M Chabert, and H Bodiguel. Yield stress fluid behavior of foam in porous media. *Physical Review Fluids*, 5(9):094004, 2020.

[60] CJ Radke and JV Gillis. A dual gas tracer technique for determining trapped gas saturation during steady foam flow in porous media. In *SPE Annual Technical Conference and Exhibition?*, pages SPE–20519. SPE, 1990.

[61] F Friedmann, WH Chen, and PA Gauglitz. Experimental and simulation study of high-temperature foam displacement in porous media. *SPE reservoir engineering*, 6(01):37–45, 1991.

[62] Z Pang, X Lyu, F Zhang, T Wu, Z Gao, Z Geng, and C Luo. The macroscopic and microscopic analysis on the performance of steam foams during thermal recovery in heavy oil reservoirs. *Fuel*, 233:166–176, 2018.

[63] CA Conn, K Ma, GJ Hirasaki, and SL Biswal. Visualizing oil displacement with foam in a microfluidic device with permeability contrast. *Lab on a Chip*, 14(20):3968–3977, 2014.

[64] A Telmadarreie and JJ Trivedi. New insight on carbonate-heavy-oil recovery: pore-scale mechanisms of post-solvent carbon dioxide foam/polymer-enhanced-foam flooding. *SPE Journal*, 21(05):1655–1668, 2016.

[65] WR Rossen. Theory of mobilization pressure gradient of flowing foams in porous media: I. incompressible foam. *Journal of Colloid and Interface Science*, 136(1):1–16, 1990.

[66] SJ Cox, SJ Neethling, WR Rossen, W Schleifenbaum, P Schmidt-Wellenburg, and JJ Cilliers. A theory of the effective yield stress of foam in porous media: the motion of a soap film traversing a three-dimensional pore. *Colloids and Surfaces A: Physicochemical and Engineering Aspects*, 245(1-3):143–151, 2004.

[67] FP Bretherton. The motion of long bubbles in tubes. *Journal of Fluid Mechanics*, 10(2):166–188, 1961.

[68] H Wong, CJ Radke, and S Morris. The motion of long bubbles in polygonal capillaries. part 1. thin films. *Journal of Fluid Mechanics*, 292:71–94, 1995.

[69] H Wong, CJ Radke, and S Morris. The motion of long bubbles in polygonal capillaries. part 2. drag, fluid pressure and fluid flow. *Journal of Fluid Mechanics*, 292:95–110, 1995.

[70] GJ Hirasaki and JB Lawson. Mechanisms of foam flow in porous media: apparent viscosity in smooth capillaries. *Society of Petroleum Engineers Journal*, 25(02):176–190, 1985.

[71] WT Osterloh and MJ Jante. Effects of gas and liquid velocity on steady-state foam flow at high temperature. In *SPE/DOE Enhanced Oil Recovery Symposium*. OnePetro, 1992.

[72] JM Alvarez, HJ Rivas, and WR Rossen. Unified model for steady-state foam behavior at high and low foam qualities. *SPE journal*, 6(03):325–333, 2001.

[73] K Kornev and G Shugai. Thermodynamic and hydrodynamic peculiarities of a foam lamella confined in a cylindrical pore. *Physical Review E*, 58(6):7606, 1998.

[74] I Cantat, N Kern, and R Delannay. Dissipation in foam flowing through narrow channels. *Europhysics Letters*, 65(5):726, 2004.

[75] C Raufaste, A Foulon, and B Dollet. Dissipation in quasi-two-dimensional flowing foams. *Physics of Fluids*, 21(5):053102, 2009.

[76] O Gassara, F Douarche, B Braconnier, and B Bourbiaux. Calibrating and interpreting implicit-texture models of foam flow through porous media of different permeabilities. *Journal of Petroleum Science and Engineering*, 159:588–602, 2017.

[77] F Friedmann, ME Smith, WR Guice, JM Gump, and DG Nelson. Steam-foam mechanistic field trial in the midway-sunset field. *SPE Reservoir Engineering*, 9(04):297–304, 1994.

[78] TW Patzek and MT Koinis. Kern river steam-foam pilots. *Journal of Petroleum Technology*, 42(04):496–503, 1990.

[79] J Bear and J-M Buchlin. *Modelling and applications of transport phenomena in porous media*, volume 5. Springer, 1991.

[80] SK Govindarajan. An overview on extension and limitations of macroscopic darcy's law for a single and multi-phase fluid flow through a porous medium. *International Journal of Mining Science (IJMS) Volume*, 5:1–21, 2019.

[81] SM Hassanizadeh and WG Gray. Thermodynamic basis of capillary pressure in porous media. *Water resources research*, 29(10):3389–3405, 1993.

[82] Q Kang, D Zhang, and S Chen. Immiscible displacement in a channel: simulations of fingering in two dimensions. *Advances in water resources*, 27(1):13–22, 2004.

[83] H Li, C Pan, and CT Miller. Pore-scale investigation of viscous coupling effects for two-phase flow in porous media. *Physical Review E*, 72(2):026705, 2005.

[84] SH Chang, LA Owusu, SB French, and FS Kovarik. The effect of microscopic heterogeneity on co2-foam mobility: Part 2-mechanistic foam simulation. In *SPE Improved Oil Recovery Conference?*, pages SPE–20191. SPE, 1990.

[85] L Chen, A He, J Zhao, Q Kang, Z Li, J Carmeliet, N Shikazono, and W Tao. Pore-scale modeling of complex transport phenomena in porous media. *Progress in Energy and Combustion Science*, 88:100968, 2022.

[86] TC Lavoratti, S Heitkam, U Hampel, and G Lecrivain. A computational method to simulate mono-and poly-disperse two-dimensional foams flowing in obstructed channel. *Rheologica Acta*, 60:587–601, 2021.

[87] KA Brakke. The surface evolver. *Experimental mathematics*, 1(2):141–165, 1992.

[88] TE Green, A Bramley, L Lue, and P Grassia. Viscous froth lens. *Physical Review E*, 74(5):051403, 2006.

[89] N Kern, D Weaire, A Martin, S Hutzler, and SJ Cox. Two-dimensional viscous froth model for foam dynamics. *Physical Review E*, 70(4):041411, 2004.

[90] F Rouyer, S Cohen-Addad, M Vignes-Adler, and R Höhler. Dynamics of yielding observed in a three-dimensional aqueous dry foam. *Physical Review E*, 67(2):021405, 2003.

[91] JA Glazier and D Weaire. The kinetics of cellular patterns. *Journal of Physics: Condensed Matter*, 4(8):1867, 1992.

[92] C Pozrikidis. *Boundary integral and singularity methods for linearized viscous flow*. Cambridge university press, 1992.

[93] A Zinchenko and R Davis. A boundary-integral study of a drop squeezing through interparticle constrictions. *Journal of Fluid Mechanics*, 564:227–266, 2006.

[94] JR Gissinger, AZ Zinchenko, and RH Davis. Drop squeezing between arbitrary smooth obstacles. *Journal of Fluid Mechanics*, 908:A33, 2021.

[95] H Zhou and C Pozrikidis. The flow of suspensions in channels: single files of drops. *Physics of Fluids A: Fluid Dynamics*, 5(2):311–324, 1993.

[96] H Zhou and C Pozrikidis. Pressure-driven flow of suspensions of liquid drops. *Physics of Fluids*, 6(1):80–94, 1994.

[97] J. Blawzdziewicz. *Boundary integral methods for Stokes flows*, page 193–236. Cambridge University Press, 2007.

[98] R. Farajzadeh, A Andrianov, R Krastev, GJ Hirasaki, and WR Rossen. Foam–oil interaction in porous media: Implications for foam assisted enhanced oil recovery. *Advances in Colloid and Interface Science*, 183–184:1–13, 2012.

[99] K Ma, G Ren, K Mateen, D Morel, and P Cordelier. Modeling techniques for foam flow in porous media. *SPE Journal*, 20(03):453–470, 2015.

[100] IB Bazhlekov, PD Anderson, and HEH Meijer. Nonsingular boundary integral method for deformable drops in viscous flows. *Physics of Fluids*, 16(4):1064–1081, 2004.

[101] V Doyeux, Y Guyot, V Chabannes, C Prud'Homme, and M Ismail. Simulation of two-fluid flows using a finite element/level set method. application to bubbles and vesicle dynamics. *Journal of Computational and Applied Mathematics*, 246:251–259, 2013.

[102] C Zhang, F Wang, Z Li, and H Chen. Dynamic simulation and experimental verification of foam transport in porous media based on level set method. *Energy Science & Engineering*, 7(5):1795–1807, 2019.

[103] M Starnoni and D Pokrajac. Numerical study of the effects of contact angle and viscosity ratio on the dynamics of snap-off through porous media. *Advances in Water Resources*, 111:70–85, 2018.

[104] BA Nichita, I Zun, and JR Thome. A level set method coupled with a volume of fluid method for modeling of gas-liquid interface in bubbly flow. *Journal of fluids engineering*, 132(8), 2010.

[105] T Inamuro, T Ogata, S Tajima, and N Konishi. A lattice boltzmann method for incompressible two-phase flows with large density differences. *Journal of Computational physics*, 198(2):628–644, 2004.

[106] E Sattari, SP Zanous, M Farhadi, and A Mohamad. Numerical investigation of the vapor bubble's scenarios passing through aerophobic/aerophilic porous structures using lattice boltzmann method. *Journal of Power Sources*, 454:227929, 2020.

[107] RI Saye and JA Sethian. Multiscale modeling of membrane rearrangement, drainage, and rupture in evolving foams. *Science*, 340(6133):720–724, 2013.

[108] Y Kim, M-C Lai, CS Peskin, and Y Seol. Numerical simulations of three-dimensional foam by the immersed boundary method. *Journal of Computational Physics*, 269:1–21, 2014.

[109] I Chatzis and FAL Dullien. Modelling pore structure by 2-d and 3-d networks with applicationto sandstones. *Journal of Canadian Petroleum Technology*, 16(01):97–108, 1977.

[110] WR Rossen. Theories of foam mobilization pressure gradient. In *SPE Enhanced Oil Recovery Symposium*. OnePetro, 1988.

[111] WR Rossen. Theory of mobilization pressure gradient of flowing foams in porous media: III. asymmetric lamella shapes. *Journal of Colloid and Interface Science*, 136(1):38–53, 1990.

[112] WR Rossen. Theory of mobilization pressure gradient of flowing foams in porous media: I. incompressible foam. *Journal of Colloid and Interface Science*, 136(1):1–16, 1990.

[113] Q Xu and WR Rossen. Effective viscosity of foam in periodically constricted tubes. *Colloids and Surfaces A: Physicochemical and Engineering Aspects*, 216(1-3):175–194, 2003.

[114] RA Ettinger and CJ Radke. Influence of texture on steady foam flow in berea sandstone. *SPE reservoir engineering*, 7(01):83–90, 1992.

[115] DJ Ferguson and SJ Cox. The motion of a foam lamella traversing an idealised bi-conical pore with a rounded central region. *Colloids and Surfaces A: Physicochemical and Engineering Aspects*, 438:56–62, 2013.

[116] SJ Cox and IT Davies. Simulations of quasi-static foam flow through a diverging-converging channel. *Korea-Australia Rheology Journal*, 28(3):181–186, 2016.

[117] WR Rossen. Theory of mobilization pressure gradient of flowing foams in porous media: II. effect of compressibility. *Journal of Colloid and Interface Science*, 136(1):17–37, 1990.

[118] SJ Cox. A viscous froth model for dry foams in the surface evolver. *Colloids and Surfaces A: Physicochemical and Engineering Aspects*, 263(1-3):81–89, 2005.

[119] C Raufaste, SJ Cox, RE Goldstein, and AI Pesci. Collapse of a hemicatenoid bounded by a solid wall: instability and dynamics driven by surface plateau border friction. *Soft Matter*, 18(26):4944–4952, 2022.

[120] SJ Cox, D Weaire, and G Mishuris. The viscous froth model: steady states and the high-velocity limit. *Proceedings of the Royal Society A: Mathematical, Physical and Engineering Sciences*, 465(2108):2391–2405, 2009.

[121] W Drenckhan, SJ Cox, G Delaney, H Holste, D Weaire, and N Kern. Rheology of ordered foams—on the way to discrete microfluidics. *Colloids and Surfaces A: Physicochemical and Engineering Aspects*, 263(1-3):52–64, 2005.

[122] C Torres-Ulloa. *Modelling foam flow through confined geometries.* PhD thesis, University of Strathclyde, 2021.

[123] C Torres-Ulloa and P Grassia. Viscous froth model applied to the dynamic simulation of bubbles flowing in a channel: three-bubble case. *Proceedings of the Royal Society A*, 478(2267):20220487, 2022.

[124] C Torres-Ulloa and P Grassia. Viscous froth model applied to multiple topological transformations of bubbles flowing in a channel: three-bubble case. *Proceedings of the Royal Society A*, 479(2275):20220785, 2023.

[125] D Vitasari and SJ Cox. A viscous froth model adapted to wet foams. *Colloids and Surfaces A: Physicochemical and Engineering Aspects*, 534:8–15, 2017.

[126] D Vitasari, SJ Cox, P Grassia, and R Rosario. Effect of surfactant redistribution on the flow and stability of foam films. *Proceedings of the Royal Society A*, 476(2234):20190637, 2020.

[127] H Zhang, PR Brito-Parada, SJ Neethling, and Y Wang. Yield stress of foam flow in porous media: The effect of bubble trapping. *Colloids and Surfaces A: Physicochemical and Engineering Aspects*, 655:130246, 2022.

[128] IB Bajlekov. *Non-singular boundary-integral method for deformable drops in viscous flows.* PhD thesis, Mechanical Engineering, 2003.

[129] P Persson. *Mesh generation for implicit geometries.* PhD thesis, Massachusetts Institute of Technology, 2005.

[130] M Loewenberg and EJ Hinch. Numerical simulation of a concentrated emulsion in shear flow. *Journal of Fluid Mechanics*, 321:395–419, 1996.

[131] A Zinchenko, M Rother, and R Davis. A novel boundary-integral algorithm for viscous interaction of deformable drops. *Physics of Fluids*, 9(6):1493–1511, 1997.

[132] C Geuzaine and J-F Remacle. Gmsh: A 3-D finite element mesh generator with built-in pre-and post-processing facilities. *International journal for numerical methods in engineering*, 79(11):1309–1331, 2009.

[133] Y Saad and M Schultz. Gmres: A generalized minimal residual algorithm for solving nonsymmetric linear systems. *SIAM Journal on scientific and statistical computing*, 7(3):856–869, 1986.

[134] QP Nguyen, PK Currie, and PL Zitha. Motion of foam films in diverging–converging channels. *Journal of colloid and interface science*, 271(2):473–484, 2004.

[135] R Ojala and A Tornberg. An accurate integral equation method for simulating multiphase stokes flow. *Journal of Computational Physics*, 298:145–160, 2015.

[136] S Pålsson and A Tornberg. An integral equation method for closely interacting surfactant-covered droplets in wall-confined stokes flow. *International Journal for Numerical Methods in Fluids*, 92(12):1975–2008, 2020.

[137] S Hao, AH Barnett, P Martinsson, and P Young. High-order accurate methods for nyström discretization of integral equations on smooth curves in the plane. *Advances in Computational Mathematics*, 40(1):245–272, 2014.

[138] P Kolm and V Rokhlin. Numerical quadratures for singular and hypersingular integrals. *Computers & Mathematics with Applications*, 41(3-4):327–352, 2001.

[139] N Kofman, S Mergui, and C Ruyer-Quil. Three-dimensional instabilities of quasi-solitary waves in a falling liquid film. *Journal of fluid mechanics*, 757:854–887, 2014.

[140] JC Bird, R De Ruiter, L Courbin, and HA Stone. Daughter bubble cascades produced by folding of ruptured thin films. *Nature*, 465(7299):759–762, 2010.

[141] C Torres-Ulloa and P Grassia. Viscous froth model applied to the motion and topological transformations of two-dimensional bubbles in a channel: three-bubble case. *Proceedings of the Royal Society A*, 478(2258):20210642, 2022.

[142] C Torres-Ulloa and P Grassia. Viscous froth model applied to the dynamic simulation of bubbles flowing in a channel: three-bubble case. *Proceedings of the Royal Society A*, 478(2267):20220487, 2022.